EARLY NUCLEOSYNTHESIS STUDIES WITH QUASAR ABSORPTION LINE SPECTROSCOPY

Peter Erni

PhD thesis

Erni, Peter:
Early Nucleosynthesis Studies with Quasar Absorption Line Spectroscopy

223 pages, 63 figures, 20 tables

Peter Erni
Argelander-Institut für Astronomie
Universität Bonn
Auf dem Hügel 71
53121 Bonn, Germany
Email: perni@astro.uni-bonn.de

Online version available under
http://hss.ulb.uni-bonn.de/diss_online/math_nat_fak/2007

Cover picture:
Quasar absorption line spectroscopy with UVES/VLT (illustration ESO)

This document was written using LaTeX.

EARLY NUCLEOSYNTHESIS STUDIES WITH QUASAR ABSORPTION LINE SPECTROSCOPY

Dissertation

zur

Erlangung des Doktorgrades (Dr. rer. nat.)

der

Mathematisch-Naturwissenschaftlichen Fakultät

der

Rheinischen Friedrich-Wilhelms-Universität zu Bonn

vorgelegt von

Peter Erni

aus Altishofen / Schweiz

Bonn, im Januar 2007

Angefertigt mit Genehmigung der Mathematisch-Naturwissenschaftlichen Fakultät der Rheinischen Friedrich-Wilhelms-Universität Bonn.

Erstgutachter:	Prof. Dr. Peter Schneider
Zweitgutachter:	Prof. Dr. Klaas S. de Boer
fachnahes Mitglied:	Prof. Dr. Herbert Petry
fachangrenzendes Mitglied:	Prof. Dr. Reinhard Klein
Tag der Promotion:	5. März 2007

There is no problem so complicated that you cannot find a very simple answer to it if you look at it in the right way.

Douglas Adams

Contents

List of Tables

List of Figures

1. Summary

Studying the light of celestial objects in different wavelengths is a fundamental approach and very common in astronomy, where large ground based telescopes and sophisticated high-resolution spectrographs became recently available to the scientific community. The smaller spectrographs aboard satellites are equally important because they are not restricted to the optical band and not affected by any atmospheric aberrations. Both, the large ground based instruments and satellites made it possible to extend the spectroscopic study of the Universe onto a cosmological scale.

The Universe is almost empty and has an average density of only about one atom per cubic meter. However, the density is clearly not uniform and ranges from regions almost devoid of any matter (voids) through regions with relatively high densities (galaxy clusters and galaxies) to objects with very high densities (stars). Only about 30 % of the baryonic matter content in the present-day Universe is found in a condensed phase, i.e., in the form of stars and galaxies. In the past there were fewer stars and more matter was present in gaseous form. At a redshift of $z \approx 2-3$, i.e., more than 10^{10} years ago, when the Universe had only about $15-25$ % of its present age, over 95 % of the (ordinary) baryonic matter was solely present in the form of gas. This epoch is of particular interest because it marks the time when most of the galaxies started to form and to condense out of the intergalactic medium.

Quasars, a kind of cosmological beacons, are extremely bright and some of the most distant objects known to date. Their light was emitted at a time when the Universe had only about 10 % of its present age. Hence, their light travels over vast distances before we observe it here on Earth. Light that encounters gas is absorbed in very well defined wavelength ranges. Following the laws of quantum mechanics, only photons with specific energies are absorbed and will cause specific absorption lines that arise mostly from the Lyman transitions of neutral hydrogen, the most abundant element in the Universe. The expansion of the Universe stretches the photons' wavelengths (Hubble redshift) on their way to Earth. Since neutral hydrogen clouds at different distances will always encounter photons at different wavelengths, each individual cloud leaves its fin-

gerprint in form of an absorption line at a different position, λ, in the observed spectrum. The Lyman absorption lines, and in particular lines that arise from the Lyman α transition, are so frequent and densely packed that it is common to speak of them as the Lyman α forest. With the Lyman α forest absorption lines it is possible to investigate the properties of the intergalactic medium, e.g., to determine the density, temperature or occurrence of the intervening gas clouds containing neutral hydrogen. Furthermore, the search for lines from other elements (matching in redshift), like carbon, nitrogen, oxygen, silicon, etc., allows us to study the abundance of heavier elements, too.

A damped Lyman α system is a gas cloud with a high column density of neutral hydrogen and shows broad absorption lines with typical Lorentzian damping wings. Number statistics of damped Lyman α systems imply that these objects dominate the neutral gas content of the Universe at $z > 1$, making them prime candidates to be the progenitors of present-day galaxies. The present work is about damped Lyman α absorption line systems and their involvement in early nucleosynthesis enrichment. Chapters $3-5$ are a general introduction to the properties of the intergalactic medium, intergalactic absorption lines, and the technique of quasar absorption line spectroscopy. The subsequent chapters focus on the analysis and interpretation of particular lines of sight that had been studied in detail, except for Chapter 7 that extends the finding from the previous chapter and gives more general considerations on very early nucleosynthesis.

Chapter 3 – A short overview of the properties of the intergalactic medium is given. Different environments, ranging from low to high densities, are introduced. The common classification for quasar absorption line systems is given and I show that the gas density is closely related to the gas temperature. Further, the process of ionization is exemplified and I give clear arguments why the bulk of the gas in the intergalactic medium is ionized by photons from the UV background radiation, and why collisional ionization only becomes significant in hotter and denser regions such as the gas in galaxy clusters or the gas in galaxies.

Chapter 4 – In this chapter I discuss the nature of absorption lines that arise when the quasar's light travels through intergalactic or interstellar gas. I derive the line profile (Voigt profile), a convolution of the Lorentz function that describes the finite width and the Maxwellian velocity distribution function that accounts for the intrinsic particle motion in the gas itself (Doppler velocity or temperature, respectively). Measures, such as the radiation intensity, the optical

depth, the column density, and the Doppler parameter are introduced and set in context to each other. Finally, I discuss different effects of line broadening and saturated absorption lines.

Chapter 5 – This chapter is dedicated to the data reduction techniques I have used in this work. The technical specifications and observing capabilities of the UVES/VLT spectrograph are given and the different setup configurations are explained. After column densities and Doppler parameters are measured in the observed spectra, using the previously described measuring methods, the data have to be corrected for altering effects due to photoionization and dust within the absorption line system itself. In general, only a few ionization states can be observed and, hence, the derived column densities contribute only partially to the total column density of an element (ionization correction). Dust also plays an important role because gas-phase atoms will stick onto dust grains and eventually cause a change in the observed metal abundance pattern (dust depletion). Finally, I give some details on logarithmic error calculus because in log-space the normal distribution and therefore the standard error calculus methods are no longer applicable.

Chapter 6 – In this chapter I report on the damped Lyman α system at $z_{\rm abs} = 2.6183$ toward the quasar Q 0913+072. I have analyzed UVES/VLT high-resolution data from the ESO archive in detail and discovered remarkable facts: not only is this damped Lyman α the most metal deficient absorption line system of its kind at $z < 3$, it was also possible to measure its CNO elements with high accuracy. This and the comparison of its characteristic metal abundance pattern with yields from model calculations allows us to conclude on the type of stars that must have previously enriched this absorption line system.

Chapter 7 – I discuss the mechanism for star formation in primordial or poorly enriched gas clouds, where the cooling function is of particular interest. The different fragmentation mechanism in pristine gas clouds implies that the first stars in the Universe might have been very massive with masses of up to $600\,M_{\odot}$. Stars that are so massive do no longer explode as (typical) core-collapse supernovae but undergo a different explosion mechanism due to an electron-positron pair instability. This in mind, I make use of the same approach as in the previous chapter and compare the abundance pattern of very metal deficient objects with results from model calculations to derive constraints on the first stellar generations in the Universe. The method is applied to 59 damped Lyman α systems,

to 21 extremely metal-poor stars, and to 2 hyper metal-poor stars.

Chapter 8 – The line of sight toward the quasar Q 0420−388 represents a particular case of its own. At a redshift of $z_{\rm abs} = 3.088$ we can identify two interacting absorption line systems, only separated by $160\,{\rm km\,s^{-1}}$ ($\Delta z = 0.0005$), that are manifestly different in their structure and their metal content. While one of these two absorption line systems shows a metal content of 5 % solar and a clear structure with six individual subcomponents, we can identify in the other absorption line (almost) no substructure but a metal content of 35 % solar. Additionally, this line of sight offers one of the rare opportunities to measure deuterium at high redshift. Even though the D/H ratio is nowadays measured by the cosmic microwave background radiation, it is important to study the deuterium abundance also directly. The deuterium abundance we derive is in very good agreement with the predictions from the standard big bang nucleosynthesis model and other measurements. Further, we detect highly ionized species in between the two absorption line systems that are most likely heated by collisional ionization – clear indications that we are witnessing the merging of two early galaxies at high redshift.

Chapter 9 – So-called *dark clumps* are putative non-luminous mass concentrations with masses on the orders of galaxies or galaxy clusters, found in large weak gravitation lensing surveys. Yet, there is no known mechanism that could efficiently prohibit star formation in such an object. Hence, the nature of dark clumps or their mere existence remains mysterious. The technique of quasar absorption line spectroscopy, completely independent of gravitational effects and the luminosity of the object under study, offers an elegant alternative approach to this problem. I compared 63 dark clump candidates with over 60 000 known quasars and found, by pure coincidence, a quasar with adequate redshift, brightness, and separation in projection, in order to detect any gas that would be associated with one of these dark clumps – if present. From the observational data we derive restrictive upper limits for the transition lines of single ionized magnesium (and other species). Thus, we conclude that the detected lensing signal in this particular case (line of sight toward the quasar 004345.8−294733) is most likely not due to the presence of a significant (baryonic) mass concentration but presumably the result of statistical inhomogeneities, i.e., a so-called statistical fluke.

Chapter 10 – The aim of our ESO proposal 077.B–0758(A), as presented in

this chapter, is the investigation of the temperature and ionization of the intergalactic medium at a redshift of $z \approx 2$. We have applied for very high-resolution ($R \sim 75\,000$) observation with the UVES/VLT spectrograph that would allow us to resolve the subcomponent structures of C IV and O VI absorption lines toward the quasar PKS 1448–232. These subcomponent structures could not be resolved in the past because any previous high-resolution observation of such systems are carried out with resolutions on the order of typically $R \sim 45\,000$. Although our observation was only partially carried out, we have obtained a spectrum with very high resolution but a somewhat modest signal-to-noise ratio. Yet, the quality of the data was already sufficient to resolve some subcomponents. The remaining observation blocks are reported to the forthcoming observation period P79. The complete data set will allow us accurate measures of the component structure and line widths of the intervening O VI and C IV absorbers.

2. Preface

Doing PhD research is an extraordinary venture between a multitude of concepts and tools one has to understand, learn how to use, and the challenge of undertaking one's own research and eventually be able to contribute to the scientific progress in a particular field.

The data I have been using consisted predominantly of spectra taken from quasars. I was – and in fact I still am – overwhelmed by the amount of information on the intergalactic medium that can be retrieved from such a spectrum, only an inconspicuous wiggly line at first sight. These data can be used to investigate a large range of different topics which are of highest interest to the scientific community. In my case, I have analyzed in detail four different lines of sight toward background quasars, and in each case there were new and challenging findings, ranging from merging galaxies at high redshift, testing the existence of a non-luminous mass concentration as predicted by gravitational lensing studies, to very early nucleosynthesis and the first stars in the Universe.

It was a privilege to have been able to work on so many different aspects while basically the same observational approach was used throughout. It is, of course, necessary that one focuses and specializes on a certain topic or technique during his (or her) PhD thesis period. On the other hand, I find it also of high importance that one broadens his (or hers) horizon and way of thinking. Looking at the same object or question from different points of view will always reveal new aspects. Sometimes, nature shows that an object can be utterly different, or even in contradiction with previous findings, when looking at it from a different point of view. Hence, it should be kept in mind that analyzing intervening absorption line systems along a line of sight to a quasar is somewhat similar to looking at a given object from *one* specific point of view. Arriving at a general conclusion or interpretation is therefore always a multidisciplinary task. The wealth of information coded in quasar absorption line spectra, in combination with the ability of probing a large range of utterly different fields, makes the technique of quasar absorption line spectroscopy an indispensable tool in modern cosmology.

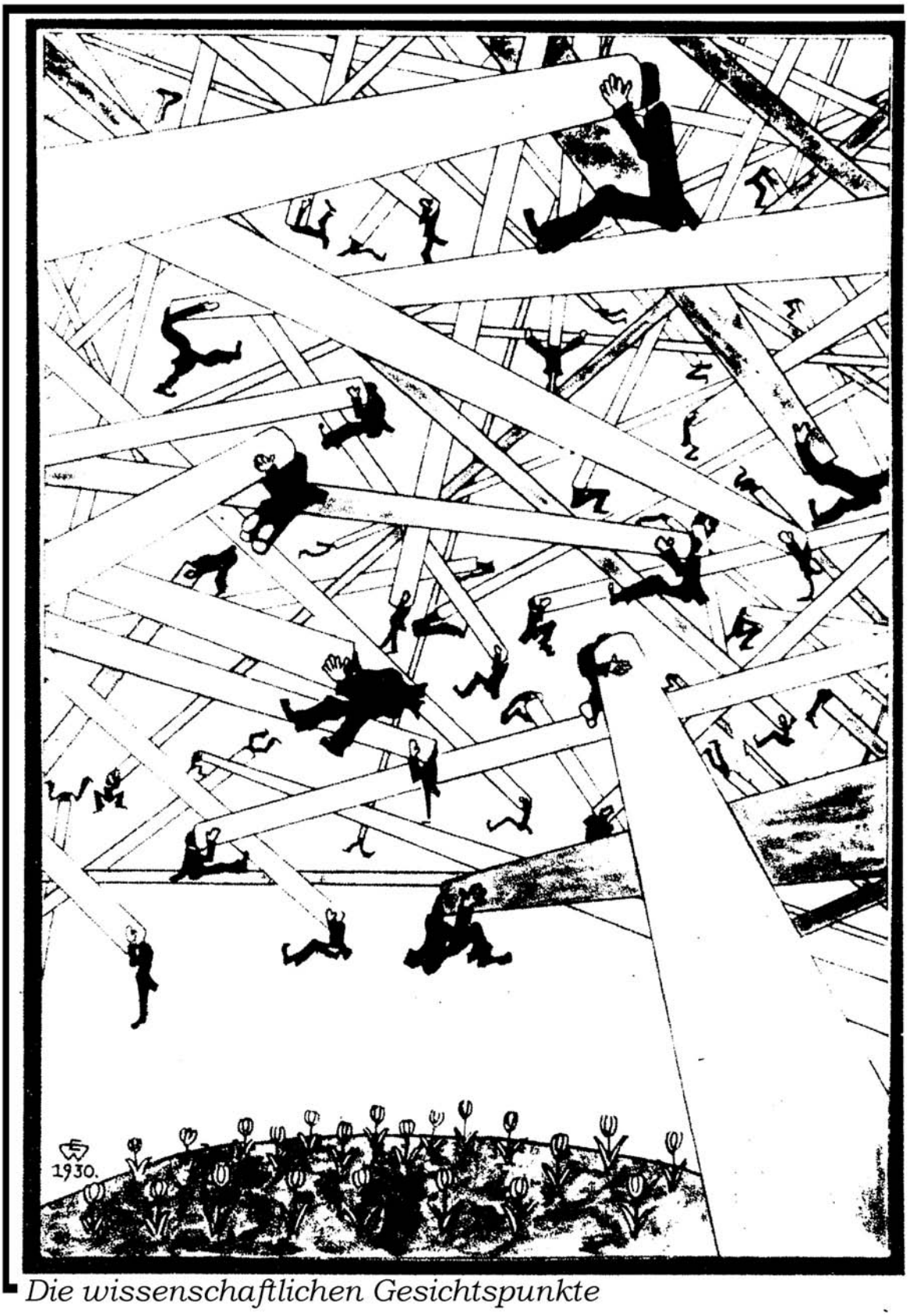

Figure 2.1.: *The Scientific Viewpoints* (Wegmann 1939).

Due to their high resolving capacity, spectrographs on ground based telescopes allow the study of a wide range of quasars. However, they are restricted to the optical and near UV bands, limited by the atmospheric cut-off at ~ 3000 Å. Currently, only the FUSE, GALEX, and SWIFT satellites can access the interesting far UV band, and hence the absorbers at very low redshifts (however, only a few dozen quasars are bright enough to be observed by the relatively small satellite spectrographs). Within the frame of the upcoming service mission SM4[1] on HST in mid- to late-2008, a new spectrograph, the Cosmic Origins Spectrograph (COS), will become available for quasar absorption line studies at wavelengths below ~ 3000 Å. Aside from the UV and the visual band, toward longer wavelengths, the Atacama Pathfinder Experiment (APEX) and eventually the Atacama Large Millimeter Array[2] (ALMA) will make submillimeter wavelengths, an almost unexplored spectral range, accessible and hence push open a new window and very promising field in astronomy.

[1] Next to a new wide field camera, the Wide Field Camera 3 (WFC3), an attempt to repair the Space Telescope Imaging Spectrograph (STIS) is planned. In addition, new gyroscopes and batteries will enable HST to extend its lifetime through 2013.

[2] Construction planned to be finished by 2012.

3. Introduction to the Intergalactic Medium

3.1. Overview

The density of the Universe[1] is clearly not uniform and ranges from vast volumes almost devoid of any matter (so-called *voids* with typically $50\,h^{-1}\,\mathrm{Mpc}$ in diameter[2]) through relatively high densities in galaxy clusters ($\sim 10^{-27}\,\mathrm{g\,cm^{-3}}$) and galaxies ($\sim 10^{-24}\,\mathrm{g\,cm^{-3}}$) to very high densities in stars ($> 1\,\mathrm{g\,cm^{-3}}$). The Intergalactic Medium (IGM) is, simply speaking, the gaseous medium in-between galaxies. More precisely: the IGM is the material out of which galaxies formed, the repository of the dominant component of ordinary (baryonic) matter in the Universe. The IGM is also a sort of dumping place for baryons ejected from galaxies, where interactions of the IGM with galaxies invoke a number of feedback processes that are essential for the understanding of the formation and evolution of galaxies.

[1] Average (critical) density of the Universe: $\rho_{\mathrm{crit}} = 0.94^{+0.06}_{-0.09} \times 10^{-29}\,\mathrm{g\,cm^{-3}}$ (Spergel et al. 2006).

[2] By definition: $h \doteq H_0 / \left(100\,\mathrm{km\,s^{-1}\,Mpc^{-1}}\right)$, with H_0 the Hubble constant

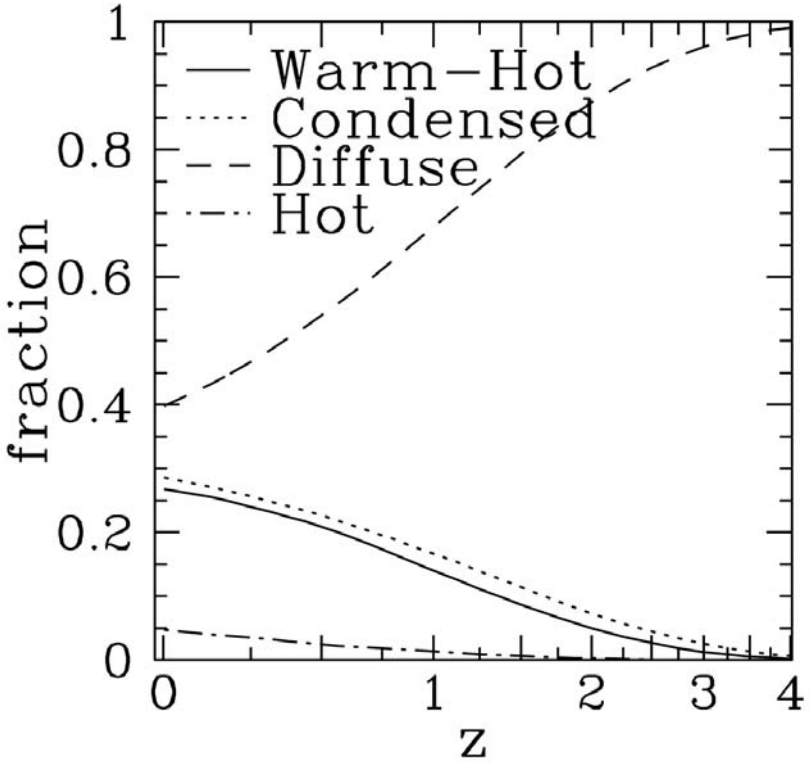

Figure 3.1.: Evolution of the baryons in the Universe (Davé et al. 2001): Observations indicate that most of the baryonic matter in the Universe does not reside in galaxies. At high redshifts ($z \gtrsim 2$), the overwhelming majority of baryons is in a diffuse, photoionized medium in which the galaxies are embedded (the IGM, dashed line), observable as H I absorption lines[3]in quasar spectra. As structures form, diffuse gas is partly shock heated, producing warm-hot gas (the WHIM, solid line). Gas that is driven to higher densities by gravitational instabilities is able to cool into the condensed phase (dotted line) and to form stars. At lower redshifts ($z \lesssim 2$), large potential wells of galaxy clusters shock heat the gas to $T > 10^7\,\mathrm{K}$, giving rise to hot cluster gas (the ICM, dot-dashed line).

The IGM has a very low density yet fills a large volume. It is arranged in a cosmic filamentary structure that is slightly denser[4] than the average of the Universe and consists mostly of ionized hydrogen (ionized by photons or collisions).

The vast majority of the IGM is ionized through photons from the metagalactic UV background. Fewer atoms get heated up to temperatures of $\sim 10^5 - 10^7\,\mathrm{K}$ $(10 - 1000\,\mathrm{eV})$ when the gas is falling from voids into the po-

[3]In astronomy it is common to note neutral atoms with X I, single ionized species with X II, double ionized species with X III, and so forth.

[4]$\sim 10^{-29} - 10^{-28}\,\mathrm{g\,cm^{-3}}$

tential wells of cosmic filaments. These temperatures are too hot for hydrogen nuclei to retain their electrons (the ionization potential (IP) for hydrogen is 13.6 eV, see also Table C.1) and hence, the hydrogen atoms are collisionally ionized. At these high temperatures the gas is called the Warm-Hot Intergalactic Medium (WHIM). In galaxy clusters, the intersection of cosmic filaments, the gas reaches even temperatures of $10^7 - 10^8$ K and higher. This gas is called the Intra-Cluster Medium (ICM).

Table 3.1.: Scales (approximated) and regimes of the IGM. The IGM extends over a large range in size and density, where the latter is an important indicator for the gas temperature and ionization processes. In low density regions, the gas will be ionized by photons from the energetic tail of the metagalactic UV background radiation. With higher density, as it is the case for galaxy clusters and especially for galaxies, ionization can also proceed by particle collisions. Dense regions sometimes are optically thick to the ionizing photons, thus shielding their interior from being ionized, too.

	size	density [g cm^{-3}] [atoms m^{-3}]	temperature [K] [eV]	ionization	synonym
Universe (critical density)		10^{-29} 10^{-6}	2.735 0.2×10^{-3}		
filamentary structure	200 Mpc	$10^{-29} - 10^{-28}$ $10^{-5} - 10^{-4}$	10^5 10	photons	IGM
unstable filaments		$10^{-29} - 10^{-27}$ $10^{-5} - 10^{-3}$	$10^5 - 10^6$ $10 - 1000$	collisions	WHIM
galaxy clusters	1 Mpc	10^{-27} 10^{-3}	$10^7 - 10^8$ $10^3 - 10^4$	photons and collisions	ICM
galaxies	20 kpc	10^{-24} 1	$100 - 10\,000$ $0.01 - 1$	mostly collisions	ISM

Fig. 3.1 manifestly shows that in the past the baryonic matter was mostly in the form of gas, or more precisely, that almost all the baryonic matter in the Universe at redshifts higher than $z \sim 3 - 4$ was solely present in gaseous form. Thus, observing and understanding the gaseous content of the Universe is of eminent importance in order to understand such fundamental processes like star- and galaxy formation, from ancient epochs to present times.

3.2. Quasar Absorption Lines Systems

The H I Ly α λ1216 line[5] is, next to the radio 21 cm line, the most important line for the study of neutral hydrogen in the Universe. The atmospheric cut-off at around 3000 Å is limiting ground based spectroscopy to redshift regimes of $z \gtrsim 1.5$, which corresponds to a time when the Universe had about 30% of its current age.[6] A wealth of narrow Ly α absorption features is observed in quasar[7] spectra, even down to very low redshifts[8]. These absorption lines, according to (4.15), starting from the quasar's own H I Ly α emission at $\lambda_{\mathrm{Ly}\,\alpha}(1+z_{\mathrm{em}})$ and extending blueward down to the Lyman limit at $\lambda_{\mathrm{LL}}(1+z_{\mathrm{abs}})$, are caused by H I resonance lines in the Lyman series and associated with photons with energies of $E_\gamma \geq 10.2\,\mathrm{eV}$ (see also Tab. 3.2). The absorption lines are caused by intervening foreground structures like gas clouds, (proto-) galaxies, or filaments. Hence, in that way the quasar light can probe components of the IGM that remain invisible when otherwise observed.

Quasar absorption line (QAL) spectroscopy is a powerful tool for the study of a large variety of different aspects regarding the IGM, in a cosmological context, but also for the study of confined objects like galaxies, via the cross section of their gas content. Unlike optical galaxy surveys, the depth of quasar absorption line surveys is not limited by a magnitude threshold but only by the redshift of the background quasar. Yet, quasar absorption line surveys suffer from their very own set of biases[9], in particular the selection bias due to the cross section of the gaseous structures observed[10] (see, e.g., Weymann et al. 1981; Blades et al. 1988; Petitjean & Charlot 1997; Rauch 1998).

[5] with an absorption oscillator strengths of $f_{\mathrm{Ly}\alpha} = 0.4164$ and a cross section $\sigma_{\mathrm{Ly}\alpha} = 4.5 \times 10^{-18}\,\mathrm{cm}^2$

[6] using $H_0 = 71\,\mathrm{km\,s^{-1}}$, $\Omega_{\mathrm{m}} = 0.27$, and $\Omega_{\mathrm{tot}} = 1$

[7] Quasars are extremely bright and some of the most distant objects known to date. More details are given in Chapter 4.

[8] HST provided the first possibility of measuring Ly α transition lines at very low redshifts with the required accuracy. It was found that a few of these Ly α absorption line systems reside in the local Universe, some perhaps associated with the Virgo complex. However, they cannot be clearly identified in position and redshift with specific neighboring galaxies and it appears that they are not associated with galaxies in general (Keel 2000).

[9] A bias is a prejudice, usually in the sense of a preference to one particular property or characteristic. For example, a biased sample is one that is falsely taken to be typical of a population from which it is drawn.

[10] With decreasing redshift, galaxies forming in the denser regions may contribute an increasing part of the Lyman absorption cross section.

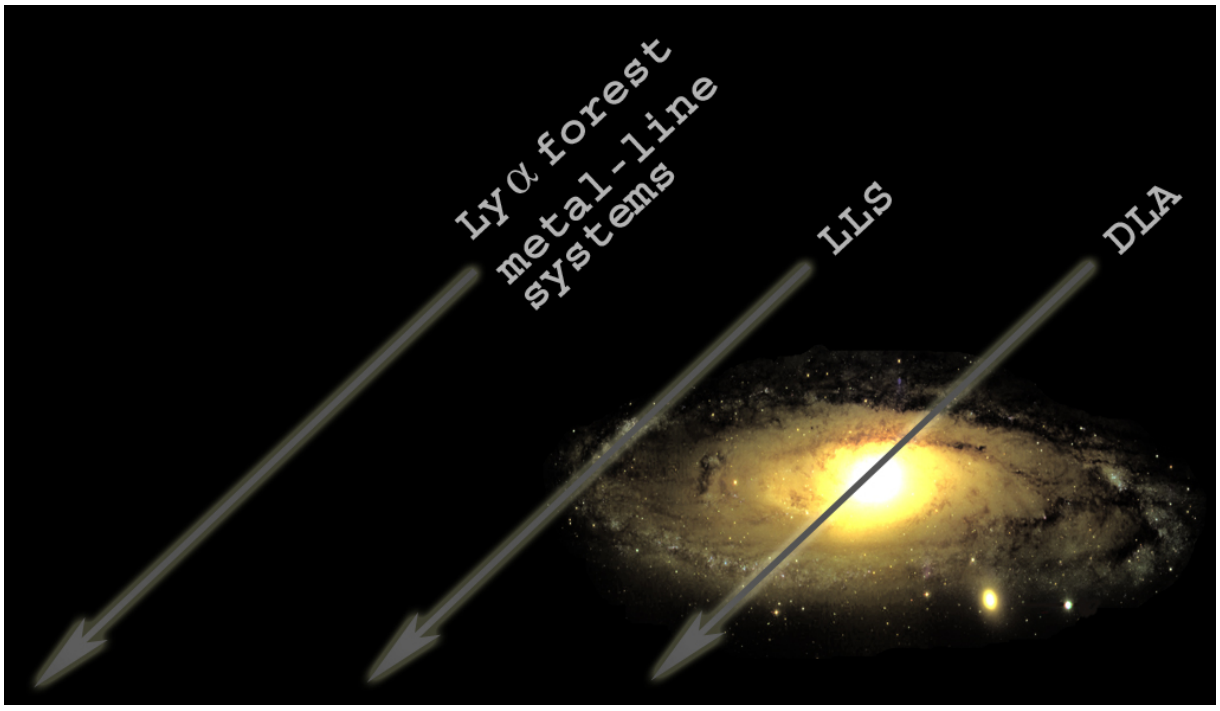

Figure 3.2.: Unified model of quasar absorption line systems. Commonly, quasar absorption line systems are classified according to their column densities of neutral hydrogen, $N(\mathrm{H\,I})$. Damped Lyman α (DLA) systems ($\log N(\mathrm{H\,I}) \leq 20.3$) and Lyman limit (LL) systems ($17.2 \leq \log N(\mathrm{H\,I}) < 19$) may be associated with large galaxies, where metal-line systems ($15 \leq \log N(\mathrm{H\,I}) < 17.2$) and Ly α forest line systems ($\log N(\mathrm{H\,I}) < 15$) most likely are not directly associated with galaxies, but caused by truly intergalactic gas.

3.2.1. The Column Density Distribution Function (CDDF)

The column density, N, in units of cm^{-2}, is a measure for the number of absorbing particles of an element (e.g., $N(\mathrm{C})$) or an ion (e.g., $N(\mathrm{C\,II})$) along a column with a normalized area of $1\,\mathrm{cm}^2$. A mathematical definition of the column density is given by (4.26) in Section 4.2. Throughout this thesis I will follow the commonly used notation in interstellar and intergalactic studies in which $\log N$ always represents $\log \frac{N}{1\,\mathrm{cm}^{-2}}$.

A very striking feature of the observed H I column density distribution function (CDDF) in the IGM is the fact that it can be very accurately approximated

over an ample range of ten orders of magnitude in N by a simple power law[11]:

$$f(N_{\rm HI},z) \propto N^{-\beta}. \tag{3.1}$$

Tytler (1987), among others, determined a value of $\beta = 1.51 \pm 0.02$ for the range of $\log N({\rm H\,I}) = 13-22$ (see also Fig. 3.3). Note, however, that there is evidence for at least one break in the power law with an observed deficit of absorption line systems in the region of $\log N({\rm H\,I}) \approx 15-17$. The observed absorption lines vary over a large range in their column densities. Generally, the relative occurrence of the different column densities can be described by

$$f(N_{\rm HI},z) = \frac{\partial^2 \mathcal{N}}{\partial(\log N_{\rm HI})\partial z}, \tag{3.2}$$

where $\mathcal{N}$ is the number of Ly α absorption lines.

3.2.2. Ly α Absorbers and the Ly α Forest

The region blueward of the quasar's H I Ly α emission down to the Lyman limit, i.e., the region with photons with $E_\gamma = 10.2-13.6\,{\rm eV}$, contains a very high density of H I Ly α $\lambda 1216$ absorption features (see also Fig. 3.4). This is what we refer to as the *Lyman α forest* (Weymann et al. 1981). The multitude of these narrow absorptions are caused by hydrogen gas with column densities $\log N_{\rm HI} \lesssim 15$ along the line of sight (LOS). H I Ly α is by far the most prominent transition line and responsible for most of the absorption seen in the absorption forest, though also H I Ly β, H I Ly γ, and consequent transitions are present and contribute to the absorption, too. Hydrogen gas clouds with column densities of $\log N_{\rm HI} \geq 17.2$, so-called Lyman limit (LL) systems, are capable of absorbing the quasar's entire radiation below $\lambda_{\rm LL} = 912\,{\rm \AA}$. Hence, we observe that the quasar's flux below $\lambda = \lambda_{\rm LL}(1+z_{\rm abs})$ decreases to zero (the so-called *Lyman break*), as this is for example clearly seen in Fig. 3.4.

The large incidence of these absorption line systems, identified within the Ly α forest, and the ability to measure them out to the highest quasar redshifts makes the Ly α forest region very important for the investigation of a broad variety of fundamental cosmological properties. Hydrogen gas clouds with higher

[11] The redshift evolution in simple uniform cloud models can be used to infer the redshift dependence of the density of the gas within the clouds. It is found that ionization of these clouds cannot be explained by background quasars (metagalactic UV background), if the quasar density distribution cuts off between $z \sim 2-4$ as is commonly thought (Carswell et al. 1987).

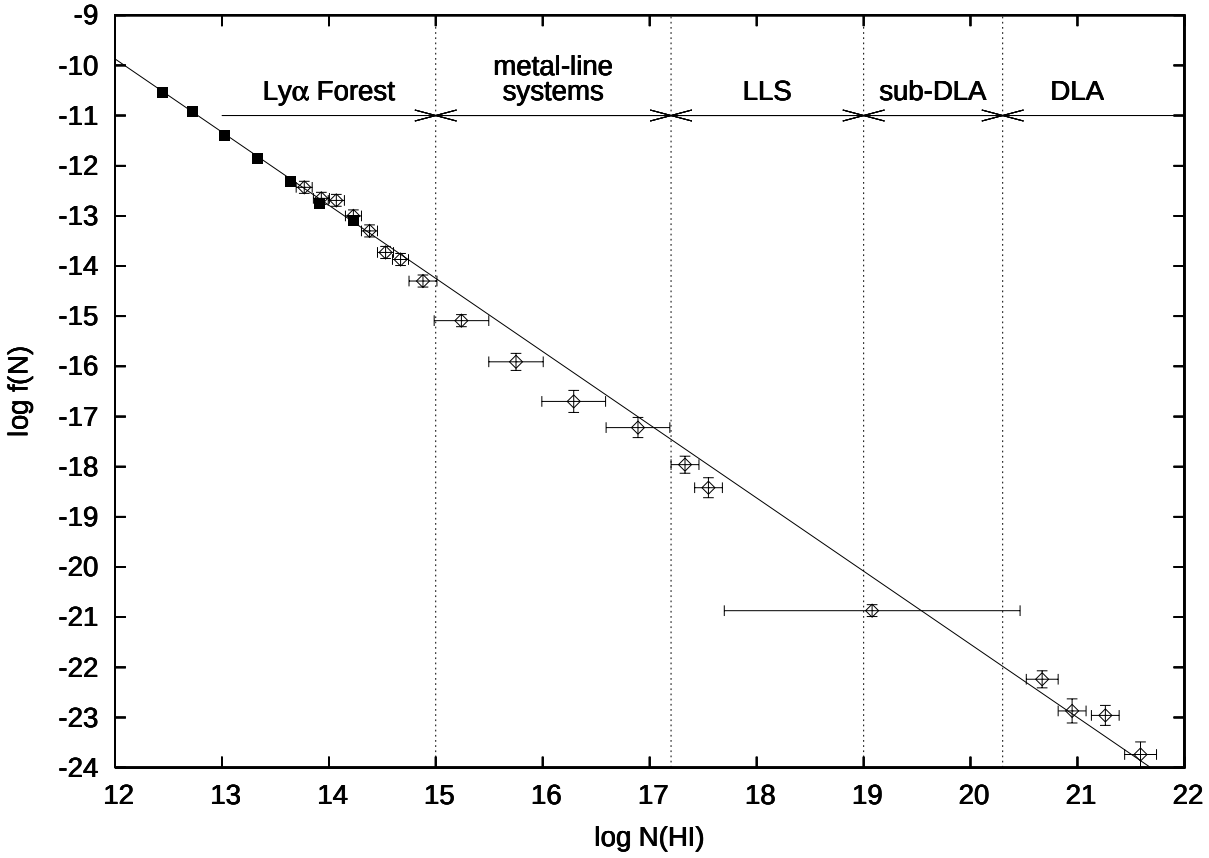

Figure 3.3.: Column density distribution function (CDDF) of neutral hydrogen for absorbing systems with $\log N(\mathrm{H\,I}) = 12 - 22$. A single power law, $f(N) \propto N^{-\beta}$, is a very accurate approximation over 10 orders of magnitude in column density. Note that $f(N)$ is the number of systems per unit N, and not per $\log N$. The squares represent the data from a survey by Hu et al. (1995) with the solid line being the best power law fit over this region ($\beta = -1.46$). This fit has been extrapolated to higher column densities, where results from an other survey by Petitjean et al. (1993) are shown (diamonds).

hydrogen column densities will cause deeper / broader absorptions. Absorptions caused by damped Ly α (DLA) systems, i.e., systems with $\log N(\mathrm{HI}) \geq 20.3$, will show very broad absorption lines with extended Lorentzian damping wings (more details in Chapter 4).

It was suggested by Tytler (1987) that different types of absorption line systems, i.e. absorption line systems with different hydrogen column densities,

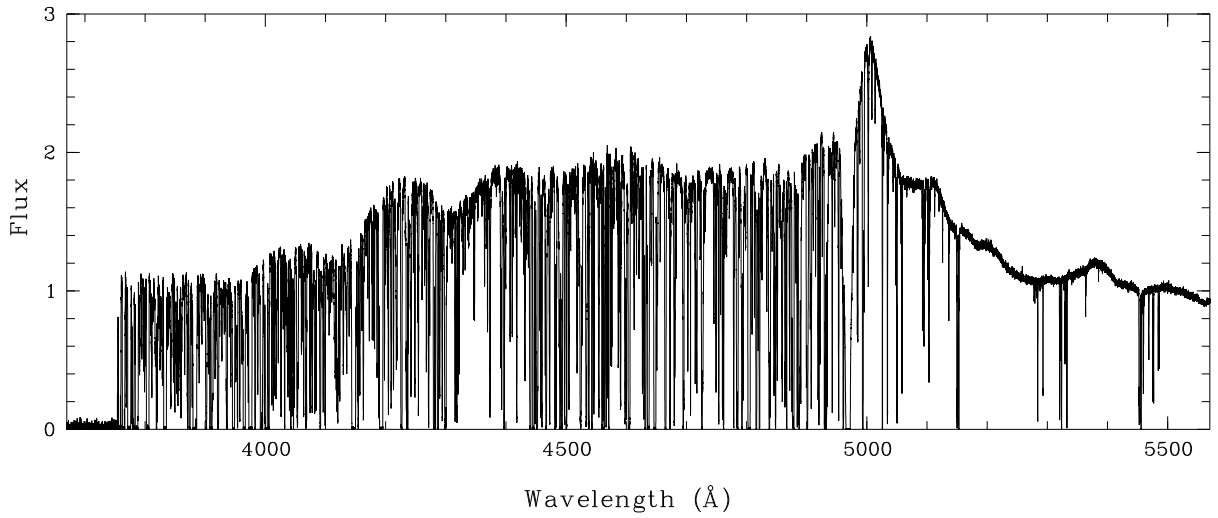

Figure 3.4.: Line of sight toward the quasar Q 0420−388 ($V = 16.^{\mathrm{m}}9$, $z_{\mathrm{em}} = 3.123$). At $\lambda_{\mathrm{Ly}\,\alpha}(1+z_{\mathrm{abs}}) = 4969.66\,\text{Å}$, a sub-DLA system is identified. We clearly see the Lyman break at $\sim 3727\,\text{Å}$, the QSO emission at $\lambda_{\mathrm{Ly}\,\alpha}(1+z_{\mathrm{em}}) = 5012.21\,\text{Å}$, and in between the Ly α forest. Most of the metal-lines absorb in the "clean" part of the spectrum, i.e., in wavelengths redward of the quasar's H I Ly α emission (UVES/VLT LP data, see also Chapter 8).

do not arise within different types of gas clouds but could be caused by different lines of sight trough *one* type of gas cloud (as schematically exemplified in Fig. 3.2). Ly α lines with $\log N_{\mathrm{HI}} \lesssim 14$ then would be due to highly ionized and thin outer regions, whereas the LL systems, and especially DLA systems, would originate from neutral regions of the inner part of the absorbing gas cloud. Although (depending on the LOS) the whole range of different absorption line systems can arise from a single object like the Milky Way, for example, there is wide agreement in the scientific community that different types of absorption line systems are, in general, associated with different types of gas clouds. Strong evidence for this scenario comes from large spectroscopic surveys, where absorption line systems with lower column densities are found to cluster around those with higher column densities. However, the reader should note that the galaxy / absorber relation is very complex.

Quasars with redshifts large enough to be observed in wavelengths $\lambda_{\mathrm{obs}} < \lambda_{\mathrm{abs}}(1+z)$, i.e., shortward the quasar's H I Ly α emission, show numerous sharp absorption features (the Ly α forest) due to the presence of intergalactic clouds absorbing the strong hydrogen Ly α line along the LOS. Most of the common,

Table 3.2.: Hydrogen Lyman and Balmer series.

Transition		$E_{ij} = E_j - E_i$ [eV]	$\lambda = hc/E_{ij}$ [Å]
$n_1 \rightarrow n_2$	Ly α	10.2	1215.67
$n_1 \rightarrow n_3$	Ly β	12.1	1025.72
$n_1 \rightarrow n_4$	Ly γ	12.8	972.54
...			
$n_1 \rightarrow n_\infty$	Lyman limit	13.6	911.75
$n_2 \rightarrow n_3$	H α	1.9	6562.85
$n_2 \rightarrow n_4$	H β	2.6	4861.33
$n_2 \rightarrow n_5$	H γ	2.9	4340.47
...			
$n_2 \rightarrow n_\infty$	Balmer limit	3.4	3646.03

i.e., easily observable metal[12] lines have longer rest wavelengths and lie redward the H I Ly α emission[13]. In Fig. 3.4, by the way of illustration, the main characteristics of a QAL spectrum are demonstrated, using a spectrum toward the quasar Q0420−388 (see also Chapter 8).

The Ly α forest and metal-line systems are believed to contain a large fraction of the baryonic content of the Universe. Ly α forest gas is responsible for about $80-90\%$ of the baryonic matter at redshift $z = 2$, and, according to Penton et al. (2004), for about 30% in the present-day Universe. Note that the incidence of Ly α forest lines does apparently not depend on the sightline, indicating that the IGM is uniform over large scales (Dobrzycki et al. 2002). However, there is evidence for clustering on smaller scales ($\Delta v_{z\approx 0.7} \lesssim 250\,\mathrm{km\,s^{-1}} \lesssim \Delta v_{z\approx 1.7-4} \lesssim 500\,\mathrm{km\,s^{-1}}$) as pointed out by Ulmer (1996).

Number Density

The observational statistical characteristics of the Ly α forest can be summarized by the H I *column density distribution* (see above), the *number density evolution* that is well fitted to

$$\frac{\mathrm{d}\mathcal{N}}{\mathrm{d}z} \propto (1+z)^\gamma, \tag{3.3}$$

[12] According to the standard nomenclature in astronomy, I will use the term *metals* for all elements heavier than helium.

[13] Ly α forest absorption should not be confused with *metal-line systems* identified with "normal" intervening galaxies (see 3.2.5), or with *broad-absorption line systems* that are intrinsic to the quasar.

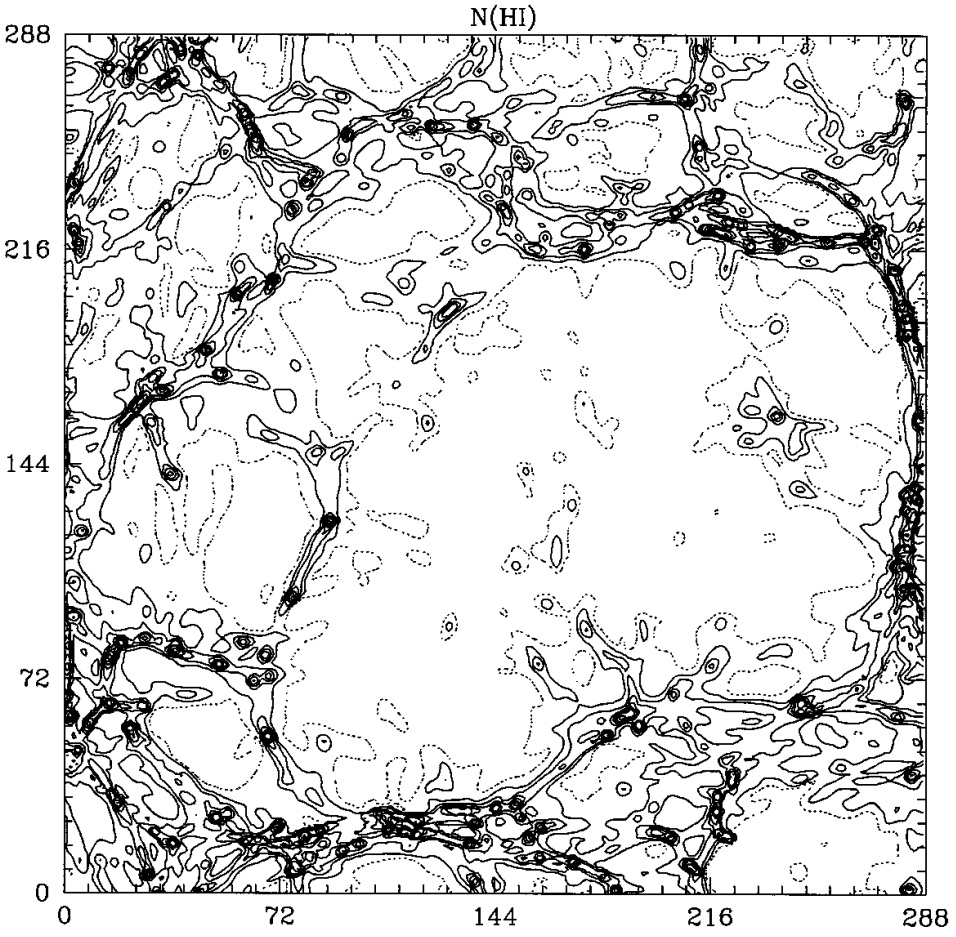

Figure 3.5.: Perspective view of the H I density in a $10h^{-1}$ Mpc comoving cube at $z = 3$ in a flat ΛCDM model from Miralda-Escudé et al. (1996). A typical filament is $\sim 500h^{-1}$ kpc long, $\sim 50h^{-1}$ kpc thick (proper units), and has a baryonic mass of $\sim 10^{10}h^{-1}M_{\odot}$. The gas temperature is in the range $10^4 - 10^5$ K, and increases with time as overdense structures collapse gravitationally. Contours are column densities, where $N(\mathrm{H\,I}) = 10^{12+0.5i}\,\mathrm{cm}^{-2}$, with $i = 1$ shown dotted and $i = 2, 3, \ldots$ shown solid.

with $\gamma \approx 2$ (Sargent et al. 1980; Hunstead et al. 1988), and the rapid decrease of absorbing systems near quasars, caused by the so-called *proximity effect*[14] (see below).

[14]Sometimes also called the *inverse effect* (Tytler 1987).

Proximity Effect

The Ly α clouds are neither exact matches to material associated with particular galaxies nor can they be observed in Hα emission. Observations show that Ly α lines are underabundant at redshifts close to that of the background quasar as a result of the quasar's strong ionizing radiation within its vicinity of some megaparsecs (Bajtlik et al. 1988). All species, and especially hydrogen, are in an ionized state. Consequently, it appears that there is no hydrogen present in the proximity of the quasar, because H II is not detectable in absorption.

Absorbers below the Lyman Limit

Systems that are optically thick below the Lyman limit ($\lambda_{\mathrm{LL}} = 912\,\text{Å}$) are only partially ionized or neutral and sample dense regions and usually are associated with galaxies. If the column density drops below $\sim 10^{17}\,\mathrm{cm}^{-2}$ they become optically thin and are partly ionized by the metagalactic UV background radiation. In the latter case, these systems can also be associated with galaxies but are at relatively large galactocentric distances (Nestor 2004).

Sizes

Absorbers and background quasars that are (in projection) only separated by a few arcseconds, lensed quasars, and numerical simulations suggest a typical absorber size (correlation scale) of a few tens of kiloparsecs up to $\sim 100\,\mathrm{kpc}$.

Mass

The estimation of the mass of a Ly α absorber is, similar to the estimation of its size, a very delicate process and often leads only to a rough and, to some extent, speculative estimation. A major lack of information arises from the fact that only radial velocities can be measured. And even then, due to intrinsic velocities, the absorber's size along the LOS remains rather uncertain. Although the column densities of the absorbing species along the LOS can be determined with high precision, the size and consequently the absorber's mass remain unclear. Various properties like the absorber's geometry, its virial mass (i.e., assuming a gravitationally bound system), and especially its ionization state[15] have to be taken into consideration.

[15] The H I content seen in Ly α is, in most cases, only a trace constituent of the total hydrogen content present.

3.2.3. Damped Ly α Absorbers

Damped Ly α (DLA) systems have, by definition, $N_{\rm HI} \geq 2 \times 10^{20}\,{\rm cm}^{-2}$ (Wolfe et al. 1986). This definition is historical (for practical reasons related to the sensitivity of surveys at the time) and does not represent any physically distinct regime. Systems with $19 \leq \log N_{\rm HI} < 20.3$ are commonly referred to as sub-DLA systems. Fig. 3.3 exemplifies this common classification in Ly α forest ($\log N_{\rm HI} < 15$), metal-line systems ($15 \leq \log N({\rm H\,I}) < 17.2$), LL systems ($17.2 \leq \log N_{\rm HI} < 19$), sub-DLA systems ($19 \leq \log N_{\rm HI} < 20.3$), and DLA systems ($\log N_{\rm HI} \geq 20.3$). Weak Ly α absorption line systems are very numerous

Table 3.3.: Common classification for quasar absorption line systems according to their column densities of neutral hydrogen. Note that some authors refer to the Ly α forest as absorption line systems with column densities below $10^{17.2}\,{\rm cm}^{-2}$, i.e., they do not distinguish between metal-line absorption systems and the Ly α forest. Further, the reader should note that there is no sharp borderline between the different types of absorbers. The definitions are historical (for practical reasons related to the sensitivity of surveys at the time) and do not represent any physically distinct regime. For the sake of mathematical correctness, however, I have adopted throughout this thesis a sharp distinction between the different absorption line systems.

$N({\rm H\,I})$	acronym
$< 10^{15.0}\,{\rm cm}^{-2}$	Ly α forest
$\geq 10^{15.0}\,{\rm cm}^{-2}$	metal-line systems
$\geq 10^{17.2}\,{\rm cm}^{-2}$	LLS
$\geq 10^{19.0}\,{\rm cm}^{-2}$	sub-DLA
$\geq 10^{20.3}\,{\rm cm}^{-2}$	DLA

but the strongest systems are, as can be seen from the CDDF, very sparse. Blind searches for strong absorbers with high $N_{\rm HI}$ are therefore very time consuming and highly inefficient. In fact, the *HST Quasar Absorption Line Key Project* (e.g., Weymann et al. 1998) found only one single DLA system in a redshift path[16] of $\Delta z = 49$ (Jannuzi et al. 1998).

DLA systems exhibit a modest evolution in metallicity with time, where the small scatter in Fig. 3.6 is a good indicator for this smooth enrichment behavior. Note, however, that at lower H I column densities, i.e., in the case of sub-DLA systems, this behavior seems to change. Péroux et al. (2003) reckon that sub-DLA systems might be associated with a different class of objects than DLA

[16]The redshift path is defined as $dX \doteq (1+z)^2(\Omega_\Lambda + \Omega_{\rm m}(1+z)^3)^{-1/2}dz$, or $dX/dz \approx ((1+z)/0.3)^{1/2}$ when $z > 1$ (Bergeron & Herbert-Fort 2005).

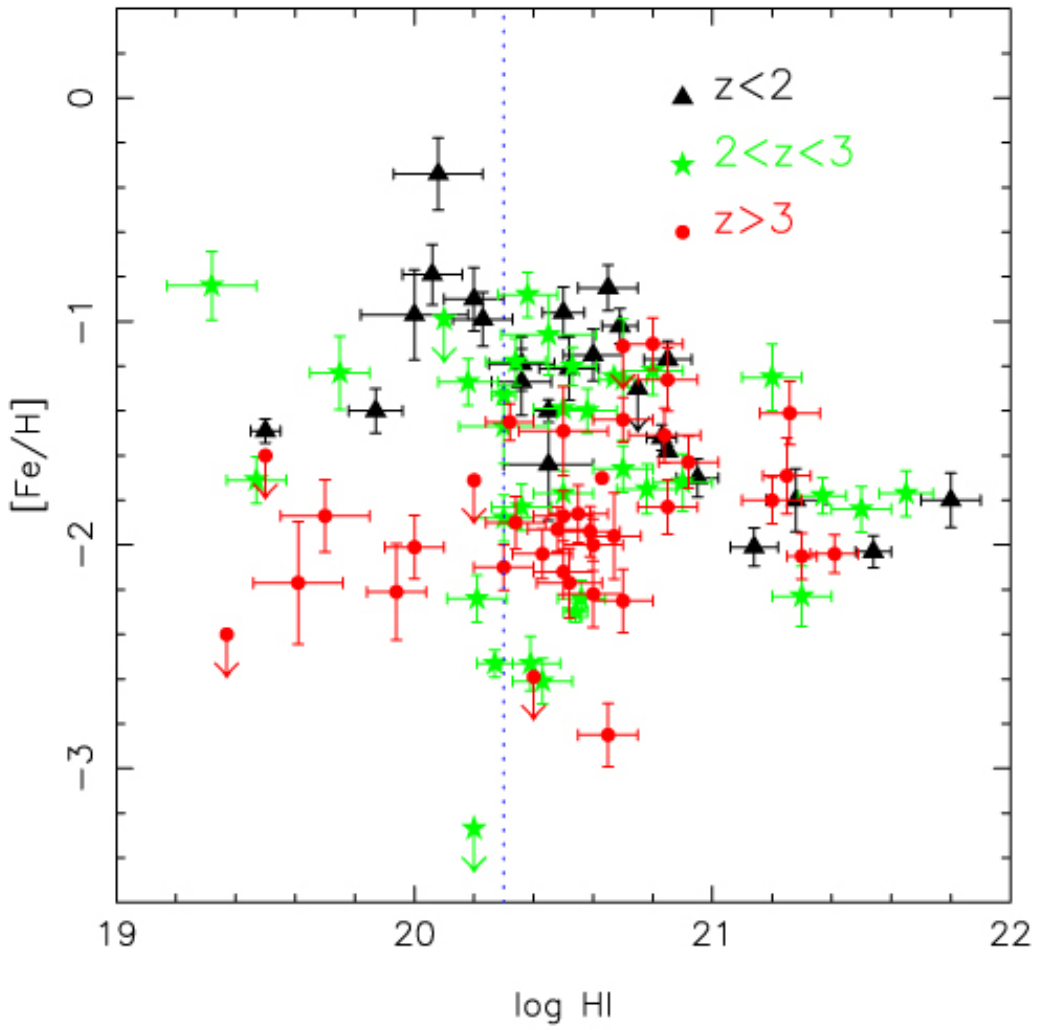

Figure 3.6.: [Fe/H] and [Zn/H] as a function of the H I column density in DLA and sub-DLA systems. The dotted line at $\log N_{\mathrm{HI}} = 20.3$ marks the formal transition from sub-DLA to DLA systems (Péroux et al. 2003).

systems. Prochaska et al. (2003) find that DLA systems are likely to be unbiased or transient population disconnected from the general galactic evolution. They note further that the metallicities[17] of all 125 DLA systems in their sample are confined within $-3 < [\mathrm{M/H}] < 0$, where the lower bound is a good indicator that no primordial gas may exist in the neutral phase within high-z galaxies (see also Fig. 3.7). DLA systems, even the most underabundant ones, have higher metallicities than what is found for the Ly α forest (e.g. Songaila 2001). This

[17] See (3.4) for a definition of the common notation to express an object's metallicity as the logarithmic ratio of its metal abundance compared to that of the Sun.

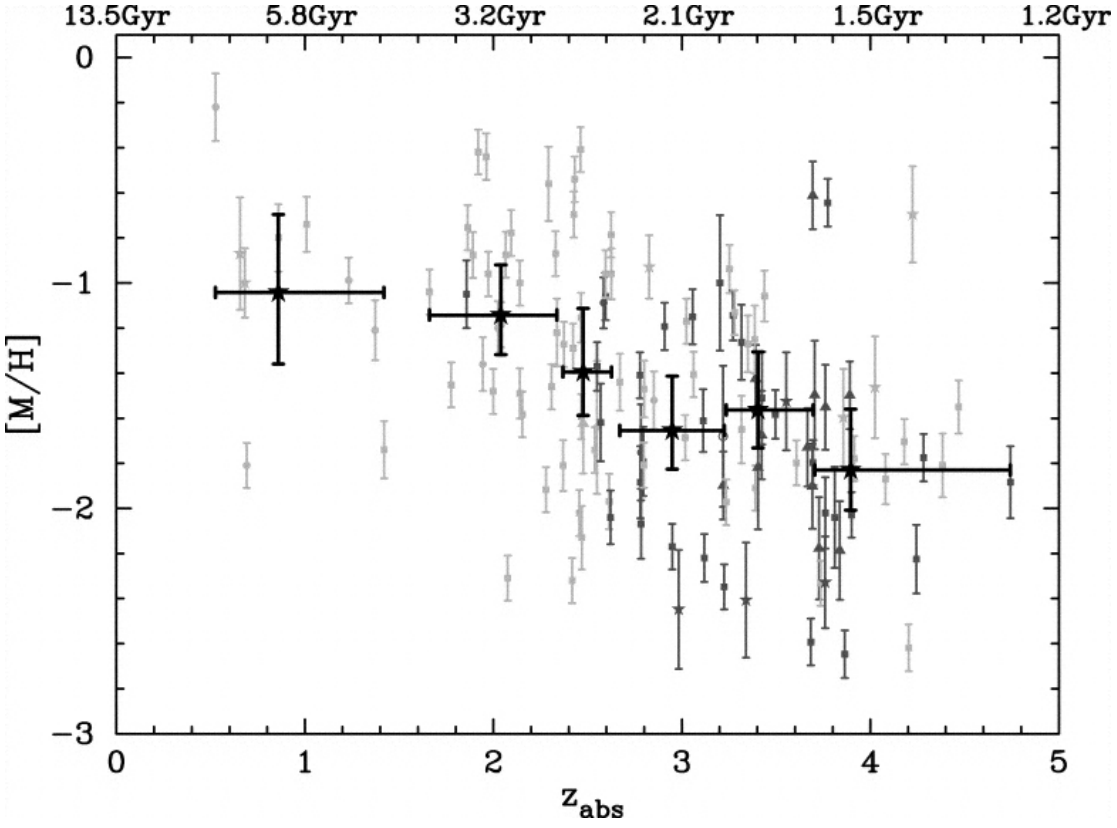

Figure 3.7.: The metallicity [M/H] as a function of $z_{\rm abs}$ from a sample of 125 DLA systems. We notice a smooth increase in metallicity with time. The values are from the ESI survey (dark-grey data points) and also from HIRES and UVES (light-grey data points). The symbols indicate the method by which the values for [M/H] were derived: α-element measurement (filled square), Zn measurements (filled circle); α-elements and limits from Zn measurements (filled triangle), Fe measurements $+0.4$ dex (filled star), and Fe limits $+0.4$ dex (open circle). The unweighted mean of the metallicity (black star and bold error bars) were calculated with a confidence level of 95 % (Prochaska et al. 2003).

metallicity offset between the Ly α forest and DLA systems suggests that the enrichment in the latter case was dominated by metal enrichment from stars *within* these galaxies.

DLA systems are believed to be the progenitors of present-day galaxies and they are most suitable for the study of chemical abundances. DLA systems dominate the neutral content of the Universe (Wolfe et al. 1995; Rao & Turnshek 2000), and the comoving baryonic mass density in the gas inferred from DLA systems at $z \approx 2-3$ does nearly coincide with the baryonic mass density in stars today (Wolfe et al. 1995; Storrie-Lombardi & Wolfe 2000). The large column densities of DLA systems allows us to also measure the abundance of a

large number of elements (e.g. C, N, O, Mg, Al, Si, Fe, Ni, Zn, and many others). Further, their large neutral hydrogen column densities require, in general, only little ionization corrections (Viegas 1995; Vladilo et al. 2001). This work focuses in particular on DLA systems, and it will clearly be shown that those interesting properties and advantages make DLA systems worthwhile objects to investigate and study in great detail.

3.2.4. DLA Galaxies

To date, despite the wealth of available data at redshifts $z \gtrsim 1.5$ from numerous and extensive studies, the nature of DLA systems remains unknown to a large extent. Identifying galaxies associated with the observed absorptions through imaging studies is a demanding task. One reason is the fact that the apparent surface brightness of an extended object decreases as $(1+z)^{-4}$, but also that the extent of an absorbing system, assuming a reasonable impact parameter[18], corresponds to very small angular separations from the bright background QSO. Moreover, confirming that the redshift derived from the absorption spectrum coincides with the emission of an observed galaxy requires a spectrum containing emission features from high redshift galaxies, which is still a very demanding observation, even for $8-10$ m class telescopes.

Table 3.4.: H I regions causing QAL systems. DLA systems, LL systems and regions in the Ly α forest with higher column densities could plausibly be produced by galaxies like the Milky Way.

Object	$\log N_{\mathrm{HI}}$	Reference
MW halo	> 19.15	Westphalen et al. (1997)
MW disk and lower part the halo	20.67	Spitzer & Fitzpatrick (1995)
MW halo > 1 kpc	19.6 ± 0.3	Lockman et al. (1986)

In very few cases and at fairly low redshifts only ($z \sim 0.1$), it was possible to spatially resolve galaxies in 21 cm emission that give rise to DLA absorbers (see, e.g., Bowen et al. 2001). Thus, the interpretation of the nature of QAL systems, and DLA systems in particular, has largely been limited to theoretical models and simulations. Models of disks that are the progenitors of present-day spirals (Prochaska & Wolfe 1997) and other pictures like the concept of

[18] In analogy to nuclear physics, we use the term *impact parameter* as a measure to indicate the distance between the center of the absorbing system and the LOS.

protogalactic clumps (Haehnelt et al. 1998) have been equally successful. More recent models (e.g., Le Brun et al. 1997; Rao et al. 2003) invoke a combination of different components and complex processes such as disks, tidal streams, and halo clouds.

3.2.5. Metal-Line Absorbers

Metal transition lines are observed in absorption line systems with column densities above $\sim 10^{15}\,\mathrm{cm}^{-2}$. Not all but most of the common (i.e., easily observable) metal transitions that fall into the optical and near infrared band are located at rest wavelengths $\lambda > 1216$ Å, redward of the quasar's H I Ly α emission and therefore in the "clean" part of the spectrum that has not been strongly contaminated by intervening H I absorbers, unlike the region of the Ly α forest. This, and also the fact that metals cause very narrow absorption lines and hence are only rarely blended by other metals, allows very precise measurements. The longest rest wavelengths amongst the common strong metal-line transitions are due to a magnesium doublet, Mg II $\lambda\lambda$2796, 2803, which can be observed by ground based telescopes down to a redshift of $z \approx 0.07$. All Mg II absorptions are tightly related to H I. Note also that H I Ly α absorbers with large hydrogen column densities always exhibit relatively strong Mg II absorption (Rao & Turnshek 2000). More detailed information can be found in Chapter 9 where a detailed analysis of a Mg II absorber is given.

C IV Absorbers

The C IV $\lambda\lambda$1548, 1551 doublet is the most common pair of metal lines associated with the highly ionized Ly α forest (Sargent et al. 1988). This prominent ion may originate from large-scale outflows (superwinds) from nearby starforming galaxies that have gradually enriched the IGM (Adelberger 2005). Alternatively, the IGM could have been enriched by an early stellar population (Madau et al. 2001), preferentially in regions with very high matter overdensities (Porciani & Madau 2005). The attempt to study and measure the amount of C IV in the IGM over a large range in redshift was accomplished by Songaila (2001), using a sample of 32 QSOs observed with the Keck telescope on Mauna Kea, Hawaii (see also Songaila 2005). The somewhat surprising result of these observations was that the cosmological C IV mass density, Ω_{CIV}, shows only very little, if any, evolution between $z = 1.5 - 4.5$. This may be an indication that the metal content of the IGM was enriched at redshifts much greater than 5, perhaps

by the sources responsible for its reionization[19].

The aim of searches for C IV beyond $z \sim 5$ is essentially to constrain the origin of metals in the IGM, where $z \sim 5$ corresponds to that redshift at which the star formation rate appears to begin to decline (Bunker et al. 2004; Giavalisco et al. 2004; Bouwens & Illingworth 2006). If the mass density of metals in the IGM was observed to decrease, then the favored scenario would be winds from massive star-forming galaxies that pollute the IGM with metals. On the other hand, if the mass density of metals remained constant, this may point to an epoch of very early enrichment of the IGM.

The limitation to redshifts of $z \lesssim 5$ is set by the finite resolution of the spectrographs and CCD detectors. At redshifts beyond $z \sim 5$, the C IV $\lambda\lambda$1548, 1551 doublet is shifted to wavelengths beyond 9300 Å, requiring an equipment for spectroscopic observations in the near-infrared (NIR) band. This is, with a few exceptions (see, e.g., Kobayashi et al. 2002), a largely unexplored wavelength regime in QAL spectroscopy. On the other hand, near 1 μm there are several windows relatively free of terrestrial water vapor absorption where, with suitably long exposure times, it should be possible to achieve the signal-to-noise ratio (SNR) and spectral resolution required for narrow absorption line work. To this end, Ryan-Weber et al. (2006) have conducted a pilot investigation with the Infrared Spectrometer And Array Camera (ISAAC) on VLT/UT1 (Moorwood et al. 1998) and targeted two of the most distant quasars with redshifts $z = 6.28$ and $z = 5.99$[20]. They report two definite and one marginal C IV absorption line systems between $z = 5.40 - 6.0$ and conclude that their findings are consistent with only mild or no evolution of $\Omega_{\rm CIV}$ for $z < 5$. This findings provide tantalizing evidence for an early epoch of metal production. Consequently, if a substantial fraction of metals are already present in the IGM at the highest redshifts, then QAL studies can supply evidence. However, this particular result has to be viewed with caution until larger surveys of similar objects can confirm or reject these findings.

O VI Absorbers

The IGM is expected to be the main repository of baryons at all epochs. Its physical characteristics are predicted to change from predominantly warm and photoionized gas ($T \sim 10^4$ K) at high redshifts to predominantly shock-heated

[19] Alternatively, the C IV systems may be associated with outflows from massive star-forming galaxies at later times, while the truly intergalactic metals may reside in regions of lower density than those probed up to now (Pettini et al. 2003). Reionization of the IGM: see Section 3.3.3

[20] The most distant quasar known to date is SDSS J114816.64+525150.3 with $z_{\rm abs} = 6.419$ (Fan et al. 2003).

"warm-hot" gas ($T \sim 10^5$ to 10^7 K) at present day (Cen & Ostriker 1999b; Davé et al. 1999). The matter and energy exchange between galaxies and the IGM (e.g., gas accretion or supernova-driven feedback) may play a profound role in the evolution of individual galaxies, galaxy groups, and galaxy clusters (Voit 2005). Observations with STIS aboard HST or with the FUSE satellite have shown that O VI absorption lines are frequently detected in the spectra of low-redshift quasars (e.g., Tripp et al. 2000; Danforth & Shull 2005; Lehner et al. 2006)

O VI has its largest abundance in collisional ionization equilibrium (CIE) at $T \sim 10^5$ K and can therefore, in principle, be used as a tracer for the WHIM and hot galactic outflows. However, the tracer properties are limited by the facts that O VI can also arise in photoionized intergalactic gas at high z or in gas that is not in ionization equilibrium. So far only a few O VI systems show definitive evidence of hot gas (see, e.g., Savage et al. 2005). The nature of O VI absorbers and their relationships with nearby galaxies or galaxy structures was investigated by several groups (see, e.g., Sembach et al. 2004; Bregman et al. 2004; Stocke et al. 2006; Prochaska et al. 2006). However, there is no full consensus to date on the origin of the oxygen enrichment in the IGM or whether O VI absorption line systems as a matter of fact arise in collisionally ionized metal-poor WHIM gas (Tripp et al. 2006).

3.2.6. Metal Abundances

In astronomy, the metallicity (also *metal abundance* or *chemical abundance*) of an object is the proportion of its baryonic matter that is made up of elements other than hydrogen or helium compared to that of hydrogen (i.e., its metal content). The metallicity of an object can give an indication of its age or of the enrichment mechanism. Further, the metallicity of stars is used for their classification into population I (solar like), population II (metal deficient), and population III (extremely metal deficient). See also Chapter 7 for a more detailed discussion on early enrichment processes, population III stars, and very metal deficient quasar absorption line systems.

It is common to express an object's metallicity as the *logarithmic* ratio of its metal abundance compared to that of the Sun, where the Sun's metallicity is, by definition, zero. The common notation for the chemical abundance is

$$[\mathrm{X/H}] = \log\left(N(\mathrm{X})/N(\mathrm{H})\right) - \log\left(N(\mathrm{X})/N(\mathrm{H})\right)_{\odot}, \tag{3.4}$$

with N the column density. An object's metallicity can also be expressed as the

linear ratio of its metal abundance compared to that of the Sun. In this case, it is common to use Z as identifier to indicate the metal abundance. For example, an object with a metallicity of $[\mathrm{M/H}] = -2.47$ can alternatively be expressed as $Z = 0.0034$ or $^1/_{300}$ solar [21].

3.3. Physical Properties of the IGM

The IGM is composed of atoms (mostly ions), free electrons, very little dust, and is almost devoid of molecules. It contains most of the baryonic matter in the present-day Universe (IGM $\sim$ 70%, Galaxies $\sim$ 30%) and can be observed in emission (e.g., X-ray emission, H α emission, H I 21 cm emission) and in absorption (against QSOs, AGN, galaxies, GRBs, etc.). Hence, studying the IGM allows us to unveil a wealth of fundamental information. Let us now have a closer look at the almost omnipresent process of ionization as well as the relation between the gas density and the gas temperature. The physics of interstellar and intergalactic absorption will be discussed in Chapter 4.

3.3.1. Ionization

Photoionization

Energetic photons, i.e., photons with energies larger than an atom's ionization potential (see Table C.1), will be able to unbind an electron and hence ionize the atom:

$$\mathrm{atom} + \mathrm{h}\nu \rightarrow \mathrm{atom}^+ + e^-.$$

In the case of hydrogen that has an ionization potential of 13.6 eV, any photon with $h\nu \geq 13.6\,\mathrm{eV}$ ($\lambda \leq 912\,\text{Å}$) can ionize the atom. The photoionization cross section for hydrogen, in units of cm^2, is given by

$$\sigma_{\mathrm{phot,H}}(\nu) = 2.8 \times 10^{29} g_{\mathrm{bf}}(\nu, T) \nu^{-3}, \tag{3.5}$$

with $g_{\mathrm{bf}}(\nu, T)$ the so-called *Gaunt factor* for the bound-free transition. From (3.5) we note that for hydrogen and hydrogen-like atoms, i.e., atoms in which the valence electron is bound by a strong force (as this is for example the case

[21] Note that solar metallicity, using the above notation, corresponds to $[\mathrm{M/H}] = 0$ or $Z = 1$. This notation should not be confused with an other common notation, e.g., with $Z = 0.015$, $Y = 0.25$, and $X = 0.735$, that indicates the Sun's metal, helium, and hydrogen mass fraction, respectively.

in highly ionized atoms), we can write

$$\sigma_{\mathrm{phot,H}}(\nu) \propto \nu^{-3}. \tag{3.6}$$

However, this is no longer the case for heavier atoms where the photoionization cross section turns out to be distinctly more complex. Note further, that in order to describe the absorptivity of the ISM or the IGM as a whole, one has, in principle, to account for the contribution from metals, too. However, even when considering a case with solar metal abundances, the photoionization cross section remains dominated by the cross sections of hydrogen and helium (Fig. 3.8).

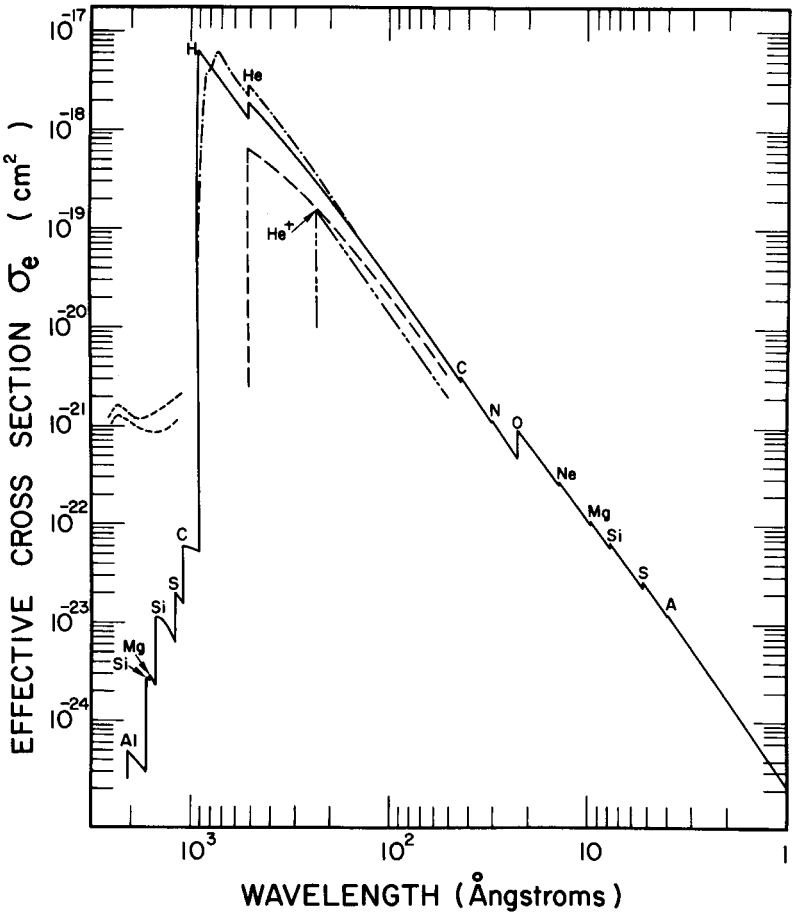

Figure 3.8.: Photoionization cross section (Cruddace et al. 1974). The photoionization cross section remains dominated by the cross sections of hydrogen and helium, even when considering a case with solar metal abundances.

The Ly α absorption in quasar spectra is caused by neutral hydrogen. However, most of the hydrogen gas is strongly ionized (i.e., $n_{\mathrm{HI}} \ll n_{\mathrm{HII}}$). Conse-

quently, the IGM must consist of (mostly) ionized hydrogen, H II. This photoionization is predominantly caused by UV photons from the metagalactic UV background radiation. In equilibrium, i.e., when the photoionization rate is equal to the recombination[22] rate, the ionization fraction is:

$$\frac{n_{\mathrm{HII}}}{n_{\mathrm{HI}}} = \frac{\Gamma_{\mathrm{ph}}}{\alpha_{\mathrm{rec}}\, n_{\mathrm{HII}}}, \tag{3.7}$$

where $\alpha_{\mathrm{rec}} = 4 \times 10^{-13}\,\mathrm{cm^3\,s^{-1}}$ is the hydrogen recombination coefficient, Γ_{ph} the photoionization rate[23] (in $\mathrm{s^{-1}}$), and $\sigma_{\mathrm{ph}} = 6 \times 10^{-18}\,\mathrm{cm^2}$ the photoionization cross section.

Collisional Ionization

In regions with higher densities, say galaxy clusters or galaxies, the atoms are close enough to each other so that collisions with electrons[24] become important. In the case of a CIE[25], and when neglecting charge exchange reactions[26], the ionization fraction becomes

$$\frac{n_{\mathrm{i}}^{\mathrm{u}+1}}{n_{\mathrm{i}}^{\mathrm{u}}} = \frac{\alpha_{\mathrm{coll}}^{\mathrm{u}}}{\alpha_{\mathrm{rec}}^{\mathrm{u}+1}}, \tag{3.8}$$

where $n_{\mathrm{i}}^{\mathrm{u}}$ is the atomic volume density with i the ionization level and u the excitation state, and α_{coll} the collisional and α_{rec} the recombination coefficient.

The hydrogen ionization fraction,

$$f_{\mathrm{H}} = \frac{n_{\mathrm{HII}}}{n_{\mathrm{HI}} + n_{\mathrm{HII}}} \approx \frac{n_{\mathrm{HII}}}{n_{\mathrm{HI}}}, \tag{3.9}$$

can be approximated (in the case of CIE and with $\log T$ representing $\log \frac{T}{1\,\mathrm{K}}$) as a function of the gas temperature (Richter et al. 2006):

$$\log f_{\mathrm{H}} \approx -13.9 + 5.4 \log T - 0.33 (\log T)^2. \tag{3.10}$$

[22] Recombination: $\mathrm{ion} + e^- \rightarrow \mathrm{atom} + \mathrm{h}\nu$

[23] It is $\Gamma_{\mathrm{ph}} = \int_{\nu_{\mathrm{ion}}}^{\infty} \frac{\sigma_{\mathrm{ph}}(\nu) U_\nu c}{h\nu}\,\mathrm{d}\nu$, with U_ν the ionizing radiation.

[24] Not only electrons do collide with hydrogen atoms but also protons or other hydrogen atoms. In the case of the interstellar and intergalactic medium, interactions with electrons are, due to their smaller weight, the most common.

[25] Note that in the case of CIE (e.g., in gas clouds with high densities) all atoms are in the ground state, contrary the case of LTE (e.g., in gas clouds with low densities), where a substantial fraction of the atoms is ionized. If LTE can be assumed, the ionization of the gas is described by the Saha equation (see Appendix A).

[26] also *charge transfer reaction*, i.e., reaction of an ion with a neutral species, in which some or all of the charge of the reactant ion is transferred to the neutral species.

That ionization through collisions becomes insignificant in low-density regions of the IGM can be demonstrated with a short example. The mean collisional free path is given by

$$l_c = (n_{\mathrm{H}}\sigma_{\mathrm{c}})^{-1}. \tag{3.11}$$

The mean time between collisions then is

$$t_{\mathrm{c}} = \frac{l_{\mathrm{c}}}{\upsilon} = \left(\frac{2k_{\mathrm{B}}T}{3m_{\mathrm{H}}}\right)^{-1/2} \frac{1}{n_{\mathrm{H}}\sigma_c}, \tag{3.12}$$

with υ the mean particle velocity. When assuming a typical gas density of $n_{\mathrm{H}} = 10^{-4}\,\mathrm{cm}^{-3}$ and a temperature of $T = 10^6\,\mathrm{K}$, we find a mean time between collisions of $t_{\mathrm{c}} \approx 45\,000\,\mathrm{yrs}$. Therefore, low-density regions are, due to the insignificance of collisional ionization (and the absence of self shielding[27]), almost entirely ionized by photons from the energetic tail (i.e., $E_\gamma \geq 13.6\,\mathrm{eV}$) of the metagalactic UV background radiation distribution.

3.3.2. Temperature and Density

The temperature of the gas is, as seen above, strongly dependent on the region in question. The gas of the low-density IGM gets heated up when compressed and, as long as the compression is adiabatic, T essentially depends on the gas density, ρ_{g}, in the way that

$$T = T_0 \left(\frac{\rho_{\mathrm{g}}}{\overline{\rho}_{\mathrm{g}}}\right)^{\alpha}, \tag{3.13}$$

where the average gas temperature, T_0, and the exponent α depend on the ionization history and the spectrum of the ionizing photons. Typical values are $4000\,\mathrm{K} \lesssim T \lesssim 10\,000\,\mathrm{K}$ and $0.3 \lesssim \alpha \lesssim 0.6$. Because the IGM is almost fully ionized, and assuming equilibrium between ionization and recombination, the mean H I density is given by (3.7). With (3.7) and (3.13), the optical depth[28] for H I Ly α absorption can be written as

$$\tau_{\mathrm{Ly}\,\alpha} = A \left(\frac{\rho_{\mathrm{g}}}{\overline{\rho}_{\mathrm{g}}}\right)^{\beta}, \tag{3.14}$$

[27] The lowering of the flux density in the inner part of an object due to absorption in its outer layers.

[28] The optical depth, τ, is a measure of transparency. See Chapter 4, pg. 42.

where typically $\beta \approx 1.6$. The factor A depends on z, $\Gamma_{\rm HI}$, and the mean temperature of the gas, T_0. Fig. 3.9 shows the distribution of the optical depth as a function of the gas density at $z = 3$ according to an smooth particle hydrodynamics (SPH) simulation of a standard cold dark matter (CDM) model from Weinberg et al. (1998). The tight correlation between the density fluctuation and the optical depth for Ly α absorption is an indicator that the bulk of the gas in the IGM was not heated by shock fronts, i.e., through collisional excitation or ionization, but through photoionization and adiabatic compression (because infall and eventual shock heating would result in a larger spread due to large peculiar velocities). Hence, the observed distribution of $\tau_{\rm Ly\,\alpha}$ allows us to conclude on the distribution of the (baryonic) matter overdensity, where the latter essentially coincides with the overdensities of the dark matter (DM) distribution.[29]

3.3.3. The Reionization of the IGM

The *epoch of reionization* begins with the end of the so-called *Dark Age*, i.e., the time when the first stars in the Universe were formed. Although the epoch of reionization is not essential for the present work, I shall, for the sake of completeness, give a very brief overview.

At some time between the epoch of recombination and redshift $z \sim 5$, the Universe experienced an epoch of reionization. This ionization process started with the appearance of the first stars at $z \sim 17 \pm 5$ (Spergel et al. 2003) and eventually the first active galactic nuclei (AGN). At $z \sim 5$ most of the IGM was (virtually) fully ionized. This is inferred from observation where in quasar absorption line (QAL) spectra a distinct depression of the continuum, an extended H I Ly α absorption trough, blueward of the quasar's H I Ly α emission-line could be identified. This so-called *Gunn-Peterson (GP) Effect* (Gunn & Peterson 1965; Scheuer 1965) was the premier test for the presence[30] of neutral gas

[29] It is common to suppose that the evolution of the IGM traces the evolution of DM since DM is the dominant matter component in the Universe (about 90%). However, although the evolution of the IGM is dynamically governed by the gravity of the underlying DM field, many statistical properties of the IGM inevitably decouple from those of the DM once the nonlinearity of the dynamical equations and the stochastic nature of the field is considered. Many features of cosmic large scales structures can be explained with this discrepancy (Fang et al. 1993).

[30] The IGM at very high redshift must be neutral. However, the GP effect is not a proof for an IGM composed out of (only) neutral gas. This is because already small amounts of H I atoms are sufficient give rise to dense H I Lyman absorption and, consequently, to cause the observed effect.

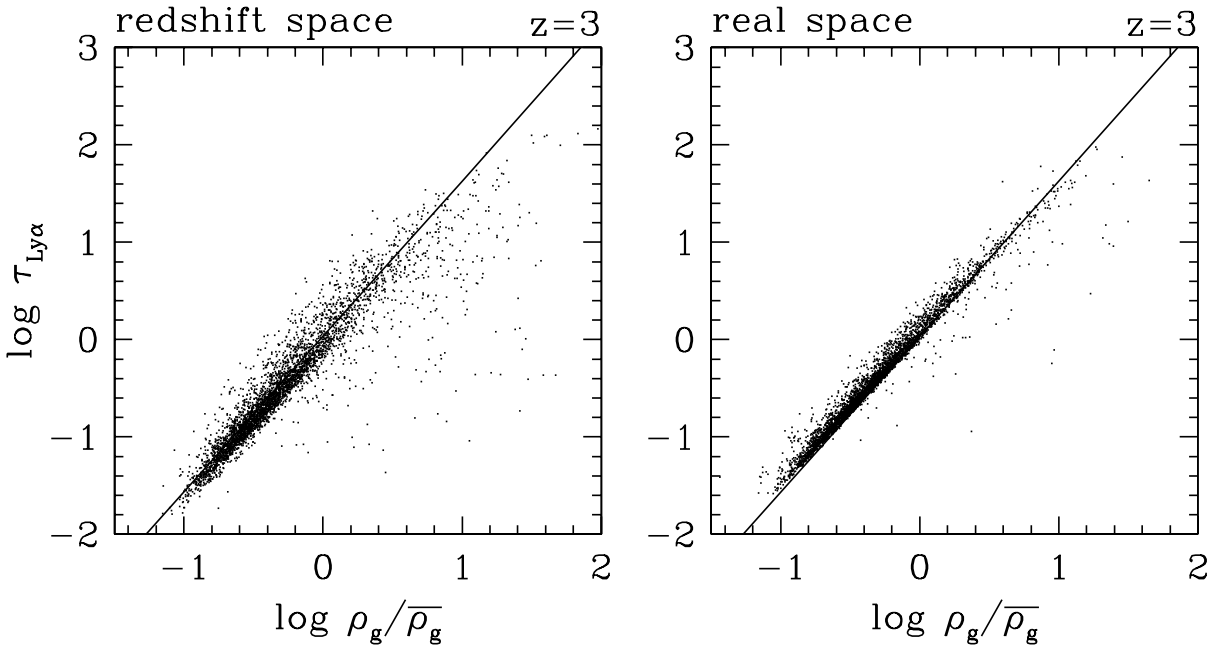

Figure 3.9.: Relation between the Ly α optical depth and the gas overdensity in the IGM as seen in a simulation from Weinberg et al. (1998). The tight relation between the Ly α optical depth, $\tau_{\mathrm{Ly}\,\alpha}$, and the density fluctuation, $\rho_\mathrm{g}/\overline{\rho}_\mathrm{g}$, indicates that the major part of the IGM (at $z = 3$) was not heated by shock fronts but through adiabatic compression. The data points (each symbolizing a line of sight through a gas distribution) are given in redshift space and in real space.

at redshifts beyond $z \sim 5$. H I Ly α absorbers have typically an optical depth of

$$\tau_{\mathrm{Ly}\,\alpha} \approx 1.7 \times 10^{11} \frac{n_\mathrm{H}(z)}{(1+z)^{3/2}}, \tag{3.15}$$

with $n_\mathrm{H}(z)$ the neutral hydrogen volume density in units of cm^{-3}. Becker et al. (2001) find that at redshifts above $z \sim 6$, the IGM becomes almost opaque in the Lyman continuum, i.e., for photons with $h\nu \geq 13.6\,\mathrm{eV}$ ($\lambda \leq 912\,\text{Å}$). The H I Ly α absorption in the IGM leads with increasing redshift to an apparently continuous absorption due to the general cosmological expansion. Accurate measures of this effect give a strong limit to the overall mass density of neutral hydrogen in the recent Universe:

$$\Omega_\mathrm{GP}(\mathrm{H\,I}) < 3 \times 10^{-7}. \tag{3.16}$$

This again shows that the IGM is highly ionized. However, the theory of the reionization era is still not fully understood and remains a critical missing link in the theory of galaxy formation.

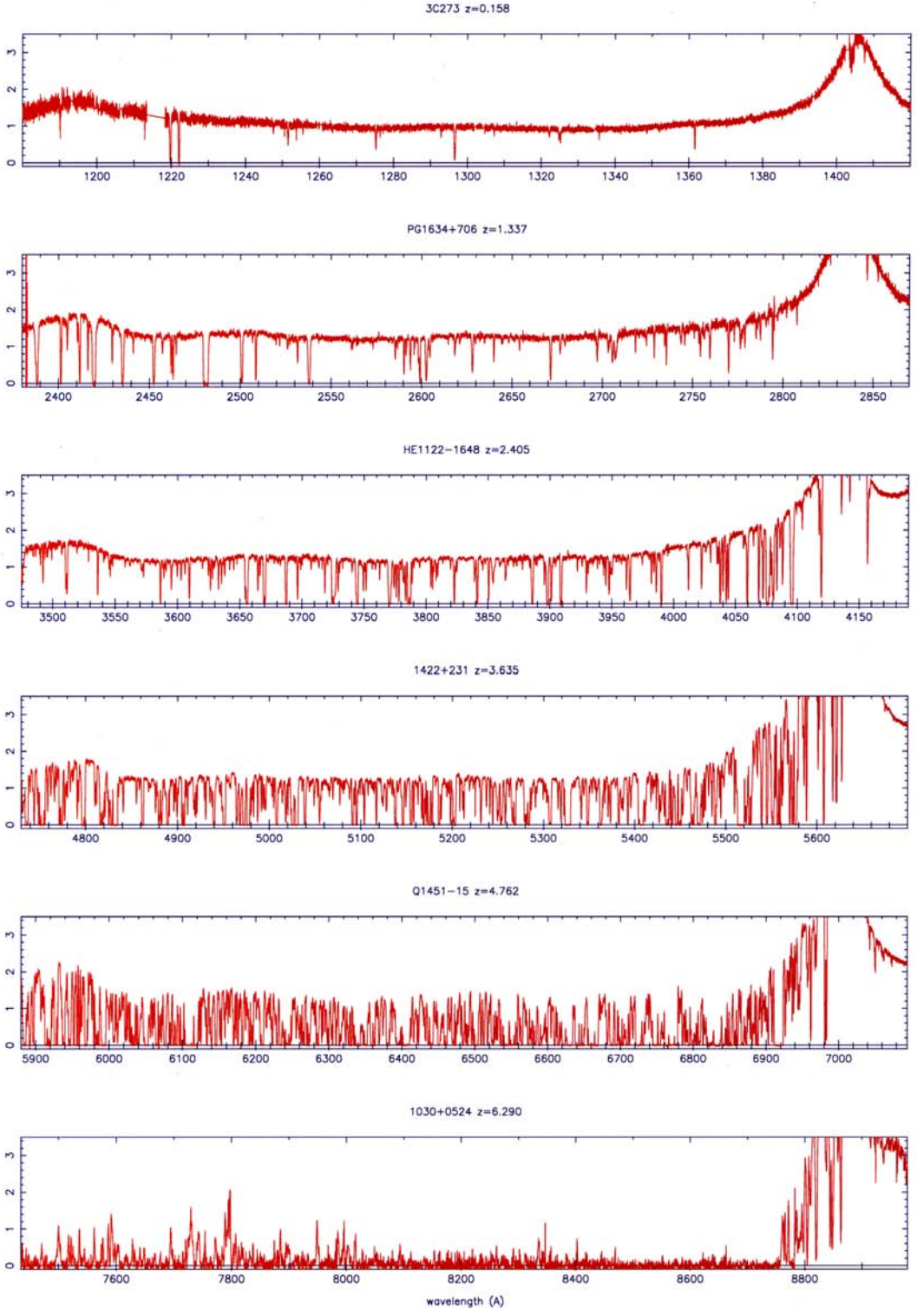

Figure 3.10.: QAL spectra illustrating the increase in absorption due to intervening neutral hydrogen with increasing redshift. At the highest redshifts, the spectra show a Gunn-Peterson absorption trough, i.e., the complete absorption of wavelengths shortward the H I Ly α emission-line, implying that the reionization epoch must have continued, at least in some areas, until redshifts of about $z \sim 6$ (Hook 2005).

4. Interstellar and Intergalactic Absorption Lines

4.1. Overview

The most widely accepted notion is that quasars (contraction of QUASi-stellAR radio sources), or QSOs for short, are AGN, i.e., galaxies with an active supermassive black hole at their centers. Quasars are extremely bright objects with an enormous energy output of up to $10^{47}\,\mathrm{erg\,s^{-1}}$. They produce X-rays, strong radio waves, and visible light. The first quasar, 3C 273 at a redshift of $z = 0.15$, was discovered in 1963 with the 200-inch telescope at Mount Palomar, CA, USA (Schmidt 1963). Later, Bahcall & Salpeter (1966) predicted that intervening material along the line of sight should produce observable discrete absorption features in quasar spectra. Shortly afterwards, Greenstein & Schmidt (1967) and Burbidge et al. (1968) announced the detection of the first quasar absorption lines.

Today, the most distant quasar known, J104845.05+463718.3, is at a redshift of $z = 6.43$ (Fan et al. 2003), i.e., emitted its radiation at a time when the Universe had only about 6 % of its present age[1]. As a result of the Sloan Digital Sky Survey (SDSS), the most ambitious astronomical survey ever undertaken, and numerous previous surveys, more than 60 000 quasars are know to date. In combination with $8-10$ m class telescopes that allow us to do high resolution spectroscopy at resolutions on the order of $R \sim 45\,000$ ($\sim 7\,\mathrm{km\,s^{-1}}$) and even higher, present-day observations provide a wealth of extensive data with redshifts ranging from $z = 0.06$ to the recent maximum of $z = 6.43$.

Parts of the ultraviolet (UV) spectrum (below ~ 3000 Å) and most of the infrared (IR) spectrum (above $\sim 15\,000$ Å) are absorbed by the atmosphere. This limits quasar absorption line studies with ground based telescopes to the optical and the near infrared band. The UVES spectrograph[2] covers a range from

[1] using $H_0 = 71\,\mathrm{km\,s^{-1}}$, $\Omega_\mathrm{m} = 0.27$, and $\Omega_\mathrm{tot} = 1$

[2] See more details about the UV Echelle Spectrograph (UVES) at VLT/UT2 in Chapter 5.

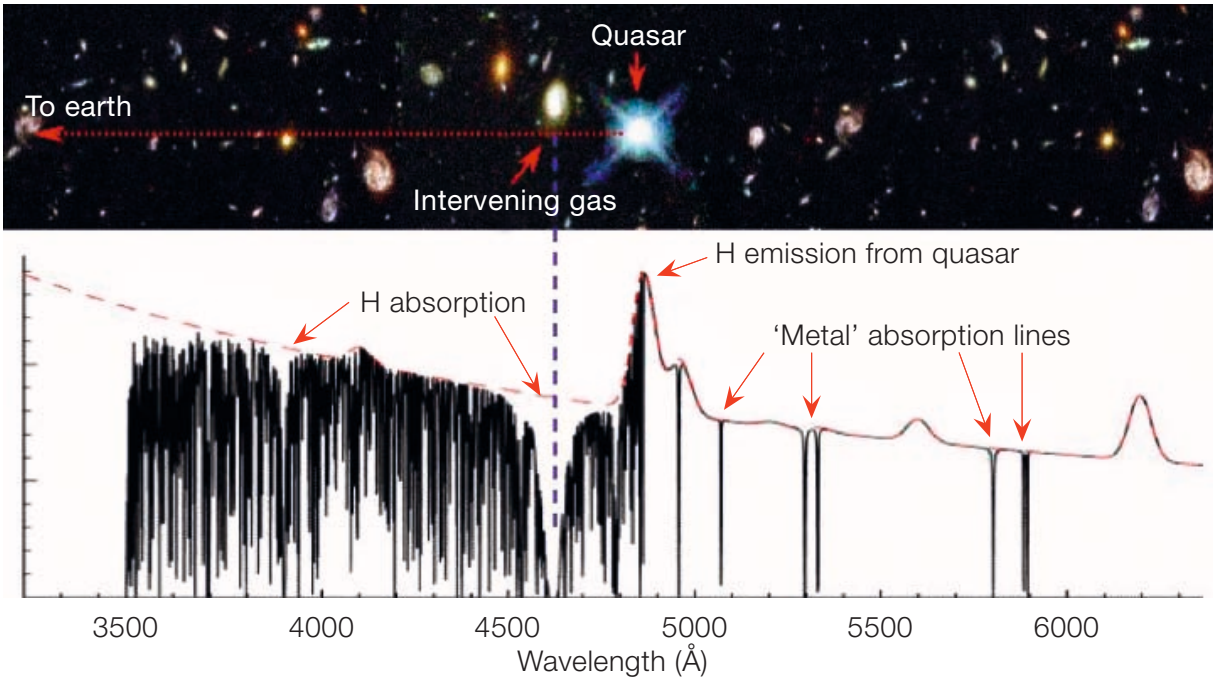

Figure 4.1.: Schematic illustration of absorption due to intervening gas (galaxies) along the line of sight (illustration by Michael T. Murphy).

3000 – 11 000 Å, corresponding to a redshift range of $1.5 \lesssim z \lesssim 8$ in the case of the H I Ly α λ1216 absorption line. Absorption line systems at lower redshifts can only be observed from space like for example with the Faint Object Spectrograph (FOS) or the Space Telescope Imaging Spectrograph (STIS)[3], both aboard HST, or with satellites like FUSE, GALEX, and SWIFT.

The analysis of QAL spectra has developed into a powerful tool in the study of galaxy evolution and large-scale structure (LSS). Quasar absorption line spectra can be used, at least in principle, for an unbiased and detailed study of the gaseous content and environment of galaxies over large scales, from the present back to the highest redshifts at which quasars are observed[4]. Absorption features allow us to determine many information, e.g., the redshift of the absorbing galaxy, its metal content and abundance pattern, ionization parameter, temperature, velocity distribution, etc., without the need of any emission line or even a spectral or visual identification of the quasar host itself.

There are two basic approaches to the study and analysis of quasar absorp-

[3]Due to technical problems STIS stopped science operations on August 3, 2004, and is currently in "safe" mode.

[4]At the time of writing, the Sloan Digital Sky Survey (SDDS) and other large area surveys have discovered about 1000 QSOs at $z > 4$, about 50 QSOs at $z > 5$, and nine QSOs at $z > 6$ (Fan 2006), with 104845.05+463718.3 at $z = 6.43$ (Fan et al. 2003) the QSO with the highest redshift ever discovered.

tion line systems: the study of large samples at low resolution[5] or the study of individual systems at high resolution. The observations presented hereafter in Chapters 6, 8, 9, and 10 were analyzed using the latter approach.

4.2. Line Absorption

In the following I discuss the case of Ly α absorption of neutral hydrogen (H I) in the IGM along a LOS toward a background quasar. Metal absorption lines are also of great importance but the discussion below is exemplary for any kind of absorption lines.

4.2.1. Line Profiles and Voigt Profile

The probability that an electron in a bound level will make a transition to a higher (or lower) level is described by the Einstein transition probability, A_{ij}. In the case of the H I Ly α line transition, it is $A_{\mathrm{HI\,Ly}\alpha,21} = 4.4 \times 10^7\,\mathrm{s}^{-1}$. If a transition takes place between two levels, labeled u (upper) and l (lower), then the intrinsic line broadening, characterized by transitions from those levels, can be written as the sum of A_{ij} over all lower energy levels, i.e.,

$$\Delta_k = \frac{1}{4\pi} \sum_{i<u} A_{ui}. \tag{4.1}$$

The natural (intrinsic) broadening of the H I Ly α line is $\Delta_{k,\mathrm{HI\,Ly}\alpha} = 6 \times 10^{-3}$ Å. Note that it is common in this context to refer to the damping constant,

$$\gamma \doteq 4\pi\Delta_k, \tag{4.2}$$

instead.

The frequency dependence of the absorption capability is described by the Lorentz function

$$\phi_L(\nu) = \frac{1}{\pi} \frac{\Delta_k}{{\Delta_k}^2 + \Delta\nu^2}, \tag{4.3}$$

with $\Delta\nu = \nu - \nu_0$, where ν_0 is the transition frequency.

[5] With the third data release (Abazajian et al. 2005) from the Sloan Digital Sky Survey (SDDS) more than 53 000 QSO spectra with $R \sim 1700 - 2000$ and a wavelength coverage of $3800 - 9200$ Å are available today (see, e.g., York et al. 2006).

However, lifetime broadening is not the only reason for absorption lines having finite widths. The atoms move about with Doppler velocity corresponding to the temperature. This thermal motion of the gas will cause a so-called Doppler broadening of the absorption line, which is described by the Maxwellian velocity distribution function

$$\phi_{\mathrm{D}}(\nu) = \frac{1}{\sqrt{\pi}\Delta_{\mathrm{t}}} \mathrm{e}^{-(\Delta\nu/\Delta_{\mathrm{t}})^2}, \tag{4.4}$$

where

$$\Delta_{\mathrm{t}} = \frac{b_{\mathrm{th}}\nu_0}{c} \tag{4.5}$$

is the most probable deviation from the rest frequency, ν_0, and b_{th} the thermal part of the so-called *Doppler parameter* in units of $\mathrm{km\,s^{-1}}$. In the case of the H I Ly α line transition, it is $\Delta_{\mathrm{t,HI\,Ly}\alpha} \approx 0.04\,\text{Å}$. The thermal part of the Doppler parameter can be written as

$$b_{\mathrm{th}} = \sqrt{\frac{2k_{\mathrm{B}}T}{m}} \approx 1.29 \times 10^4 \sqrt{\frac{T}{A}}\,\mathrm{cm\,s^{-1}}, \tag{4.6}$$

with T the gas temperature in units of K, m the particle mass, and A the atomic weight in units of u. Note that the measured Doppler parameter, b, is composed of a a thermal, b_{th}, and a turbulent term, b_{turb}, in the way that

$$b^2 = b_{\mathrm{th}}^2 + b_{\mathrm{turb}}^2. \tag{4.7}$$

The real frequency dependent profile of an absorption line is given by the convolution of (4.3) and (4.4):

$$\phi(\nu) = \phi_{\mathrm{L}}(\nu) \otimes \phi_{\mathrm{D}}(\nu) = \int_{-\infty}^{+\infty} \phi_{\mathrm{L}}(\nu - x)\phi_{\mathrm{D}}(x)\mathrm{d}x = \ldots = \frac{1}{\sqrt{\pi}2\pi\Delta_{\mathrm{t}}} H(\alpha, z), \tag{4.8}$$

where

$$H(\alpha, z) = \frac{\alpha}{\pi} \int_{-\infty}^{+\infty} \frac{e^{-x^2}}{(z-x)^2 + \alpha^2}\mathrm{d}x \tag{4.9}$$

is the so-called *Voigt function*, with

$$\alpha = \frac{\gamma}{4\pi\Delta_{\mathrm{t}}} \quad \text{and} \quad z = \frac{\nu - \nu_0}{\Delta_{\mathrm{t}}}. \tag{4.10}$$

4.2.2. Radiation Intensity and Optical Depth

Photons emitted from the quasar are shifted toward longer wavelengths (lower energies) along their way to the observer. As long as $E_\gamma > 10.2\,\mathrm{eV}$, they are capable of exciting the $1s \rightarrow 2p$ hydrogen Lyα transition (see Fig. 4.2). The excited electron then will almost instantaneously fall back to the ground state while emitting a Ly α photon. The emitted photon has no direction preference so that the absorbed photon can be regarded as scattered out of the LOS. This causes a change of the radiation intensity along an infinitesimal distance element, dx, along the LOS that is given by

$$\mathrm{d}I(x) = -I(x)\, n_{\mathrm{HI}}(x)\, \sigma_{\mathrm{Ly}\alpha}(\lambda, x)\, \mathrm{d}x, \tag{4.11}$$

with n_{HI} the neutral hydrogen volume density, and $\sigma_{\mathrm{Ly}\alpha}$ the hydrogen Ly α line scattering cross section, where $\sigma_{\mathrm{Ly}\alpha} = 4.5 \times 10^{-18}\,\mathrm{cm}^2$.

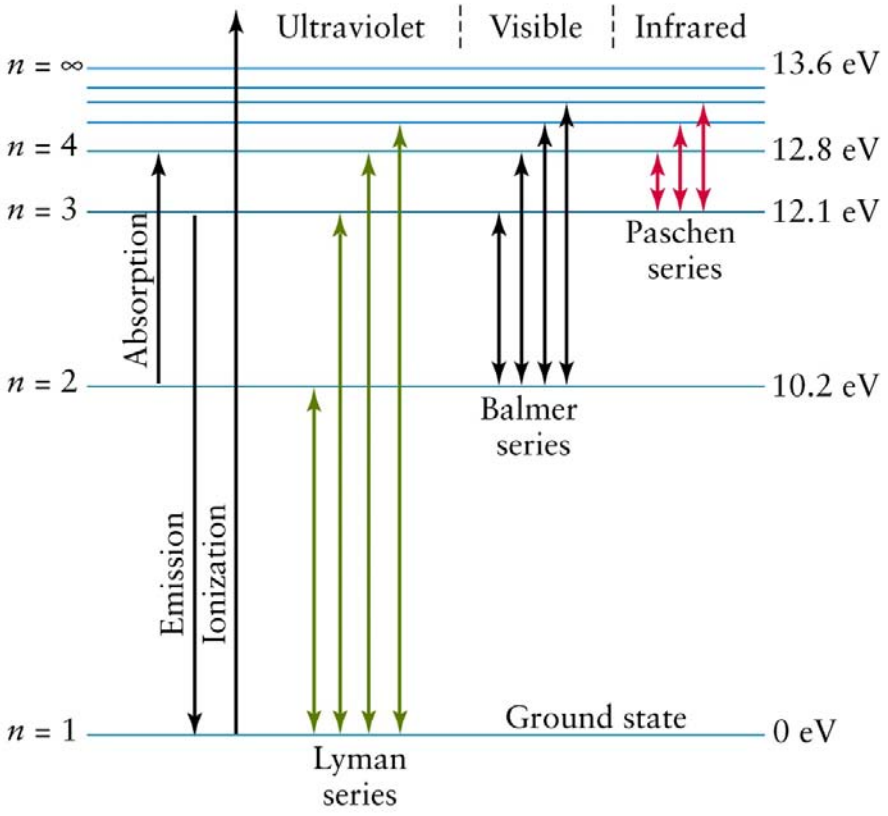

Figure 4.2.: Hydrogen term diagram. Ionization potentials and wavelengths for the hydrogen Lyman and Balmer series are given in Table 3.2, page 19.

At this point, let us now introduce a new measure, the optical depth, τ. The optical depth is a measure of transparency[6], and expresses the quantity of light removed from a beam by scattering or absorption during its path through a medium. At a given (observed) wavelength, $\lambda_{\rm obs}$, the optical depth in-between a point a to a point b of an absorption line system is defined as

$$\tau(\lambda_{\rm obs}) \doteq \int_{x_1}^{x_2} n_{\rm HI}(x)\, \sigma_{{\rm Ly}\alpha}\left(\lambda(x,\lambda_{\rm obs})\right) {\rm d}x, \tag{4.12}$$

and when using (4.8) can be written as

$$\tau_\lambda = \int_{x_1}^{x_2} \frac{\pi e^2}{m_{\rm e} c} n_{\rm l} f_{\rm lu} \phi(\lambda) {\rm d}x, \tag{4.13}$$

with $m_{\rm e}$ the electron mass, $n_{\rm l}$ the volume density of the atoms in a lower state (in ground state, i.e., $n_{\rm l=1}$, in the case of H I Ly α absorption), $f_{\rm ul}$ the oscillator strength ($f_{{\rm Ly}\alpha} = 0.4164$), and $\phi(\lambda)$ the line profile function as described by the Voigt function.

Integrating (4.11) and using the definition of the optical depth given in (4.12) will yield the observed intensity:

$$I(x=0) = I(x=x_{\rm qso})\, {\rm e}^{-\tau(\lambda_{\rm obs})}. \tag{4.14}$$

The observed (redshifted) wavelength, $\lambda_{\rm obs}$, depends on the rest wavelength, λ, and the redshift, z, where

$$\lambda_{\rm obs} = (1+z)\,\lambda. \tag{4.15}$$

In an Einstein-de Sitter universe, the relation between the physical spatial distance, x, and the redshift, z, is given by

$$x = \frac{2c}{3H_0}\left(1-(1+z)^{-\frac{3}{2}}\right). \tag{4.16}$$

Now, (4.12) can be solved for $\tau(\lambda_{\rm obs})$ using (4.15) and (4.16). In order to simplify the calculations, I will consider two common borderline cases for (4.12):

[6] *Optically thick* absorption line systems with $\log N_{\rm HI} \gtrsim 20$ show absorption line profiles that are dominated by Lorentzian (damping) wings. *Optically thin* absorption line systems with $\log N_{\rm HI} \lesssim 16$ show absorption line profiles that are dominated by a Gaussian core (see also Section 5.3.1).

a) Continuous H I Distribution

When considering a continuous distribution, the line profile can be approximated by a delta function, $\delta(\lambda/\lambda_{\mathrm{Ly}\alpha} - 1)$, with $\lambda_{\mathrm{Ly}\alpha} = 1215.67\,\text{Å}$ the central rest wavelength of the Ly α absorption line. The integral in (4.12) can be solved analytically, which then yields an expression for the optical depth as a function of redshift and wavelength. From (4.15) and (4.16) follows that

$$\frac{\mathrm{d}x}{\mathrm{d}\lambda} = -\frac{c}{H_0}\left(\frac{\lambda}{\lambda_{\mathrm{obs}}}\right)^{\frac{1}{2}}\frac{1}{\lambda_{\mathrm{obs}}}, \tag{4.17}$$

valid in an Einstein-de Sitter universe. The cross section, σ, that is dependent of the wavelength, is given by

$$\sigma = \sigma_{\mathrm{Ly}\alpha}\,\delta\left(\frac{\lambda}{\lambda_{\mathrm{Ly}\alpha}} - 1\right), \tag{4.18}$$

where δ is a delta function with

$$\int_{x_1}^{x_2}\delta\left(\frac{\lambda}{\lambda_{\mathrm{Ly}\alpha}} - 1\right)\frac{\mathrm{d}\lambda}{\lambda_{\mathrm{Ly}\,\alpha}} = 1. \tag{4.19}$$

Inserting (4.17) and (4.18) into (4.12) for $\lambda_{\mathrm{obs}} = \lambda_{\mathrm{Ly}\alpha}(1+z)$ then leads to

$$\tau(\lambda_{\mathrm{obs}}) = -\int_{\lambda_{\mathrm{obs}}}^{\lambda_{\mathrm{obs}}/(1+z_{\mathrm{qso}})} n_{\mathrm{HI}}(z)\,\sigma_{\mathrm{Ly}\alpha}\,\delta\left(\frac{\lambda}{\lambda_{\mathrm{Ly}\alpha}} - 1\right)\frac{c}{H_0}\left(\frac{\lambda}{\lambda_{\mathrm{obs}}}\right)^{\frac{1}{2}}\frac{\mathrm{d}\lambda}{\lambda_{\mathrm{obs}}}$$

and using (4.15) finally yields

$$= \frac{\sigma_{\mathrm{Ly}\alpha}\,c}{H_0}\,n_{\mathrm{HI}}(z)\,(z+1)^{-\frac{3}{2}}, \tag{4.20}$$

valid in an Einstein-de Sitter universe. Such a line scattering in a homogeneous (intergalactic) medium is also know as the *Gunn-Peterson* (GP) *effect*.

b) Discrete Absorption Line

In the case of a discrete absorption line, we consider a sharp maximum in the density distribution. For the sake of simplicity, I will consider the gas to be

restricted within a distance interval Δx, with $x_{\rm abs}$ the site on the LOS where the absorption takes place. Consequently, an absorption maximum will be seen at $\lambda = \lambda_{{\rm Ly}\alpha}(1+z_{\rm abs})$. The optical depth for wavelengths near the absorption maximum is then given by

$$\tau(\lambda_{\rm obs}+\Delta\lambda) = \sigma(\lambda) \int_{x_{\rm abs}-\frac{\Delta x}{2}}^{x_{\rm abs}+\frac{\Delta x}{2}} n_{\rm HI}(x){\rm d}x, \tag{4.21}$$

and the cross section, in the case of Ly α absorption, can be approximated by

$$\sigma_{{\rm HI}\,{\rm Ly}\alpha} \approx 7.6\times10^{-13}\left(\frac{b}{1\,{\rm km\,s^{-1}}}\right)^{-1} g(\lambda)\,{\rm cm}^2, \tag{4.22}$$

where g is a dimensionless form function with $g(\lambda=\lambda_{\rm obs})=1$.

4.2.3. Equivalent Width

The total area in a spectral line divided by the continuum flux is called the line equivalent width, or just equivalent width for short. In other words: if one imagines an absorption that takes out the same amount of energy (or surface) but with 100 % absorption depth ($I=0$ everywhere), then its width will correspond to the equivalent width, i.e.,

$$W_\lambda \doteq \int_{\lambda_1}^{\lambda_2} \frac{I_{\rm c}-I_\lambda}{I_{\rm c}}{\rm d}\lambda = \int \left(1-{\rm e}^{-\tau_\lambda}\right){\rm d}\lambda, \tag{4.23}$$

with $I_{\rm c}$ the continuum intensity, I_λ the intensity at a given wavelength, and τ_λ the optical depth as defined in (4.12). Note that, due to

$$\frac{W_\lambda}{\lambda} = \frac{W_\nu}{\nu}, \tag{4.24}$$

(4.23) can be written as a function of wavelength, λ, or frequency, ν. With the optical depth expressed as a function of the line profile and the oscillator strength, $f_{\rm ul}$, the equivalent width can be written as (see Appendix B for derivation)

$$W_\lambda = \int_{\lambda_1}^{\lambda_2}\left[1-\exp\left(-\int_{\rm a}^{\rm b}\frac{\pi e^2}{m_{\rm e}c}n_{\rm l}f_{\rm lu}\frac{\lambda_0}{\sqrt{\pi}2\pi b_{\rm th}}H(\alpha,z){\rm d}x\right)\right]{\rm d}\lambda. \tag{4.25}$$

4.2.4. Column Density

Besides the Doppler parameter, b, the column density, N, units of cm^{-2} is the other quantity used in order to describe an absorption line profile (see Fig. 4.3). The column density is a measure for the number of absorbing particles along a

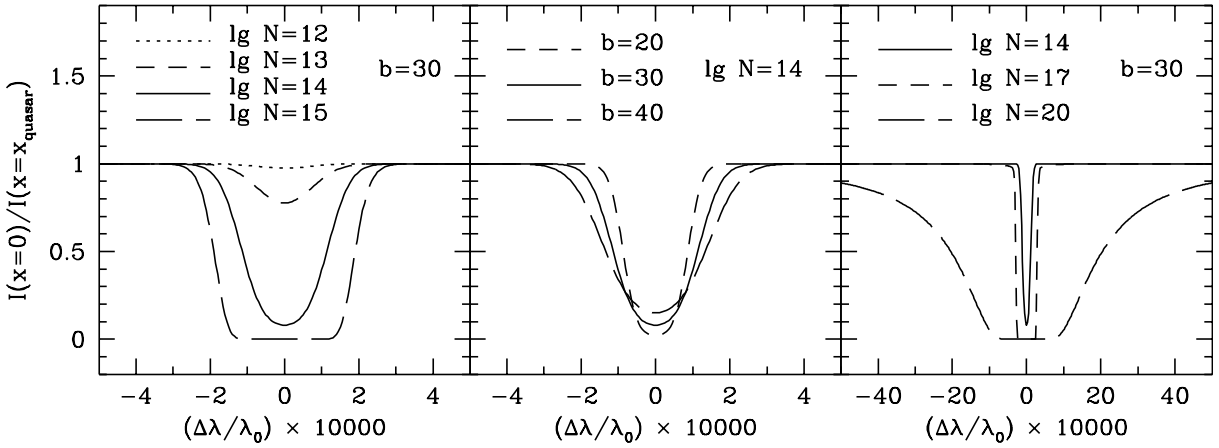

Figure 4.3.: Absorption line profiles with varying b and N values. The natural (observed) absorption line profile is described by the Voigt function, a convolution of a Gaussian and a Lorentzian line profile for the linear and the saturated regime, respectively (see Section 4.2.1).

column within a normalized area of 1 cm^2 and is defined as

$$N_{\mathrm{HI}} \doteq \int_{x_1}^{x_2} n_{\mathrm{HI}}(x)\mathrm{d}x. \tag{4.26}$$

Knowing the Doppler parameter, the column density, and the transition (and hence the accordant rest wavelength, λ, the oscillator strength, f_{ul}, and the damping constant, γ) will be sufficient to reproduce the corresponding absorption line profile (see Voigt profile fitting method in Section 5.3.3).

4.2.5. Line Broadening

Observed spectral lines are always broadened, partly due to intrinsic physical causes and partly due to the finite resolution of the spectrograph. The principal causes for the broadening observed in quasar absorption line spectra are Doppler, turbulent, and pressure broadening. The different mechanisms causing line broadening are briefly described below (see also Drake 1996).

- *Natural broadening* – Arises from the quantum mechanical uncertainty in the energy according to the electron energy states of the absorbing atom. A quantum state of an atom is not perfectly defined but presents a dispersion of energy (uncertainty principle). That means that photons will be absorbed within a small frequency range only. Its intensity distribution is described by the Lorentz profile (Mitchell & Zemanski 1971).

- *Thermal broadening*[7] – Since the absorbing atoms inevitably undergo thermal motion, they will all be in different reference frames relative to the light being absorbed. This velocity distribution will cause a frequency distribution (Doppler shift effect), giving rise to a Gaussian type line profile, i.e., the line shape of a Maxwellian velocity distribution. The broadening, $\Delta\lambda$, depends on the (kinetic) temperature of the gas, T, in the way that (Mitchell & Zemanski 1971)

$$\Delta\lambda = \lambda_0 \sqrt{\frac{k_B T}{mc^2}}. \tag{4.27}$$

- *Collisional broadening* – Originates from the interaction of the absorbing atom with the host gas. The electron energy states of the absorbing atom will be altered and the random energy perturbation will consequently cause a broadening of the absorption line. Collisional broadening may be due to various causes: (1) *Stark broadening* originates from long range interaction with charged gas particles (electrons and ions) and basically depends on the electron density and the gas temperature (Griem 1974; Konjević 1999). (2) *Pressure broadening* is due to collisions of the absorbing particle with neighboring particles. This effect turns out to be a function of the gas pressure, thus the name. The line profile is approximately Lorentzian. (3) *Resonance broadening* (or *self-broadening*) occurs only between identical species and is confined to lines with the upper or lower level having an electric dipole transition (resonance line) to the ground state. (4) *Van der Waals broadening* arises from the dipole interaction on an excited atom with the induced dipole of a ground state atom. (5) *Broadening from self-absorption* is due to the absorption of the emitted radiation by another atom of the same species present in the gas. This process reduces the spectral line intensity, basically the central part of the profile (Cowan & Dieke 1948).

[7] also called *Doppler broadening*

- *Turbulent Broadening* – When considering the case of two absorption lines arising in the same isothermal gas cloud, one line from an atom with mass m_1 and the other with m_2, then it is

$$\frac{b_1}{b_2} = \sqrt{\frac{m_2}{m_1}} \tag{4.28}$$

and therefore

$$m_1 > m_2 \Leftrightarrow b_1 < b_2, \tag{4.29}$$

with $b_{1,2}$ the corresponding Doppler parameters. If there is turbulence present in the gas, then (4.28) and (4.29) will break down. Unfortunately, it is not clear how to describe the turbulence function and thus correct for this type of broadening mechanism. Note that the thermal component depends on the atom mass, whereas the turbulent component is independent of mass. Therefore, all absorption lines (of similar species) in a given gas cloud with $b_{\rm th} \ll b_{\rm turb}$ will be characterized by the same b-value. In a more general case where $b_{\rm th} \sim b_{\rm turb}$, it is possible to deconvolve the total Doppler parameter and express the turbulent term as a function of transitions from two or more atoms (for more details see, e.g., Churchill 1997).

- *Instrumental Broadening* – This broadening effect is due to the finite resolution of the spectrograph. The instrumental broadening- or spread function is usually known. If this is not the case, it can also be deduced from the observed spectrum (see, e.g., Nissen et al. 2005).

4.2.6. Saturated Absorption Lines

An absorption line is said to be saturated when the transmitted intensity at the line center is zero[8] – more precisely, when no discernable signal can be detected. No photons (within the measurement accuracy) with wavelengths corresponding to the line center are transmitted through the absorbing gas cloud and the strength of the absorption line is no longer proportional to the amount of material present. Even the very accurate line profile fitting method does not yield absolutely reliable values in that case because the line profile of a saturated line does not significantly vary with column density.

[8] see also (5.4) on page 57

Note that heavily saturated absorption lines are additionally characterized by their damping wings that can improve the accuracy of the line profile fitting method. However, an additional source of errors in that case is the uncertain continuum (see also Section 5.3.3). Nevertheless, note that the equivalent width of a saturated absorption line remains an accurate measure, and with the curve of growth method (see Section 5.3.1) accurate values for b and N can be derived.

The curve of growth in Fig. 5.3 illustrates the case for H I. We can see that in the linear part (where $W \propto \log N$), i.e., around $\log N = 10^{15} - 10^{17}$, the equivalent width does not significantly vary with column density[9]. Hence, in this case, Doppler parameters and column densities should always be derived from two or more transition lines.

[9] We note that this is the same range in which we observe a discontinuity in the CDDF (Fig. 3.3) in Chapter 3. However, it is not clear if this deviation from the assumed power-law can be directly linked to measurement uncertainties due to saturation.

5. The UVES Spectrograph, Data Reduction Methods, Effects that alter Metal Abundance Measurements, and Error Handling

5.1. Overview

The aim of this chapter is to summarize the most common procedures of the day-to-day business for the analysis of quasar absorption line spectra. A short introduction to the UVES spectrograph, its parameter settings, and an overview of other currently operating spectrographs is given. Consecutively, I introduce the three main approaches for the data reduction of absorption line spectra (curve of growth method, the apparent optical depth method, and the line-profile fitting method).

Next to observational errors[1], such as atmospheric effects (like seeing, humidity, light pollution, etc.) and systematic instrumental errors, we also have to account for errors that are due to intrinsic physical processes in the absorption line system (photoionization and dust depletion). Further, additional errors originate from the data reduction itself, where the most likely source of errors is due to an uncertain continuum placement. Finally, I explain how to calculate the detection significance of an absorption line and give a brief introduction to error calculus in log-space.

[1] In the case of the UVES spectrograph, these errors are accounted for by the UVES data reduction pipeline (Ballester et al. 2000) that includes, among others, flat-fielding, bias- and sky-subtraction, and a relative wavelength calibration.

5.2. The UV Echelle Spectrograph at VLT/UT2

The UV Echelle Spectrograph (UVES) is a high-resolution optical spectrograph installed at the Nasmyth B focus of Kuyen, the Unit Telescope 2 of the ESO Very Large Telescope (VLT) array on Mount Paranal, Chile. It is a powerful cross-dispersed echelle spectrograph designed to operate from the atmospheric cut-off at $\sim 300\,\mathrm{nm}$ to the long wavelength limit of the CCD detectors at $\sim 1\,150\,\mathrm{nm}$ with an order separation of at least 10 arcseconds. The light beam from the telescope is split into two arms (UV to a blue arm, and Visual to a red arm). The two arms can be operated separately, or in parallel via a dichroic beam splitter. The resolving power is about $R \sim 40\,000$ when a $1''$-slit is used. With narrower slits or an image slicer, i.e., in order to avoid excessive slit losses, a maximum resolving power (two-pixel resolution) of 80 000 and 115 000 in the blue and the red arm, respectively, can be achieved. The UVES spectro-

Table 5.1.: UVES at VLT/UT2: spectroscopic modes. The magnitude limits listed are estimated based on the following conditions: continuum source, 0.7 arcsec seeing, $1''$-slit, no binning, 3-hour integration time, SNR of 10 (per resolution element) at the peak of the central order, no moon.

instrument mode	accessible λ range [nm]	maximum resolution $[\lambda/\Delta\lambda]$	covered λ range [nm]	magnitude limits [mag]
BLUE	300−500	80 000	80	17−18
RED	420−1100	110 000	200−40	18−19
DICHROIC1	300−400	80 000	80	17−18
	500−1100	110 000	200	18−19
DICHROIC2	300−500	80 000	80	17−18
	600−1100	110 000	400	18−19
iodine cell	500−600	110 000	200	17

graph can be operated in four different modes: BLUE, RED, DICHROIC1, and DICHROIC2. For each mode standard settings have been defined. An iodine

cell can be inserted in the light beam for observations requiring extremely high accuracy for radial velocity measurements. Table 5.1 indicates the accessible wavelength range, the maximum resolving power that can be obtained, the approximate wavelength range covered in one exposure, and an estimate of the limiting magnitude for a given operation mode.

According to the observation requirements, the CCD cameras in the blue- (Blue CCD) and red arm (Red CCD), the cross dispersers in the blue (CD #3 and CD #4) and the red arm (CD #1 and CD #2), the beam splitters (DIC #1, DIC #2, Blue, and Red), and of course the slit or an image slicer (IS1, IS2, and IS3), can be assembled according to the UVES standard settings (in service mode) or according to specific needs (in visitor mode only). Whether an image slicer should be used or not depends on the trade off between slit losses due to the seeing limitations and the reduced transmission (reduction between 20 and 40 %) when using an image slicer. For estimating the SNR, the ESO/UVES Exposure Time Calculators (ETC) should be used. UVES also supports the use of several filters in the red arm (in visitor mode only) in order to isolate certain echelle orders and thereby to use the maximum slit length of 30 arcsec. More details can be found in Dekker et al. (2000) or in the UVES User Manual.

UVES is, within the VLT Observatory, one possible choice for conducting spectroscopic observations in the ultraviolet (UV), visual (V), and infrared (IR) band. In choosing the best instrument for a given observing program, the following trade-offs between the different instruments have to be taken into consideration:

Spectroscopy in the UV-Visual-Red regions (300 − 1100 nm)

FORS1 at UT2: Spectral range 360 − 1110 nm. Its overall efficiency is on average 2 times higher than UVES but the maximum resolving power is only 2500 for a $0.5''$-slit.

FORS2 at UT1: FORS2 is a replica of FORS1, but it will eventually include two transmission echelle gratings, which – when used in conjunction with a grism cross disperser – will provide a resolving power of up to 6000 and a wider spectral coverage comparable to that of UVES.

GIRAFFE at UT2: GIRAFFE is part of the FLAMES instrument at the opposite Nasmyth platform of UT2. It is the instrument which approaches closest to the UVES resolution. An automatic fiber-positioning unit can use up to 132

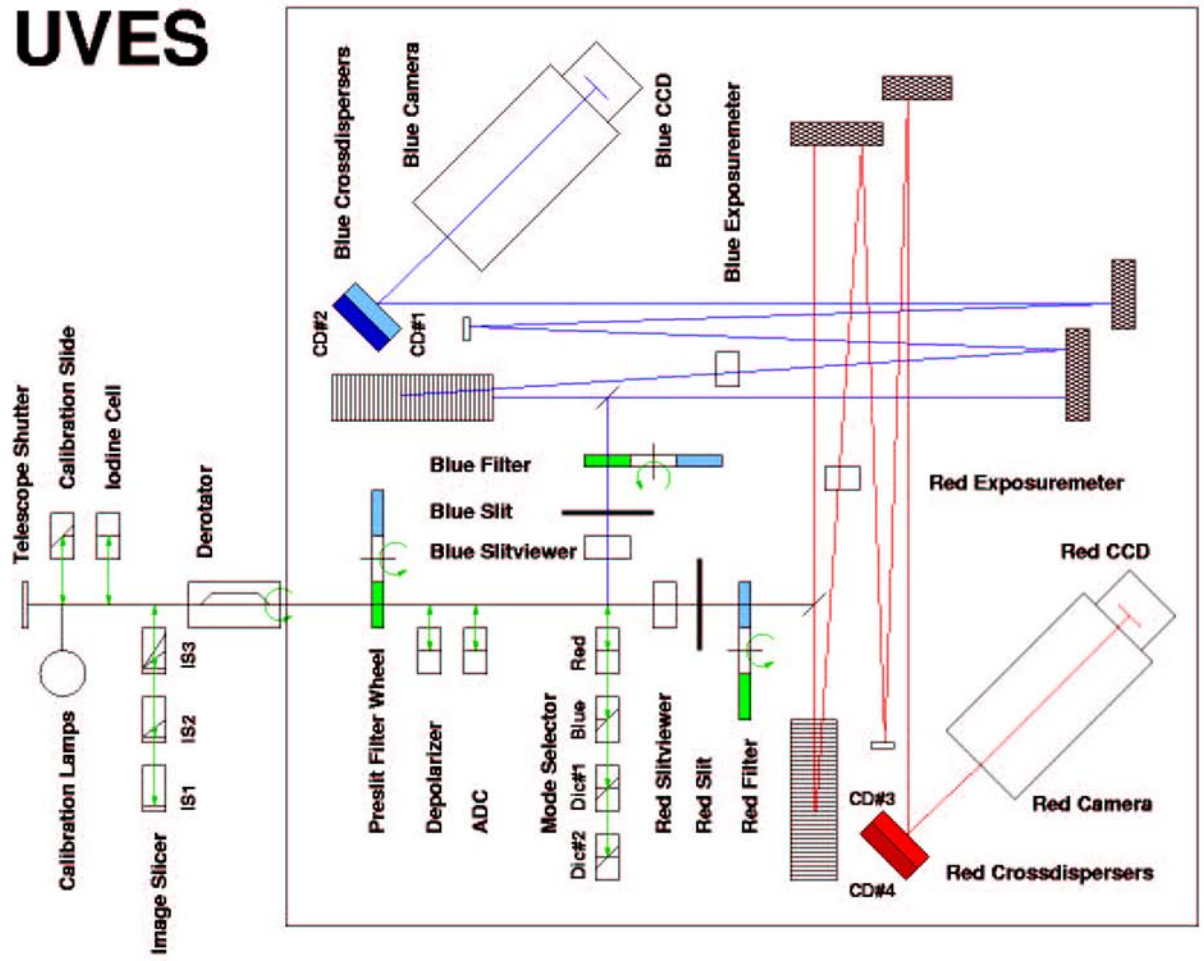

Figure 5.1.: Schematic overview of the UVES spectrograph (from the UVES User Manual).

fibers in a field of view of 25 arcminutes. GIRAFFE is (with a limiting resolving power of 20 000) on average 30 % less efficient than UVES, but the multiplexing gain when observing up to 132 objects in parallel can make it the best choice if the observing program includes many objects in a single field at intermediate spectral resolution.

Spectroscopy at infrared wavelengths (1−5 μm)

ISAAC at UT1: The infrared imager-spectrometer ISAAC can be used to obtain spectra in the $1-5\,\mu$m spectral region with a resolving power of up to 10 000 if a $0.5''$-slit is used. ISAAC is an IR ($\sim 0.7-100\,\mu$m) imager and spectrograph that is installed at the Nasmyth B focus of UT1. It has two arms, one equipped

with a 1024×1024 Hawaii Rockwell array, and the other with a 1024×1024 InSb Aladdin array from the Santa Barbara Research Center. The Hawaii arm is used at short wavelengths ($1-2.5\,\mu$m). Prior to P70, the Aladdin arm was used exclusively at long wavelengths ($3-5\,\mu$m). From P70 onwards this arm is also offered for JHK imaging.

CRIRES at UT1: First commissioning (first light) of the high-resolution infrared spectrometer CRIRES, the counterpart of UVES in the $1-5\,\mu$m spectral region, was successfully performed in June 2006. CRIRES is a cryogenic high-resolution IR spectrograph that has been conceived for the VLT in order to exploit the enormously enhanced sensitivity provided by a dispersive instrument with a large detector array at an 8 m telescope. The gain entails a quantitative and qualitative improvement of the observational capabilities. It can boost all scientific applications aiming at fainter objects, higher spatial, spectral, and temporal resolution.

Other high-dispersion, echelle format spectrographs available at ESO La Silla, Chile, are FEROS at the MPG/ESO 2.2 m telescope ($R \sim 48\,000$), EMMI at the NTT ($R \sim 7700$-$60\,500$), and HARPS ($R \sim 110\,000$) and CES ($R \sim 220\,000$) at the ESO 3.6 m telescope.

5.3. Data Reduction Methods

5.3.1. Curve of Growth

The aim of each analysis of an absorption line profile is to retrieve the information about the amount of absorbing material along the LOS, i.e., to measure the column density, N. To do so, one can make use of the so-called curve of growth (COG) method, possibly the most straightforward and also most basic method: once the equivalent widths of the absorption lines are measured, a theoretical COG will yield the corresponding column densities and b values.

The equivalent width can be easily measured by numerical integration over the intensity in the absorption line. A simpler but very efficient approach consists in fitting a Gauss profile to weak lines or lines which are at most only very mildly saturated. For strong, saturated lines this is no longer accurate because extended damping wings (Lorentz profile) dominate the absorption line.[2]

[2]Fitting a Voigt line profile – a convolution of the Doppler- and the Lorentz distribution function – will yield

The link between the measured equivalent width, W_λ, and the column density, N, is provided by the COG as given in (4.25). Examples for COGs with $b = 5, 10, 15,$ and $20\,\mathrm{km\,s^{-1}}$ are shown in Fig. 5.2. The COGs in a particular case, i.e., in the case of H I Ly α transitions, are shown in Fig. 5.3, where logarithmic equivalent width is plotted versus logarithmic column density. The linear part at low ($\tau \ll 1$) and high ($\tau \gg 1$) column densities, respectively, and the non-linear inner part at intermediate column densities ($\tau \sim 1$) can be regarded as three different cases, quantified by the optical depth, τ:

- $\tau \ll 1$

  Doppler part: The profile is dominated by the Gaussian core. This is the case for $\tau \ll 1$, or if the Doppler parameter dominates over the damping constant ($\alpha \ll 1$). The equivalent width depends on the column density in a linear way, i.e., $W_\lambda \propto N$, or

$$\frac{W_\lambda}{\lambda} = \frac{\pi e^2}{m_\mathrm{e} c^2} N f_\mathrm{ul} \lambda . \tag{5.1}$$

- $\tau \sim 1$

  Intermediate part: The profile depends strongly on the Doppler parameter. The equivalent width dependency on the column density is a power law, i.e., $W_\lambda \propto \log N$, or

$$\frac{W_\lambda}{\lambda} \propto \log N f_\mathrm{ul} \lambda . \tag{5.2}$$

- $\tau \gg 1$

  Damping part: The profile is dominated by Lorentzian wings (or damping wings). This is the case for $\tau \gg 1$, or for very low Doppler broadening and strong damping ($\alpha \gg 1$). There is a square root dependency of the equivalent width on the column density, i.e., $W_\lambda \propto \sqrt{N}$, or

$$\frac{W_\lambda}{\lambda} = \sqrt{\frac{\gamma e^2 \lambda}{m_\mathrm{e} c^3}} \cdot \sqrt{N f_\mathrm{ul} \lambda} . \tag{5.3}$$

directly the associated column density and Doppler parameter, regardless of whether the absorption line is saturated or not (see also Section 5.3.3).

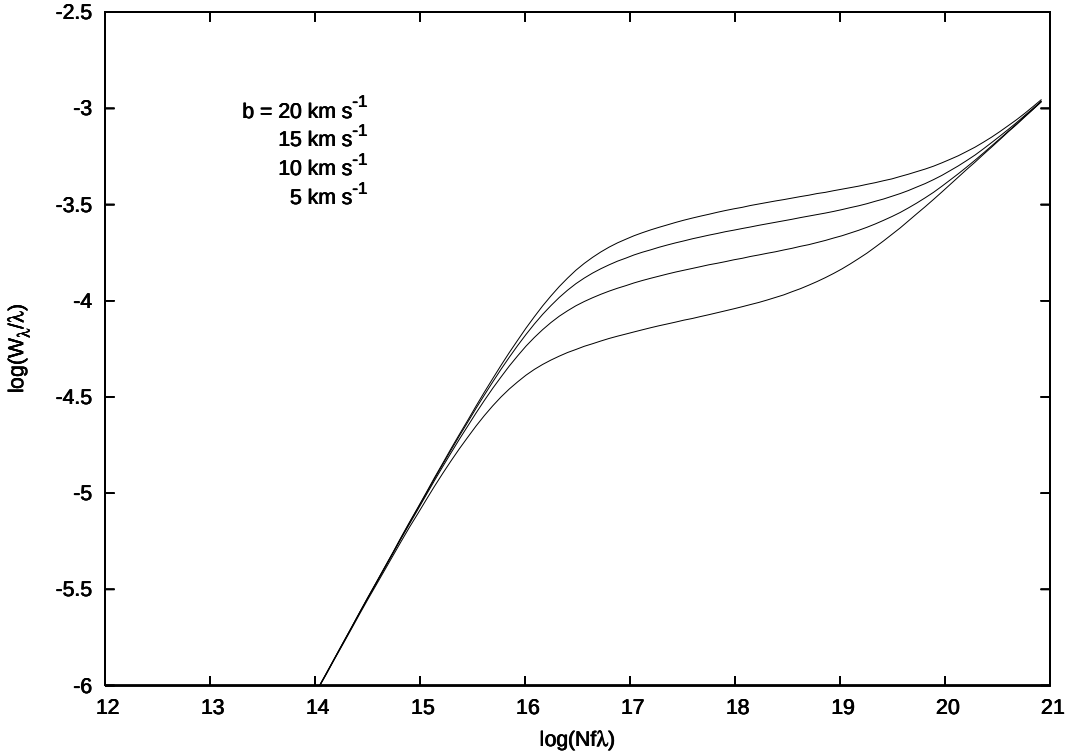

Figure 5.2.: Theoretical curves of growth showing the relation of the normalized line strength W_λ/λ to the optical depth parameter $Nf\lambda$ for different Doppler parameters $b = 5, 10, 15,$ and $20\,\mathrm{km\,s^{-1}}$. We can clearly distinguish three different regimes: a linear regime at lower column densities, a logarithmic regime at intermediate column densities, and a square root regime at high column densities (see also Fig. 5.3). The damping parameter was chosen to be $\gamma = 1.45 \times 10^9\ \mathrm{s}^{-1}$ in this example.

Modus operandi – After W_λ is measured for a transition with known oscillator strength and wavelength, the COG will yield the corresponding column density for a given b-value. The main difficulty is, though, that in most cases the b-parameter is unknown. In this case, one can first determine W_λ for a sample of different absorption lines from the same element[3] (and thus with the same column density) in order to afterwards fix the b-value using an array of curves of growth. If possible, the transition set should cover a large range of oscillator strengths. Once the b-value for the gas is fixed, then the column densities, also for elements with fewer observed transitions, can be easily determined by a horizontal shift to the data points of the corresponding COG. Note that the equivalent width remains an accurate measure, even in the case of saturated lines (see also Section 4.2.6).

[3] more precisely: from the same element *and* the same ionization level

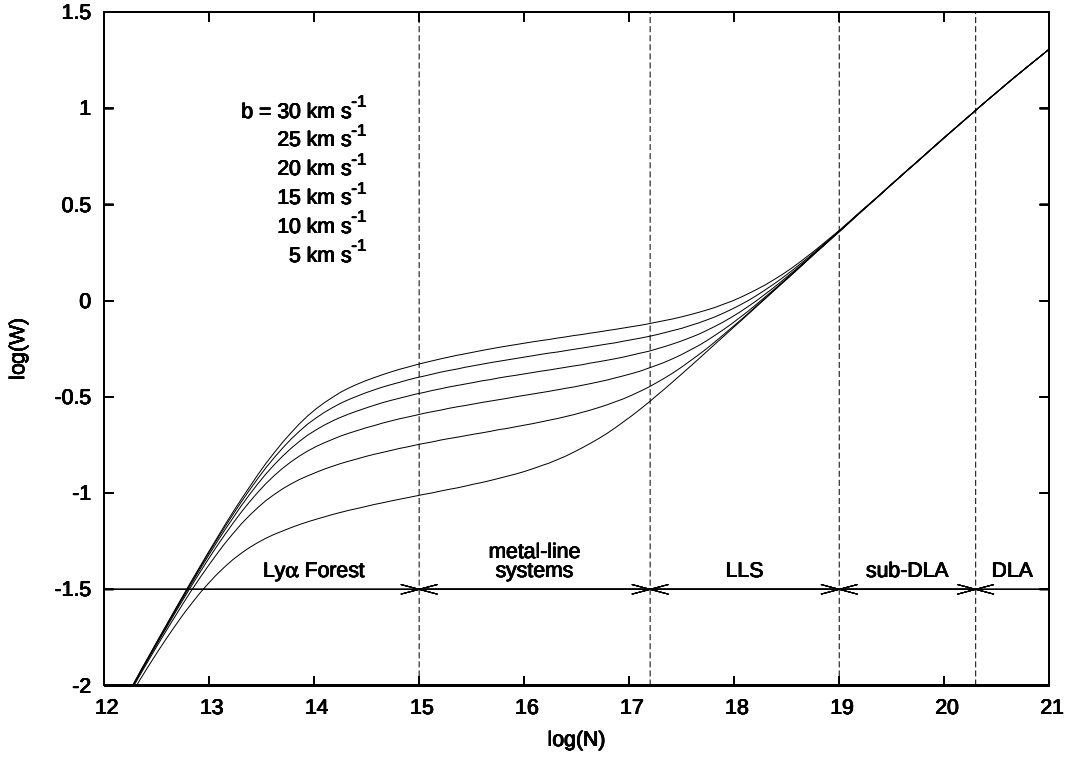

Figure 5.3.: Theoretical curves of growth for the case of H I Ly α, showing the equivalent width, W, as a function of the column density, N. Six different cases with Doppler parameters ranging from $b = 5 - 30\,\mathrm{km\,s^{-1}}$ are given. Further, the common classification for H I absorption line systems according to their column density (see also Section 3.2) is illustrated.

Drawbacks – The COG method works well in the case that W_λ can be accurately measured, i.e., in the case of a well defined single line, or a group of lines for which the sum of the individual transitions' equivalent widths, $\sum_i W_{\lambda,i}$, is linked to the sum of the corresponding oscillator strengths. The latter is the case if a transition of an element whose individual f_{ul} values *and* whose sum of f_{ul} values are located on the Doppler part of the COG ($\tau \ll 1$). In case of high column densities – and thus absorption lines with strong damping wings – uncertainties in the continuum placement may lead to inaccurate results. Additionally, blending of unrelated lines, a poor resolution, or both, can aggravate the quality of the equivalent width measure.

5.3.2. Apparent Optical Depth Method

Note that the equivalent width is a fudge, made necessary by the fact that spectrographs are limited in resolution. Their spectra do not resolve all of the intrinsic profiles within the absorption lines but show the convolution of the intrinsic line shape with the instrument's broadening function, i.e., important information encoded in the line profile will be lost (see also Chapter 10). The equivalent width is, however, invariant to the convolution and consequently a conserved quantity. Hence, it is still possible to recover the absorber's column density, N, from measurements of the equivalent width, W_λ.

Unlike the COG method with a *direct* conversion of the absorption line data, the apparent optical depth (AOD) method (Savage & Sembach 1991) converts the observed absorption line profiles into profiles of apparent optical depth, τ_a, and apparent column density (per unit velocity), N_a. As already shown in Section 4.2, an absorption line with a given optical depth will appear as

$$I(\lambda) = I_0(\lambda)\mathrm{e}^{-\tau_\lambda}, \tag{5.4}$$

where $I(\lambda)$ and $I_0(\lambda)$ are the intensities with and without the absorption, respectively. Each spectrograph has a finite resolution, defined by its instrumental spectral spread function, $\phi_{\rm sf}(\Delta\lambda)$, where the observed spectrum is a convolution of the intrinsic spectrum and the spread function. It is

$$I_{\rm obs}(\lambda) = \left(I_0(\lambda)\mathrm{e}^{-\tau(\lambda)}\right) \otimes \phi_{\rm sf}(\Delta\lambda). \tag{5.5}$$

Because $I_0(\lambda)$ changes only slowly over the width of the spread function we can write

$$I_{\rm obs}(\lambda) = I_0(\lambda)\left(\mathrm{e}^{-\tau(\lambda)} \otimes \phi_{\rm sf}(\Delta\lambda)\right). \tag{5.6}$$

From (5.4) and (5.6) we can now define two kinds of optical depth, the *true* optical depth,

$$\tau(\lambda) = \ln\frac{I_0(\lambda)}{I(\lambda)}, \tag{5.7}$$

and an *apparent* optical depth

$$\tau_a(\lambda) = \ln\frac{I_0(\lambda)}{I_{\rm obs}(\lambda)} \tag{5.8}$$

$$= \ln\frac{1}{\mathrm{e}^{-\tau(\lambda)} \otimes \phi_{\rm sf}(\Delta\lambda)}, \tag{5.9}$$

which is an instrumentally blurred version of the true optical depth. If the instrumental resolution is very high compared to the line width, then the apparent optical depth will be a good approximation for the true optical depth, i.e., $\tau_a \approx \tau$. In this case, the connection between optical depth and column density is

$$\tau(\lambda) = \frac{\pi e^2}{m_e c^2} f_{ul} \lambda^2 N(\lambda), \tag{5.10}$$

with $N(\lambda)$ the column density per unit wavelength. More commonly expressed in velocity space, (5.10) becomes

$$\tau(v) = \frac{\pi e^2}{m_e c} f_{ul} \lambda N(v) = 2.654 \times 10^{-15} f_{ul} \lambda N(v), \tag{5.11}$$

where λ is in units of angstroms and $N(v)$ in atoms $\mathrm{cm}^{-2}\,(\mathrm{km\,s}^{-1})^{-1}$. The total column density is, according to (4.26) and using (5.9), given by

$$N = \int N(v)\mathrm{d}v = \frac{m_e c}{\pi e^2 f_{ul} \lambda} \int \tau(v)\mathrm{d}v = \frac{m_e c}{\pi e^2 f_{ul} \lambda} \int \ln \frac{I_0(v)}{I(v)} \mathrm{d}v. \tag{5.12}$$

This method has been widely employed in past studies of the IGM for which high resolution data were available and where single lines belonging to the same species have been measured. Note that the AOD is only valid for unsaturated absorption lines.

Modus operandi – The AOD method requires *two or more* absorption lines of a given species which differ in $f_{ul}\lambda$. The absorption line data are converted into different measures of τ_a. These are then converted into measures of the apparent column density, N_a, via (5.10), which can be expressed in units of atoms $\mathrm{cm}^{-2}\,\mathrm{km\,s}^{-1}$ and written in logarithmic form as

$$\log N_a(v) = \log \tau_a(v) - \log (f_{ul}\lambda) + 14.576. \tag{5.13}$$

Comparing $N_a(v)$ for lines with different $f_{ul}\lambda$ provides an empirical way of assessing the degree of line saturation present. The comparison also yields information about the accuracy to which the derived $N_a(v)$ profiles are valid representations of the true $N(v)$ profiles (blurred by the instrumental spread function).

The effects of unresolved saturated structure in the true (blurred) profiles are

- not large at those velocities where the different $N_a(\upsilon)$ profiles are the same or very similar. In this case $N_a = \int N_a(\upsilon)d\upsilon$ yields valid values for the instrumentally smeared column densities over those regions.
- significant if the $N_a(\upsilon)$ profile of the stronger lines is significantly smaller than that of the weaker lines.

Note further that

- $N_a \neq N$ for cases in which the line is unresolved (unless the integration extends over an entire line for which no saturated structure is present).
- saturation effects can be quantified when lines with sufficiently different $f_{ul}\lambda$ are compared to each other.

5.3.3. Voigt Profile Fitting by χ^2-Minimization

Profile fitting aims at determining Doppler values and column densities based on the shape of the observed absorption line profile. The observed profile is always a convolution of the true line profile, described by the Voigt function, and the broadening caused by the instrumental spread function. The latter is, unfortunately, not always precisely known. Profile fitting is a straightforward procedure if the instrumental resolution is high enough to resolve the absorption line with the required precision. A theoretical profile (that accounts for instrument broadening) is compared to the observed profile. Eventually, the χ^2 deviation of the two then is minimized in order to determine the best-fit parameters. Simultaneous fitting of one or more components, components of different transitions and even of different elements (with certain restrictions), does not only generate more accurate results but also allows us the study and analysis of (partially) blended or very weak lines. However, a few important points have to be taken into consideration.

Continuum placement – Although QSO spectra are relatively clean and relatively smooth at large scales if compared to stellar spectra or spectra from galaxies, the normalization is nevertheless an important and not always straightforward task. In particular, the continuum placement in the case of DLA systems, i.e., dense absorption line systems with strong damping wings, is not simple because it is hard to tell where the H I Ly α trough begins and where the pure

continuum (without any attenuation due to the extended damping wings) ends. A detailed discussion on the issue of continuum placement in an explicit DLA system is given in Chapter 8.

Doppler parameter – Line profile fitting for DLA systems can be performed by assuming the same Doppler parameter for all ions with similar ionization potentials for a given velocity component, i.e., it can be assumed that bulk motion dominates over thermal motion. This is a reasonable assumption as long as a DLA system consists of cold gas and the ions under study are rather heavy. In order to determine the b-value, ions with a large number of transitions and which cover a large range in $f_{\rm ul}$ values are required. When using line profile fits, the b-parameter is mainly determined by those transitions with equivalent widths between the transition of the Doppler part ($\tau \ll 1$) and the intermediate part ($\tau \sim 1$) on the COG. In the case of higher column densities ($\tau \gg 1$), however, the line profile fitting method might not be able to fully account for line saturation, i.e., the variation in the line profile might be too insignificant to properly determine the Doppler parameter. For that reason it makes sense, in some cases, to determine the b-values apriori by using the COG method, before proceeding with the line profile fitting method.

Instrumental broadening – The instrumental spread function is not always well known. If this is the case, it is possible to determine the instrumental spread function from line profiles fits. Note further that the instrumental spread function may vary over the spectral range.

Modus operandi – To fit an absorption line system, one needs to select a set of unsaturated lines of similar strengths. Strong lines should be avoided because they may show additional components that will tend to boost the b-values of the main components of the system if not properly taken into account. Likewise, saturated lines should also be excluded from any fiducial sample because saturated lines lead in practice to less accurate results, regardless of the analyzing method used. The fiducial sample can consist of different species from different elements but with similar ionization potentials. It should always be tried to fit not only one but at least two lines from the same ion. Once the best-fit parameters are determined, and when assuming local thermodynamic equilibrium[4] (LTE), it is a fair approximation to assume low-ionization species to have

[4] The rate of collisional ionization must equal the rate of collisional recombination.

the same b value, i.e. the b-values determined by the fit of the fiducial sample. The same procedure holds for high-ionized species like, for example, C IV and O VI.

5.4. Intrinsic Effects that alter Metal Abundance Measurements

5.4.1. Photoionization Correction

In Section 3.3, a general introduction to ionization, caused by photons or collisions, was given. Here, I want to focus on photoionization – the most common form of ionization in DLA systems – and to derive the ionization correction factor (ICF), $f(\mathrm{i},\mathrm{j})$. The ICF is used (see, e.g., Chapter 8) in order to correct the measured metal abundances and, hence, to correct for altering photoionization effects.

Ionization caused by Photons and the Ionization Correction Factor (ICF)

The ionization probability depends on the electron ionization potential, $\mathrm{E_{ion}}$, and on the photon energy, E_γ. If $E_\gamma = \mathrm{E_{ion}}$, then an electron will be detached but no energy will be added to the gas. As the photon energy increases, the probability of ionization will decrease as $(\mathrm{E_{ion}}/E_\gamma)^3$. Eventually, the detached electron will add a kinetic energy of

$$E_{\mathrm{kin}} = \frac{1}{2} m_e \upsilon^2 = E_\gamma - \mathrm{E_{ion}} \tag{5.14}$$

to the surrounding gas. The ionization cross section is given by

$$\sigma_\lambda = \sigma_0 \left(\frac{\lambda}{\lambda_0}\right)^3, \tag{5.15}$$

with $\lambda_0 = hc/\mathrm{E_{ion}}$ the wavelength at the ionization edge and, in the case of hydrogen, with

$$\sigma_0 = 6.3 \times 10^{-18} \left(\frac{E_\gamma}{13.6\,\mathrm{eV}}\right)^{-3} \mathrm{cm}^2, \tag{5.16}$$

the cross section at $E_\gamma = \mathrm{E_{ion}}$. Analog, it is

$$\sigma_\nu = \sigma_0 \left(\frac{\nu}{\nu_0}\right)^{-3}, \tag{5.17}$$

with $\nu_0 = \mathrm{E_{ion}}/h$ being the frequency at the ionization edge. Using the ionization cross section and (4.12), the optical depth can be written as

$$\tau_\lambda = N\sigma_\lambda = N\sigma_0\Big(\frac{\lambda}{\lambda_0}\Big)^3, \tag{5.18}$$

with N the column density (only valid if dust is ignored).

It is important to note that column densities derived from observed spectra are always ionic column densities. Therefore, the total metal column density, i.e., the total quantity of particles (atoms *and* ions) of a certain element per unit surface along the LOS depends on *all* ionization states present in the absorbing gas. An ionization correction is necessary because, in general, only few ionization stages can be observed and hence the ionic column densities derived from observation do only partially contribute to the total metal column density.

Let us consider two elements X and Y, where $N(\mathrm{X_i})$ and $N(\mathrm{Y_j})$ are the respective column densities obtained from the observed spectrum. The (true) relative abundance of the elements X and Y is given by

$$\frac{\mathrm{X}}{\mathrm{Y}} = f(\mathrm{i,j})\frac{N(\mathrm{X_i})}{N(Y_j)}, \tag{5.19}$$

where $f(\mathrm{i,j})$ is the ICF, taking account for the presence of unobserved ions or neutral species, $N(\mathrm{X_k})$ and $N(\mathrm{Y_l})$, respectively (Viegas 1995). The ionization correction factor is given by

$$f(\mathrm{i,j}) = \frac{1+\frac{\sum_{\mathrm{k}\neq\mathrm{i}}N(\mathrm{X_k})}{N(\mathrm{X_i})}}{1+\frac{\sum_{\mathrm{l}\neq\mathrm{j}}N(\mathrm{Y_l})}{N(\mathrm{Y_j})}}. \tag{5.20}$$

A practical example of ionization correction in a QAL spectrum, using a photoionization model based on `Cloudy` (Ferland et al. 1998), is given in Chapter 8. See below for a short program description of the `Cloudy` software package.

Photoionization Simulations with `Cloudy`

In many regions diluted gas is heated and eventually ionized by a radiation field. It is possible to predict the physical conditions (i.e., the distribution of ionization, density, and temperature) across the cloud, and its resulting emission-line

spectrum, in a unique and self-consistent manner. This is done by simultaneously solving the equations of statistical and thermal equilibrium, equations that balance ionization-recombination processes, and heating-cooling processes, respectively. The physics governing such environments is described by Osterbrock & Ferland (2006).

The `Cloudy` software package[5] is designed to simulate emission-line regions ranging from very low-density regions, such as the IGM, to high-density regions where local thermodynamic equilibrium still can be assumed (LTE limit).

One powerful asset of photoionization analysis is that from only a few input parameters (essentially the incident continuum, the chemical composition, geometry, and density dependence of the gas) a large number of observables (intensities of many millions of spectral lines) are predicted.

5.4.2. Dust Depletion

In astronomy, micron-sized particles which absorb and scatter light and cause extinction are commonly referred to as *dust*[6]. Dust plays an important role in the thermal balance of matter and provides the first solid surfaces in the Universe on which reactions like H_2 formation or other more complex reactions can take place. Dust strongly affects radiative transfer because it can radiate, reflect, and absorb light. Dust in the interstellar medium (ISM) within galaxies lives in a multi-phase and multi-timescale environment. This medium is decomposed into three classical phases: the hot medium (HM), the warm intercloud medium (WIM), and the cold medium (CM), connected to each other through a large number of loops (McKee & Ostriker 1977).

The presence of dust at high redshifts has implications both for the chemical evolution and for observational strategies. There are a few lines of evidence that indicate the presence of dust in QSO absorption line systems. Fall et al. (1989) and Pei et al. (1991) compared the spectral slope of quasars with and without DLA absorption line systems and found that quasars with DLA systems are redder. Malhotra (1997) could show that the same broad dust feature at 2175 Å observed in local galaxies (MW, LMC, SMC, M31, and M101) is seen in QSO absorption line systems.

[5] `Cloudy`, as well as the extensive program documentation `Hazy`, are available at http://www.nublado.org/.

[6] Note that interstellar dust grains with sizes on the order of fractions of a micron are much smaller than the dust found around us in everyday life. Interstellar dust is irregularly shaped, composed of carbon and/or silicates, and most evident by its absorption. Dust grains are clearly associated with young stars but important contributions come also from evolved stars, through mass loss, and supernovae, through their ejecta. A nice review on the formation, composition, and evolution of dust is given by Dartois (2005).

Gas-phase atoms from *refractory elements*[7] will stick onto dust grains and eventually cause a change in the observed metal abundance pattern. In combination with cosmological abundances, these observations provide powerful constraints on the nature, size, motion, and distribution of dust grains throughout the gas cloud. On the other hand, *volatile elements*, like for example zinc, are not depleted. Zinc is a widespread indicator for the metallicity in DLA systems, where the zinc abundance ratio,[8] [Zn/H], is believed to be not at all, or at most very little, affected by dust depletion. Pettini et al. (1994) demonstrated that the majority of DLA systems exhibit an enhancement of Zn relative to Cr, i.e. $[\mathrm{Cr/Zn}] < 0$, which they interpreted as evidence of dust depletion. Therefore, the expression

$$\left[\frac{\mathrm{Cr}}{\mathrm{Fe}}\right] = \log\frac{N(\mathrm{Cr\,II})}{N(\mathrm{Zn\,II})} - \log\frac{\mathrm{Z_{Cr}}}{\mathrm{Z_{Zn}}}\bigg|_{\odot} \tag{5.21}$$

is an accurate measure for the amount of dust present, where a deficit of chromium[9] compared to zinc, i.e., $[\mathrm{Cr/Zn}] < 0$, implies the presence of dust (Kahre 2006). Further, zinc is interesting in this context because: (1) it closely tracks Fe in galactic stars, (2) its absorption lines are usually unsaturated and often lie outside the Ly α forest, (3) ionization corrections are relatively small for Zn II, and (4) Zn is relatively undepleted on dust grains (Kulkarni & Fall 2002).

5.5. Detection Significance and Error Handling

5.5.1. Detection Significance

The resolution of a spectrograph describes its ability to resolve narrow spectral lines, i.e., the minimum wavelength separation (in Å) per resolution element[10], $\Delta\lambda_{\mathrm{r}}$, or per pixel element, $\Delta\lambda_{\mathrm{p}}$, respectively.

The resolving power (although not correct, often simply referred to as *resolution*) is a basic parameter of the spectrograph and a direct measure for the

[7] Elements normally found to be heavily depleted, e.g., Ca, Ti, Cr, and Zn.

[8] Note that abundance ratios, compared to absolute abundances, are better suited to study the chemical evolution of DLA systems because they do not depend strongly on the particular model parameters, but mainly on the stellar nucleosynthesis and the initial mass function (IMF).

[9] Chromium is used in this context because its strongest transition lines (Cr II $\lambda\lambda$2056, 2062, 2066) have similar wavelengths as those of zinc (Zn II $\lambda\lambda$2062, 2026) and they both arise in the "clean" part of the spectrum, i.e., are easy to measure.

[10] Note that according to sampling theory, a resolution element must always be at least two pixels in each direction.

instrument's ability to resolve narrow spectral lines. The resolving power is defined as

$$R \doteq \frac{\lambda}{\Delta\lambda}, \tag{5.22}$$

with $\Delta\lambda$ the resolution (per resolution element or per pixel element), and λ the wavelength. Another important parameter is the signal-to-noise ratio (SNR), defined as

$$\mathrm{SNR} \doteq \frac{1}{\sigma}, \tag{5.23}$$

with σ the signal standard deviation.[11] Before we proceed, and in order to specify what is meant by the standard deviation, σ, we have to pay attention to the noise that is altering the signal (for a more detailed discussion see, e.g., Irwin 2006; Knuth 1996). Random independent events, e.g., photons arriving at a detector, occur at a rate

$$r(t)\,\mathrm{d}t = \kappa\,\mathrm{d}t, \tag{5.24}$$

with $\kappa \in (0,\infty)$. The *Poissonian distribution* is a discrete probability distribution. It expresses the probability, $P(n,t)$, of a number of n events occurring in a fixed period of time, $0 \rightarrow t$, if these events occur with a known rate, $r(t)$, and are independent of the time since the last event. It is

$$P(n,t) = \frac{(\kappa t)^n \exp(-\kappa t)}{n!}. \tag{5.25}$$

In the case of a Poissonian distribution the parameter κ is not only the *mean* number of occurrence, $\langle n\rangle$, but also its variance, $\sigma_\mathrm{n}^2 \doteq \langle n^2\rangle - \langle n\rangle^2$. The number of observed occurrences fluctuates about its mean κ with a standard deviation

$$\sigma_\mathrm{n} = \sqrt{\kappa}. \tag{5.26}$$

These fluctuations are denoted as *Poisson noise*. For sufficiently large values of κt (what is the case for high-resolution spectroscopy), the normal (Gaussian) distribution with mean κ and variance κ is an excellent approximation to the Poisson distribution. Hence, the signal standard deviation, σ, as introduced in (5.23), can be given as

$$\sigma = \sqrt{\frac{1}{\mathrm{n}}\sum_{\mathrm{i}=1}^{\mathrm{n}} \left(I_\mathrm{i}(\lambda) - \bar{I}(\lambda)\right)^2}, \tag{5.27}$$

[11] Note that $\mathrm{SNR} \doteq \frac{\mathrm{I}}{\sigma}$, with I the intensity. Hence, (5.23) applies in the case of a normalized spectrum only.

with $\bar{I}(\lambda)$ the mean of the flux, I, over the sample wavelength range with n measuring points. Now, in order to obtain the SNR per resolution element, the SNR given in (5.23) must be multiplied by the square root of the number per pixel in a resolution element, i.e.,

$$\mathrm{SNR_r} = \sqrt{\frac{\Delta\lambda_\mathrm{r}}{\Delta\lambda_\mathrm{p}}} \cdot \mathrm{SNR}. \tag{5.28}$$

Now, the limiting equivalent width on an unresolved line at wavelength λ_0 is given by

$$W_\lambda = \frac{\mathrm{x}\,[\sigma] \cdot \lambda_0}{R \cdot \mathrm{SNR_r}}, \tag{5.29}$$

with x the detection significance in units of σ, R the resolving power, and $\mathrm{SNR_r}$ the signal-to-noise ratio per resolution element in the close vicinity of the expected line position (Tumlinson et al. 2002). Thus, the detection significance, commonly given in units of σ[12], can be calculated using (5.29). For a concrete example of the detection significance calculus described here, please refer to Section 6.2.2, page 76.

5.5.2. Error Calculus in log-space

It is not untypical to find substructures in an absorption line systems. Consequently, the absorption lines are fitted not by one but several Voigt profiles. Hence, we do not have one over-all but several smaller, individual values for N and b, respectively. Therefore, summing up column densities requires a proper treatment of the error propagation because each single value is afflicted with a measurement error.

Error calculation in log-space is not simple. Note that standard error calculation explicitly assumes normal distribution and, consequently, is not valid in log-space. Therefore, I want to specify the logarithmic error calculation adopted for this work (see also Noterdaeme 2005).

Let upper-case letters, N_i, denote the values for column densities in linear space and lower-case letters, n_i, the column densities in log-space, i.e., $N = 10^n$. Given k components with respective column densities, n_i, then the total column

[12] $1\,\sigma = 68.3\%$, $2\,\sigma = 95.4\%$, and $3\,\sigma = 99.7\%$

density is given by

$$n_{\mathrm{t}} = \log\left(N_{\mathrm{t}}\right) = \log \sum_{\mathrm{i}=1}^{\mathrm{k}} 10^{n_{\mathrm{i}}}. \tag{5.30}$$

The error can be calculated using the standard error propagation method (see, e.g., Appendix V in Schultz (2004)):

$$\Delta n_{\mathrm{t}}^2 = \sum_{\mathrm{i}=1}^{\mathrm{k}} \left(\frac{\partial n_{\mathrm{t}}}{\partial n_{\mathrm{i}}}\right)^2 \cdot \Delta n_{\mathrm{i}}^2, \tag{5.31}$$

where Δn_{t} is the error of the total column density. This finally yields

$$\Delta n_{\mathrm{t}} = \frac{\sqrt{\sum_{\mathrm{i}=1}^{\mathrm{k}} \Delta n_{\mathrm{i}}^2 \cdot 10^{2n_{\mathrm{i}}}}}{10^{n_{\mathrm{t}}}}. \tag{5.32}$$

Let us now assume a case with k components in total, of which l components, $n_{\mathrm{i}=1,..,\mathrm{l}}$, were detected but for j components only respective upper limits, $u_{\mathrm{i}=1,..,\mathrm{k}-\mathrm{l}}$, could be given. Then the total column density is given by

$$n_{\mathrm{t}} = \log\left(\sum_{\mathrm{i}=1}^{\mathrm{l}} 10^{n_{\mathrm{i}}} + \sum_{\mathrm{i}=1}^{\mathrm{k}-\mathrm{l}} 10^{u_{\mathrm{i}} - \log 2}\right), \tag{5.33}$$

and the corresponding error is

$$\Delta n_{\mathrm{t}} = \frac{\sqrt{\sum_{\mathrm{i}=1}^{\mathrm{l}} \Delta n_{\mathrm{i}}^2 \cdot 10^{2n_{\mathrm{i}}} + \sum_{\mathrm{i}=1}^{\mathrm{k}-\mathrm{l}} (\log 2)^2 \cdot 10^{2(u_{\mathrm{i}} - \log 2)}}}{10^{n_{\mathrm{t}}}}. \tag{5.34}$$

Note that a quite common, efficient, and surprisingly accurate method to determine the error of an absorption line is by making use of the human eye. The approach is straightforward: After the best parameters were found through line profile fitting (for example), one can increase / decrease the column density up to a point where (by eye) the (forced) fit becomes inaccurate. The upper / lower limit then can be considered as error boundary.

Example 1

Let $n_\mathrm{B} := \log N_\mathrm{B}(\mathrm{N\,I}) = 19.10 \pm 0.10$[13] and $n_\mathrm{C} := \log N_\mathrm{C}(\mathrm{N\,I}) = 19.25 \pm 0.10$ be the two components of an absorption line, where both, n_B and n_C, respectively, are clear detections. Using (5.34) yields

$$\Delta n_\mathrm{t} = \frac{\sqrt{0.1^2 \cdot 10^{2 \cdot 19.10} + 0.1^2 \cdot 10^{2 \cdot 19.25}}}{10^{19.10} + 10^{19.25}} = 0.0718.$$

Example 2

Let $n_1 := \log N_1(\mathrm{N\,I}) = 12.2 \pm 0.1$ and $u_1 := \log N_2(\mathrm{N\,I}) = 11.8$ be the two components of an absorption line, where n_1 was a clear detection but, on the other hand, u_1 represents only an upper limit. Using (5.33) yields $n_\mathrm{t} = 12.279$ and with (5.34) we find an error of $\Delta n_\mathrm{t} = 0.097$.

[13] This notation is sometimes subject to confusion because $\log N_1(\mathrm{N\,I}) = 19.1 \pm 0.1$ can be interpreted as the range $[10^{19.0}; 10^{19.2}]$ but it can also be read as to be a 10%-error, i.e., $[0.9 \times 10^{19.1}; 1.1 \times 10^{19.1}]$. For this work, the indicated errors will always be considered to be written as dex.

6. The Line of Sight toward Q 0913+072: Constraints on early Nucleosynthesis[1]

6.1. Introduction

Recent theoretical studies (e.g., Omukai & Palla 2003) predict that the first (Pop III) stars[2] must have been very massive ($\sim 100-600\,M_{\odot}$), thus indicating an initial mass function (IMF) that favors the formation of more massive stars (top-heavy IMF). Stellar evolution studies (Heger & Woosley 2002) show that primordial stars with main-sequence (ms) masses between $\sim 50-140\,M_{\odot}$ and above $\sim 260\,M_{\odot}$ inevitably collapse into black holes and are unable to eject their metals. Furthermore, stars with masses below $M_{\rm ms} \sim 10\,M_{\odot}$ do not significantly contribute to the chemical feedback on galactic scales (Ciardi & Ferrara 2005). Hence, only massive stars of $\sim 10-50\,M_{\odot}$, exploding as core-collapse Supernovae (SNe) and/or Hypernovae (HNe), or super-massive stars of $\sim 140-260\,M_{\odot}$, exploding as Pair-Instability Supernovae (PISNe), will eventually enrich the ISM and subsequently the IGM (see Fig. 6.1).

[1] First published in: Erni, P., Richter, P, Ledoux, C., and Petitjean, P. 2006, A&A 451, 19

[2] Please refer to Chapter 7, p. 91 ff, for more details on the particular origin, nature, and evolution of Pop III stars.

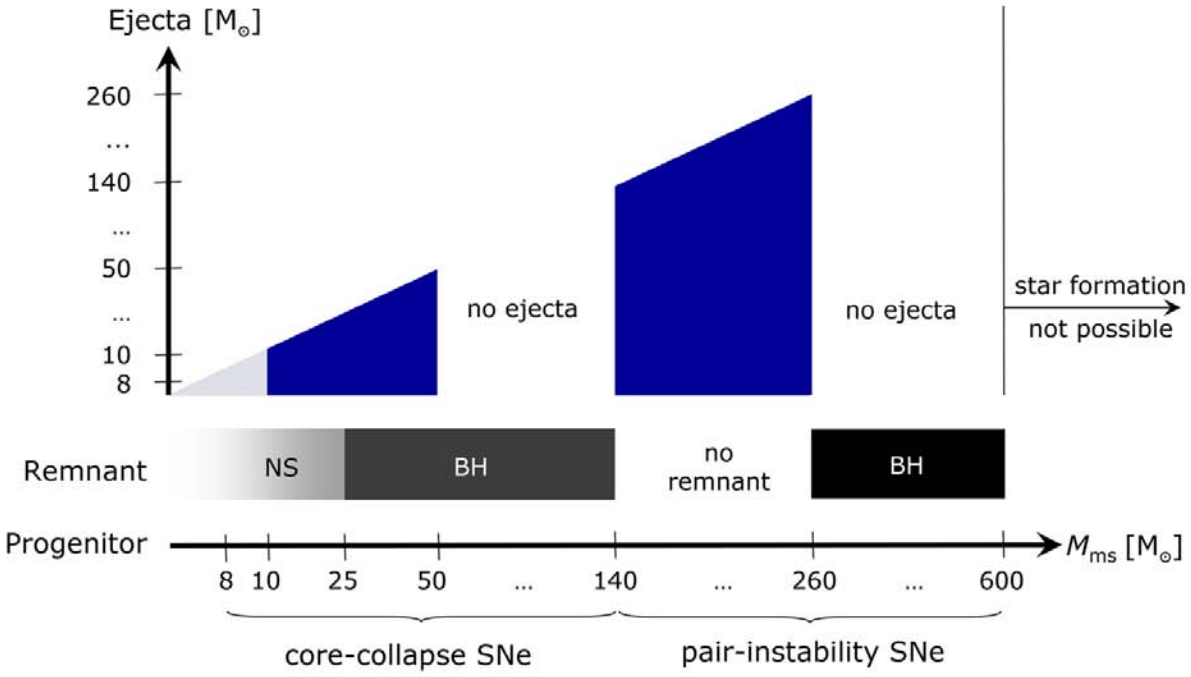

Figure 6.1.: Sketch about the fate of massive stars, inspired by Heger & Woosley (2002).

It has been proposed that metal enrichment is the mechanism responsible for a transition from a top-heavy to a more conventional power law IMF as observed in the present-day Universe (Bromm et al. 2001; Schneider et al. 2002). The metallicity is believed to reach a critical value at $[Z_{cr}/H] \approx -4$, marking a transition from a high-mass to a low-mass fragmentation mode of the protostellar gas cloud. Conversely, recent observations of hyper metal-poor (HMP) stars, e.g., HE 0107−5240 with $[Fe/H] = -5.2 \pm 0.02$ (Christlieb et al. 2002) or HE 1327−2326 with $[Fe/H] = -5.4 \pm 0.02$ (Frebel et al. 2005) might, at first sight, rule out a top-heavy IMF for Pop III stars. Other scenarios like a bimodal IMF (Nakamura & Umemura 2001; Omukai & Yoshii 2003) binary star formation, or a nonstandard nucleosynthesis (Oh et al. 2001) for Pop III stars could solve this disagreement.

In order to constrain the mass range and explosion mechanism for Pop III stars, which contribute to the chemical feedback on galactic scales, we have analyzed an extremely metal-poor protogalactic structure at high redshift by QAL spectroscopy.

QAL systems are important objects to study the IGM at low and high redshifts. QAL systems sample both low and high density regions in the Uni-

verse and thus provide important information on structure formation and early chemical evolution. Metal abundance measurements in QAL systems at high redshift are particularly important to learn about the first generations of stars in the Universe, as these objects should have left a characteristic signature in the abundance pattern of chemically young systems. DLA absorption systems, QAL systems with large hydrogen column densities ($N(\mathrm{H\,I}) \geq 2 \times 10^{20}\,\mathrm{cm}^{-2}$), are most suitable for studies of the chemical evolution at high redshift (e.g., Péroux et al. 2003; Richter et al. 2005). Number statistics of DLA systems imply that these objects dominate the neutral gas content of the Universe at $z > 1$ (Lanzetta et al. 1995; Wolfe et al. 1995; Rao & Turnshek 2000). While most of the observable baryonic content of today's galaxies is concentrated in stars, in the past it must have been in the form of gas. The general agreement between the estimated baryonic mass density for DLA systems (Ω_{DLA}) at $z \approx 2$ and the baryonic mass density in stars at $z = 0$ makes DLA systems prime candidates to be the progenitors of present-day galaxies (Wolfe et al. 1995; Storrie-Lombardi & Wolfe 2000). The most important absorption lines of atomic and molecular species in DLA systems at high redshift ($z \approx 2-3$) fall into the optical band. Background quasars at these redshifts are usually faint ($V \approx 17^{\mathrm{m}}$-$20^{\mathrm{m}}$), however, so that one needs $8-10$ m class telescopes to obtain high-resolution and high SNR absorption spectra that provide accurate information on these objects.

The DLA system discussed in this chapter is characterized by a very low overall metallicity. It exhibits an abundance pattern that points to an enrichment of only one or at most a few stellar generations. Thus, the UVES high-resolution data of the DLA system toward Q 0913+072 provide a unique insight into the early enrichment history of a protogalactic structure at $z \approx 2.6$.

6.2. The Line of Sight toward Q 0913+072 and Metal Abundance Measurements

6.2.1. The Line of Sight toward Q 0913+072

An earlier analysis of the DLA system at $z_{\mathrm{abs}} = 2.6183$ toward Q 0913+072 ($V = 17.^{\mathrm{m}}1$, $z_{\mathrm{em}} = 2.785$) has been presented by Ledoux et al. (1998). These authors have used the F/8 Cassegrain focus of the ESO 3.6 m telescope and the Nasmyth focus of the ESO 3.5 m New Technology Telescope (NTT) at La Silla, Chile. A total neutral hydrogen column density of $\log N(\mathrm{H\,I}) = 20.2 \pm 0.1$ was derived from a fit of the Ly α line. With a resolution of $R \sim 13\,000$, only one

single component in the low-ionization absorption lines of O I, C II, and Si II could be identified. An analysis of these lines suggested metal abundances of $[O/H] \approx -2.8$ and $[Si/H] \approx -2.4$ together with a Doppler parameter of $b \approx 7\,\mathrm{km\,s^{-1}}$. At this resolution, however, the true velocity structure in the gas is barely resolved. This leads to systematic uncertainties for the derived metallicities, since for several unresolved components the true b-values may be significantly lower, and thus the column densities could be underestimated. An analysis of this very interesting DLA system with higher-resolution data holds the prospect of deriving more accurate abundances for C, N, O, Si, and other elements and to investigate the abundance pattern in this system in the context of the metal enrichment of protogalactic structures at high redshift.

The data used in this study were obtained with UVES/VLT between January 17 and February 16, 2002, mostly during dark time[3]. The total integration time amounts to 6.8 hours (DIC #1 + DIC #2) while the seeing-conditions were on average $1''$. Q 0913+072 was observed through a $1''$-slit with two setups using dichroic beam splitters for the blue and the red arm (DIC #1 with B390 and R580 nm, and DIC #2 with B437 and R860 nm, respectively). This setup covers a wavelength range from $\sim 3250-10\,200$ Å with small gaps at $\sim 5750-5840$ Å and $\sim 8520-8680$ Å, respectively. The data have high spectral resolution ($R \sim 45\,000$) together with a high SNR. The SNR typically varies between $\sim 30-70$ per pixel (width $= 1.9\,\mathrm{km\,s^{-1}}$) over the wavelength range between $3500-6000$ Å. The CCD pixels were binned 2×2 and the raw data were reduced using the UVES data-reduction pipeline implemented in the `ESO-MIDAS` software package. These data are public and can be found in the UVES database of ESO's Science Archive Facility[4].

6.2.2. Metal Abundance Measurements

The spectrum was analyzed using the `FITLYMAN` program (Fontana & Ballester 1995) implemented in the `ESO-MIDAS` software package. The routine uses a χ^2-minimization algorithm for multi-component Voigt profile fitting. Simultaneous line fitting of the high-resolution spectrum allows us to determine the column density, N, and the Doppler parameter, b, with high accuracy. The b-values of the DLA system toward Q 0913+072 are assumed to be composed of a thermal component, b_{th}, and a turbulent component, b_{turb}, in the way that

[3]ESO project 68.B-0115(A) – "[α/Fe] Ratios to probe the early chemical Evolution of DLA systems" (PI / CoIs: Molaro /Levshakov / Centurión / Bonifacio / Dessauges-Zavadsky / Vladilo)

[4]http://archive.eso.org

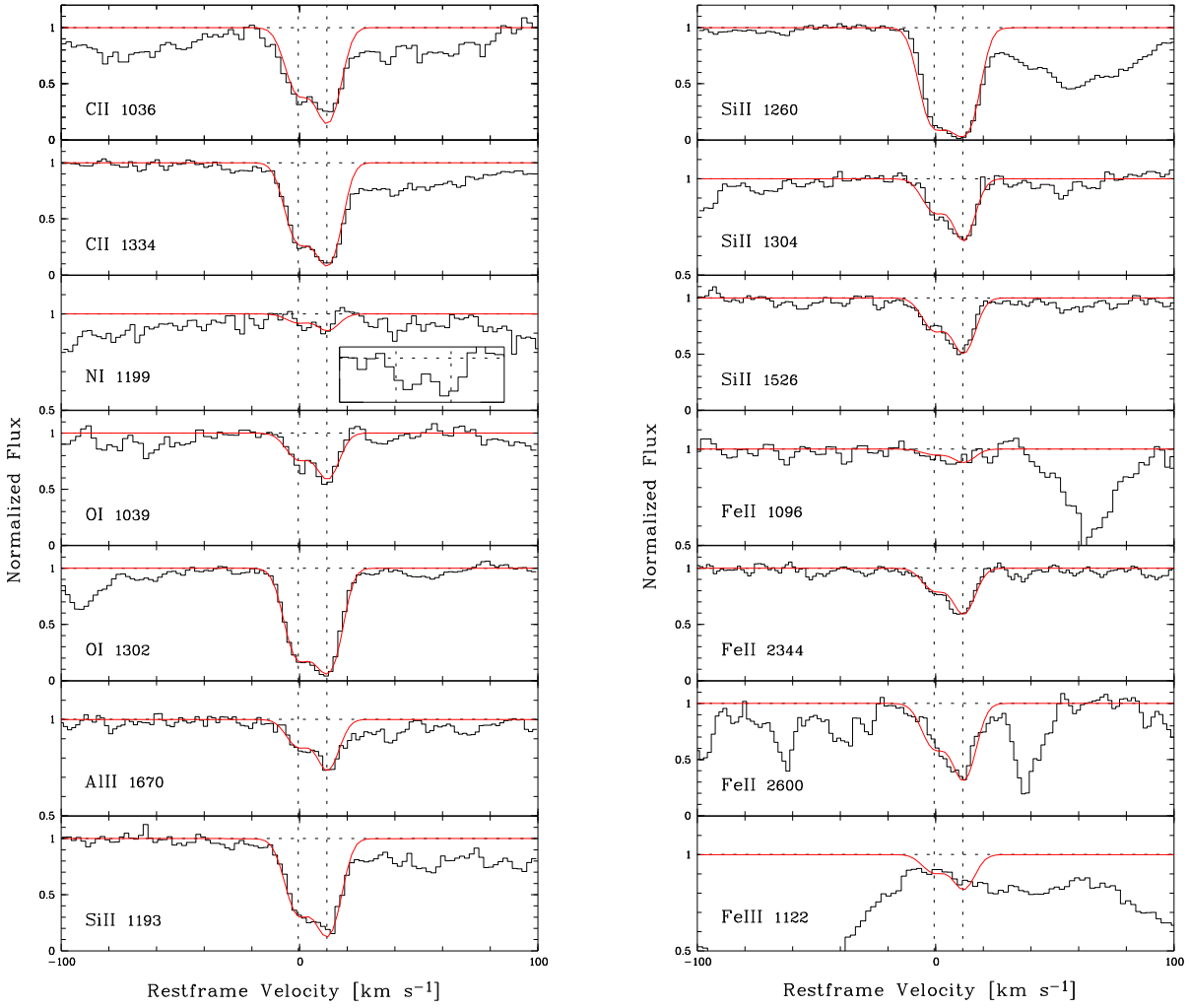

Figure 6.2.: Absorption profiles of various ions are plotted against the restframe velocity. Two dominant absorption components are identified at $-1\,\mathrm{km\,s^{-1}}$ and $+11\,\mathrm{km\,s^{-1}}$ (vertical dashed lines).

$b^2 = b_{\mathrm{th}}^2 + b_{\mathrm{turb}}^2$. The non-thermal component may include processes like macroscopic turbulence, unresolved velocity components, and others. Note that in our case $b_{\mathrm{th}}^2 \ll b_{\mathrm{non-th}}^2$.

Due to the low overall metallicity of this system, metal absorption is detected only in the strong lines of C II, N I, O I, Al II, Si II, and Fe II. No other low ion or other element could be identified. Upper limits for elements like sulfur or zinc can be derived but they are of no further use. Fitting the detected low-ionization lines we can identify two dominant velocity components at $-1\,\mathrm{km\,s^{-1}}$ and $+11\,\mathrm{km\,s^{-1}}$ in the $z_{\mathrm{abs}} = 2.6183$ restframe (Fig. 6.2), as well as three satellite components at $+114$, $+152$, and $+181\,\mathrm{km\,s^{-1}}$, respectively.

For the study presented in this work we will concentrate on the two dominant components.

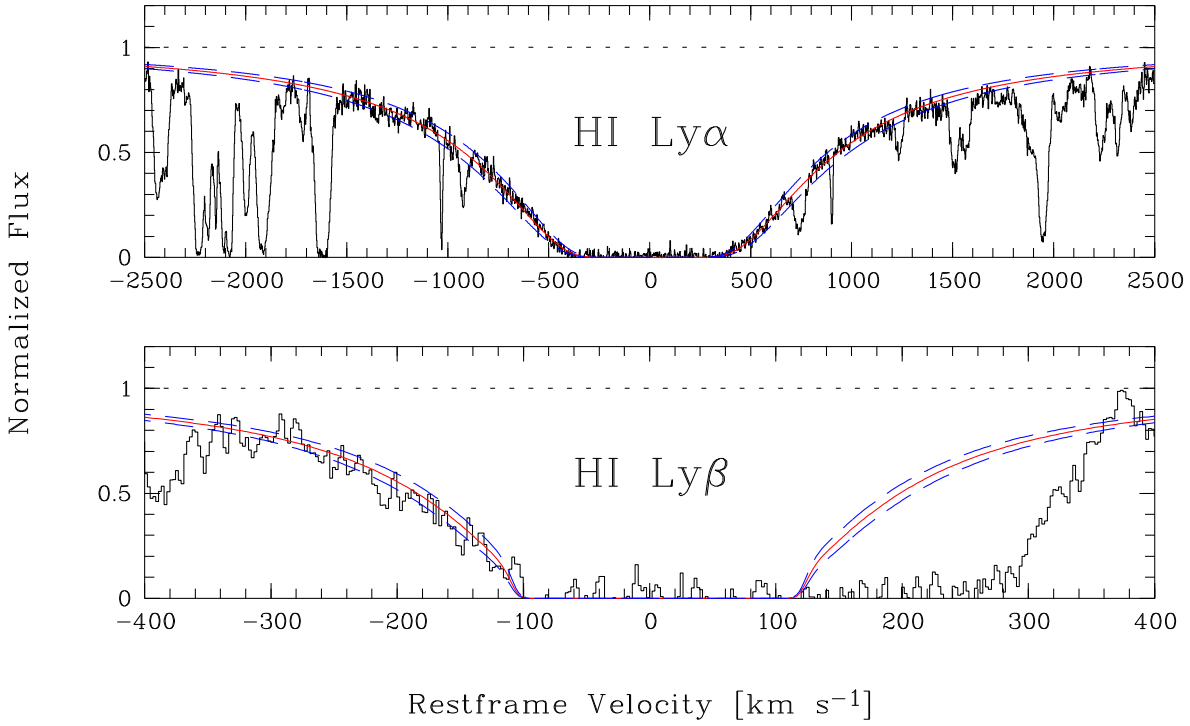

Figure 6.3.: The Ly α and Ly β absorption profiles of the DLA system at $z_{abs} = 2.6183$ toward the quasar Q 0913+072 are plotted on a restframe velocity scale. The solid line shows the optimum single-component fit with $\log N(\mathrm{H\,I}) = 20.36$, the dashed lines indicate the 1σ error range of ± 0.05 dex.

Due to the large neutral hydrogen column density, the H I Ly α absorption spans several Å, so that all sub-components are superposed in one big Lyman trough (Fig. 6.3). Therefore, it is impossible to decompose the H I absorption line profile into the various velocity subcomponents. From a simultaneous single-component fit of the Ly α and Ly β absorption we obtain a total neutral hydrogen column density of $\log N(\mathrm{H\,I}) = 20.36 \pm 0.05$. This value, together with the total column densities derived for the species listed above, is used to determine metal abundances. These range from -3.84 (nitrogen) to -2.47 (oxygen), implying that the overall metal abundance ($[\mathrm{M/H}] = [\mathrm{O/H}] = -2.47$ or $Z = 0.0034$) of the gas is very low. All individual column densities and abundances in the $z = 2.6183$ absorber are summarized in Table 6.1. The errors in this paper represent the $1\,\sigma$ fitting errors given by the `FITLYMAN` program. Additional uncertainties arise from to the continuum placement (on the order of

0.1 dex) and the fixing of the line centers and *b*-values. Note that these additional error sources are not included in the error estimates listed.

Table 6.1.: Summary of chemical abundances using the common notation $[\mathrm{X/H}] = \log(N(\mathrm{X})/N(\mathrm{H})) - \log(N(\mathrm{X})/N(\mathrm{H}))_\odot$. The column densities represent the sum over the two main absorption components at $-1\,\mathrm{km\,s^{-1}}$ and $+11\,\mathrm{km\,s^{-1}}$, as derived from simultaneous multi-component Voigt profile fits. The total neutral hydrogen column density is $\log N(\mathrm{H\,I}) = 20.36 \pm 0.05$. Oscillator strengths are taken from Morton (2003). Solar reference abundances are listed in Table 6.2.

Species	Transition lines used	$\log N(\mathrm{X}) \pm \sigma_{\log N}$	$[\mathrm{X/H}] \pm \sigma_{[\mathrm{X/H}]}$
H I	1025,1215	20.36 ±0.05	
C II	1036,1334	14.05 ±0.01	−2.83 ±0.05
N I	1199	12.47 ±0.10	−3.84 ±0.11
O I	1039,1302	14.58 ±0.02	−2.47 ±0.05
Al II	1670	11.84 ±0.01	−3.01 ±0.05
Si II	1304,1526	13.35 ±0.01	−2.57 ±0.05
Fe II	1096,2344,2600	13.09 ±0.01	−2.77 ±0.05
Fe III	1122	≤13.33	
Ni II	1370	≤12.17	≤ −2.44

Our measurements confirm the previous abundance estimates from Ledoux et al. (1998). However, due to the higher resolution of the UVES data, the system is now resolved into two major and three satellite components for the low ions (instead of one), and five components for the high ions (instead of two). The new detection of Al II and upper limits for Fe III and Ni II provide additional information about the chemical composition of the gas. With $[\mathrm{M/H}] = -2.47$ ($\sim {}^1/_{300}$ solar) this absorber has one of the lowest metallicities ever measured in DLA systems. More precisely, it is among the four lowest in the sample of 100 DLA systems from Prochaska et al. (2003) and the system with the lowest metallicity in the redshift range $2 < z < 3$. Also, this DLA system is (to our knowledge) the only system for which an accurate carbon abundance can be determined. Due to the low metallicity the strong C II absorption is not heavily saturated (or very mildly at most) in contrast to all other known DLA systems.

Curve of Growth Method versus Line Profile Fitting

As mentioned above it might be reasonable, in certain cases, to determine the *b*-value rather by the COG method than by line profile fitting. Fig. 6.4 shows a

consistency check between the two methods. The error bars show an increasing error for lower column densities. This trend is expected due to the lower detection significance (see also Section 5.5.1) for lower column densities. However, the lion's share in this error in W_λ/λ is due to the fact that the output of the equivalent width in FITLYMAN program is limited to three digits only.

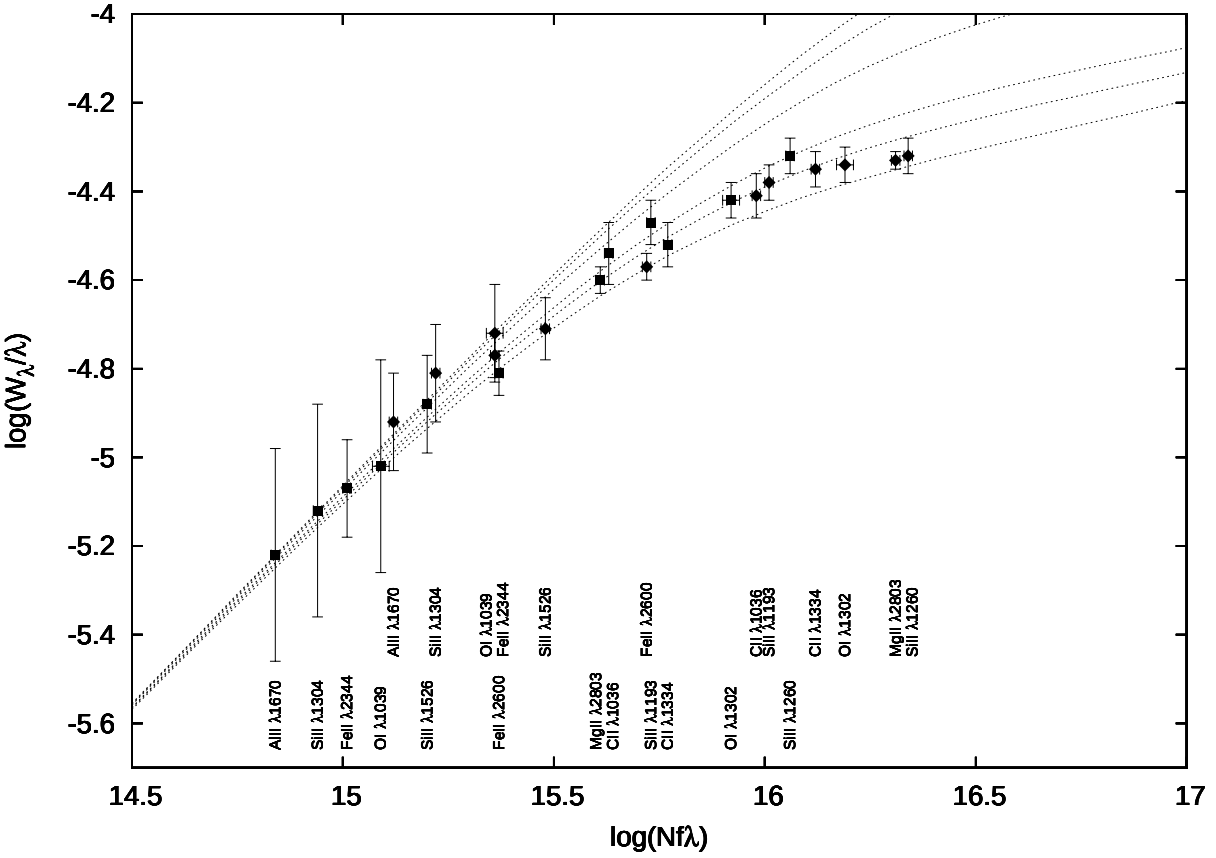

Figure 6.4.: COG and results from multi line fitting for the DLA system toward Q 0913+072. Theoretical curves for $b = 4, 5, 6, 10, 15$, and $20\,\mathrm{km\,s^{-1}}$. This DLA system shows two main components (see also Chapter 6). A multi line fit of the low-ionized species yields to $b = 5.3\,\mathrm{km\,s^{-1}}$ and $b = 4.7\,\mathrm{km\,s^{-1}}$ for the blue (squares) and the red component (diamonds), respectively.

Nitrogen Detection Significance

Note while the two-component structure is clearly seen in the N I λ 1199 line, the observed absorption profile slightly deviates from the expected shape. The reason for this is unclear, but possibly related to noise features that are present

in this wavelength range (see Fig. 6.2). In order to quantify the detection significance of the N I λ 1199 line, the formalism presented in Section 5.5.1 can be applied.

The sample standard deviation as a measure of the noise present in the spectrum is taken from the continuum in the vicinity (at 4340 Å and over 96 km s^{-1}) of the expected line center, λ_0. It is $\sigma_{\rm noise} = 0.033$ and consequently

$$\mathrm{SNR} = \frac{1}{\sigma_{\rm noise}} = 30.3.$$

Using (5.22), the UVES resolving power of $R = 45\,000$ at $\lambda = 4340$ Å yields a pixel element of $\Delta\lambda_{\rm p} = 0.096$ Å. $\lambda \pm 5$ Å corresponds to 348 pixel or a resolution element $\Delta\lambda_{\rm r} = 0.029$ Å.[5] With (5.28) the SNR per resolution element is

$$\mathrm{SNR}_{\rm r} = \sqrt{3.359} \cdot \mathrm{SNR} \approx 55.$$

The measured equivalent width (in the normalized spectrum) is $W_\lambda = 0.007$. From (4.15) and (5.29) then follows

$$\frac{W_\lambda}{\lambda_0} R \cdot \mathrm{SNR}_{\rm r} \approx 4,$$

i.e., we find that the red component of the N I λ 1199 line has a detection significance of $4\,\sigma$. Note that in this case the (unresolved) absorption was compared to the noise of the spectrum, where neither the line profile nor the relative position were taken into account. The procedure for the blue component is identical and we conclude that the detection significance exceeds $3\,\sigma$ and $4\,\sigma$ for the blue and the red component, respectively. However, the main source of uncertainty for the column density derived from the N I λ 1199 line is related to the choice of the continuum level.

6.3. Constraints on early Nucleosynthesis

6.3.1. Metal Abundance Pattern

The redshift of $z_{\rm abs} = 2.6183$ of this system corresponds to a lookback time of 11.1 Gyr (i.e., to an age of the Universe of 2.5 Gyr at that redshift)[6]. Given

[5] Note that the spectrum is with $\Delta\lambda_{\rm p}/\Delta\lambda_{\rm r} = 3.359$ pixel per resolution element oversampled.

[6] using $H_0 = 71$ km s^{-1}, $\Omega_{\rm m} = 0.27$, and $\Omega_{\rm tot} = 1$, see also Appendix F.

the very low overall abundance level and the observed abundance pattern, the chemical evolution of this system is lagging behind the evolution of other DLA systems at similar redshifts. The DLA system toward Q 0913+072 can be compared with the nearby dwarf galaxy *I Zwicky 18* (at a distance of ~ 15 Mpc), which contains no stars older than 500 Myr (Izotov & Thuan 2004). Either these kinds of galaxies have formed just recently, or they have been existing as protogalactic structures for several Gyr. An alternative explanation for the poor enrichment we observe in the DLA system toward Q 0913+072 would be that an initial violent starburst might have disrupted the integrity of the protogalactic structure and consequently would have prevented further star-formation activity. This would bring the nucleosynthesis processes to a halt and the chemical composition of the gas would reflect the enrichment pattern produced by the initial starburst.

In the following we focus on the abundances of individual elements that could shed light on the chemical evolution history of the DLA system toward the quasar Q 0913+072.

Nitrogen – Comparing our results with a database of 66 DLA systems (Centurión et al. 2003; Lanfranchi & Friaça 2003), the nitrogen abundance is among the lowest ever measured (see also Richter et al. 2005). There is general consensus that oxygen is almost entirely produced by (massive) SNe, the contribution from low- and intermediate-mass stars is practically irrelevant. Carbon, on the other hand, is produced in stars of nearly all masses (essentially by helium burning). In contrast to oxygen and carbon, however, the initial formation of nitrogen is still not well understood. If nitrogen is formed directly from helium, it is called *primary*. If the nitrogen production is dependent on pre-existing carbon seed nuclei, it is called *secondary* and is obviously dependant on the star's initial metallicity. While all stars which reach the CNO cycle (nitrogen is formed at the expense of carbon and oxygen) produce secondary nitrogen, it cannot be decided at present whether primary nitrogen is produced mostly in massive stars (exploding as SNe) or in intermediate-mass stars ($\sim 4-8\,M_{\odot}$) during their AGB phase, or both (Spite et al. 2005). The role of low-mass stars ($< 4\,M_{\odot}$) for the nitrogen enrichment at high z is not well understood yet, but needs to be explored in future studies (see, e.g., Pettini et al. 2002). Pettini et al. suggest that a significant fraction of DLA systems with oxygen abundances between $\sim {}^{1}/_{10}$ and $\sim {}^{1}/_{100}$ solar have not yet attained the full primary level of nitrogen enrichment (i.e., $\log[\mathrm{N/O}] < -1.5$) and may represent protogalactic

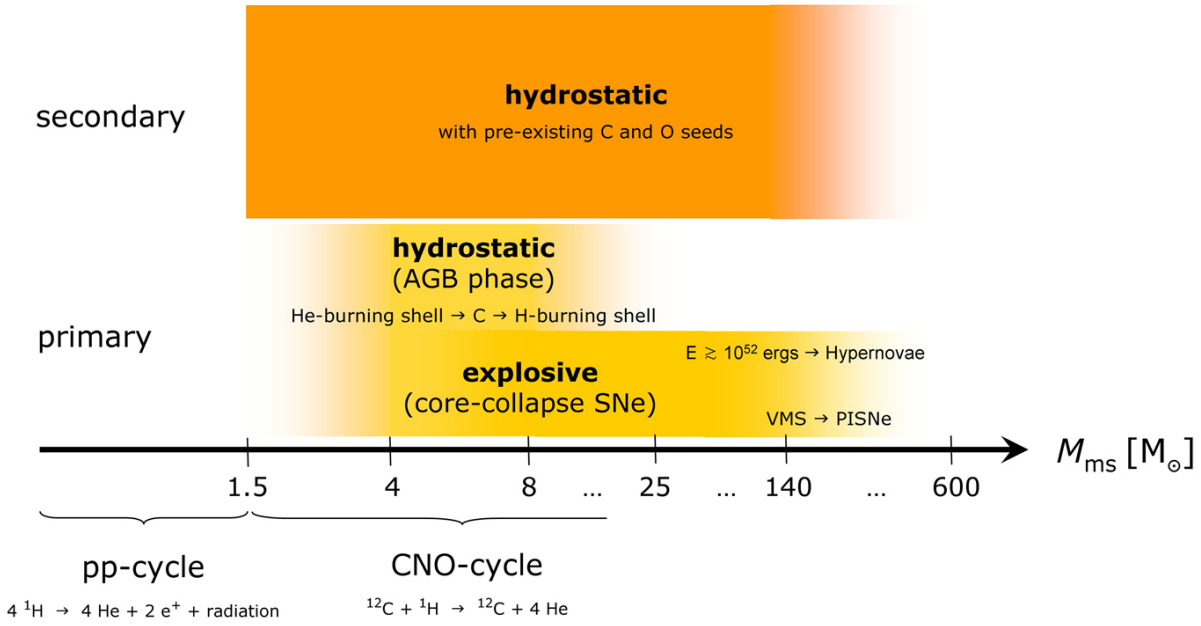

Figure 6.5.: A schematic overview of primary and secondary nitrogen production. Illustration based on data from the literature.

structures that just recently have formed out of the IGM.

For the α-elements[7], the enrichment depends critically on the star formation rate (SFR). Different absorber systems have different star formation histories, which means that they can reach the same amount of α-enrichment at different epochs. However, the nitrogen production depends more critically on the lifetime of the progenitor stars rather than on the SFR. Intermediate-mass stars dominate the nitrogen production and will follow the massive stars ($M > 8\,M_{\odot}$), which are the main production sites for carbon, with a typical lag time of ~ 250 Myr (Henry et al. 2000). The two plateaus in a [N/Si,O] versus [N,O/H] plot for a sample of 33 DLA systems (Fig. 6.6) nicely reflect this bimodal nitrogen production scenario (see Prochaska et al. 2002). The observed range in the [N/O] ratio at low [O/H] then is a natural consequence of the delayed release of nitrogen into the ISM relative to the oxygen produced by SNe. In the DLA system toward Q 0913+072 we measure $[\mathrm{N/O}] = -1.37 \pm 0.10$, i.e, primary nitrogen. This is what we would expect when observing a chemically young system that has just recently condensed out of the IGM.

Our value of $[\mathrm{N/O}] = -1.37 \pm 0.10$ does not favor a very small dispersion

[7]Referes to nuclei which are built up from α-particle nuclei (^{4}He), i.e., ^{16}O, ^{20}Ne, ^{24}Mg, ^{28}Si, ^{32}S, ^{36}Ar, ^{40}Ca, and (as an exception) ^{48}Ti.

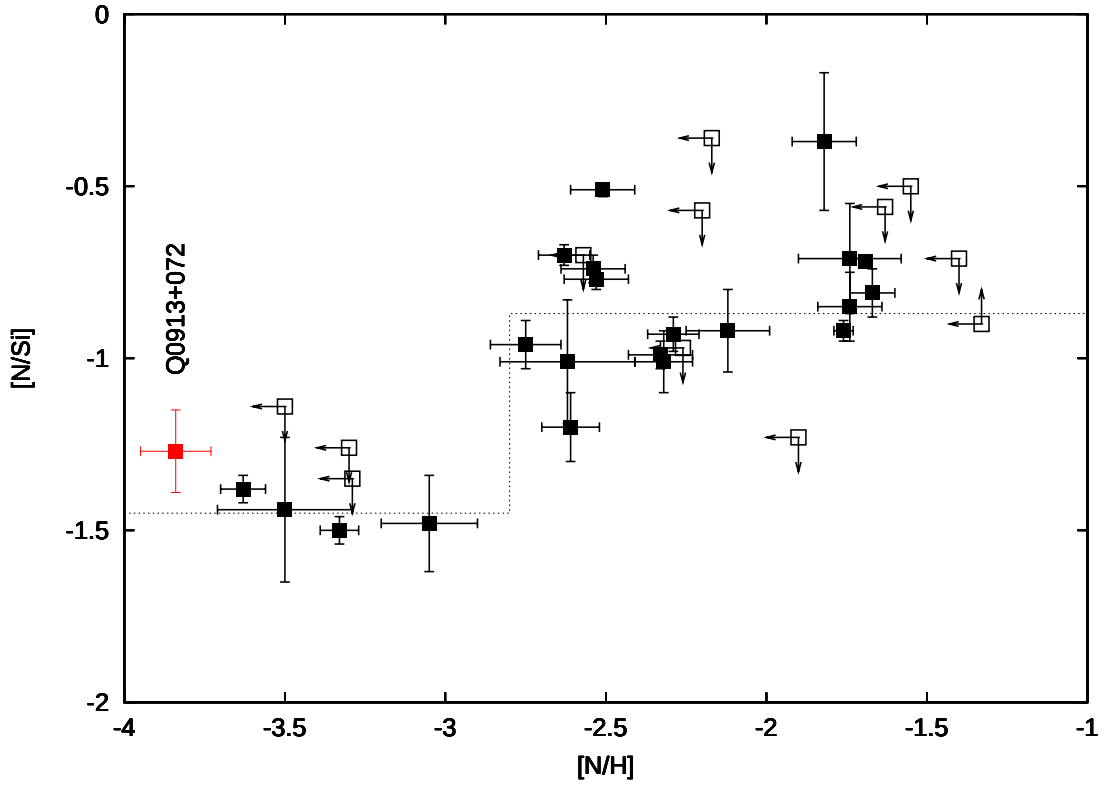

Figure 6.6.: We compare the [Ni/Si] ratio versus [Si/H] abundances for a sample of 33 DLA systems from Centurión et al. (2003) and Lanfranchi & Friaça (2003) with the abundances found for the DLA system toward the quasar Q 0913+072 (Erni et al. 2006). Open symbols represent upper limits, and the dotted line indicates the two plateaus for primary and secondary nitrogen (see Section 6.3.1 for more details).

in low-nitrogen DLA systems, i.e., $[\mathrm{N}/\alpha] = -1.45 \pm 0.05$, as suggested earlier by (Centurión et al. 2003). Matteucci & Calura (2005) argue that Pop III stars alone cannot be responsible for the abundance ratios in low-metallicity DLA systems. They conclude that the intermediate-mass Pop II stars must have played an important role for the early nitrogen enrichment in the Universe, even at redshift of $z = 5$. However, the redshift alone is not a good indicator for the evolutionary state of a galaxy. The very low abundances measured in the DLA system toward Q 0913+072 together with the very low nitrogen content, when compared to yields from explosive nucleosynthesis model calculations, indeed speak against a major contribution from intermediate mass Pop II stars to the nitrogen enrichment in this DLA system.

Carbon – Reliable carbon measurements in QAL systems are very sparse, since

in most cases the C II absorption in DLA systems, sub-DLA systems, and LLSs is heavily saturated. Levshakov et al. (2003a) have measured C II absorption in a LLS at $z_{\rm abs} = 2.917$[8]. D'Odorico & Molaro (2004) also reported a carbon measurement in a DLA system at $z_{\rm abs} = 4.383$, but their C II and O I lines presumably are mildly saturated. Although the results of the LLS depend on photoionization calculations, all cases seem to have $[{\rm C/Fe}] \sim 0.0$ and $[{\rm C}/\alpha] < 0$ in common. For the DLA system toward Q 0913+072 we derive $[{\rm C/Fe}] = -0.06 \pm 0.01$, $[{\rm C/O}] = -0.36 \pm 0.02$, and $[{\rm C/Si}] = -0.26 \pm 0.01$, thus very similar to what has been derived for the other systems. In all four cases, carbon appears to be underabundant compared to the α elements. Although LLSs and DLA systems are expected to trace different cosmological objects or sites (at least in general), the observed underabundance of carbon may provide information on the early metal enrichment in the Universe. Clearly, more carbon measurements in DLA systems and LLSs are desired to investigate this interesting behavior in detail.

Oxygen – Oxygen is the element best suited to infer the α-element abundance in interstellar and intergalactic gas, as O I and H I have similar ionization potentials (see Table C.1) and both are coupled by a strong charge-exchange reaction, i.e.,

$$\mathrm{H\,II} + \mathrm{O\,I} \leftrightarrow \mathrm{H\,I} + \mathrm{O\,II}. \tag{6.1}$$

The reaction's large charge exchange cross-section couples the ionization fraction of atomic oxygen to that of hydrogen (Field & Steigman 1971). Hence, the intensity of O I absorption with respect to H I is a sensitive indicator for the ionization present.

In the most widely cited set of solar abundances from Grevesse & Anders (1991), the solar oxygen abundance was reported to be $\log(N({\rm O})/N({\rm H}))_\odot + 12 = 8.93$. However, recent estimates lead to significant revisions of the Sun's oxygen abundance. In this work we adopted the value of $\log(N({\rm O})/N({\rm H}))_\odot + 12 = 8.69$ from Allende Prieto et al. (2001). Further, uncertainties in stellar nucleosynthesis inputs such as the $^{12}{\rm C}(\alpha,\gamma)^{16}{\rm O}$ reaction rate, convection, fallback and mass loss could alter these and previous results, which therefore have to be viewed with caution.

Dust Depletion – No trace of molecular hydrogen was found in the DLA system

[8] All previous measurements of metal abundances in LLSs lie in the range of $[{\rm M/H}] \geq -2.4$ (Fan 1995; Songaila & Cowie 1996; Levshakov et al. 2002a, 2003b).

toward Q 0913+072. The logarithmic ratio of hydrogen nuclei in molecules to the total hydrogen nuclei is

$$\log f_{H_2} = \log \frac{2N(H_2)}{N(H)} \leq -6.9, \tag{6.2}$$

where $\log N(H_2) \leq 13.2$, i.e., the total upper limits of the rotational ground states $J = 0$ and $J = 1$ in the Werner band of molecular hydrogen. Because of the lack of H_2 (which predominantly forms on dust grains) and the extremely low overall metallicity we do not expect dust depletion to alter significantly the abundance pattern in this absorption line system (Ledoux et al. 2003; Vladilo 2002).

Photoionization Corrections – Given the large neutral hydrogen column density in this absorber, it is not expected that photoionization has any significance on the abundances listed in Table 6.1. This is supported by our photoionization model for a DLA system at $z = 2.5$ based on `CLOUDY` (Ferland et al. 1998). In the case that photoionization should nonetheless be relevant, i.e., in view of the observed two-component structure, the fact that the ionization potential (IP) of H I is lower than the IPs of C II, N I, Al II, Si II, and Fe II means that correcting for ionization effects would further decrease these abundances.

Comparison with Metal-Poor Stars[9] – It is legitimate to compare very metal-poor DLA systems to very metal-deficient stars which are believed to retain information of a preceding single SN event or at most a few (McWilliam et al. 1995). Comparing the abundances from this DLA system with a sample of 9 (unmixed) extremely metal-poor (EMP) Galactic halo giants ($-4.0 \leq [Fe/H] \leq -2.0$) from Spite et al. (2005), we find a very good agreement for carbon, a reasonable agreement for oxygen and iron (typically ± 0.2 dex), but clearly higher values for nitrogen (in average by ~ 1 dex) in the EMP stars. In Fig. 6.7, we include a sample of 34 F and G dwarf and subgiant stars belonging to the halo population ($-3.2 \leq [Fe/H] \leq -0.7$) from Akerman et al. (2004). Although their mean values for [C/H] and [O/H] are higher by more than 1 dex, their lowest values for carbon and oxygen are very similar to our observations.

An interesting aspect is this analysis to compare the two existing carbon measurements in DLA systems (D'Odorico & Molaro 2004; Erni et al. 2006) with

[9]The reader should note that only very recently a uniform nomenclature for stars of different metallicities was suggested (Beers & Christlieb 2005). Until to date, there is, unfortunately, no clear denomination but there is well founded hope that the nomenclature suggested by Beers & Christlieb (2005) given in Table 7.1 will become largely accepted in the scientific community.

these halo stars (Fig. 6.7). We find a reasonable agreement for the carbon evolution in the DLA systems and the halo stars. When comparing with predictions from yields from Pop III stars (Chieffi & Limongi 2002) for the case of an IMF with $M_{\rm ms} \geq 10\,M_{\odot}$ (Fig. 6.7, dashed line), we notice that the carbon abundances in the two DLA systems match these theoretical predictions extremely well.

Ultra-metal-poor giants with high [O/Fe] ratios, such as presented by Israelian et al. (2004), seem to demand a new type of SNe (Aoki et al. 2002) where most of the matter is absorbed by the iron core. Smaller [O/Fe] ratios possibly indicate that a significant fraction of iron is incorporated in the SN ejecta, leading to a smaller mass cut and thus less compact remnants, possibly neutron stars. Stars with very low metallicities and DLA systems obviously are extremely important objects to derive constraints on Pop III stars. The nitrogen production mechanism clearly plays a key role but yet requires more detailed work.

6.3.2. Additional Constraints from Numerical Models

The DLA system toward Q 0913+072 is a chemically very young DLA system, enriched by one or at most a few stellar generations that have left their typical abundance signature in the gas. We now want to compare the abundance pattern of this system with predictions from recent model calculations to learn more about the origin of this absorber.

SNe Ia vs. SNe II – The absence of a clear-cut [α/Fe] ratio leaves the possibility open that SNe Ia might have contributed to the metal enrichment of the observed DLA system, especially to the iron-peak elements.[10] On the other hand, there are arguments against any significant contribution from SNe Ia: (1) Based on results from the *Hubble Higher z Supernova Search*, Strolger et al. (2004) constrain the delay times for SNe Ia, i.e., the time from the formation of the progenitor stars to the explosion, in the range of $2-4$ Gyr, where the lower barrier of 2 Gyr distinctly exceeds the age of the DLA system toward Q 0913+072, recalling that the age of the Universe at $z_{\rm abs} = 2.6183$ was only 2.5 Gyr. (2) Metallicity effects influence the SNe Ia rate. This kind of low-metallicity inhibition of SNe Ia could occur if the iron abundance of the accreted matter from the companion is as low as $[{\rm Fe/H}] \lesssim -1$ (Kobayashi et al. 1998 and references therein). The companion star in a single-degenerated scenario is typically a

[10] Elements wit $A = 50-62$, i.e., Cr, Mn, Fe, Co, Ni, Cu, and Zn.

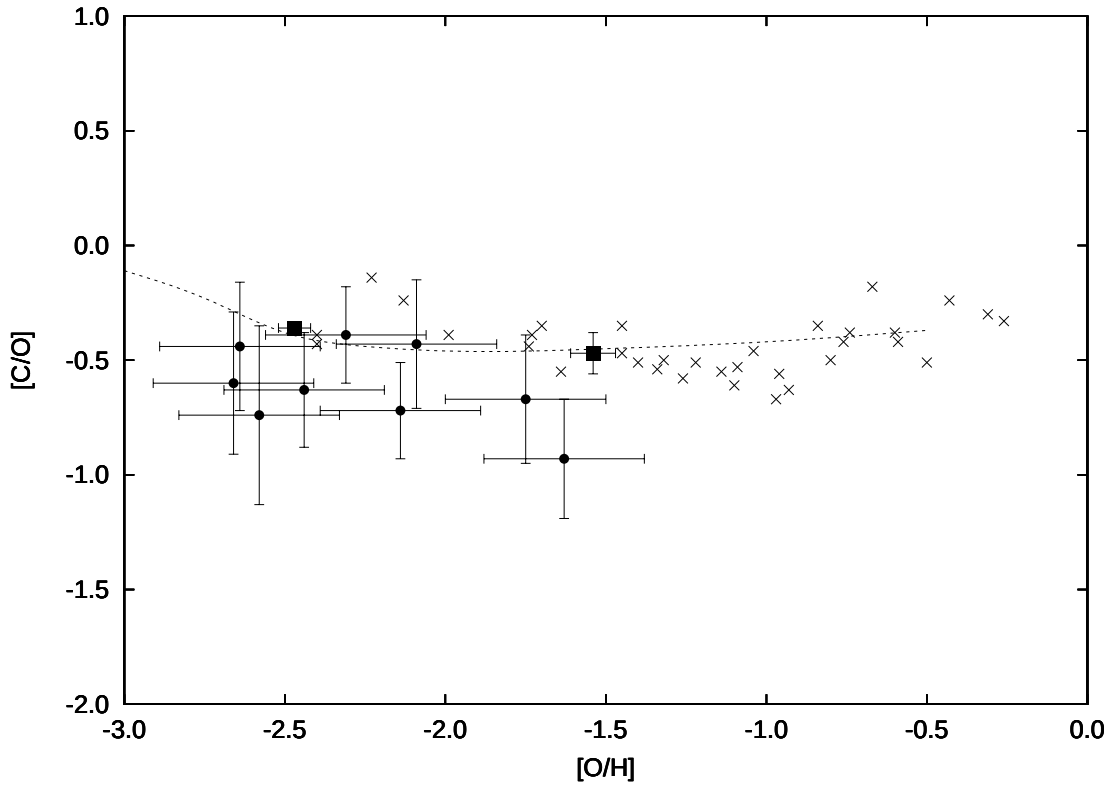

Figure 6.7.: We compare the only two existing (reliable) carbon abundance measurements in DLA systems (squares; from D'Odorico & Molaro (2004); Erni et al. (2006)) with extremely metal-poor halo stars (crosses) from Akerman et al. (2004), and (circles) from Spite et al. (2005). The dashed line shows predictions from Pop III star yields from Chieffi & Limongi (2002) for the case of an IMF with $M_{\rm ms} \geq 10\,M_{\odot}$ (Erni et al. 2006).

red-giant (RG) with an initial mass of $M_{\rm RG} \sim 1\,M_{\odot}$ or a near main-sequence star with an initial mass of $M_{\rm ms} \sim 2-3\,M_{\odot}$. Both stars are not massive enough to ignite silicon burning. Consequently, an iron abundance, as low as measured in our case, must inhibit the occurrence of SNe Ia. The observed low [O/Fe] ratios (more generally: the [α/Fe] ratios) thus should reflect the enrichment pattern of the first generations of stars that have enriched this protogalaxy, most likely by SNe II and probably HNe as well. We observe $[{\rm O/Fe}] = +0.30 \pm 0.02$ and $[{\rm O/Si}] = +0.10 \pm 0.02$, which is consistent with the yield ratios of SNe II from massive stars from Kobayashi et al. (2006). Furthermore, the ratios of $[{\rm Si/H}] = -2.57 \pm 0.05$ and $[{\rm Fe/H}] = -2.77 \pm 0.05$ are roughly consistent with numerical investigations from Kawata (2001), which predict that a typical SN II is producing more silicon ($\sim 5:1$) and slightly less iron ($\sim 0.8:1$) than a typical SN Ia.

Very Massive Stars (VMS) – VMS with $M_{\rm ms} \approx 130 - 300\,M_{\odot}$, exploding as PISNe, show a tendency to produce too much silicon, but not enough carbon and oxygen when compared to this DLA system. The observed $[{\rm Si/C}] = +0.26 \pm 0.01$ or $[{\rm C/O}] = -0.36 \pm 0.02$, and $[{\rm Si/Al}] = +0.44 \pm 0.01$ ratios imply an IMF in which the first stars cannot have been very massive (Tumlinson et al. 2004).

Yields from explosive nucleosynthesis models – The metallicity of the DLA system we probed is only slightly higher than what cosmological models predict for the IGM at this redshift. We speculate that this primeval metal enrichment we observe originates from only one single star generation, i.e., from Pop III stars. If there was only one enrichment cycle, or at most a few, then the ISM will carry the imprint from these stars and their typical enrichment pattern. As mentioned earlier, only stars in the range of $M_{\rm ms} \sim 10 - 50\,M_{\odot}$ and $M_{\rm ms} \sim 140 - 260\,M_{\odot}$ will contribute to the enrichment on galactic scales. In other words, the questions we ask is: have the first stars been massive ($\sim 10 - 50\,M_{\odot}$) or super-massive ($\sim 140 - 260\,M_{\odot}$), i.e., did they explode as core-collapse S/HNe or PISNe?

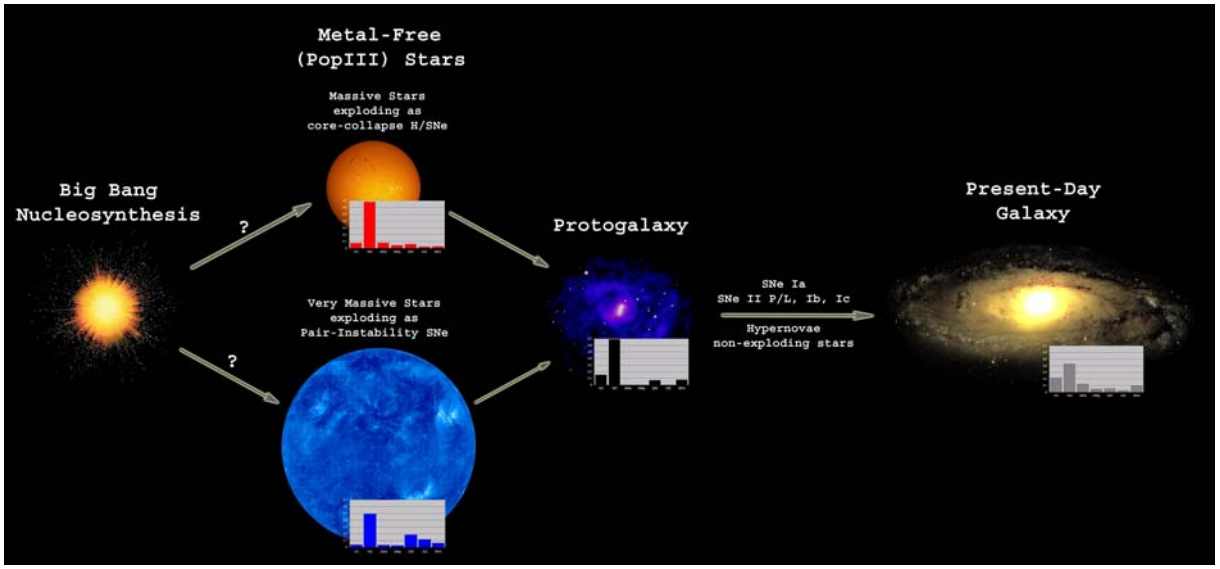

Figure 6.8.: How massive were the first stars that enriched the DLA system toward Q 0913+072? We compare two possible scenarios: massive stars with $\sim 10 - 50\,M_{\odot}$ (exploding as core-collapse S/HNe) and super-massive stars with $\sim 140 - 260\,M_{\odot}$ (exploding as PISNe). Illustration based on data from the literature.

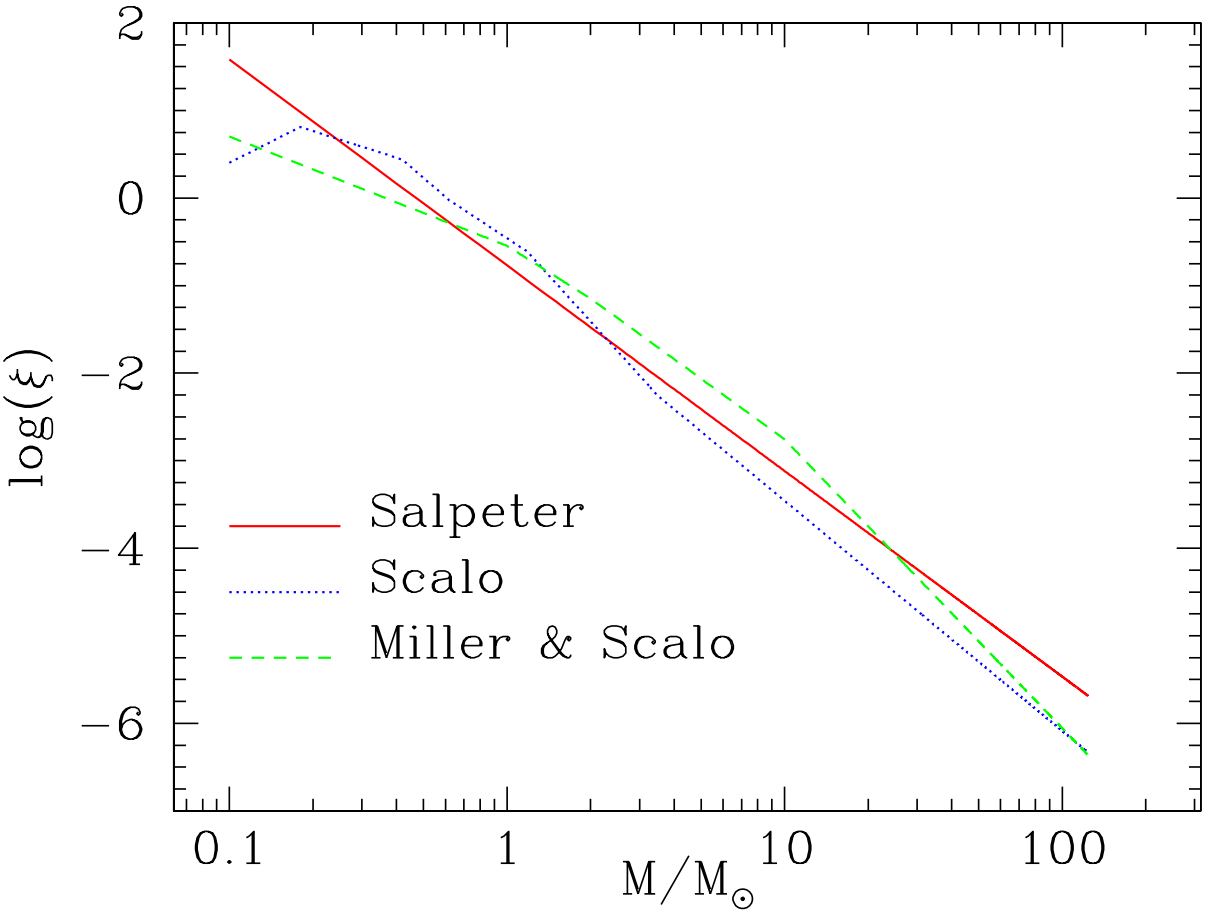

Figure 6.9.: Standard initial mass functions (IMF) from Salpeter (1955), Scalo (1986), and from Miller & Scalo (1979). The different slopes of the three laws produce different spectral energy distributions: the Scalo and Miller & Scalo laws are flat at small masses and less rich of massive stars with respect to the Salpeter law. The large number of massive stars in the Salpeter law produces an excess of UV flux, whereas the Scalo law generates too many solar mass stars, making the spectrum too red when compared to observations. The Miller & Scalo law is a good compromise between the two. More recent studies predict slightly higher values for massive stars (see, e.g., Kroupa et al. 1993). However, the IMF for metal-free and / or very massive stars remains completely unknown.

We make use of the latest yield calculations from explosive nucleosynthesis models from Kobayashi et al. (2006) for the case of "ordinary" (core-collapse) SNe, the typical SNe II, with an explosion energy of $E = 1 \times 10^{51}$ erg[11], hyper-energetic (i.e., $E/E_{51} > 1$) core-collapse HNe, and PISNe. Two mass-energy

[11] common notation: 1×10^{51} erg $= 1\,E_{51} = 1$ foe $= 10^{44}$ J $= 1$ B, where the unit B was named after Hans Bethe.

relations were set: a constant $E/E_{51} = 1$ for SNe with 13, 15, 18, 20, 25, 30, and 40 $M_{\odot}$, and E/E_{51} =10, 10, 20, and 30 for HNe with 20, 25, 30, and 40 $M_{\odot}$, respectively. The yields for PISNe with 150, 170, 200, and 270 $M_{\odot}$ were taken from Umeda & Nomoto (2002). The metal abundance pattern of this DLA

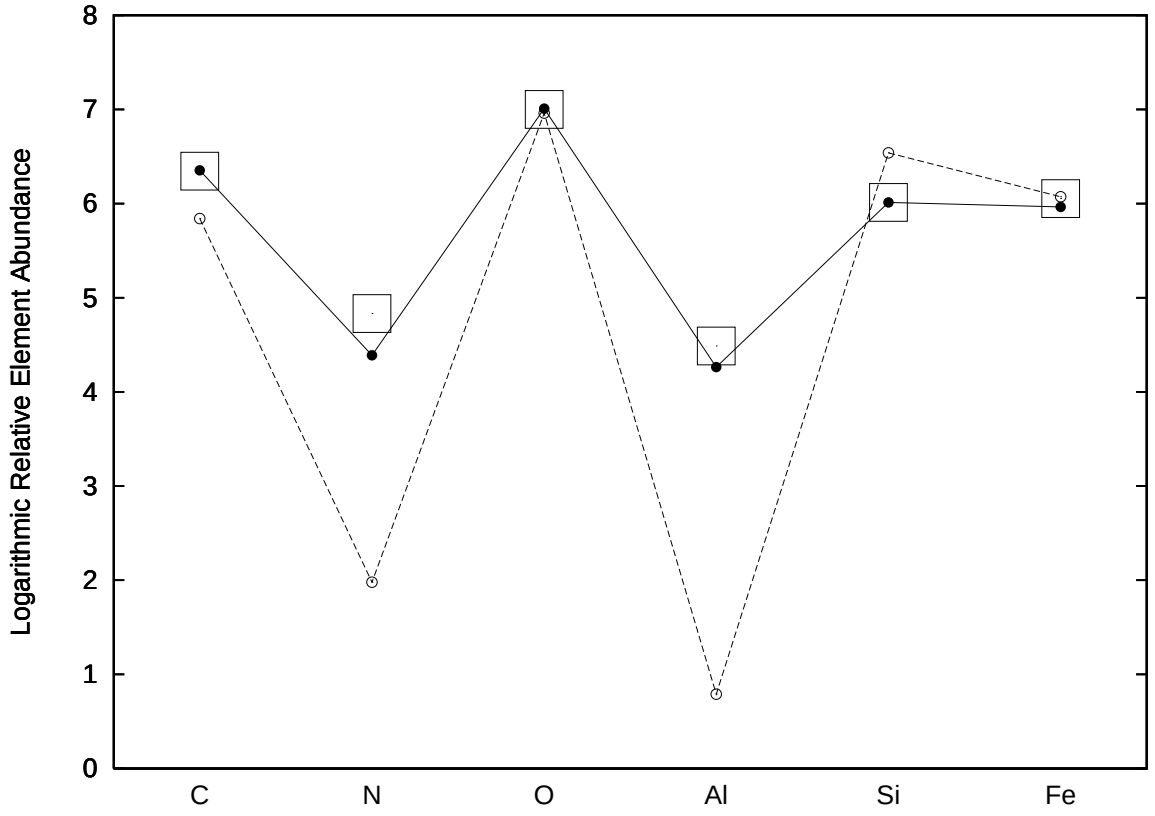

Figure 6.10.: Comparison of relative element abundances from the DLA system toward Q 0913+072 and model calculations for explosive nucleosynthesis. The open boxes show the measured abundances in the DLA system toward Q 0913+072 where the box size corresponds to an assumed *total* error of ± 0.2 dex. Yields from numerical model calculations of a core-collapse SN with 15 $M_{\odot}$ and $E/E_{51} = 1$ are indicated with filled circles and continuous lines, and yields of a PISN with 200 $M_{\odot}$ are shown as open circles with dashed lines. The reader should note that *relative* abundances are compared. For this the sum of the abundances for C, N, O, Al, Si, and Fe of each set was normalized to unity and then shifted arbitrarily (oxygen$_{\rm DLA} = 10^7$) to the scale shown on the y axis to indicate the full range of the measured and predicted element abundances (Erni et al. 2006).

system was then compared with these yields for metallicities of $Z = 0$, 0.001, 0.004, and 0.02. We assumed a simple power law IMF[12]

$$\xi(M_\star) = \left(\frac{M_\star}{M_\odot}\right)^\gamma, \tag{6.3}$$

varying γ from -5 to $+2$ (where $\gamma = -2.35$ corresponds to the Salpeter IMF). We find that there is no significant difference between a scenario of SNe combined with HNe and a scenario of SNe only. On the other hand, Z and γ are very sensible indicators. We find that zero-metallicity stars produce the most accurate abundance pattern in the case of a steep IMF ($\gamma \lesssim \gamma_{\rm Salpeter}$). This and the fact that yields from PISNe do not match the abundance pattern observed in the DLA system toward Q 0913+072 (see Fig. 6.10) excludes any significant contribution of PISNe, yet puts a question mark on their existence. Considering the case of an initially enriched ISM, we compared the observed abundance pattern as well with yields from SNe and HNe with progenitors stars having metallicities of $Z = 0.001$ and $Z = 0.004$. For these second-generation stars (exploding as S/HNe), the abundance pattern is generally reproduced with less accuracy but we notice that a top-heavy IMF partially can reduce these inaccuracies.

The reader should not take this analysis as a proof against a possible existence of PISNe but rather as a strong indication that PISNe events must have been – at most – very rare. We also have to recall that the explosion energy, as well as the mass cut (i.e., the limiting radius between the remnant and the ejecta) for the core-collapse scenario are still two important parameters which are not very well understood, yet could lead to noticeable errors.

Kobayashi et al. (2006) are using basically the same code as Umeda & Nomoto (2001) and Umeda & Nomoto (2002), but with a different treatment of the mixing-fallback mechanism, in order to explain the chemical evolution of the solar neighborhood. Umeda & Nomoto, on the other hand, focus on iron-peak elements, and, in particular, try to reproduce the large [Zn/Fe] ratio observed in EMP stars. Using the yields from Umeda & Nomoto, we find that the IMF should peak around stars with $25\,M_\odot$ and $E/E_{51} = 10$ in order to reproduce the abundance pattern we observe in the DLA system toward Q 0913+072. When using the results from Kobayashi et al. we find that the IMF should peak around stars with typically $15\,M_\odot$ and $E/E_{51} = 1$.

Galactic and cosmic chemical evolution – In a recent paper Daigne et al.

[12]The IMF $\xi(M_\star)$ specifies the distribution in mass of a newly formed stellar population and it is frequently assumed to be a simple power law.

Table 6.2.: Solar abundances as listed in Morton (2003), based on data from Grevesse & Sauval (2002), except for oxygen, for which we adopt the value given in Allende Prieto et al. (2001). Note that different groups use different values for the solar abundances. A summary of the most common values from Grevesse & Sauval (2002) and Asplund et al. (2005) is given in Tab. C.1.

Element	$\log(N(\mathrm{X})/N(\mathrm{H}))_\odot + 12.00$
Carbon	8.52
Nitrogen	7.95
Oxygen	8.69
Aluminum	6.49
Silicon	7.56
Iron	7.50
Nickel	6.25

(2004) have modeled the chemical evolution of condensed cosmic structures (galaxies) and the IGM as a function of redshift including the process of reionization. They consider various different SFRs and IMFs for the progenitor stars that drive the metal enrichment in the early Universe. Following their calculations, a bimodal (or top-heavy) IMF with a moderate mass range of $40-100\,M_\odot$ yields both the required number of ionizing photons to reionize the Universe at $z = 17$ and the correct chemical composition of nucleosynthesis products of these stars to match the observations of metal abundances in metal-poor halo stars and in the IGM. When comparing the mass fractions of C, N, O, Si, and Fe presented in their models with those derived for the DLA system toward Q 0913+072, we find that the abundances of these elements in the DLA system are slightly (< 1 dex, typically) above the values predicted for the IGM at $z = 2.6$, but substantially lower than what is expected for the ISM in galaxies at that redshift. This implies that the DLA system toward Q 0913+072 represents a protogalactic structure that has just recently formed, so that local star formation activity in this system had not enough time to significantly enhance the abundance level above that of the surrounding IGM.

6.4. Summary and Conclusions

The DLA system at $z = 2.6183$ toward Q 0913+072 is characterized by a very low overall metal abundance ($[\mathrm{M/H}] = [\mathrm{O/H}] = -2.47$ or $Z = 0.0034$), a pronounced deficiency of nitrogen ($[\mathrm{N/H}] = -3.84$), and a mild underabundance

of carbon ([C/H] = −2.83). These values mark this system as the most metal-poor DLA system observed at $z < 3$. We further report this absorber to be the first DLA system at present date with a reliable carbon measurement. The low nitrogen abundance implies that this system has not yet attained the full level of primary nitrogen enrichment. This, and the fact that the overall abundance level is only slightly above that of the IGM at that redshift, point toward a protogalaxy that has just recently condensed out of the IGM.

The comparison of the abundances in this DLA system with a sample of extremely metal-poor halo giants shows a very good agreement for carbon, and a reasonable agreement for oxygen and iron. Predictions from yields from Pop III stars for the case of an IMF with $M_{\rm ms} \geq 10\,M_{\odot}$ match the carbon measurements of the two available DLA systems extremely well.

Stars with main-sequence masses below $\sim 10\,M_{\odot}$ do not essentially contribute to the metal budget in the gas on galactic scales, and primordial stars in the range of $M_{\rm ms} \sim 50 - 140\,M_{\odot}$ and above $\sim 260\,M_{\odot}$ are believed to collapse without being able to eject any enriched gas. The only stars with a chemical feedback must therefore be stars with $M_{\rm ms} \sim 10 - 50\,M_{\odot}$, exploding as core-collapse S/HNe, or stars with progenitors in the mass range $\sim 140 - 260\,M_{\odot}$, exploding as PISNe. Scenarios of progenitor stars with a non-zero metallicity, a top-heavy IMF, other explosion mechanism like SNe Ia or PISNe, or a combination of the foregoing, cannot satisfactorily explain the observed chemical abundance pattern. Comparing the metal abundance pattern of the DLA system at $z_{\rm abs} = 2.6183$ toward Q 0913+072 with yields from explosive nucleosynthesis model calculations, we conclude that the most likely scenario for the observed abundance pattern is massive (but not super-massive) Pop III stars with $M_{\rm ms} \approx 10 - 50\,M_{\odot}$, exploding as core-collapse S/HNe.

7. The First Stars in the Universe and Present-Day Observations

7.1. Early Objects and Chemical Evolution

7.1.1. The First Stars

Before the first stars formed out of the gas produced by the Big Bang nucleosynthesis (BBN), the Universe was dark everywhere. Even the light from the Big Bang that rapidly shifted out of the visible range into the infrared did not (visibly) illuminate the Universe. This epoch lasted several million years[1] and is know as the *Dark Ages*. At the dawn of the Universe, i.e., when the first luminous sources lighted up, already a large number of protogalactic systems were in the process of forming. Yet, while the first stars are not within reach of even the most powerful telescopes available at present time, this situation will change soon with upcoming new generations of instruments like the 6.5 m James-Webb Space Telescope (JWST), scheduled for launch in 2013, or ground based instruments with extremely large apertures. ESO is planning to have its first Extremely Large Telescope (ELT) Observatory, the European Extremely Large Telescope (E-ELT)[2], operational around 2015. Other similar ELT projects are the american-canadian Thirty Meter Telescope (TMT), the 30 m California Extremely Large Telescope (CELT), the 30 m Giant Segmented Mirror Telescope (GSMT), the Giant Magellan Telescope (GMT) with the resolving power of a 24.5 m primary mirror, the 20 m Canada-France-Hawaii Telescope (CFHT), the 25 m infrared Large Atacama Telescope (LAT), the European 50 m Telescope (EURO50), or the 30 m Japanese ELT Telescope (JELT). All these projects are scheduled to operate within the next 10 to 15 years. However, the situation at

[1] Our best guess to date is about 200 Myr what corresponds to a redshift of $z \sim 20$. Determining the end of the Dark Ages, and with it the beginning of the reionization epoch, is the focus of considerable observational and theoretical efforts in present-day extragalactic astronomy.

[2] The diameter in ESO's E-ELT project studies ranges from 30 to 60 m. The highly ambitious project of an Overwhelmingly Large (OWL) Telescope with primary mirror of 100 m was abandoned because of its uncomfortably high overall cost, time frame and level of complexity.

present regarding the exploration of the end of the Dark Ages is less unfavorable than it might look at first sight because theory *and* observations are slowly but steadily filling in the gaps in our understanding.

The first stars are not only very different from subsequent stellar generations but are also of greatest importance because of their dramatic impact on their surrounding environment. This interaction, a complex network of physical processes, often is – somewhat ambiguously – referred to as *feedback*. The first stars are the key to our understanding of structure formation and chemical processes in the very early Universe. Because of their particularity and importance, their formation and evolution shall be discussed below in detail (see also Ferrara 2007).

Star Formation in Primordial Gas

Stars form out of a collapsing gas cloud. Coolants can radiate thermal energy away and thereby allow the gas cloud to contract and eventually to collapse. While the gas in the present-day Universe contains about 2% of heavy elements, among those also very efficient coolants such as C^+, O, CO, and dust grains, this is not the case for primordial gas which is – by definition – devoid of any metals. H and He atoms are very poor radiators for temperatures below $\sim 10^4$K and the gas cloud would follow an almost adiabatic evolution if the gas was to remain purely atomic.

Although primordial gas is deprived of efficient coolants, there exist four main cooling processes for *atomic* gas that allow a metal-free gas cloud to cool, to form molecular hydrogen, and thereby to collapse in order to form a Pop III star:

- *Radiative recombination* – The recombination of a proton with an electron will set free thermal energy, eventually carried away by a photon. In general, the recombined atom is in an excited stage and will subsequently decay to the lowest energy level by emitting photons. Accordingly, the energy loss is the difference between the electron energy in the bound state of the hydrogen atom and the kinetic energy of a free electron, i.e, $\Delta E = E^{e^-}_{\rm bound} + E^{e^-}_{\rm kin}$.

- *Cooling through collisional ionization* – The energy loss in the process of collisional ionization is associated to the ionization potential, where the thermal electron energy is used to detach the electron from its nucleus

(ionization energy). Note that the cooling function, $\Lambda(T)$, is dominated by collisional excitation of H and He in the range of $T = 10^4 - 10^{5.5}$ K.

- *Bound-bound transition* – Collisionally excited atoms emit radiation energy equal to the energy difference between two energy levels when the excited stage decays. Note that this is the most important cooling process at temperatures around 10^4K in a primordial gas.

- *Bremsstrahlung emission (or free-free emission)* – This radiation is produced by the acceleration of a charged particle (such as an electron) in a Coulomb field of another charged particle (such as an atomic nucleus). Note that the cooling function is dominated by bremsstrahlung for temperatures $T > 10^{5.5}$ K.

Knowing the cooling rates for H and He and further assuming thermal ionization-recombination equilibirium[3], we can estimate the cooling rate $\Lambda(T)/n_{\rm H}^2$, with T the gas temperature and $n_{\rm H}$ the hydrogen density.

Cooling can be both a very slow or a very rapid process. Therefore, it is important to consider the timescale on which the cooling process takes place. The cooling time, i.e., the time for a system to dissipate its energy, is defined as

$$t_{\rm c} = \frac{3k_{\rm B}T}{2n\Lambda(T)}, \tag{7.1}$$

where n is the total gas number density and $\Lambda(T)$ the cooling function. The free-fall time, i.e., the time it takes for a test particle to reach the center of the gas cloud, is given by

$$t_{\rm ff} = \left(\frac{3\pi}{32G\rho}\right)^{-\frac{1}{2}}, \tag{7.2}$$

where G is the gravitational constant and ρ the total matter density (including dark matter). Finally, the Hubble timescale is

$$t_{\rm H} = H(z)^{-1} = H_0^{-1}\left[\Omega_\Lambda + \Omega_{\rm m}(1+z)^3\right]^{-\frac{1}{2}}, \tag{7.3}$$

where Ω_Λ and $\Omega_{\rm m}$ are the nondimensional vacuum energy and matter density, respectively. The interplay among these three timescales governs both, star and

[3] In some applications this assumption is not adequate and full time-dependent equations must be solved to determine the ionization level.

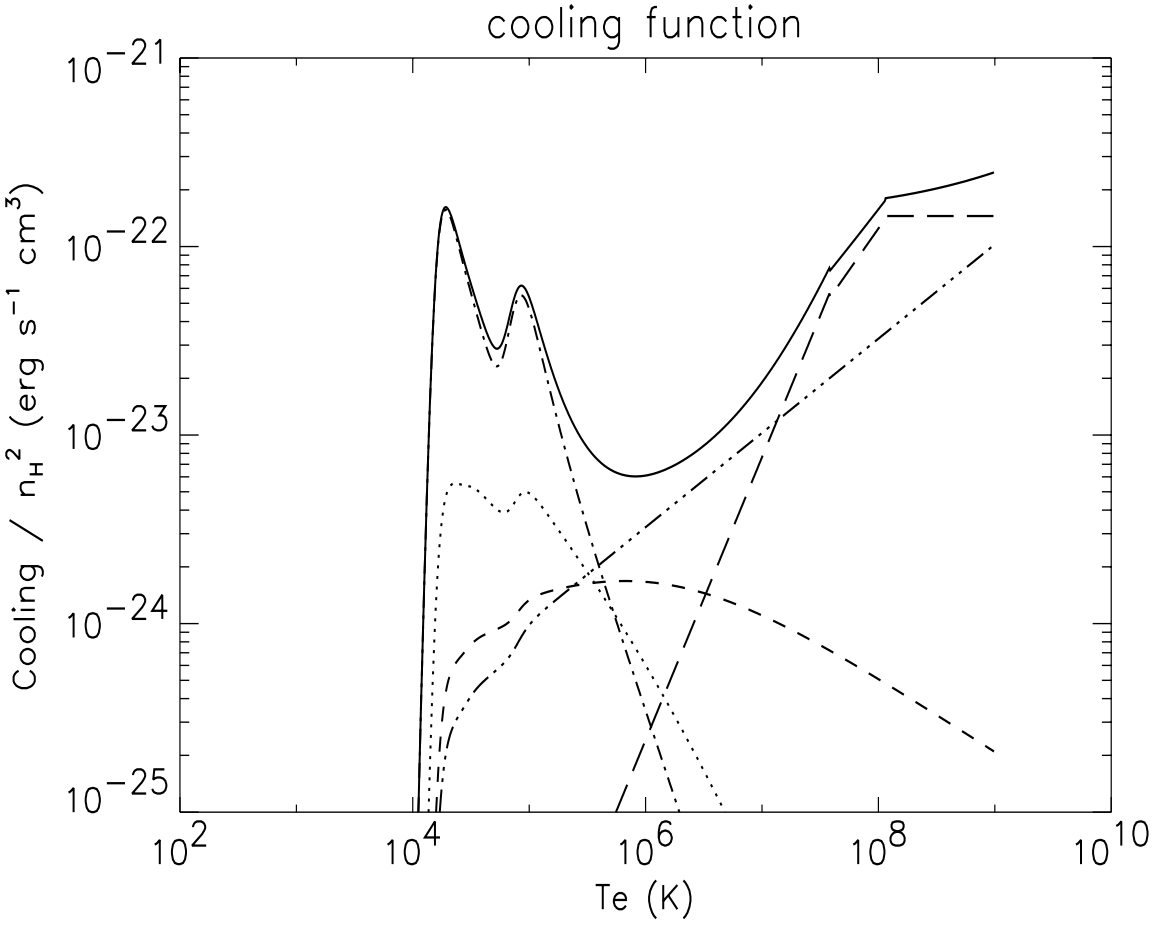

Figure 7.1.: Total cooling rate $\Lambda/n_{\rm H}^2$ in erg s^{-1} cm^3 (solid line) from Montier & Giard (2004), with $X = 0.75$, $Y = 0.25$, a dust-to-gas mass ratio $Z_{\rm d} = 10^{-4}$, and without any UV radiation field. Individual contributions are: collisional ionization (dotted), recombination (dashed), collisional excitation (dash-dot), bremsstrahlung (dash-dot-dot-dot), and dust emission (long dashes).

galaxy formation. Let us therefore, and for the sake of clarity, examine three examples:

- If the cooling time is shorter than the typical dynamical time, i.e., if $t_{\rm c} \ll t_{\rm ff}$, the thermal energy of a gas cloud can effectively be carried away by radiation.

- In the opposite case, i.e., if $t_{\rm c} \gg t_{\rm ff}$, the cloud collapses almost adiabatically.

- Finally, if $t_{\rm c} > t_{\rm H}$, it is clear that, at a given redshift, the cloud did not have

sufficient time to contract.

We conclude that for a primordial gas cloud with $T < 10^4$ K, the drop-off of the cooling function (see also Fig. 7.1) causes the cooling time to increase dramatically, thus preventing its collapse. Hence, the conditions required for a primordial gas cloud to collapse and to form stars can only be achieved thanks to the only other available coolant in the early Universe: molecular hydrogen.

Molecular Hydrogen

Molecular hydrogen, H_2, is stable at low temperatures. This and the cosmic abundance of hydrogen ensures that H_2 is by far the most abundant molecule in the Universe (though not the most readily detectable[4]). The cooling of astrophysical media, generally low-density gas, by molecular hydrogen is of great importance and common to many branches of astronomy (for a review, see, e.g., Le Bourlot et al. 1999).

H_2 consists of two protons covalently bound by two electrons with a binding energy of 4.476 eV. As H_2 is homonuclear, it does not possess a permanent dipole moment. *Rovibrational*[5] *transitions* within the electronic ground state occur by electric quadrupole radiation. Because the associated transition probabilities are small, the photons that are emitted escape from the medium, thereby contributing to its cooling. It is interesting to note that the quadrupole transition probability is proportional to the transition energy, i.e., that

$$A(j \rightarrow i) \propto E_{ji}^5, \tag{7.4}$$

with $A(j \rightarrow i)$ the electric quadrupole transitions probabilities, and E_{ji} the transition energy.

The electronic ground state of molecular hydrogen is described by $X^1\Sigma_g^+$, with X the electron configuration, and Σ the orbital angular momentum state for the case that M_L, the magnetic quantum number, is zero ($^+$ and $_g$ label symmetry properties of the electronic wave function). *Electronic transitions* between the electronic ground state and two excited electronic stages are known as the *Lyman band*,

$$X^1\Sigma_g^+ \rightarrow B^1\Sigma_u^+, \tag{7.5}$$

[4] Due to the lack of fine and hyperfine structure, cold H_2 is only detectable in absorption (because the first rotational transition requires temperatures > 500 K.

[5] contraction of *rotational* and *vibrational*

at $< 1108\,\text{Å}$, and the *Werner band*,

$$X^1\Sigma_g^+ \rightarrow C^1\Pi_u, \tag{7.6}$$

at $< 1008\,\text{Å}$.

A further consequence of the homonuclear nature of H_2 is that it exists in two forms, *ortho*-H_2 and *para*-H_2, which possess distinct values for the total nuclear spin ($I = 1$, and 0, respectively) and for which only odd or even values, respectively, of the rotational quantum number, J, are allowed ($\Delta J = -2$ selection rule). Transitions between these two forms of H_2 can only occur through reactive collisions, e.g., with H atoms, or with H^+ or H_3^+ ions, which will result in a change of the relative orientation of the individual nuclear (proton) spin. However, the ortho-to-para conversion is extremely slow ($\Delta J = \pm 1$ transitions are radiatively forbidden).

An additional peculiarity of H_2 is its large rotational constant. As a consequence, the rotational levels are widely spaced. It follows that the rotational excitation of H_2 becomes important only for kinetic temperatures $T < 1000\,\text{K}$, where rovibrational excitation require $T > 1000\,\text{K}$ (see below). We note that at temperatures above $\sim 10^4\,\text{K}$ molecular hydrogen is collisionally dissociated.

Formation and Dissociation of Molecular Hydrogen

Molecular hydrogen is a very fragile molecule and its abundance depends on a large number of processes and environmental conditions. The formation of molecular hydrogen is somewhat more complicated than one might expect at first sight because of the molecule's simple structure. A process like $H(H^-, \gamma)H_2$ will rarely take place because of the very low quadrupole transition probabilities in the ground electronic state, and the newly formed H_2 molecule would not be able to shed its formation energy of $\geq 4.5\,\text{eV}$ and hence will dissociate immediately. In the present-day Universe dust provides a most favorable reaction site for H I atoms to combine to H_2 molecules and therefore plays a decisive role as a catalyst in the molecular hydrogen formation process (Gould & Salpeter 1963). At low temperatures, hydrogen atoms may stick onto the surface of dust grains, move randomly around and eventually form a H_2 molecule. A part of the formation energy is absorbed by the dust grain while the rest goes into excitation and kinetic energy of the H_2 molecule itself. In the early Universe, however, no dust and consequently no such reaction place for H_2 formation was available. In the case of primordial gas the formation of H_2 molecules has to go through

much less efficient gas phase channels. The two most important reactions are through the H^--channel,

$$H(e^-, \gamma)H^-(H, e^-)H_2, \tag{7.7}$$

and through the H^+-channel,

$$H(H, \gamma)H_2^+(H, H^+)H_2. \tag{7.8}$$

We note that the H^--channel as well as the H^+-channel require electrons or protons as catalysts, implying that the degree of ionization of the gas is decisive for the formation of H_2 molecules.

Molecular hydrogen is easily destroyed either by collisional dissociation at temperatures $T \geq 4000\,\mathrm{K}$ or by radiative (photo-) dissociation. The latter, the so-called Solomon process, is a two-step reaction in which the first step is the photoexcitation of the H_2 molecule via the absorption of a Lyman or Werner band UV photon. The second step is the radiative de-excitation into an unbound vibrational level of the electronic ground state, followed by the dissociation of the H_2 molecule, i.e.,

$$H_2(\gamma,)H_2^*(\gamma,)2H. \tag{7.9}$$

On average about $11-13\,\%$ of all radiative decays following absorption in the Lyman / Werner bands result in a spontaneous decay into the vibrational continuum of the ground electronic state, which is enough to make photodissociation the dominant mechanism for H_2 dissociation (Abgrall et al. 1992). This process is a *radiative feedback* and particularly important because soft UV background radiation in the Lyman / Werner bands will have a negative feedback on the gas cooling and on the star formation inside small halos. In addition to an external background radiation, the structure evolution can also be affected by internal dissociating radiation. In fact, a single star can seriously deplete the H_2 content of a gas cloud with a metallicity smaller than $Z_{\mathrm{crit}} \sim 10^{-4} Z_\odot$ (Schneider et al. 2002) so that subsequent star formation becomes almost impossible (Omukai 2000).

Cooling by Molecular Hydrogen

The process of H_2 radiative cooling is indispensable for primordial gas to cool below $10^4\,\mathrm{K}$. Molecular hydrogen can, like all other molecules, vibrate and rotate around an axis. When a vibrational or rotational state of the molecules

discretely changes, obeying quantum dynamics, they emit or absorb line radiation, like in the case of electron transitions. Vibrational transitions are more important at high temperatures (in the regime $T = 10^3 - 10^4\,\mathrm{K}$) while the rotational transitions are more significant at lower temperatures ($T < 10^3\,\mathrm{K}$).

The optically thin regime is the regime that is appropriate to the initial stages of the fragmentation / collapse process, when the H_2 fraction and the gas density are still low[6]. Many authors have derived fitting formulae to the H_2 cooling function, Λ_{H_2}, where Hollenbach & McKee (1989) give a very useful approximation:

$$\Lambda_{H_2} = n_{H_2}\left(n_H L^{H}_{\upsilon r} + n_{H_2} L^{H_2}_{\upsilon r}\right). \tag{7.10}$$

The first term represents the contribution from H I-H_2 collisional excitation and the second term is due to H_2-H_2 collisions.

Next to the energy loss in collisional processes, additional cooling (heating) takes place when H_2 molecules are dissociated (formed) because the hydrogen molecule has a lower potential energy than two separated neutral hydrogen atoms. The cooling function resulting from H_2 dissociation in units of $\mathrm{erg\,s^{-1}\,cm^{-3}}$ is

$$\Lambda_{\mathrm{diss}} = 7.61 \times 10^{-12}\,\frac{\mathrm{d}n_{H_2}}{\mathrm{d}t}, \tag{7.11}$$

where $\mathrm{d}n_{H_2}/\mathrm{d}t$ is the dissociation rate of H_2.

We note that the quantity of H_2 molecules formed in primordial gas, as described above, is sufficient in order to allow the pristine gas cloud to cool and eventually to collapse.

Collapse of a Metal-Free Cloud

How massive were the first stars? How did they explode and what was their impact on cosmological scales? Despite a lot of effort in the past years these and many more questions about the nature of the first stars still remain unanswered. However, we do know that the first objects[7] formed via gravitational collapse of a thermally unstable and optically thick medium. Regardless of the exact initial conditions, the primordial gas attains a characteristic temperature and density for a characteristic fragmentation scale, explained by H_2 cooling, for which the Jeans mass is a good approximation (see below). However, the overall mass

[6] At later stages (proto-stellar core phase) a proper treatment of the line radiative transfer becomes necessary.

[7] The denomination *first stars / objects* and *Pop III stars* are used as synonyms throughout this work.

range and IMF of the first stars are still unknown. In addition, it is unknown whether binaries or, more general, clusters of metal-free stars can form. These questions are likely to be answered only by the time when new observations from next generation telescopes will be available. In what follows, the cooling, fragmentation, and the eventual collapse are discussed, where the possibility of binaries or Pop III clusters is deliberately omitted.

A gas cloud starts off collapsing in free fall because, initially, no pressure gradients are present and the optically thin gas allows the compression energy to be freely radiated away (isothermal evolution). Eventually, the density will increase in the central region and decrease in the outer boundaries and hence create a pressure gradient. This will significantly retard the collapse to continue in free-fall in the outer regions, whereas the central part continues to collapse approximately in free fall. From (7.2) we can see that the free-fall time depends on $\rho^{-1/2}$, which will speed up the collapse at the center. For the subsequent evolutionary phase of the collapsing core one needs to consider a substantial amount of physical processes such as the energy equation, formation / destruction of molecules, the cooling function, and radiative transfer. The first attempt to model this complicated evolution has been successfully carried out by Omukai & Nishi (1999) and later by Ripamonti et al. (2002). From those studies I will below summarize the evolution of the central core.

In the beginning, due to the lack of H_2 molecules (mainly formed via the inefficient H^--channel), the compression will cause the gas temperature inside the collapsing (metal-free) cloud to rise adiabatically. Increasing temperature und density will then boost the H_2 formation rate, so that a sufficient amount of H_2 molecules is formed (within the free-fall timescale) that allows the gas temperature to drop to about 300 K. Although the gas becomes optically thick when the density reaches $n \approx 10^8\,\mathrm{cm}^{-3}$, the cooling remains efficient enough to allow the central region to further collapse on the dynamical timescale. At $n > 10^{20}\,\mathrm{cm}^{-3}$ the gas then becomes virtually adiabatic and after a minor further contraction a small hydrostatic core, or protostar, with $M_{\mathrm{protostar}} \approx 10^{-3}\,M_\odot$, $n_{\mathrm{protostar}} \approx 10^{22}\,\mathrm{cm}^{-3}$, and $T_{\mathrm{protostar}} \approx 3 \times 10^4\,\mathrm{K}$ forms.

Fragmentation of a Metal-Free Cloud

A star forming gas cloud will fragment into smaller gas clumps, where these clumps are the direct progenitors of the subsequently formed stars. The mass of the star will depend on the accretion of the remaining gas envelope onto the core, because the mechanisms to stop the accretion, such as magnetic fields,

dust, and heavy element opacity, fail under primordial conditions. Next to the accretion rate from the outer gas envelope, the star's mass will largely depend on the initial mass of the collapsing gas clump, i.e., on the fragmentation of the initial gas cloud. The question we have to ask here is whether most of the gas goes into a few larger or rather into many smaller objects.

Fragmentation can be investigated using thermal physics within the framework of the classical Jeans criterion (Larson 2003) because fragmentation occurs at the end of an efficient cooling phase where $t_c \ll t_{ff}$ is no longer valid. As soon as H_2 becomes inefficient as coolant, the temperature decreases for an increasing density and isothermality breaks. That is the case when $\gamma > 1$ (because $T \propto n^{\gamma-1}$). The typical fragmentation mass-scale is $M_{frag} \sim 10^3 M_\odot$, given by the thermal Jeans mass. Note that this scenario holds for metallicities $\lesssim 10^{-6} Z_\odot$ (see also Fig. 7.2).

7.1.2. Explosive Nucleosynthesis

Nucleosynthesis during the hydrostatic burning phases takes place in all stars of all sizes and origins, where a large variety of elements, starting from He through Fe, are produced. However, stars with masses larger than about $8 M_\odot$ will additionally go through a much more spectacular process: explosive nucleosynthesis. The very energetic thermonuclear reactions can produce elements heavier than Fe (that only form in endothermic reactions) and have an important impact on structure formation and the metal enrichment history on small and large scales.

As we have seen above, the first stars are rather particular, not only in metallicity but also in mass. Certain models assume mass ranges for Pop III stars of up to $600 M_\odot$ and even more[8]. More realistic values are in the range of a few tens to about 300 solar masses. The possible existence of such massive stars has inspired many new concepts in the recent past. One approach is that very massive Pop III stars no longer explode as "ordinary" core-collapse supernovae (ccSNe or SNe for short)[9] but as so-called pair-instability supernovae[10] (PISNe).

[8] Pop III stars are unlikely to exceed $600 M_\odot$. This is because of the fragmentation mechanism described in the previous section. It would be hard to explain how and from where a protostar could accrete those considerable amounts of matter (A. Ferrara, priv. comm.).

[9] Core-collapse supernovae are often abbreviated as SNe II or simply as SNe. For this work, SN II, SN, and ccSN will be used as synonyms.

[10] Sometimes also referred to as Pair-Production Supernova (PPSN or $SN_{\gamma\gamma}$).

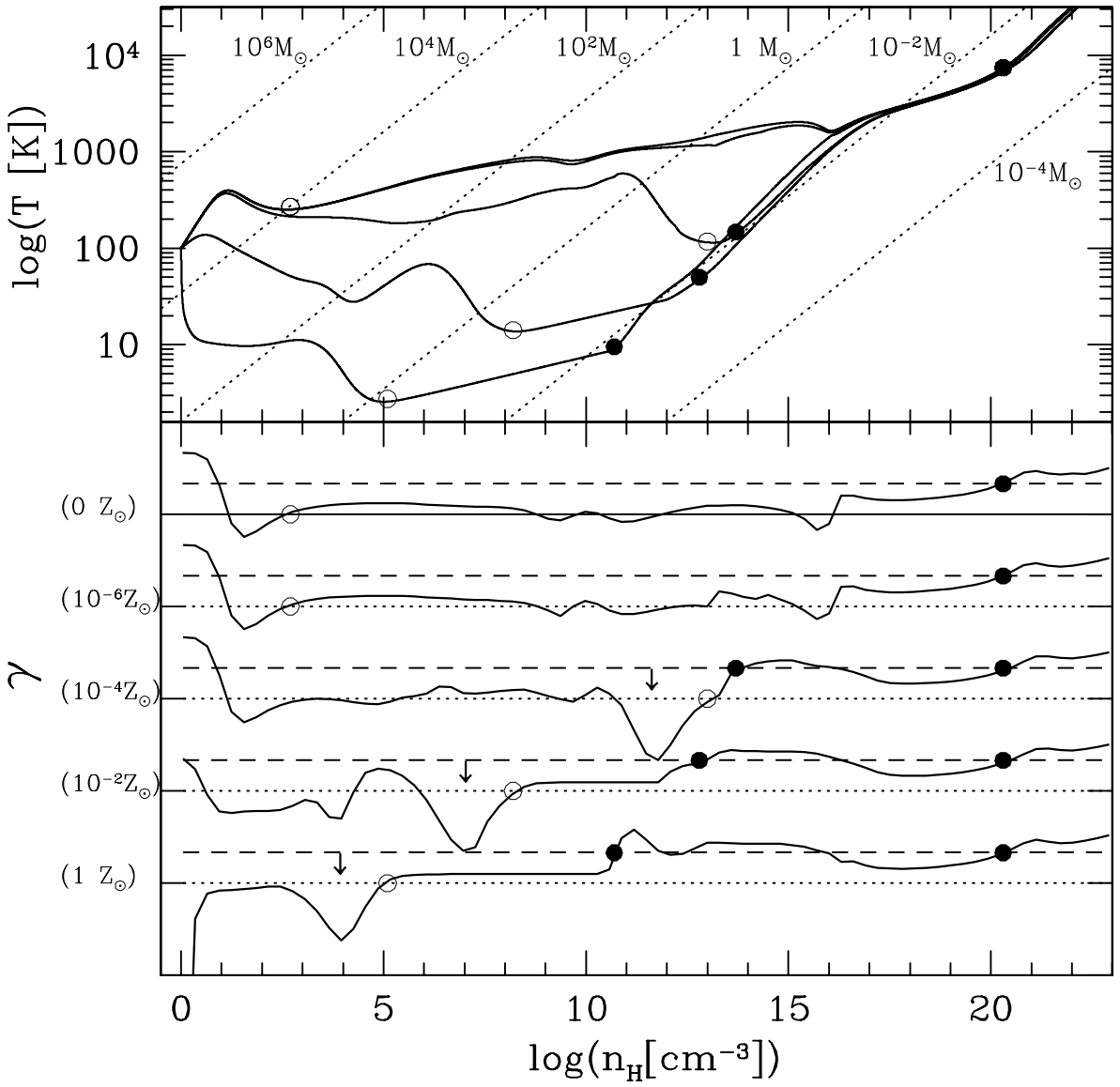

Figure 7.2.: Collapse and fragmentation of a star-forming gas cloud (from Schneider 2006). Upper panel: temperature evolution as a function of the hydrogen number density, $n_{\rm H}$, where the diagonal dotted lines correspond to a constant Jeans mass for spherical clumps. Lower panel: the corresponding evolution of the adiabatic index, γ, for different initial metallicities, where the solid (dashed) lines correspond to $\gamma = 1$ ($\gamma = {}^{1}/_{300}$). We note that the fragmentation stops (open circles) much earlier in the case of metal-free gas (top line), leading to a considerably larger envelope and therefore to a higher stellar mass. The hydrostatic cores (filled circles) form at $\sim 10^{-3}\,M_{\odot}$ in the case of $Z_{\odot} = 0$.

Supernovae, i.e., stars that go through an explosive nucleosynthesis process, are spectroscopically classified in *Type I* (no hydrogen Balmer lines) and in *Type*

II (with hydrogen Balmer lines). Those two groups are then further subdivided according to the presence of other lines and the shape of the light curve: Type Ia (Si II at 6150 Å), Type Ib (He I line at 5876 Å), Type Ic (weak or no He lines), Type II−P (plateau), and Type II−L (linear). Note that this a historical classification, solely due to the *observational* [11] and not the physical properties of supernovae.

7.1.3. A particular Case: Type Ia Supernovae

Type Ia Supernovae (SNe Ia) are clearly very important objects in view of their unique property to be (almost)[12] perfect standard candles or their significant Fe contribution[13] (see, e.g., Nomoto et al. 1994). However, they are of no relevance to the early Universe because they occur only at later epochs. The time from the formation of the progenitor star to the explosion requires $2-4\,\mathrm{Gyr}$[14] (Strolger et al. 2004). Although there are still some uncertainties in the exact nature of the development, evolution, and the explosion itself, the system that satisfactorily meets all the observational constraints is the thermonuclear explosion of a CO white dwarf (WD) accreting matter from a companion star (Hoyle & Fowler 1960; for technical details see, e.g., Nomoto et al. 1997). Three different candidates may reach this situation: (1) the explosion of a CO WD that reaches the Chandrasekhar mass by mass accretion from a main-sequence (MS) or red giant (RG) star[15] (Nomoto & Sugimoto 1977; Nomoto 1982), (2) the explosion of a sub-Chandrasekhar mass CO WD that ignites He explosively in the outer layers[16] (Nomoto 1980; Limongi & Tornambe 1991; Woosley & Weaver 1994; Hoeflich & Khokhlov 1996), and (3) the explosion of a CO WD that reaches the Chandrasekhar mass by merging with another CO WD[17] (Iben & Tutukov 1984).

[11] In the case of a Type II supernova, most of the energy powering emission at peak light is derived from the shock wave that heats and ejects the envelope. The radiation emitted by Type I supernovae, on the other hand, is entirely a result of the decay of radionuclides produced in the explosion, principally ^{56}Ni, that decays with a half-life of 6 days into ^{56}Co, and eventually, with a half-life time of 77 days, into stable ^{56}Fe.

[12] See, e.g., Domínguez et al. (2000), Howell et al. (2006), or Erni & Tammann (2006).

[13] A SNe Ia expels $0.5-1.0\,M_\odot$ of ^{56}Ni (where $^{56}\mathrm{Ni} \rightarrow {}^{56}\mathrm{Co} \rightarrow {}^{56}\mathrm{Fe}$), while a Type Ib, Ic or Type II supernova ejects only about $0.1\,M_\odot$ of ^{56}Ni.

[14] Note, however, that in the past other groups have predicted that the majority of SN Ia progenitor systems are likely to have lifetimes shorter than 1 Gyr (Hachisu et al. 1996; Kobayashi et al. 1998).

[15] single degenerated Chandrasekhar mass scenario

[16] double detonation sub-Chandrasekhar mass scenario

[17] double degenerated scenario

7.1.4. Core-Collapse Hyper-/Supernovae

Type II SNe (SNe for short) are core collapse-induced explosions of massive stars ($M \gtrsim 8\,M_\odot$) with short lifetimes (on the order of $10^6 - 10^7$ yrs). They produce more α-elements relative to Fe with respect to the solar ratios, i.e., $[\alpha/\mathrm{Fe}] > 0$.

The evolution of the progenitor star depends crucially on its main-sequence mass:

- Stars in the range of $8\,M_\odot \leq M \leq 10\,M_\odot$ undergo non-degenerated carbon burning and form a degenerated O-Ne-Mg core with $M_{\mathrm{ONeMg}} < 1.37\,M_\odot$. This is, in fact, below the Chandrasekhar mass, yet very close. The core will grow during shell C-burning until electron captures on ^{24}Mg and ^{20}Ne set in. This causes a reduction of the Chandrasekhar mass, M_{Ch}, and leads to oxygen and subsequent silicon ignition. The contraction of the iron core turns into a collapse, followed by a core bounce (more details about the Fe-core collapse below). The remnant of such a (subluminous) Type II−P SNe is a neutron star (see, e.g., Kitaura et al. 2006).

- Stars with larger masses ($10\,M_\odot \leq M \leq 140\,M_\odot$) will go through all burning stages until silicon burning leaves a central iron core. The iron core contracts when the core mass exceeds

$$M_{\mathrm{Ch}}(Y_\mathrm{e}, S_\mathrm{e}) = 1.44\,(2Y_\mathrm{e})^2 \left[1 + \left(\frac{S_\mathrm{e}}{\pi Y_\mathrm{e}}\right)^2\right] M_\odot, \tag{7.12}$$

  where Y_e is the electron abundance ($Y_\mathrm{i} = X_\mathrm{i}/A_\mathrm{i}$), and S_e the electron entropy. In earlier burning stages the contraction phase ended in temperatures high enough to induce the next fusion reaction for a new burning stage, but during the Fe-core contraction phase this does not occur, as the material is in a state with the highest possible binding energy per nucleon. That means that the contraction is not stopped. The increasing Fermi energy of the electrons causes further electron captures by $\mathrm{e}^-(\mathrm{p},\mathrm{n})\nu_\mathrm{e}$ and, consequently, a reduction of the electron pressure. Thus, the contraction turns into a collapse. Beyond a certain density ($\rho \approx 3 \times 10^{11} - 10^{12}\,\mathrm{g\,cm^{-3}}$) neutrinos can no longer escape and the collapsing Fe-core rebounds off the stable "neutrinos sphere" (neutron degeneracy pressure). This creates a pressure wave that accelerates into a

shock wave (*prompt shock*) moving outward with supersonic speed and eventually blows off the star's outer layers. This explosion is what we refer to as a *supernova explosion*. The problem with this standard model[18] is that it is not robust in computer simulations[19].

The typical explosion energy of a core-collapse SN is on the order of 10^{51} erg $= 1\,E_{51}$. A *Hypernova* (HN) is, simply speaking, a hyper energetic core-collapse SN with an explosion energy exceeding $1\,E_{51}$. This definition will suffice for our purpose as HNe differ only in details from "ordinary" core-collapse (or Type II) supernovae.

7.1.5. Pair-Instability Supernovae

This explosion mechanism does comply with the request of the formation of very massive stars in a metal-free environment, but reproduces lower [Zn/Fe] and [Co/Fe] ratios. Low [Zn/Fe] and [Co/Fe] ratios are inevitable for PISNe because in PISNe the mass ratio between the complete and incomplete Si-burning regions is much smaller than in core-collapse SNe. This led Umeda & Nomoto (2002) to the conclusion that the abundance pattern seen in the very metal-poor halo stars does not result from PISNe.

Below some typical metallicity, $Z_{\rm crit} \sim 10^{-4}\,Z_{\odot}$, star-forming clumps have no, or at most very little, tendency to further fragment. This is why Pop III stars are thought to be much more massive than Pop II or Pop I stars. Stars with masses in the range of $140\,M_{\odot} \leq M \leq 260\,M_{\odot}$ enter into the electron-positron pair instability region ($\gamma \rightarrow {\rm e}^{+} + {\rm e}^{-}$) during the central oxygen burning stages and contract quasi-dynamically. Consequently, the central temperature increases to $3 - 6 \times 10^{9}\,{\rm K}$, which is so high that central oxygen burning takes place explosively, being much faster than neutrino energy losses. The generated nuclear energy is large enough for internal energy to exceed the gravitational binding energy. The explosion disrupts the entire star and leaves no compact remnants (Umeda & Nomoto 2002).

If stars have masses even as high as $M > 260\,M_{\odot}$, photodisintegration instability is encountered before explosive nuclear burning can reverse the implosion. The total energy of the star does not become positive after central oxygen and silicon burning and hence the core collapses into a BH. Once a proto-black

[18] which is by no means universally accepted (see, e.g., Wheeler et al. 2005)

[19] The most promising mechanism that might allow reliable computer simulations of SN II explosions is based on an additional process, the so-called neutrino heating (see, e.g., Bruenn & Haxton 1991).

hole has formed inside the star, accretion continues through a disc at a rate which can be as large as $1 - 10 M_{\odot}\,\mathrm{s}^{-1}$. Magnetic fields then drive an energetic jet and thus produce a gamma-ray burst (GRB)[20] through the interaction with the surrounding gas. The star will finally collapse into a very massive black hole (VMBH), swallowing virtually all previously produced heavy elements. The term *Collapsar* was introduced to designate these GRB-progenitors (Woosley 1993).

A major advantage of the concept of PISNe is the fact that the explosion is consistently reproduced in numerical simulations and neither the explosion energy nor the mass cut have to be estimated (as this is the case for ccSNe) but follow directly from the model itself. However, a major problem of the concept of PISNe is that the yields from numerical simulations fail to reproduce observed metallicities in very metal-deficient stars[21].

7.1.6. Extremely Metal-Poor Stars

Extremely metal-poor (EMP) stars are very old objects and provide crucial clues to the star formation history and the synthesis of chemical elements in the early Universe. This is because stars that show only very moderate burning activity (otherwise, they would have ended their lives long before they could be observed) reflect the chemical composition of the gas out of which they originate. EMP stars are believed to have formed directly after the very first stars, thus having conserved the metal contamination from Pop III stars to the pristine gas from the Big Bang.

At this place I should point out that the nomenclature for metal-deficient stars, as used in the literature, is, unfortunately, neither consistent nor precise. This is presumably due to historical reasons and the recent ample discoveries in this field. Early studies by Oort (1926) and Baade (1944) pointed out that the stars in our Galaxy can be divided into two different types of populations, to which we refer today as population I (Pop I), and population II (Pop II) stars. Regarding a star's metal content, it was for a long time sufficient to refer to it as a Pop I (solar-like) or Pop II (metal-poor) star, respectively. However, modern

[20] Gamma-ray bursts were first discovered by Klebesadel et al. (1973). They are brief (on the order of seconds), intense flashes of electromagnetic radiation with typical photon energies of $\sim 100\,\mathrm{keV}$ that arrive at Earth from unpredictable directions several times a day (see, e.g., Fishman & Meegan 1995). They are isotropically distributed on the sky and, so far, not one has ever repeated (except for the so-called *soft-gamma repeaters* witch are, however, only phenomenologically and not physically related to classic GRBs).

[21] Note that this is not the case for the intercluster medium (ICM) where the observed abundance anomalies (e.g., oxygen) can be explained by an early generation of Pop III stars exploding as PISNe (Loewenstein 2001).

large surveys and highly sophisticated instruments unveiled numerous stars with continuously lower metal contents, thus making a more detailed naming necessary. It was only very recently when Beers & Christlieb (2005) suggested an adequate and uniform nomenclature to classify stars by their metal content (see Table 7.1). As of this writing there is well-founded hope that this nomenclature will be largely accepted by the scientific community.

Table 7.1.: Nomenclature for stars of different metallicities (Beers & Christlieb 2005).

Term	Acronym	[Fe/H]
Super Metal-Rich	SMR	$> +0.5$
Solar	–	~ 0.0
Metal-Poor	MP	< -1.0
Very Metal-Poor	VMP	< -2.0
Extremely Metal-Poor	EMP	< -3.0
Ultra Metal-Poor	UMP	< -4.0
Hyper Metal-Poor	HMP	< -5.0
Mega Metal-Poor	MMP	< -6.0

The Extreme Cases of HE 0107−5240 and HE 1327−2326

HE 0107−5240 and HE 1327−2326 are two hyper metal-poor (HMP) stars and with $[\mathrm{Fe/H}] = -5.2 \pm 0.02$ (Christlieb et al. 2002) and $[\mathrm{Fe/H}] = -5.4 \pm 0.02$ (Frebel et al. 2005), respectively, the most metal-deficient stars observed so far. Christlieb et al. (2002) find that HE 0107−5240 is a giant star of the Galactic halo population (apparent magnitude $B = 15\overset{\mathrm{m}}{.}86$), located on the red giant branch, with $T_{\mathrm{eff}} = 5100 \pm 150\,\mathrm{K}$ and $M \approx 0.8\,M_{\odot}$. They give two different possible scenarios that could explain the extreme underabundance observed in HE 0107−5240. The first hypothesis is that HE 0107−5240 has formed out of a gas cloud with $[\mathrm{Fe/H}] \approx -5.3$, where the abundance pattern of elements heavier than Mg can be explained by the metal enrichment from a $20-25\,M_{\odot}$ core-collapse SN. The other possibility assumes that the IMF of Pop III stars,

the so-called first mass function (FMF), was bimodal and included stars with masses $\sim 1\,M_{\odot}$ as well as $\sim 100\,M_{\odot}$. Thus, HE 0107−5240 could have formed out of a zero metallicity gas could, with its present metallicity being due to accretion during repeated passages through the Galactic disk. This latter scenario would suggest that Pop III stars could still exist nowadays because the first generation of stars perhaps also contained long-lived low-mass objects, where the present lack of detection of these kinds of objects might be an observational selection effect.

7.2. Linking DLA Systems, EMP Stars, and Yields from Numerical Model Calculations

7.2.1. Search for Pop III Stars

The immediate physical processes after the Big Bang[22] are very well known and match exceedingly well with findings from high-energy accelerator experiments and observations of the cosmic microwave background (CMB). Important new progress in simulations and observations, especially in the very recent past, has significantly expanded our understanding of the Universe at high redshifts ($z \sim 1-6$). The gap between $z \sim 6-1100$, whereof no observational data are available at all represents a period of only about 0.95 Gyr but plays none the less a most decisive role for the ensuing evolution of the Universe. Although it remains an unanswered question to date whether the epoch of Pop III star formation was very brief or rather long-lasting, the most promising time to look for Pop III stars is at redshifts of $z \sim 14$, i.e., at a time when the first Pop III stars are expected to have formed[23].

While redshifts as high as $z = 14$ are out of the reach of today's telescopes, many promising instruments are currently being designed and constructed (see Section 7.1.1) in order to make redshift and time this range accessible for future observations. The most commonly used approach to draw conclusions from present observations on the first stars in the Universe is by comparing metal

[22] Standard Big Bang Nucleosynthesis (SBBN) Model

[23] Observations have set constraints on the epoch of reionization (EoR), corresponding to the formation epoch of the first luminous objects. Studies of Gunn-Peterson absorption indicate a rapid increase in the neutral fraction of the IGM from $n_{\rm HI}/n_{\rm H} < 10^{-4}$ at $z \leq 5.5$ to $n_{\rm HI}/n_{\rm H} < 10^{-3}$ (an perhaps up to 10^{-1}) at $z \sim 6$. The large scale polarization of the CMB, on the other hand, implies a significant ionization fraction extending to higher redshifts of $z \sim 11 \pm 3$. These results, as well as observations of galaxy populations, suggest that reionization is a process that begins as early as $z \sim 14$, and ends at $z \sim 6-8$ (Fan et al. 2006).

abundances found in EMP stars with yields from numerical model calculations. However, EMP stars are not the only objects that have preserved the abundance pattern left by the first stars, but this could also be the case for specific regions within the IGM. One example is the DLA system toward Q0913+072 with its very low overall metallicity and the remarkable fact that the CNO-elements can be measured very accurately (see Erni et al. (2006) and Chapter 6).

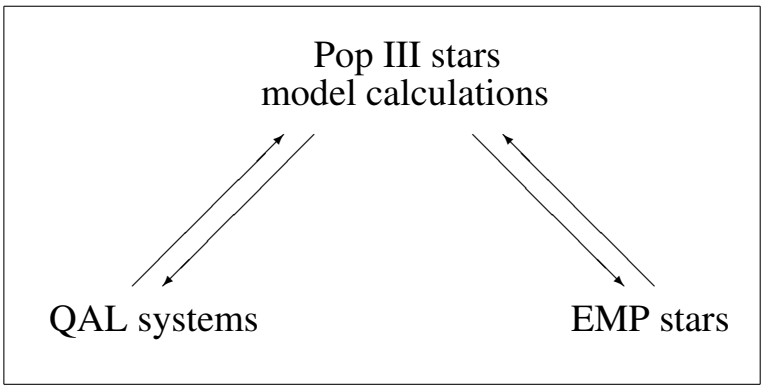

Figure 7.3.: Comparing EMP stars, QAL systems, and Pop III yields from numerical model calculations.

In what follows, I will compare EMP stars and QAL systems with yields from numerical model calculations (Fig. 7.3). The values as taken from literature are biased by several factors like the fact that they come from different surveys, or that different data-reduction techniques were used. However, the most severe discrepancy is likely due to the use of different solar abundance reference values. We note further that the available data are not unambiguous in the sense that no clear-cut criteria can be applied between the true first successor of Pop III stars and objects that have been altered by contributions from later generations.

Any mass estimation of QAL systems has to be viewed with great caution because neither their geometry nor their exact nature is known. Hence, it is impossible to estimate the number or the mass (and therefore their type) of the stars that caused the observed metal enrichment. On the other hand, abundance ratios can be measured at very high precision and are in the case of DLA systems (due to the generally negligible corrections for the interference of dust or ionization) highly reliable. It has to be kept in mind that each LOS samples only very specific regions and does, in general, not reflect the overall abundance of the whole structure. Nevertheless, metal abundance ratios are good indicators for metal enrichment processes and the evolution history of the IGM or galaxies.

The overall abundance pattern or the individual abundance ratios from different objects can be used as a qualitative test for their resemblance. For this purpose I introduce a measurable quantity, ζ, that indicates the resemblance or the offset of two objects (named A and B) based on their individual abundance pattern:

$$\zeta = \frac{1}{\mathrm{j}} \sum_{\mathrm{i}=1}^{\mathrm{j}} \left(\left(\frac{\mathrm{X}}{\mathrm{H}} \right)_{\mathrm{A,i}} - \left(\frac{\mathrm{X}}{\mathrm{H}} \right)_{\mathrm{B,i}} \right)^2, \tag{7.13}$$

with the common notation $[\mathrm{X/H}] = \log(N(\mathrm{X})/N(\mathrm{H})) - \log(N(\mathrm{X})/N(\mathrm{H}))_{\odot}$ and with j the number of common elements. The sum of the j abundance ratios from object A and B were normalized to unity, where $j \geq 2$. It is $\zeta \geq 0$, where a small ζ indicates a small deviation in the abundance patterns between the two samples.

7.2.2. Fiducial Samples Compiled from Literature

Set of 18 EMP and 2 HMP Stars

A set of 18 EMP and 2 HMP stars was compiled from literature, where the first eighteen stars in Table 7.3 are *unmixed*[24] EMP stars, analyzed with LTE model atmospheres. Only about half of the known stars with metallicities $[\mathrm{Fe/H}] < -5.0$ are unmixed, i.e., their C and N abundances in the atmosphere, in particular, have not been modified by mixing processes inside the star. In this case the surface composition of a cool star is a good diagnostic of the chemical composition of the gas out of which it formed. I have used EMP stars with abundances for C and N from Spite et al. (2006) and O to Zn from Cayrel et al. (2004). Cayrel et al. (2004) report very tight abundance relations of nearly all detected elements, with C and N being notable exceptions. As C, N, and O are the first elements to be produced after BBN, their abundances in the early protogalactic structures merit further study.

Set of 59 DLA Systems

A set of 59 DLA systems (Table 7.4) was compiled from literature, where DLA systems are considered to be the most suitable QAL systems for chemical abun-

[24] The terms "mixed" and "unmixed" may appear a bit misleading. Note that all mixed and unmixed halo giants have undergone the first dredge-up (which does, apparently, not affect the abundances of elements heavier than Li in low mass stars with $M \leq 0.9 M_{\odot}$). Cayrel et al. (2004) and Spite et al. (2005) use the term "mixed" only for stars that have undergone mixing with deep layers, thereby affecting the observed CNO abundances. Contrary, unmixed stars (Table 7.3) are expected to have not undergone deep mixing processes.

dance studies in the high-redshift Universe (see also Section 3.2.3, page 22).

Yields from Model Calculations

A set of yields from 52 different numerical model calculations (Table 7.2) was compiled from literature. The three different types of supernovae explosions, i.e., the classical Type II supernova (ccSN or just SN for short), the hyper-energetic hypernova (HN), the pair-instability supernova (PISN), and a combination of SNe and HNe with a Salpeter IMF, covers all the known processes that have enriched the IGM at early epochs. The set does not include any (typical) Pop II stars and their contribution from the CNO cycle. In a metal-free stellar environment, i.e., in an environment lacking initials CNO elements, the CNO cycle does not operate until the star contracts to much higher central temperatures ($\sim 10^8$ K) than in Pop II stars, where the triple-α reaction produces only a tiny mass fraction (on the order of $\sim 10^{-10}$) of ^{12}C (Kobayashi et al. 2006).

Those yields are arranged in four different groups, designating each one a particular enrichment scenario:

- *Core-collapse Supernovae* – Set of yields from "ordinary" (core-collapse) SNe, the typical SNe II, with an explosion energy of $E = 1 \times 10^{51}$ erg. The mass-energy relation[25] set is a constant explosion energy, i.e., $E/E_{51} = 1$, and stellar masses of $M = 13$, 15, 18, 20, 25, 30, and $40\,M_{\odot}$. Further, the progenitor's metallicity varies with $Z = 0$, 0.001, 0.004, and 0.02.

- *Core-collapse Hypernovae* – Set of yields from HNe, i.e. hyper-energetic (i.e., $E/E_{51} > 1$) core-collapse supernovae. The mass-energy relation set is $E/E_{51} = 10$, 20, and 30, stellar masses of $M = 20$, 25, 30, and $40\,M_{\odot}$, and a progenitor metallicity varying with $Z = 0$, 0.001, 0.004, and 0.02.

- *SNe combined with HNe* – In order to account for the (unknown) IMF and hence a broad range of individual initial stellar masses, Kobayashi et al. (2006) have calculated IMF weighted yields for a combination of SNe and HNe. They adopt a simple Salpeter IMF ($\gamma = -2.35$) and considered a mass-range of $M_{\rm l} = 0.07$ to $M_{\rm u} = 50\,M_{\odot}$. Note that the abundance ratios depend on the IMF, of course, but more strongly on $M_{\rm u}$.

[25] The mass-energy relation has been obtained from the light curve and spectral fitting of individual SNe.

- *Pair Instability Supernovae* – Set of yields of PISNe from Umeda & Nomoto (2002). They consider (metal-free) progenitors with masses of $M = 150$, 170, 200, and $270\,M_{\odot}$.

Table 7.2.: Mass-energy relation set for yields from 52 different numerical model calculations of SNe, HNe, PISNe, and SNe combined with HNe.

Type	Z	$M/M_{\odot}$	E/E_{51}	Ref.[a]
SNe	0	13, 15, 18, 20, 25, 30, 40	1, 1, 1, 1, 1, 1, 1	1
	0.001	13, 15, 18, 20, 25, 30, 40	1, 1, 1, 1, 1, 1, 1	1
	0.004	13, 15, 18, 20, 25, 30, 40	1, 1, 1, 1, 1, 1, 1	1
	0.02	13, 15, 18, 20, 25, 30, 40	1, 1, 1, 1, 1, 1, 1	1
HNe	0	20, 25, 30, 40	10, 10, 20, 30	1
	0.001	20, 25, 30, 40	10, 10, 20, 30	1
	0.004	20, 25, 30, 40	10, 10, 20, 30	1
	0.02	20, 25, 30, 40	10, 10, 20, 30	1
SNe+HNe	0	0.07−50		1
	0.001	0.07−50		1
	0.004	0.07−50		1
	0.02	0.07−50		1
PISNe	0	150, 170, 200, 270		2

[a] References: (1) Kobayashi et al. (2006); (2) Umeda & Nomoto (2002)

Table 7.3.: Abundances of 20 EMP stars. This sample was compiled from literature, where only *unmixed* extremely metal-deficient stars with abundances for C and N from Spite et al. (2006), and O to Zn from Cayrel et al. (2004) were used. Additionally, the two HMP stars HE 0107−5240 (Christlieb et al. 2002) and HE 1327−2326 (Frebel et al. 2005) were added. Note that the different authors do, unfortunately, not refer to one and the same set of solar abundances.

Star	[C/H]	[N/H]	[O/H]	[Ne/H]	[Na/H]	[Mg/H]	[Al/H]	[Si/H]	[K/H]	[Ca/H]	[Sc/H]	[Ti/H]	[Cr/H]	[Mn/H]	[Fe/H]	[Co/H]	[Ni/H]	[Zn/H]
BD−18 5550	−3.08	−3.42	−2.64		−3.01	−2.75	−3.65	−2.67	−2.54	−2.65	−3.02	−2.91	−3.40	−3.44	−3.06	−2.87	−3.11	−2.84
BS 16467−062	−3.52				−3.94	−3.61	−4.67	−3.35	−3.34	−3.42	−3.76	−3.48	−4.18	−4.32	−3.77	−3.22	−3.69	−3.54
BS 16477−003	−3.07				−3.29	−3.08	−3.96	−2.86	−2.89	−3.98	−3.35	−3.08	−3.73		−3.36	−2.99	−3.33	−3.18
CS 22172−002	−3.86	−3.62			−4.21	−3.66	−4.66	−3.45	−3.41	−3.49	−3.97	−3.62	−4.27	−4.45	−3.86	−3.39	−4.01	−3.37
CS 22189−009	−3.15	−3.22			−3.79	−3.38	−4.41	−3.20	−3.09	−3.29	−3.49	−3.41	−3.91	−3.74	−3.49	−3.12	−3.43	−3.03
CS 22885−096	−3.52	−3.52			−3.84	−3.59	−4.57	−3.26	−3.44	−3.43	−3.41	−3.45	−4.26	−4.32	−3.78	−3.30	−3.78	−3.34
CS 22892−052	−2.11	−2.52	−2.56	−2.98		−2.81	−3.77	−2.60	−2.59	−2.71	−3.05	−2.88	−3.35	−3.51	−3.03	−2.92	−3.24	−2.83
CS 22896−154	−2.46	−2.92	−1.75		−2.57	−2.61	−3.45	−2.15	−2.24	−2.33	−2.56	−2.39	−2.92	−3.27	−2.69	−2.31	−2.74	−2.43
CS 22897−008	−2.83	−3.17			−3.57	−3.15	−4.14	−3.00	−2.96	−3.12	−3.39	−3.19	−3.79	−3.63	−3.41	−2.99	−3.34	−2.74
CS 22953−003	−2.52	−2.72	−2.09		−2.69	−2.71	−3.82	−2.59	−2.63	−2.62	−2.85	−2.71	−3.24	−3.20	−2.84	−2.67	−2.92	−2.69
CS 22956−050	−3.06	−3.02				−2.96	−3.98	−2.55	−3.04	−2.87	−3.37	−3.01	−3.67	−3.84	−3.33	−2.94	−3.32	−3.03
CS 22966−057	−2.56	−2.52	−1.63		−2.15	−2.50	−3.48	−2.05	−2.21	−2.26	−2.56	−2.32	−2.81	−3.06	−2.62	−2.25	−2.49	−2.36
CS 22968−014	−3.30	−3.32	−2.66		−3.92	−3.36	−4.34	−3.35	−3.34	−3.53	−3.52	−3.50	−4.01		−3.56	−3.00	−3.34	−3.14
CS 29495−041	−2.86	−2.42	−2.14		−2.58	−2.49	−3.48	−2.25	−2.28	−2.44	−2.71	−2.59	−3.17	−3.31	−2.82	−2.60	−2.87	−2.67
CS 29502−042	−3.03	−3.62			−3.64	−2.96	−4.00	−2.90	−2.89	−2.97	−3.00	−2.94	−3.56	−3.75	−3.19	−2.83	−3.25	−3.00
CS 29516−024	−3.10	−3.82	−2.44		−2.70	−2.58	−3.65	−2.50		−2.51		−2.83	−3.37	−3.50	−3.06	−2.81	−3.21	−2.86
CS 30325−094	−3.28	−3.12	−2.58		−3.21	−2.92	−3.88	−2.49	−2.57	−2.92	−2.97	−3.02	−3.74	−3.85	−3.30	−3.01	−3.22	−3.06
CS 31082−001	−2.68	−3.42	−2.31		−2.63	−2.54	−3.64	−2.66	−2.25	−2.49	−2.89	−2.62	−3.24	−3.41	−2.91	−2.64	−2.88	−2.72
HE 0107−5240	−1.28	−3.00			−4.47	−5.13				−5.37		−5.64			−5.39		−5.65	
HE 1327−2326	4.10	4.50			2.50	1.70	1.30					0.60			−5.60			

Table 7.4.: Metal abundances of 59 DLA systems compiled from literature and listed with increasing [Fe/H] ratios. Note that the different authors do, unfortunately, not refer to one an the same set of solar abundances.

QSO	z_{abs}	log N(H I)	[C/H]	[N/H]	[O/H]	[Mg/H]	[Al/H]	[Si/H]	[S/H]	[Cr/H]	[Fe/H]	[Zn/H]	Ref.[a]
Q0913+072	2.618	20.36	−2.83	−3.48	−2.47		−3.01	−2.57			−2.77		21
Q2206−199N	2.076	20.43			−1.94			−2.31			−2.61		8,12
Q1946+7658	2.843	20.27		−3.61	−2.19			−2.23			−2.53		8,10
Q1409+095	2.456	20.54			−2.13			−2.01			−2.30		12
Q2348−14	2.279	20.56						−1.92	−2.03		−2.24		8,10
Q2348−01	2.615	21.30						−1.97		−2.30	−2.23		8
BRI1202−0725	4.383	20.60						−1.77			−2.22		2,4
Q2237−0608	4.080	20.52						−1.81			−2.17		2,4
BRI1108−07	3.608	20.50						−1.80			−2.12		8
HE0001−2340	2.618	20.36	−1.76	−3.50	−1.81	−2.05	−2.11	−1.81			−2.12		20
MC1331+170	1.776	21.18		−1.82				−1.45		−1.97	−2.06	−1.30	8,10
J0255+00	3.915	21.30							−1.78		−2.05		8
Q0000−2620	3.390	21.41		−2.61	−1.73			−1.91	−1.91	−2.00	−2.04	−2.07	6
Q1354+258	1.420	21.54						−1.74		−1.82	−2.02	−1.63	16
BRJ0307−4945	4.466	20.67		−3.02	−1.50			−1.54			−1.97		7
Q0100+13	2.309	21.40		−1.96				−1.37	−1.40	−1.69	−1.93	−1.62	8,4
HS0741+4741	3.017	20.48		−2.44				−1.69	−1.68		−1.93		8,10
Q2359−02	2.154	20.30						−1.58		−1.37	−1.88		8
PSS0957+33	4.178	20.50						−1.50	−1.31		−1.87		8
B2314−409	1.874	20.10						−1.87			−1.87		9
Q1223+17	2.466	21.50		−2.60				−1.59		−1.68	−1.84	−1.62	8,10
Q2344+124	2.538	20.36		−2.51				−1.74			−1.83		8,10
Q0336−01	3.062	21.20							−1.41		−1.79		8,10
Q0149+33	2.141	20.50						−1.49		−1.45	−1.77	−1.67	8
PKS0458−020	2.040	21.65								−1.50	−1.77	−1.19	8
Q0841+129	2.476	20.78		−2.59				−1.39	−1.39	−1.61	−1.75	−1.40	8,19
GC1215+3322	1.999	20.95						−1.48		−1.52	−1.70	−1.29	8
Q0347−38	3.025	20.62		−1.67	−0.73			−1.17		−1.88	−1.69	−1.50	3,10
Q2359−02	2.095	20.70						−0.78		−1.55	−1.65	−0.77	8
Q1232+0815	2.338	20.80		−2.10				−1.18	−1.17		−1.59		19
Q0841+129	2.375	20.95		−2.26				−1.27	−1.38	−1.55	−1.58	−1.51	8,19
HE1104−1805	1.662	20.85		−1.74	−0.79			−1.03		−1.47	−1.58	−1.04	15
Q0013−004	1.973	20.83						−0.95	−0.74	−1.52	−1.51	−0.75	18
BR1117−1329	3.350	20.84						−1.26		−1.36	−1.51	−1.18	13
PSS0957+33	3.279	20.32						−1.00			−1.45		8
J0255+00	3.253	20.70						−0.94			−1.44		8
Q0201+1120	3.386	21.26		−1.86					−1.25		−1.40		5
Q0836+11	2.465	20.58						−1.15			−1.40		8
Q2231−0015	2.066	20.56						−0.87		−1.06	−1.40	−0.88	8
Q2348−01	2.426	20.50						−0.69			−1.39		8
Q1425+6039	2.827	20.30		−1.53							−1.33		10
B2314−409	1.857	20.90						−1.05	−1.00	−1.21	−1.32	−1.04	9
PKS0528−2505	2.141	20.70		−2.05				−1.00	−1.07	−1.29	−1.26		2,19
PKS0528−2505	2.811	21.20						−0.76	−0.84	−1.24	−1.25	−0.78	2,19
HE2243−6031	2.330	20.67		−1.72	−0.68			−0.87	−0.85	−1.12	−1.25	−1.12	11
GB1759+7539	2.625	20.80		−1.53				−0.82	−0.76	−1.26	−1.21		8,10
Q0302−223	1.009	20.36						−0.74		−0.97	−1.19	−0.58	1
Q2343+1230	2.431	20.35		−1.60				−0.65	−0.83		−1.19	−0.57	4,17

Table 7.4.: Metal abundances of 59 DLA systems (continued)

QSO	z_{abs}	log N(H I)	[C/H]	[N/H]	[O/H]	[Mg/H]	[Al/H]	[Si/H]	[S/H]	[Cr/H]	[Fe/H]	[Zn/H]	Ref.[a]
LBQS2230+0322	1.864	20.85						−0.75		−1.12	−1.17	−0.72	8
Q1210+17	1.892	20.60						−0.87		−1.00	−1.15	−0.90	8
Q0216+0803	2.293	20.45						−0.56			−1.06		2
Q0454+039	0.860	20.69						−0.80		−0.89	−1.02	−1.03	1
Q1351+318	1.149	20.23						−0.56		−0.94	−0.99	−0.38	16
Q0216+0803	1.769	20.00						−0.67			−0.97		2
Q0551−366	1.962	20.50						−0.44	−0.32	−0.92	−0.95	−0.15	14
Q0201+36	2.463	20.38						−0.41		−0.80	−0.87	−0.29	8,10
Q2206−19	1.920	20.65						−0.42		−0.68	−0.86	−0.41	8
QXO0001	3.000	20.70		−3.22	−1.67			−1.81					10
Q0930+2858	3.235	20.18		−2.29					−1.71				4

[a] References: (1) Pettini et al. (2000); (2) Lu et al. (1996); (3) Levshakov et al. (2002b); (4) Lu et al. (1998); (5) Ellison & Lopez (2001); (6) Molaro et al. (2001); (7) Dessauges-Zavadsky et al. (2001); (8) Prochaska et al. (2001); Ellison & Lopez (2001, 2002); (10) Prochaska & Wolfe (2002); (11) Lopez et al. (2002); (12) Pettini et al. (2002); (13) Péroux et al. (2002); (14) Ledoux et al. (2002); (15) Lopez et al. (1999); (16) Pettini et al. (1999); (17) Dessauges-Zavadsky et al. (2002); (18) Petitjean et al. (2002); (19) Centurión et al. (2003) (20) Richter et al. (2005); (21) Erni et al. (2006)

7.2.3. Results and Interpretation

Fig. 7.4 and 7.5 summarize the comparison of metal abundance patterns from DLA systems and EMP stars, respectively, with yields from numerical model calculations. From Fig. 7.5 we can see clearly that abundance patterns of EMP stars match better with yields from model calculations than this is the case for the DLA sample. This does not come as a big surprise to us because it in model calculations is common to EMP stars as calibrators, for fine-tuning parameter adjustment, or, more indirectly, as a cross-check for the calculation outcome. Further, EMP stars and especially HMP stars with their extremely low overall metallicity are clearly prime candidates for objects that have preserved the abundance pattern left by the very first stars. Spite et al. (2006) convincingly argue that the surface composition of unmixed EMP stars has preserved the metal abundance patter of the protostellar gas cloud, out of which they have formed. The longevity and the extreme metal underabundance found in EMP stars clearly makes them very accurate reference objects for the determination of the metal pollution from Pop III stars to the pristine gas from the Big Bang.

The wealth of high-quality data available from high-resolution spectrographs like UVES on VLT/UT2 or HIRES installed on the Keck telescope has led to the discovery of very metal-deficient QAL systems. The combination of a very

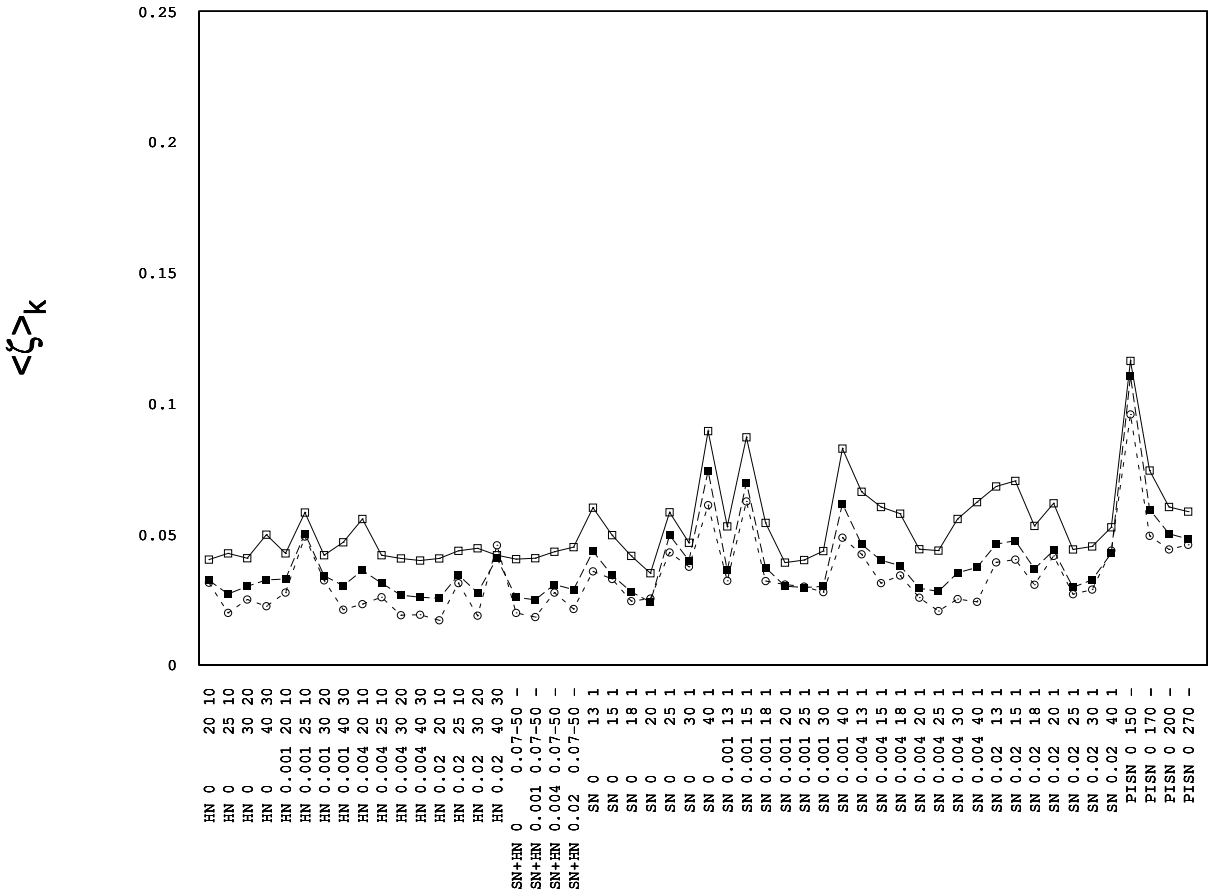

Figure 7.4.: Comparing metal abundances from QAL systems with yields from model calculations. We test the consistency, measured by ζ, of the individual abundance pattern. $< \zeta >_{\rm k}$ indicates the averaged sum over k individual QAL systems, when compared with yields from model calculations: first 10 most metal-deficient DLA systems from Table 7.4 (open squares), first 25 most metal-deficient DLA systems (filled squares), and all 59 DLA systems (open circles). On the x-axis, we indicate the explosion mechanism (HN, SN and HN with a Salpeter IMF, SN, and PISN), the star's metallicity, the explosion mechanism in E_{51}, and the star's mass in $M_{\odot}$.

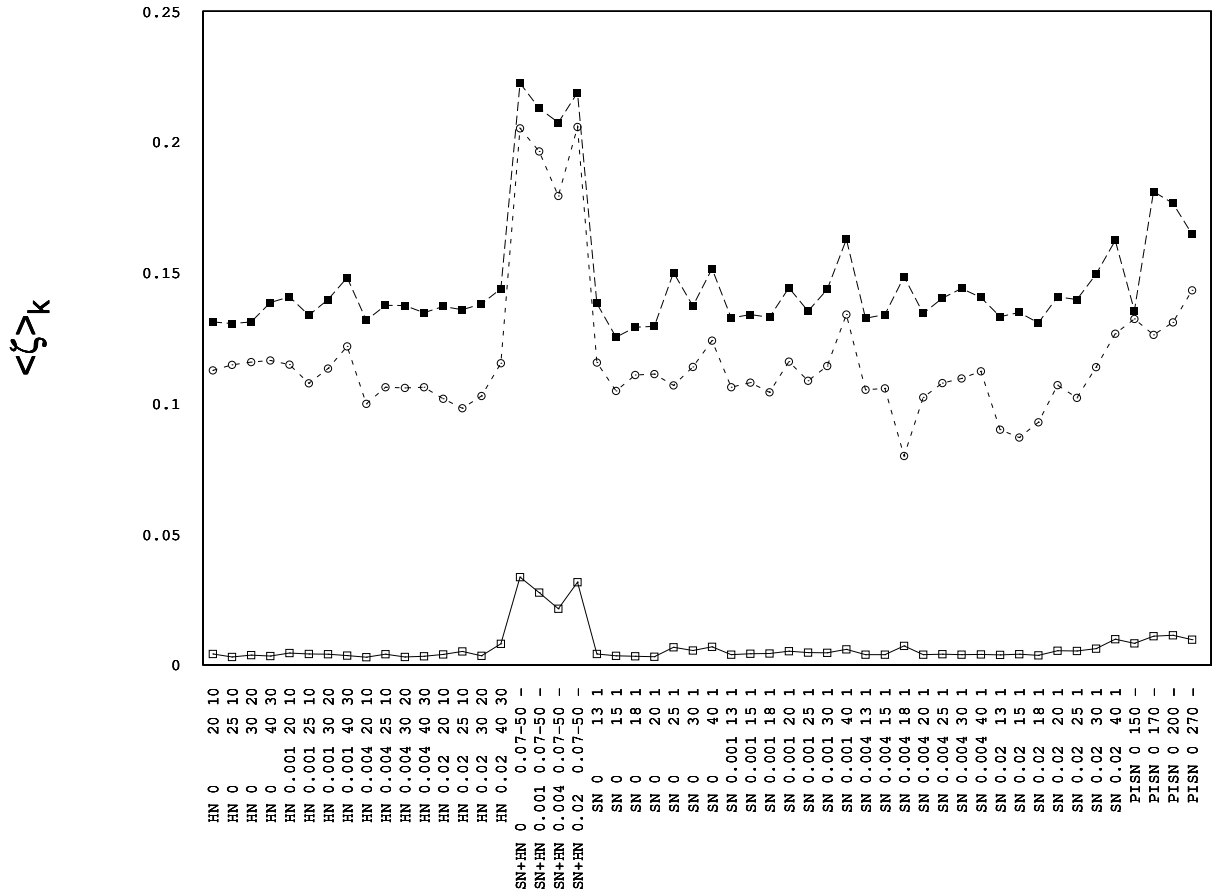

Figure 7.5.: Comparing metal abundances from EMP stars with yields from model calculations. We test the similarity, measured by ζ, of the individual abundance pattern. $< \zeta >_{\rm k}$ indicates the averaged sum over k individual EMP stars, when compared with yields from model calculations: set of 18 *unmixed* EMP stars from Table 7.3 (open squares), HMP star HE 0107−5240 (filled squares), HMP star HE 1327−2326 (open circles). On the x-axis, we indicate the explosion mechanism (HN, SN and HN with a Salpeter IMF, SN, and PISN), the star's metallicity, the explosion mechanism in E_{51}, and the star's mass in $M_{\odot}$.

low overall metallicity and the detection of key elements such as, e.g., nitrogen, carbon[26], and oxygen, justifies the assumption that QAL systems might have preserved the abundance pattern left by the very first stars, too. Thus, QAL systems offer a complementary approach to assess the validity and accuracy of results from theory and simulation of Pop III stars.

Fig. 7.4 and 7.5 further indicate some additional interesting trends:

- One might expect that the most metal-deficient DLA systems would match yields from zero-metallicity S/HNe or PISNe better that DLA systems with a higher metal content. We see that this is not the case and that the three different samples of DLA systems show rather an inverse behavior. However, we observe a common trend in those three samples.

- The abundance pattern preserved in the 18 unmixed EMP stars clearly does not match with the abundances that were computed for a combination of SNe and HNe with a Salpeter IMF and a mass range of $0.07 - 50 M_{\odot}$. Astonishingly, the same behavior holds for the two HMP stars, too. The reason for this is that the IMF weighted yields from Kobayashi et al. (2006) do produce too much carbon but not enough sodium when compared to the HMP star abundances.

- The resemblance of the abundance pattern found in EMPS stars is clearly better than this is the case for DLA systems. We see that the abundance pattern of the two HMP stars are very particular but also very similar. The reason for this offset is the lower number of detected elements in HMP stars but also the fact that HMP stars apparently are rather different objects when compared to EMP stars.

Abundance Trends

Silicon is the most common α-element measured in DLA systems. Although silicon is a refractory element, its abundance is only mildly affected in lightly depleted regions (Prochaska & Wolfe 2002). Therefore, the observed silicon column densities in DLA systems – that have generally a very low dust content and are not significantly or only weakly affected by photoionization – should nearly reflect the total amount of silicon present in the gas cloud. Additionally,

[26]Carbon is very frequently detected in DLA systems but there exist only very few C/H measurements for DLA systems. This is because the C II λ1334 line is in most cases heavily saturated.

as an α-element, silicon is a good tracer for the overall metallicity of a DLA system.[27] When plotting the occurrence of DLA systems as a function of their H I content (Fig.7.6) we note that the distribution is bell-shaped with a maximum at $\log N(\mathrm{H\,I}) \sim 20.5$. We observe a discontinuity at $\log N(\mathrm{H\,I}) \sim 21.1$. The origin of this discontinuity is not known and should, however, not be overemphasized because this might be an effect due to low-number statistics. When compared to the overall metallicity in DLA systems (as given by the silicon abundance, see Fig. 7.7) we note that there seem to be two distinct groups: very metal-poor DLA systems at $[\mathrm{M/H}] \approx [\mathrm{Si/H}] \lesssim -2$ that are rare, and DLA systems with a higher metal content, $[\mathrm{M/H}] \approx [\mathrm{Si/H}] \gtrsim -2$, that are clearly more frequent. Silicon is produced in massive stars ($M > 8\,M_{\odot}$) that have used their carbon fuel and ignite oxygen, neon, and magnesium burning. Silicon is efficiently produced in PISNe and we note only a slightly increasing silicon production with increasing metallicity when comparing to model calculations of H/SNe from Kobayashi et al. (2006). Hence, the apparent decline in frequency of DLA systems below $[\mathrm{Si/H}] \approx -2$ is likely to be associated with the SFR. This assumption is supported by Fig. 7.8 which shows a decline in $[\mathrm{Si/H}]$ with increasing redshift. Following this reasoning, we presume high starformation activity at $z \sim 2-3$. This is in good agreement with the results of optical surveys (Madau et al. 1996) or with the star-formation rate density derived from the UV luminosity density (Ferguson 2000).

When comparing DLA systems, EMP stars, and yields from nucleosynthesis model calculations as a function of the object's metal content, i.e., as a function of the $[\mathrm{Si/H}]$ ratio, we find a good and general agreement between DLA systems and EMP stars. For example, in Fig. 7.11 we note that the trend of a decreasing $[\mathrm{Fe/O}]$ ratio with increasing metallicity in EMP stars is also observed in DLA systems. The fact that PISNe produce more oxygen but less nitrogen when compared to Type II SNe ($1\,E_{51}$, $Z = 0$, and $15\,M_{\odot}$) is clearly seen in Fig. 7.10. We further observe an almost constant $[\mathrm{N/O}]$ ratio in function of Si for the case of EMP stars, and especially for the case of DLA systems.

An other interesting fact is that the $[\mathrm{C/O}]$ ratio observed in EMP stars can be well explained by PISNe as well as by Type II SNe ($1\,E_{51}$, $Z = 0$, and $15\,M_{\odot}$). In Fig. 7.9 we see an increasing $[\mathrm{C/O}]$ ratio with decreasing metallicity. This trend, at first sight, does not go along with the results from standard models

[27] Note, however, that silicon is also produced in non-negligible amounts in SNe Ia. Other α-elements produced by massive stars, such as oxygen, magnesium, or sulfur, would be more suitable (especially oxygen). However, those elements are only rarely detected in DLA systems, or their lines are saturated.

for the chemical evolution of the solar vicinity that predict a drop of [C/O] with increasing metallicity because of the carbon contribution from yields from massive stars with mass loss and from the delayed release of carbon from stars of low and intermediate mass (where the former is always the dominant factor). In fact, [C/O] drops by a factor of about $3-4$ as the metallicity decreases from solar to $\sim {}^{1}/_{10}$ solar. Akerman et al. (2004) report new measurements with UVES/VLT of carbon and oxygen abundances in 34 F and G dwarf and subgiant stars belonging to the halo population with [Fe/H] $= -0.7$ to -3.2. They find for low metallicities ([O/H] < -1) that [C/O] does not remain constant at [C/O] ~ -0.5 (as previously thought) but increases again (possibly approaching near-solar values at very low metallicities of [O/H] ~ -3), i.e. the trend we observe in Fig. 7.9. The authors note that there is no more than a $3\,\sigma$ effect seen in their sample and that this may be due to metallicity-dependent non-LTE corrections to the [C/O] ratio which have not been taken into account. However, this observed trend below [O/H] $= -1$ is of potential importance to the nucleosynthesis by Pop III stars. In a recent work Chieffi & Limongi (2002) presented model calculations for metal-free stars that successfully can reproduce the observed behavior, particularly if the IMF of Pop III stars was top-heavy.

We conclude that it is difficult to identify a clear signature in the abundance pattern of DLA systems (and EMP stars, too) that would allow us to give clear borderlines for the kind of stars and their explosion mechanisms that have enriched early objects such as very metal-deficient DLA systems or EMP/HMP stars.

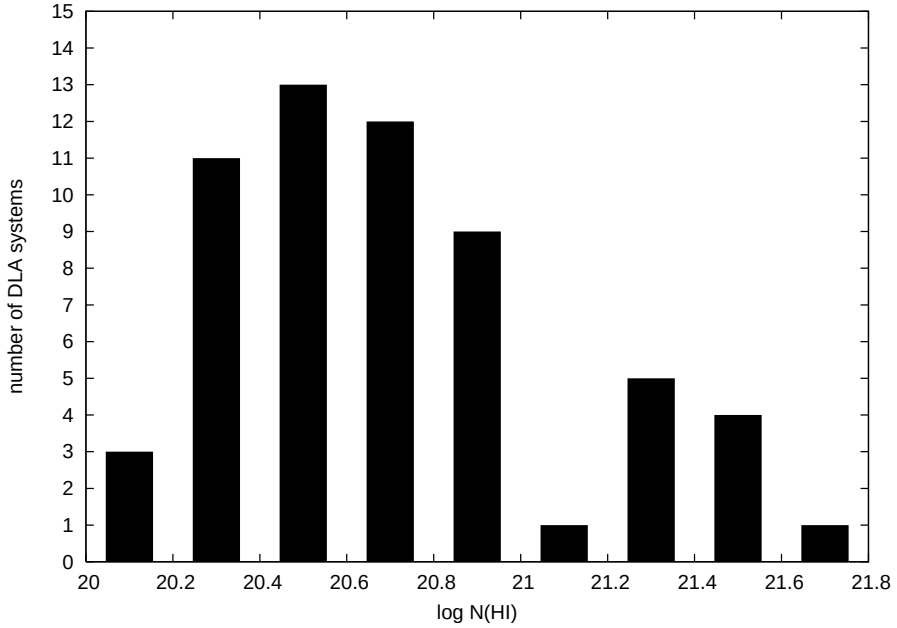

Figure 7.6.: The occurrence of DLA systems as a function of their H I content.

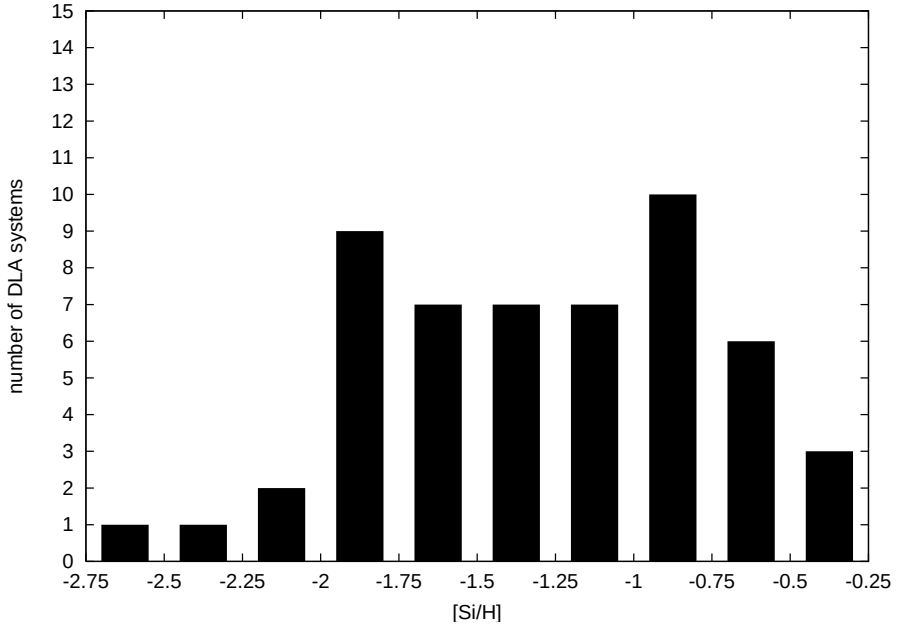

Figure 7.7.: The silicon abundance in DLA systems as a measure of their metallicity.

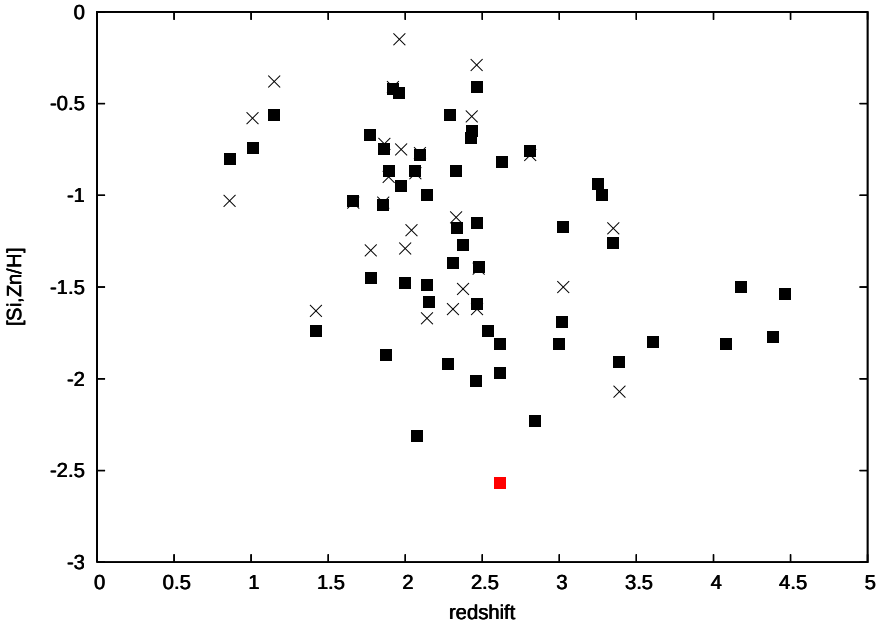

Figure 7.8.: Redshift-silicon (squares) and redshift-zinc (crosses) relation in DLA systems, where the [Si/H] abundance of the DLA system toward Q 0913+072 is plotted in red.

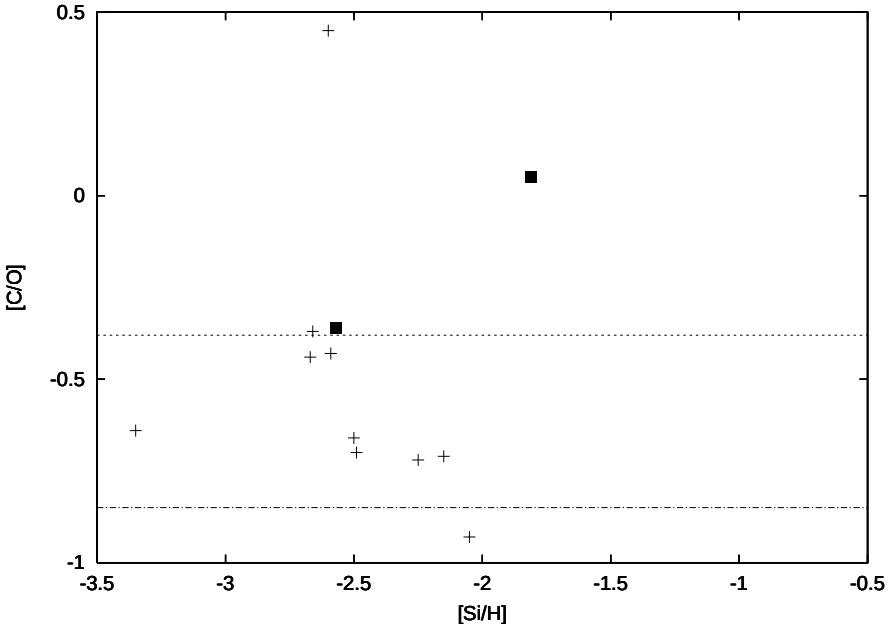

Figure 7.9.: [C/O] ratios of DLA systems (squares) and EMP stars (crosses) as a function of [Si/H]. Additionally, the [C/O] ratios for a core-collapse SN with $1\,E_{51}$, $Z = 0$, and $15\,M_{\odot}$ (dashed line) and a PISN with $200\,M_{\odot}$ (dash-dotted line) are shown.

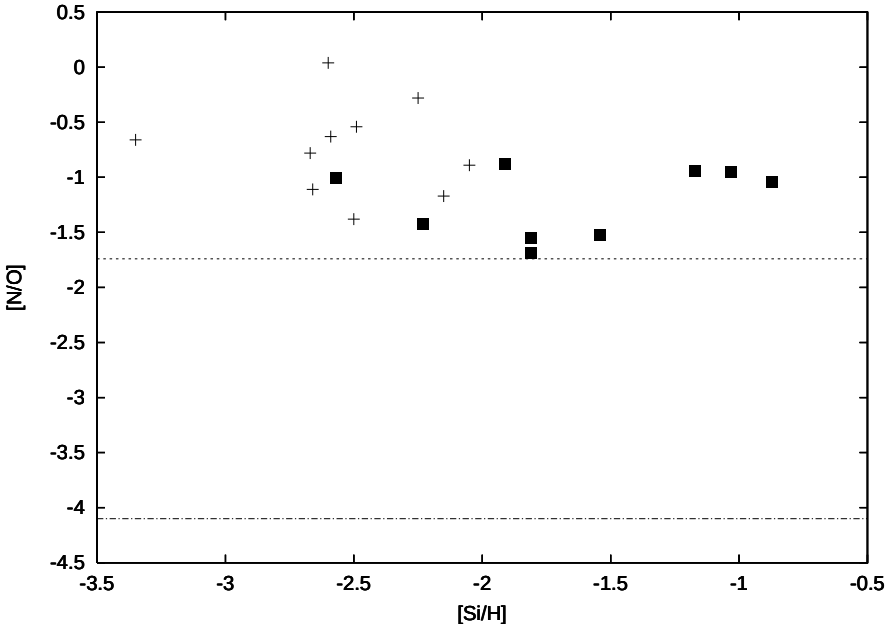

Figure 7.10.: [N/O] ratios of DLA systems (squares) and EMP stars (crosses) as a function of [Si/H]. Additionally, the [N/O] ratios for a core-collapse SN with $1\,E_{51}$, $Z = 0$, and $15\,M_{\odot}$ (dashed line) and a PISN with $200\,M_{\odot}$ (dash-dotted line) are shown.

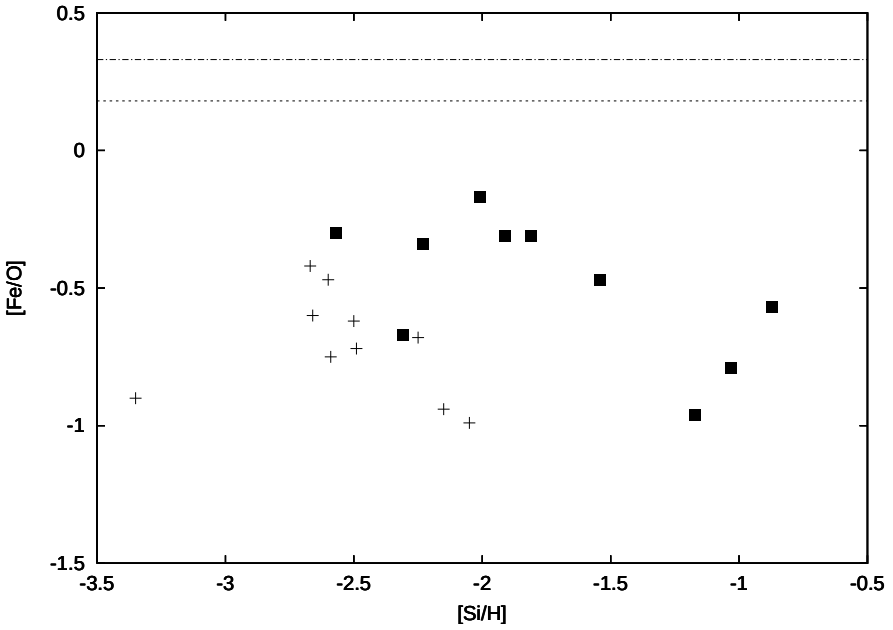

Figure 7.11.: [Fe/O] ratios of DLA systems (squares) and EMP stars (crosses) as a function of [Si/H]. Additionally, the [Fe/O] ratios for a core-collapse SN with $1\,E_{51}$, $Z = 0$, and $15\,M_{\odot}$ (dashed line) and a PISN with $200\,M_{\odot}$ (dash-dotted line) are shown.

8. The Line of Sight toward Q0420−388: Absorption Signatures of Merging Galaxies at High Redshift

8.1. Introduction

QAL systems with large hydrogen column densities ($N(\mathrm{HI}) \sim 10^{20}\,\mathrm{cm}^{-2}$) are most suitable for studies of the chemical evolution at high redshift (e.g., Péroux et al. 2003; Richter et al. 2005). In this study we present a particularly interesting case of two interacting sub-DLA absorption line systems at $z = 3.088$ toward the background quasar Q 0420−388. The two absorption line systems are only separated by $161\,\mathrm{km\,s}^{-1}$ ($\Delta z = 0.0005$) and are manifestly different in their structure and their metal content. While one of these two absorption line systems shows a metal content of 5 % solar and a clear structure with six individual subcomponents, we can identify in the other system (almost) no substructure but a metal content of 35 % solar. Additionally, this LOS offers one of the rare opportunities to measure the deuterium abundance at high redshift. Even though primordial the D/H ratio is nowadays determined by measurements of the comic microwave background (CMB) radiation, it is important to study the deuterium abundance also directly and independently from CMB measurements. The deuterium abundance we derive is in very good agreement with the predictions from the standard big bang nucleosynthesis model and other measurements. Further, we detect highly ionized species in-between the two absorption line systems, most likely related to collisionally ionized gas. This suggests that we are presumably witnessing the merging of two early galaxies at high redshift.

8.2. The Line of Sight toward Q 0420−388

The LOS toward the quasar Q 0420−388 ($V = 16.^{\mathrm{m}}92$, $z_{\mathrm{em}} = 3.12$) has been previously observed and analyzed by several groups (Carswell et al. 1996; Chernomordik 1995; Hoell & Priester 1991; Varshni 1989; Chernomordik 1988; Glass 1980; Wright & Kleinmann 1978). The data used by Carswell et al. (1996) were obtained using the echelle spectrographs at the Cerro Tololo Inter-American Observatory (CTIO) 4 m telescope, Chile, and the Anglo-Australian Telescope (AAT) 4 m telescope, Australia. They cover a wavelength range of $3600 - 6025$ Å with a resolution varying from $8 - 13\,\mathrm{km\,s^{-1}}$. We estimate the SNR per pixel element of their data to be on the order of 8 to 10 (this information is not provided by the authors). The data were analyzed using multicomponent Voigt-profile fitting. For the absorbing complex at $z = 3.086$[1] they estimate a D/H ratio of $\log(\mathrm{D/H}) = -3.9 \pm 0.4$ and a metallicity of $\sim {}^{1}/_{10}$ solar.

8.3. Observations and Data Handling

The data used in this study were obtained with UVES/VLT as part of the ESO-VLT Large Programme "The Cosmic Evolution of the IGM" (Bergeron et al. 2004), which aims at providing a homogeneous data set of high-resolution ($R \sim 45\,000$), high signal-to-noise ratio (SNR > 30) spectral data for QSO absorption line spectroscopy of the IGM in the redshift range between $z = 2.2 - 4.5$.

Q 0420−388 was observed through a $1''$-slit, mostly during dark time, with a seeing of typically 0.8, and with two different setups, using dichroic beam splitters for the blue and the red arm (DIC #1 with B346 and R580, and DIC #2 with B437 and 860, respectively). This setup provides a wavelength coverage from $3050 - 10\,400$ Å, with small gaps near 5750 Å and 8550 Å. The total integration time (DIC #1 + DIC #2) for Q 0420−388 was 12 h. The raw data was reduced using the UVES pipeline implemented in the `ESO-MIDAS` software package. The pipeline reduction includes flat-fielding, bias- and sky-subtraction, and a relative wavelength calibration. The individual spectra then have been coadded and corrected to air wavelengths[2]. The SNR in the spectrum generally is very high and attains a maximum of 190 per resolution element. The spectrum was analyzed using the `FITLYMAN` program (Fontana & Ballester 1995) implemented

[1] identical with complex C in this study

[2] The International Astronomical Union (IAU) standard for conversion from air to vacuum wavelengths is given in Morton (1991). It is $\lambda_{\mathrm{air}} = \lambda_{\mathrm{vac}} \left(1.0 + 2.735182 \times 10^{-4} + \frac{131.4182}{\lambda_{\mathrm{vac}}^2} + \frac{2.76249 \times 10^8}{\lambda_{\mathrm{vac}}^4}\right)$.

in the ESO-MIDAS software package. The routine uses a χ^2-minimization algorithm for multi-component Voigt-profile fitting. Simultaneous line fitting of the high-resolution spectrum allows us to determine the column density, N, and the Doppler parameter, b, with high accuracy.

In Fig. 8.1 a representative portion of the UVES spectrum of Q 0420−388 in the wavelength range between 4900 Å and 5100 Å is shown. Redward of the QSO H I Ly α emission we identify two sub-DLA systems (with $\log N_{\rm B}({\rm HI}) = 19.10$ and $\log N_{\rm C}({\rm HI}) = 19.25$, respectively) that are superimposed in one big H I Ly α trough.

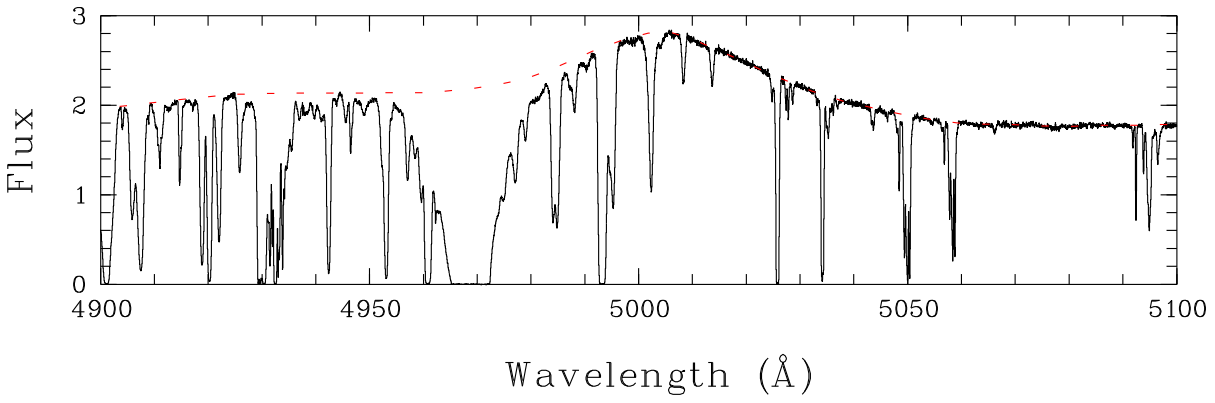

Figure 8.1.: A section from the UVES/VLT spectrum toward the quasar Q 0420−388 is shown. The quasar's H I Ly α emission at 5008.5 Å ($z_{\rm em} = 3.12$) as well as two close-by sub-DLA systems, superimposed in one big H I Ly α trough, at 4969.7 Å ($z_{\rm abs} = 3.088$) can be clearly identified. The dashed line shows the continuum placement used in this study.

The b values are assumed to be composed of a thermal component, b_{th}, and a non-thermal, turbulent component, $b_{\rm turb}$, in the way that $b^2 = b_{\rm th}^2 + b_{\rm turb}^2$. Note that we can assume for this analysis that $b_{\rm th}^2 \ll b_{\rm turb}^2$. However, this assumption has to be kept in mind for the case of complex D (the merging zone between the two main absorption lines systems), where the gas might be ionized through collisional ionization processes (see Section 8.4.6).

8.4. Metal Abundance Measurements

8.4.1. Velocity-Component Structure

We have used an absorption-component model consisting of four main absorbers, named complex A, B, C, and D, with one (A_1), two (B_1, B_2), six (C_1,..., C_6), and one (D_1) velocity sub-components, respectively (see Table 8.1). The two most dominant absorption line systems are complex B and complex C, with $\log N_{\rm B}({\rm HI}) = 19.10 \pm 0.10$ at $+16\,{\rm km\,s^{-1}}$ and $\log N_{\rm B}({\rm HI}) = 19.25 \pm 0.10$ at $-145\,{\rm km\,s^{-1}}$, respectively. The strong C II λ 1334 line suggests that there are, next to complex B and C, also two weaker absorbing systems, in the following referred to as complex A and complex D (Fig. 8.2).

Table 8.1.: We detect four absorption line systems with different radial velocities, named complex A, B, C, and D, respectively. Complex B and C show substructure and hence are further subdivided into two and six components, respectively. The indicated velocities are with respect to a velocity restframe at $z = 3.088$ (used throughout this chapter), where we indicate with $\overline{v}$ the mean velocity weighted by column density.

complex	component	v [km s^{-1}]	$\overline{v}$ [km s^{-1}]	$\log N$(HI)	b [km s^{-1}]
A			+95	16.81 ± 0.10	27
B			+16	19.10 ± 0.10	17
	B_1	+22			
	B_2	+12			
D			−42	≥ 17.3	28
C			−145	19.25 ± 0.10	26
	C_1	−92			
	C_2	−104			
	C_3	−121			
	C_4	−139			
	C_5	−157			
	C_6	−174			

Complex A is found also in H I absorption, distinctively constricted by the the red side of the Lyman trough and in Ly ι and Ly κ by some remaining flux (in the following referred to as "bump") within the Lyman trough (Fig. 8.3).

Complex B and C alone cannot entirely explain the H I Ly absorption because a significant amount of flux within the trough would remain if only those two components were considered. We therefore introduce an auxiliary absorber,

named complex D, at $-42\,\mathrm{km\,s^{-1}}$. This is manifestly justified by the corresponding absorption seen in the C II λ 1334 line (Fig. 8.2).

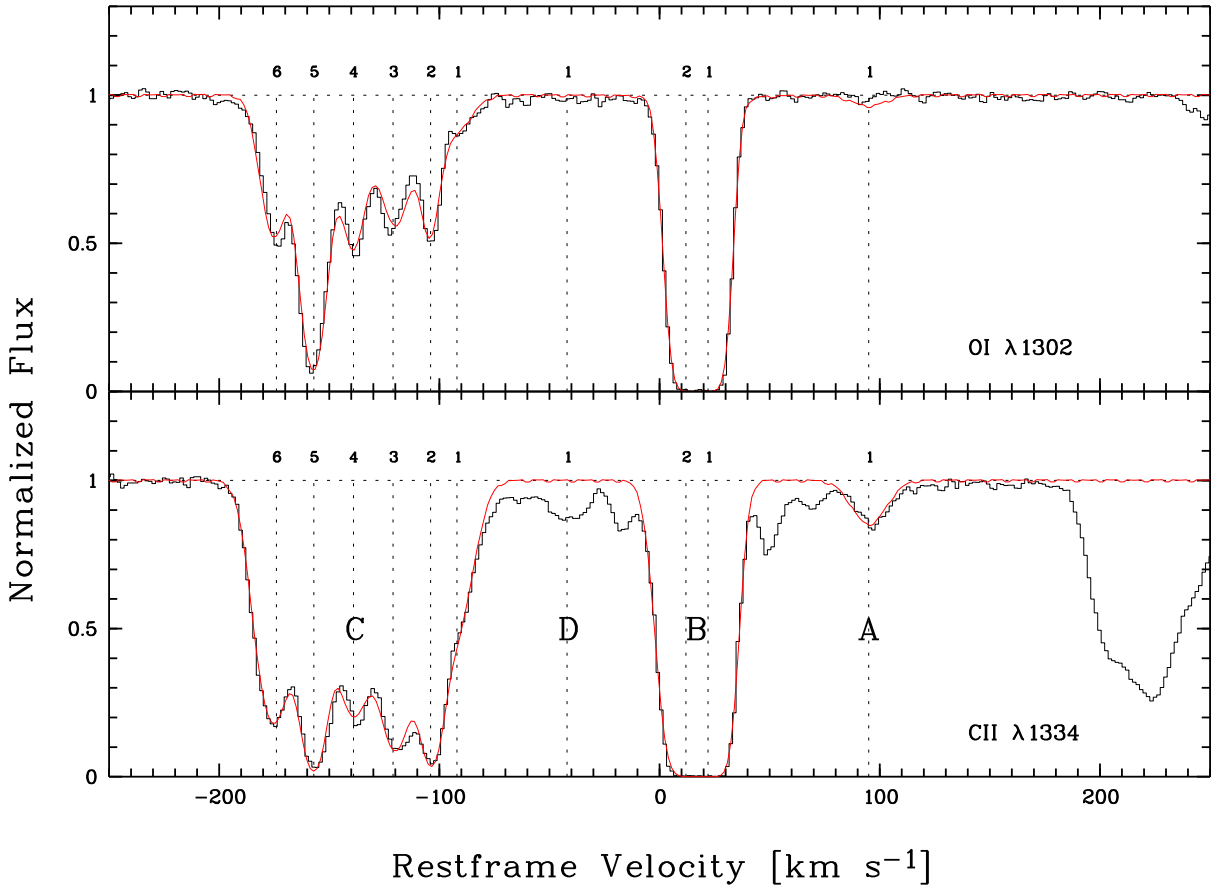

Figure 8.2.: The model that we have adopted for this study: four main absorbers, named complex A, B, C, and D, with one (A_1), two (B_1, B_2), six (C_1,..., C_6), and one (D_1) sub-components, respectively. Please note that this plot is an illustrative plot to indicate the velocity-component structure. No results are drawn from the fit shown.

8.4.2. Neutral Hydrogen Measurements

The H I Lyman lines were fitted by four components, i.e., by approximating complex A, B, C, and D, each by one component only. This assumption is appropriate because the true (smaller) *b* values might lead only to an insignificant overestimation of the true column densities, and it is necessary, because the spectrum does not provide an informative basis that would allow us to fit the H I Lyman lines with more components.

The velocity center of complex C is a for column density weighted mean derived from the measured subcomponent centers of the O I λ 1302 line. With this and the well defined blue borders of the Lyman troughs in Ly α, Ly δ, Ly ε, Ly ζ, Ly η, Ly κ, and Ly ι, we are able to precisely determine the neutral hydrogen column density of complex C (see Fig. 8.3). The fitting of complex A was, due to the "bump" in Ly ι and Ly κ, straightforward. For the H I fitting of complex B, we used the red side of the "bump" in Ly ι and Ly κ, and the blue side of the Ly α trough. Finally, the (auxiliary) complex D was chosen as an upper limit in order to reduce the flux in the Lyman trough to zero. The upper limit, i.e., the maximum amount of H I possibly within complex D, is $\log N_{\rm D}(\mathrm{H\,I}) \leq 18.9$.

Although O I and H I have similar ionization potentials and are both coupled by a strong charge-exchange reaction[3], we note that the O I/H I ratio in complex B and complex C cannot be the same: a model assuming $[\mathrm{HI/OI}]_{\rm B} = [\mathrm{HI/OI}]_{\rm C}$ cannot reproduce the observed spectrum.

Table 8.2.: O I/H I ratio in complex B and C. The model we use assumes four main absorbers, named complex A, B, C, and D, respectively. Complex D is restricted by an upper and a lower limit of its H I content, $17.3 \leq \log N_{\rm D}(\mathrm{HI}) \leq 18.9$. We note that the O I/H I ratios in complex B and C, the two major absorption systems, are clearly different.

complex	C	D	B	A
v	-145	-42	$+16$	$+95$
$\log N(\mathrm{HI})$	19.25 ± 0.10	≥ 17.30	19.10 ± 0.05	16.81 ± 0.05
$b\,[\mathrm{km\,s^{-1}}]$	26 ± 1	≥ 28	17 ± 1	27 ± 2
$\log N(\mathrm{OI})$	14.67 ± 0.02	≤ 12.2	15.34 ± 0.03	≤ 12.2
OI/HI	2.63×10^{-5}	$\leq 1.41 \times 10^{-5}$	1.74×10^{-4}	$\leq 1.29 \times 10^{-5}$
[OI/HI]	-1.27	≤ -1.54	-0.45	≤ -1.58
solar	$^1/_{20}$	$\leq\ ^3/_{100}$	$^7/_{20}$	$\leq\ ^3/_{100}$

[3] $\mathrm{HII} + \mathrm{OI} \leftrightarrow \mathrm{HI} + \mathrm{OII}$

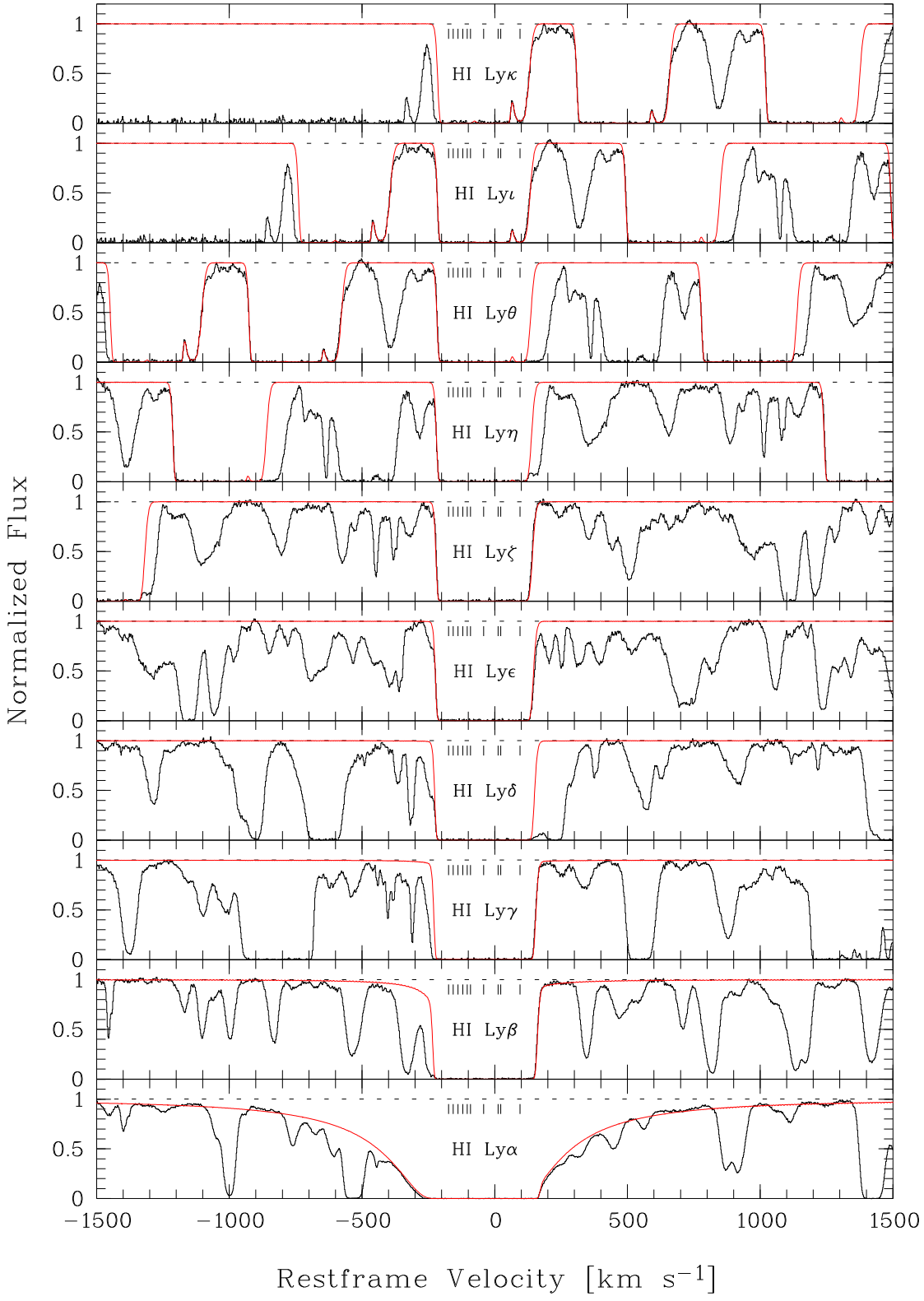

Figure 8.3.: Fit of the H I Lyman lines. Note that deuterium is *not* included in this fit in order to illustrate the clear D I detection seen in Ly γ, Ly δ, Ly ε, Ly ζ, and Ly η (see also Fig. 8.4 and Fig. 8.5). The tic marks indicate the line centers for $C_6, ..., C_1$, D, B_2 and B_1, and A (from left to right).

8.4.3. Deuterium Measurements

We can see that the red wing of the H I Lyman trough is affected from D I transitions which are expected to be situated at $-80\,\mathrm{km\,s^{-1}}$ relative to the respective H I absorption. While the D I Ly β, Ly γ, and the Ly δ lines are blended (see Fig. 8.5), possibly by intervening H I absorption systems at a slightly lower redshift, this is not the case for the D I Ly ε and D I Ly ζ transitions (Fig. 8.4). We use the Doppler parameters from complex C as derived while fitting the neutral and weakly ionized species (see Fig. 8.7), i.e., $b_{\mathrm{C}_6} = 9.1\,\mathrm{km\,s^{-1}}$ and $b_{\mathrm{C}_5} = 5.2\,\mathrm{km\,s^{-1}}$. A multi-line fit of H I with 4 components (complex A, B, C, and D) and D I with 2 components (C_6 and C_5) using the Ly ε and Ly ζ transitions, yields $\log N_{\mathrm{C}_6}(\mathrm{D\,I}) = 14.15 \pm 0.10$ ($\mathrm{H\,I/D\,I} = 2.04 \times 10^{-5}$) and $\log N_{\mathrm{C}_6}(\mathrm{D\,I}) = 14.25 \pm 0.10$ ($\mathrm{H\,I/D\,I} = 5.50 \times 10^{-5}$), i.e., $\log N_{\mathrm{C}_5+\mathrm{C}_6}(\mathrm{D\,I}) = 14.55 \pm 0.07$.

When assuming $[\mathrm{HI/OI}]_{\mathrm{C}_i} = [\mathrm{DI/OI}]_{\mathrm{C}_i}$, $\forall i$, we get:

- $\log N_{\mathrm{C}_1+\ldots+\mathrm{C}_6}(\mathrm{D\,I}) = \log N_{\mathrm{C}}(\mathrm{D\,I}) = 14.71 \pm 0.05$
- $\log N(\mathrm{H\,I/D\,I}) = -4.55 \pm 0.10$

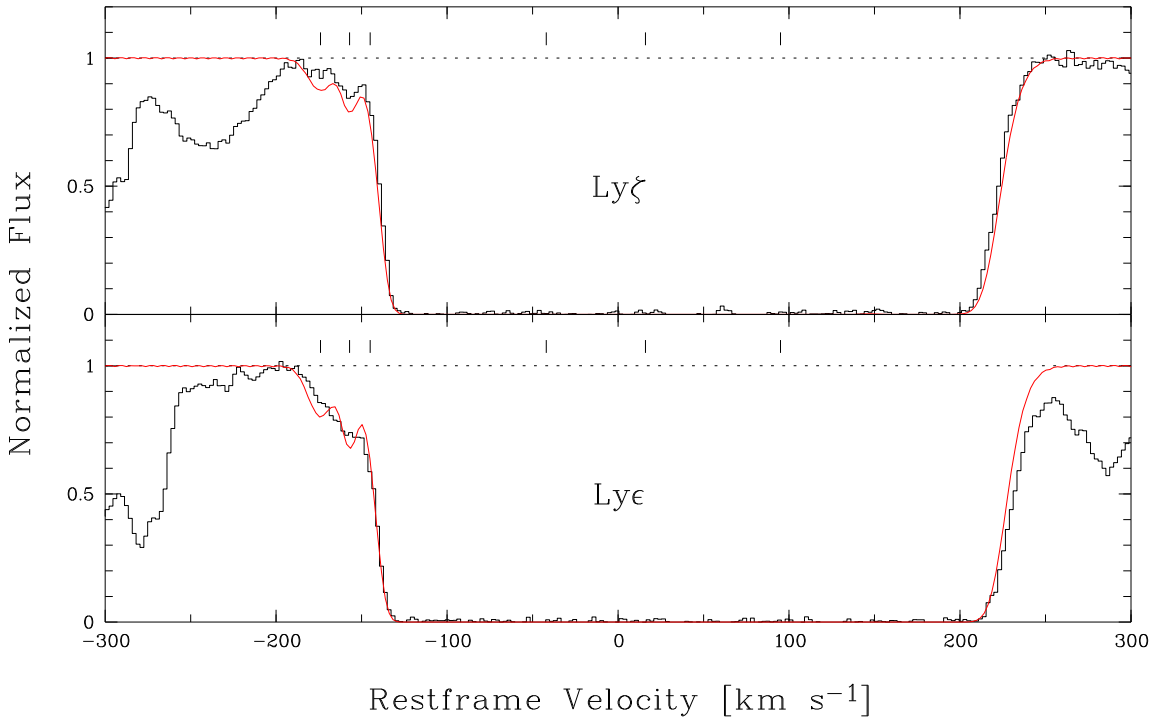

Figure 8.4.: Multi-line fit of the H I Ly ε and H I Ly ζ lines with four components (complex A, B, C, and D) and the D I Ly ε and D I Ly ζ lines with two components (C_5 and C_6). We can see clearly that the red wing of the H I Lyman trough is affected from D I transitions. The tic marks indicate the line centers at -174 and $-157\,\mathrm{km\,s^{-1}}$ (C_6 and C_5), $-145\,\mathrm{km\,s^{-1}}$ (complex C), $-42\,\mathrm{km\,s^{-1}}$ (complex D), $+16\,\mathrm{km\,s^{-1}}$ (complex B), and $+95\,\mathrm{km\,s^{-1}}$ (complex A).

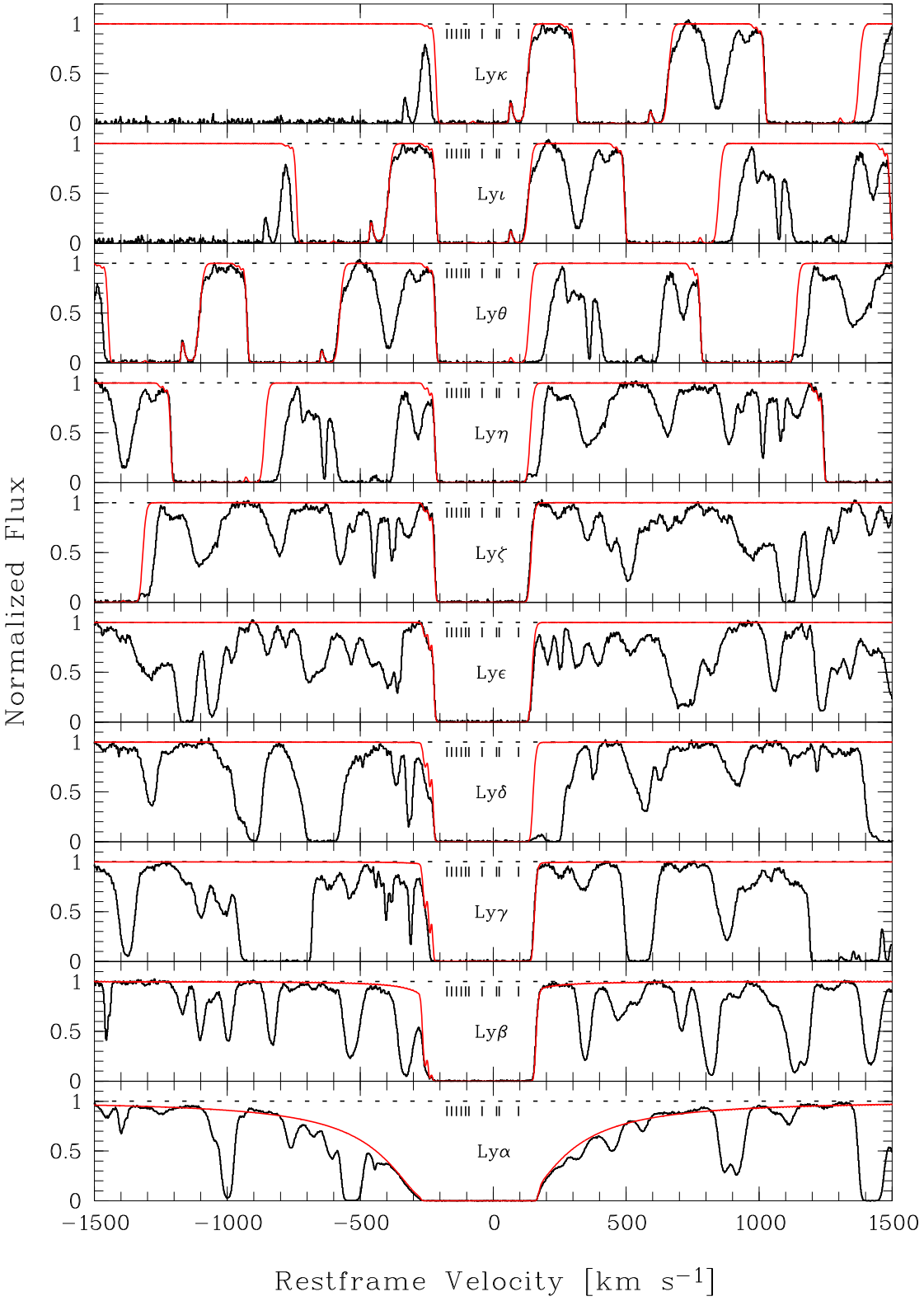

Figure 8.5.: Fit of the H I and D I Lyman lines. The most reliable D I signature is obtained from the Ly ε and Ly ζ lines (see also Fig. 8.4). The tic marks indicate the line centers for $C_6, ..., C_1$, D, B_2 and B_1, and A (from left to right).

8.4.4. Neutral and Weakly Ionized Species

Complex B

The neutral and weakly ionized species of complex B at $+12$ and $+22\,\mathrm{km\,s^{-1}}$, respectively, are fitted by making use of the following transition lines: N I λ1199, N II λ1083, O I $\lambda\lambda$1039, 950, Al II λ1670, Al III λ1854, S III $\lambda\lambda$1808, 1020, P II λ963, S II $\lambda\lambda$1253, 1250, S III λ1190, Fe II $\lambda\lambda$1608, 1063, Fe III λ1122, and N III λ1317. The C II λ1334 and Si III λ1206 lines were fitted in a second pass using the previously derived b values from the 16 transitions listed above. This procedure is necessary because blended (Si III λ1206) or heavily saturated (C II λ1334) lines lead to imprecise results for N and tend to overestimate the b value. We derive a column density for C II λ1334 but only an upper limit for Si III λ1206 because the latter was too strongly blended (see also Fig. 8.6). The results are summarized in Table 8.4, where we use $\log N_{\mathrm{B}}(X) = \log\left(N_{\mathrm{B}_1}(X) + N_{\mathrm{B}_2}(X)\right)$.

Complex C

We have chosen a set of eight transitions for the fitting of the neutral and weakly ionized species of complex C at -174, -157, -139, -121, -104, and $-92\,\mathrm{km\,s^{-1}}$, respectively. These are N II λ1083, O I $\lambda\lambda$1302, 1039, Al II λ1670, S III λ1526, and Fe II $\lambda\lambda$2382, 2344, 1608. In the same manner as for complex B, we fit the remaining transition lines in a second pass. Some lines are heavily saturated (C II λ1334), blended (Fe III λ1122), weak (Al III λ1854, S II λ1253, Ni II λ1317, S II λ1253), or uncertain (N I λ1200a, P II λ963, Si III λ1206, S IIIλ1190) detections, where in the latter case only upper limits can be derived (see also Fig. 8.7). The results are summarized in Table 8.4, where we use $\log N_{\mathrm{C}}(X) = \log\left(N_{\mathrm{C}_1}(X) + \ldots + N_{\mathrm{C}_6}(X)\right)$.

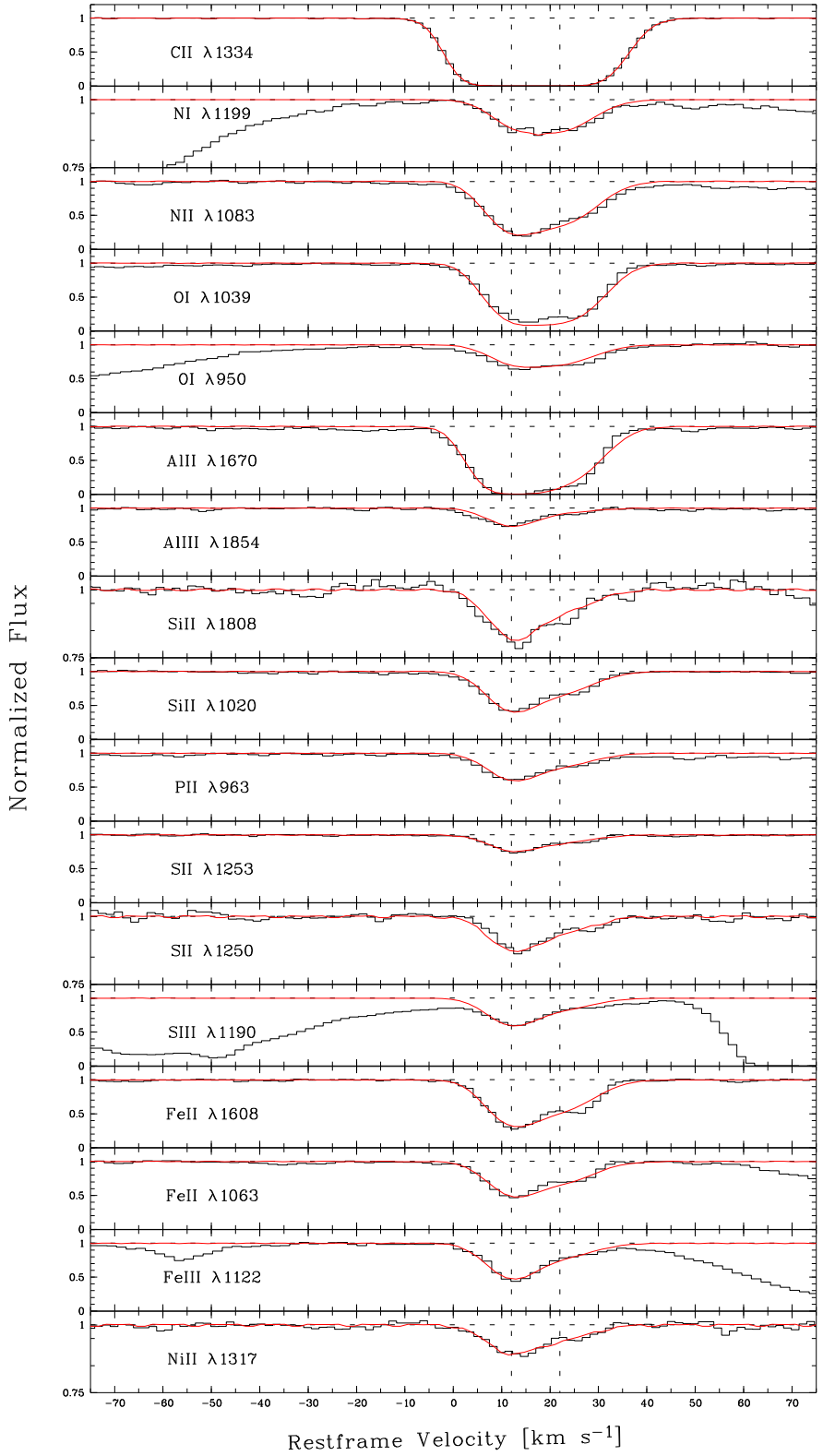

Figure 8.6.: Simultaneous multicomponent fit of the neutral and weakly ionized species in complex B. The dashed lines indicate the line centers at $+12$ and $+22\,\mathrm{km\,s^{-1}}$, respectively.

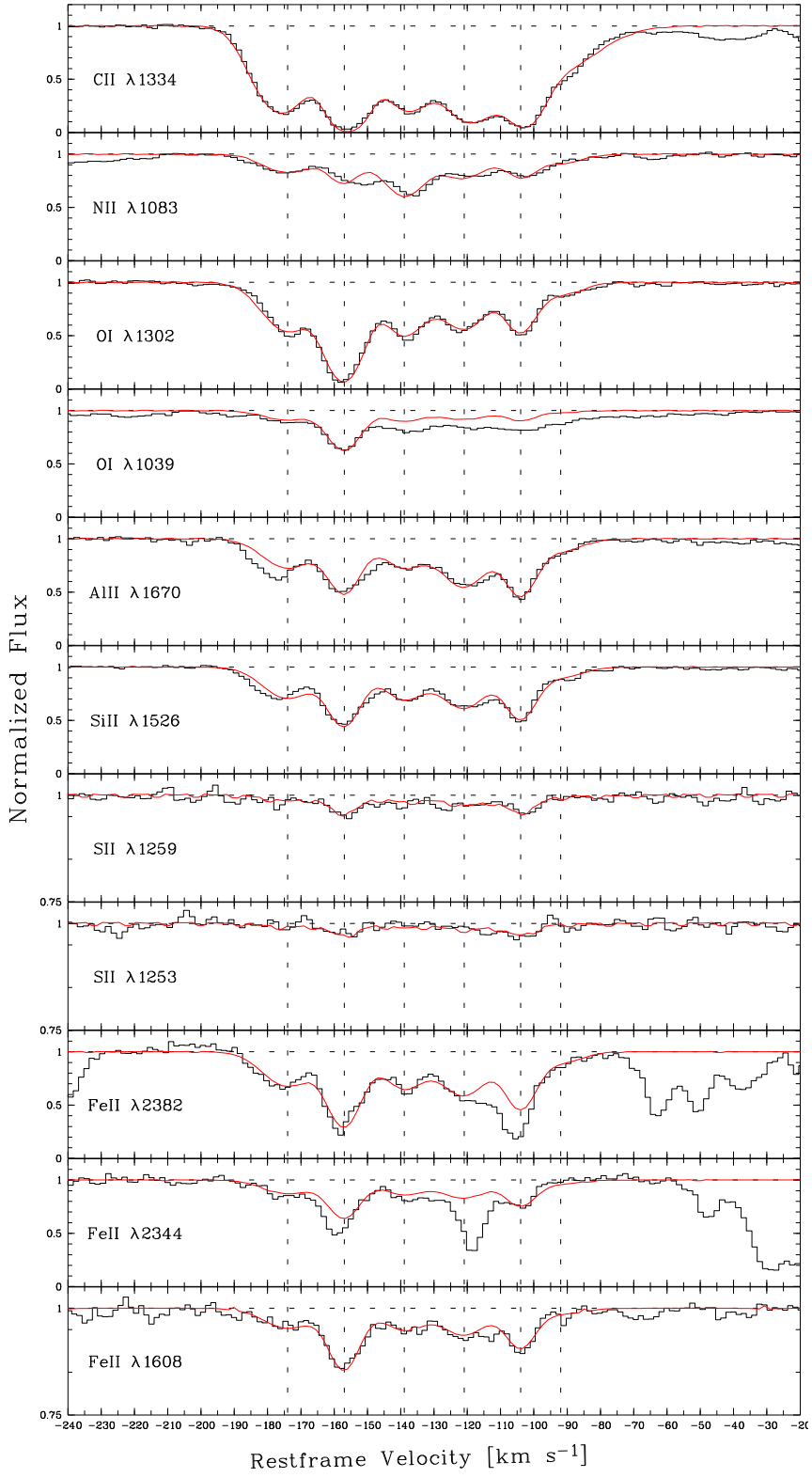

Figure 8.7.: Simultaneous multicomponent fit of the neutral and weakly ionized species in complex C. The dashed lines indicate the line centers at −174, −157, −139, −121, −104, and −92 km s^{-1}, respectively.

8.4.5. Highly Ionized Species

Si IV and C IV Absorption

Absorption lines of higher ionized species arise in a different phase than the neutral and weakly ionized species. Having similar ionization potentials, the Si IV $\lambda\lambda$1393, 1402 ($IP_{Si\,IV} = 41.1\,eV$) and the C IV $\lambda\lambda$1550, 1548 ($IP_{C\,IV} = 64.5\,eV$) lines reside in the same (or at least in a similar) phase and therefore can be fitted together. A model with 9 components, named $E_1, ..., E_9$, ranging from -180 to $+119\,km\,s^{-1}$, can be very accurately reproduced without any restrictions (e.g., forced parameters) within the fitting process (Fig. 8.8). The results from these fits are summarized in Table 8.3. We note that the Si IV and C IV absorption seen at $E_{1,2,3}$ can be associated with O VI absorption at $F_{1,2,3}$ (see below) and with complex C. Further, we can also link the Si IV and C IV absorption in E_4 with O VI absorption at F_4 and complex D, and E_5 with F_5 and complex B. The absorption lines seen around $\sim 50\,km\,s^{-1}$ might arise in a zone where the two main neutral absorbers, complex B and C, merge. Hence, the ionization would no longer be due to photoionization but the high gas density could lead to ionization by collisions as the two gaseous systems are ramming into each other. This in mind, we have fitted the Si IV and C IV lines with either thermal Doppler parameters, b_{th}, or with turbulent Doppler parameters, b_{turb}, but could not find any significant difference.

Table 8.3.: In Si IV and C IV we find nine distinct components, named E_1,..., E_9. In O VI we find five distinct component, F_1,..., F_5. Note that E_1, E_2, E_3 can be associated with F_1, F_2, F_3 and complex C. Further, E_4 can be associated with F_4 and complex D. Alike, E_5 can be associated with F_5 and complex B. The typical error associated with the column density measurements is of ± 0.02 dex.

	E_1	E_2	E_3	E_4	E_5	E_6	E_7	E_8	E_9
$\bar{v}$ [km s^{-1}]	-180	-160	-115	-58	$+11$	$+48$	$+606$	$+97$	$+119$
log N(Si IV)	12.25	12.65	12.95	12.51	12.88	12.39	12.73	12.39	11.80
log N(C IV)	12.49	12.91	13.11	13.49	12.81	12.49	13.22	12.76	12.33
	F_1	F_2	F_3	F_4	F_5				
$\bar{v}$ [km s^{-1}]	-174	-130	-96	-52	$+21$				
log N(O VI)	13.50	13.61	13.65	14.29	14.05				

O VI Absorption

The O VI $\lambda\lambda$1037, 1031 lines ($IP_{O\,VI} = 138.1\,eV$) were fitted independently from the Si IV and C IV lines because they likely arise in a different (hotter) phase. We adopted a model with 5 components, named $F_1, ..., F_5$, ranging from -174 to $+21\,km\,s^{-1}$. The reader should note that the apparent absorption seen in O VI λ1037 at ~ -160 and $\sim +60\,km\,s^{-1}$ (see Fig. 8.8) are not due to O VI but to other transition lines that arise in regions with different redshift overlapping in the observed wavelength (blending). Note that the line center of F_4 is a weighted mean of the absorption lines seen at -75, -59, and $-40\,km\,s^{-1}$, respectively. The results from fitting the O VI absorption are summarized in Table 8.3.

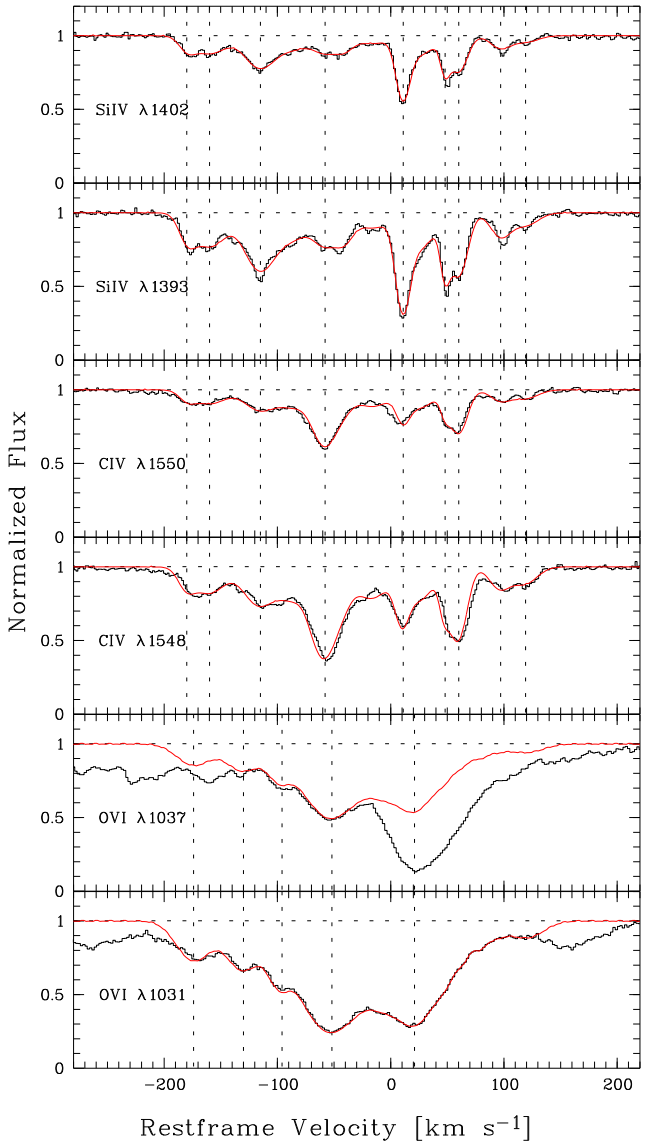

Figure 8.8.: Simultaneous multicomponent fit of the highly ionized species, where the Si IV and C IV lines were fitted together. We can distinguish 9 different components ($E_1, ..., E_9$), ranging from -180 to $+119\,\mathrm{km\,s^{-1}}$, for Si IV and C IV, and 5 different components ($F_1, ..., F_5$), ranging from -174 to $+21\,\mathrm{km\,s^{-1}}$, for O VI.

8.4.6. Photoionization Corrections

Given the large neutral hydrogen column density in this absorber, it is not expected that photoionization has any significant effect on the abundances listed in Table 8.4. This is supported by our photoionization model for a synthesized sub-DLA system at $z = 3.0$ based on CLOUDY (Ferland et al. 1998). We have assumed a uniform ionizing background, a plane parallel geometry, as well as a constant density, metallicity, and solar abundance pattern for the gas cloud. As concerning the ionizing radiation, we used the spectrum obtained by Haardt & Madau (1996) including both the contributions by quasars and young star-forming galaxies, its intensity being each time set by the ionization parameter, U. The metallicity was fixed by the observed ratio between O I and H I, while we choose to set the total hydrogen volume density to $10^{-1}\,\mathrm{cm}^{-3}$. The code was run until there was a match between predicted and observed H I column density. The outcome from our photoionization model is given in Table 8.4 (see plots in Appendix D). Our photoionization model thus confirms that the observed column densities are consistent with the assumed metal abundance and the appropriate ionizing background. For this synthesized sub-DLA system, and throughout this work, we use wavelengths and oscillator strengths from the atomic line list of Morton (2003). Solar reference abundances are listed in Table 8.5 (see also Appendix C.1).

8.4.7. Molecular Hydrogen

No traces of molecular hydrogen were found in the sub-DLA system toward Q 0420−388. The logarithmic ratio of hydrogen nuclei in molecules to the total hydrogen nuclei is $\log f_{\mathrm{H}_2} = \log 2N(\mathrm{H}_2) - \log N(\mathrm{H}) \leq -6.0$ (where we can assume that $N(\mathrm{H\,I}) \approx N(\mathrm{H})$ in the phase of interest), with $\log N(\mathrm{H}_2) \leq 13.5$, i.e., the total upper limits of the rotational ground states $J = 0$ and $J = 1$ in the Werner band of molecular hydrogen. Because of the lack of H_2 (which predominantly forms on dust grains) and the relatively low overall metallicity we do not expect dust depletion to alter significantly the abundance pattern in this absorption system (Ledoux et al. 2003; Vladilo 2002).

8.4.8. Derived Metallicities

The chemical abundances (or metallicities) were derived using the common notation $[\mathrm{X/H}] = \log(N(\mathrm{X})/N(\mathrm{H})) - \log(N(\mathrm{X})/N(\mathrm{H}))_{\odot}$. We refer to the solar

abundances as listed in Morton (2003), based on data from Grevesse & Sauval (2002), except for oxygen, for which we adopt the value given in Allende Prieto et al. (2001) (see Tables 8.5 and C.1). When assuming that $[\mathrm{M/H}] \approx [\mathrm{O\,I/H}]$ we derive a metallicity of -0.45 or $Z = 0.35$ ($= {}^{7}/_{20}$) solar for complex B, and a metallicity of -1.27 or $Z = 0.05$ ($= {}^{1}/_{20}$) solar for complex C. The metal abundances of complex B and complex C are summarized in Table 8.4.

8.5. Results and Discussion

8.5.1. The Deuterium Abundance at $z = 3$

The deuterium observed nowadays was created during the first three minutes after the Big Bang, along with other light elements such as hydrogen, helium and lithium. The primordial deuterium abundance is very sensitive to the baryonic matter density in the early Universe and thus is an important observational constraint for cosmology. Values for the primordial deuterium abundance are derived from CMB observations together with the SBBN model ($\mathrm{D/H}|_{\mathrm{p}} = 2.60^{+0.19}_{-0.17} \times 10^{-5}$, i.e., $\log \mathrm{D/H}|_{\mathrm{p}} = -4.585^{+0.031}_{-0.029}$; Coc et al. 2004) or by means of chemical evolution models that estimate the amount of astration[4] taking place over the lifetime of a galaxy ($\mathrm{D/H}|_{\mathrm{p}} \approx 3 - 5 \times 10^{-5}$, i.e., $\log \mathrm{D/H}|_{\mathrm{p}}$ from -4.52 to -4.30; Tosi 1996 and Chiappini & Matteucci 2000).

Deuterium is particularly fragile (because the deuterium nucleus can easily be broken apart by high energy photons[5]) and is destroyed (but not produced) in stellar processes. Hence, the primordial abundance should be reflected, in principle, by the highest values observed in the most remote QAL systems. The deuterium measurements in QAL systems are summarized in Table 8.6. This table was reproduced from Table 5 in O'Meara et al. (2001) and supplemented with results from Carswell et al. (1996) and the results of this work. Note that we derive in this work a deuterium abundance that is equally low as measured in the absorbing system at $z_{\mathrm{abs}} = 2.536$ toward the quasar HS 0105+1619, but with a significantly higher silicon abundance. O'Meara et al. (2001) discuss a possible correlation between [Si/H] and D/H (see their Fig. 12). They also note

[4] The conversion of an element or isotope by nuclear reactions in the interior of a star.

[5] $\mathrm{D} + \gamma \rightarrow p + n$

Table 8.4.: Summary of chemical abundances in the sub-DLA system toward Q 0420−388 with the common notation $[\mathrm{X/H}] = \log(N(\mathrm{X})/N(\mathrm{H})) - \log(N(\mathrm{X})/N(\mathrm{H}))_\odot$. The column densities and metal abundances of the two main absorption components, complex B and C, at $+16\,\mathrm{km\,s^{-1}}$ and $-145\,\mathrm{km\,s^{-1}}$, respectively, are shown as derived from simultaneous multi-component Voigt-profile fits, and values from the photoionization correction (PIC) calculus with `Cloudy`. With $\Delta\log N(\mathrm{X}) = \log N(\mathrm{X}) - \log N_{\mathrm{PIC}}(\mathrm{X})$ we give the difference between the measured column density and the predictions from our photoionization model.

Species	Transition lines used	$\log N(\mathrm{X}) \pm \sigma_{\log N}$	$[\mathrm{X/H}] \pm \sigma_{[\mathrm{X/H}]}$	$\log N(\mathrm{X}) \pm \sigma_{\log N}$ with PIC	$\Delta\log N(\mathrm{X})$
Complex B					
H I	Ly α,..., Ly κ	19.10 ±0.10			
C II	1334	16.19 ±0.04	0.57 ±0.10	15.45	0.74
N I	1199	12.84 ±0.02	−2.21 ±0.10	14.46	−1.62
N II	1083	13.99 ±0.02	−1.06 ±0.10	14.77	−0.78
O I	950,1039	15.34 ±0.03	−0.45 ±0.10	15.34	0.00
Al II	1670	13.33 ±0.02	−0.26 ±0.10	13.45	−0.12
Al III	1854	12.23 ±0.02	−1.36 ±0.10	12.34	−0.11
Si II	1808,1020	14.54 ±0.02	−0.12 ±0.10	14.54	0.00
Si III	1206	≤15.89		13.41	
P II	963	12.38 ±0.02	−0.28 ±0.10	12.51	−0.13
S II	1250,1253	14.13 ±0.02	−0.17 ±0.10	14.11	0.02
S III	1190	14.06 ±0.04	−0.24 ±0.10	13.53	0.53
Fe II	1608,1063	13.94 ±0.02	−0.66 ±0.10	14.39	−0.45
Fe III	1122	13.88 ±0.02	−0.72 ±0.10	13.89	0.01
Ni II	1317	12.61 ±0.02	−0.74 ±0.10	13.24	−0.63
Complex C					
H I	Ly α,..., Ly κ	19.25 ±0.10			
D I	Ly ε,Ly ζ	14.71 ±0.05			
C II	036,1334	14.72 ±0.04	−1.05 ±0.10	14.87	−0.15
N I	1200a	≤12.08		13.70	
N II	1083	13.85 ±0.02	−1.35 ±0.10	14.34	−0.49
O I	1039,1302	14.67 ±0.02	−1.27 ±0.10	14.67	0.00
Al II	1670	12.71 ±0.02	−1.03 ±0.10	13.00	−0.29
Al III	1854	≤11.21		12.03	
Si II	1526	13.85 ±0.02	−0.96 ±0.10	13.99	−0.14
Si III	1206	≤15.00		13.71	
P II	963	≤11.14		11.99	
S II	1250,1253,1259	13.42 ±0.04	−1.03 ±0.10	13.54	−0.12
S III	1190	≤ 13.85		13.48	
Fe II	2344,2382	13.37 ±0.02	−1.38 ±0.10	13.74	−0.37
Fe III	1122	≤13.82		13.80	
Ni II	1317	≤11.33		12.72	

Table 8.5.: Solar abundances as listed in Morton (2003), based on data from Grevesse & Sauval (2002), except for oxygen, for which we adopt the value given in Allende Prieto et al. (2001).

Element	$\log N((\mathrm{X})/N(\mathrm{H}))_\odot + 12.00$
Deuterium	7.00
Carbon	8.52
Nitrogen	7.95
Oxygen	8.69
Aluminum	6.49
Silicon	7.56
Phosphorus	5.56
Sulfur	7.20
Iron	7.50
Nickel	6.25

that some arguments (e.g., the deuterium destruction that is too large at very low [Si/H] or the decrease in D/H that is faster than expected) speak against such a correlation. In fact, the silicon measurements in our study of Q 0420−388 seriously question a correlation between [Si/H] and D/H. As deuterium is destroyed in stars in the first place, we would expect that [α/H] is a more appropriate tracer for D/H. In fact, replacing [Si/H] by [α/H], i.e., in our case by $[\mathrm{O}/\mathrm{H}] = -1.27$, leads to a more consistent trend.[6]

Table 8.6.: Deuterium measurements in QAL systems

QSO	$\log(\mathrm{D}/\mathrm{H})$	z_{abs}	$\log N(\mathrm{H\,I})$	$[\mathrm{Si}/\mathrm{H}]$	Ref.[a]
PKS 1937-1009	-4.49 ± 0.04	3.572	17.86 ± 0.02	$-2.7, -1.9$	1,2
Q 1009+2956	-4.40 ± 0.07	2.504	17.39 ± 0.06	$-2.4, -2.7$	3,4
Q 0130−4021	< -4.17	2.799	16.66 ± 0.02	-2.6	5
HS 0105+1619	-4.60 ± 0.04	2.536	19.42 ± 0.01	-1.85	6
Q 0420−388	-3.90 ± 0.40	3.088	18.67 ± 0.10	-0.96	7
Q 0420−388	-4.55 ± 0.10	3.088	19.25 ± 0.10	-0.96	8

[a] References: (1) Tytler et al. (1996); (2) Burles & Tytler (1998a); (3) Tytler & Burles (1997); (4) Burles & Tytler (1998b); (5) Kirkman et al. (2000); (6) O'Meara et al. (2001); (7) Carswell et al. (1996); (8) this work

[6] Note that oxygen is not commonly measured in high-z DLA-systems.

Carswell et al. (1996) analyze in their study of Q 0420−388 two absorption line systems at $z_{\rm abs} = 3.08595$ and $z_{\rm abs} = 3.08576$, respectively, that both can be identified with complex C in the present analysis. For the absorption system at $z_{\rm abs} = 3.08595$ they derive $\log N({\rm H\,I}) = 18.60$, $\log N({\rm D\,I}) = 14.57$, $\log N({\rm Si\,II}) = 12.80$, i.e., $\log({\rm D\,I/H\,I}) = -4.03$ and $[{\rm Si\,II/H\,I}] = -1.36$. Likewise, for the absorption system at $z_{\rm abs} = 3.08576$ they derive $\log N({\rm H\,I}) = 17.85$, $\log N({\rm D\,I}) = 14.26$, $\log N({\rm Si\,II}) = 13.46$, i.e., $\log({\rm D\,I/H\,I}) = -3.59$ and $[{\rm Si\,II/H\,I}] = +0.05$. When considering the two absorption systems as one, we have $\log N({\rm H\,I}) = 18.67$, $\log N({\rm D\,I}) = 14.74$, $\log N({\rm Si\,II}) = 13.54$, i.e., it is $\log({\rm D\,I/H\,I}) = -3.93$ and $[{\rm Si\,II/H\,I}] = -0.69$. The difference in $\log({\rm D/H})$ (see Table 8.6) between this work and the analysis of Carswell et al. (1996) is due to the fact that different models have been used: while we assume the absorbing systems to be subdivided into four main components (named complex A, B, C, and D), ranging from $z_{\rm C_6} = 3.08563$ to $z_{\rm A_1} = 3.08930$, with up to six subcomponents in the case of complex C, Carswell et al. (1996) have adopted a model with 14 different components, ranging from $z = 3.07979 - 3.09561$, where abundances for metals could be derived in the case of 6 components in the range of $z = 3.08576 - 3.08830$.

This comparison shows that the high quality of the UVES data clearly exceeds (in resolution and SNR) the previous data that have been used by Carswell et al. (1996). As a result we were able to develop a more detailed and more reliable model for the velocity-components of this system. This is particularly important in order to derive reliable hydrogen column densities for the individual components and so to obtain accurate values for D/H and the overall metallicities. Another new aspect of this more elaborated model is the fact that we can additionally identify an intermediary component, i.e., complex D, that possibly represents a merging zone (see below).

8.5.2. Gas Phase and Ionization Process

O VI can be formed through ionizing photons or collisions. Thus, the detection of O VI in a DLA system does not necessarily imply the presence of a hot medium (that would be collisionally ionized). Unfortunately, the O VI $\lambda\lambda$1037, 1031 falls into the Ly α forest and, hence, not many and reliable data from O VI absorption systems, especially in DLA systems, are available. Fox et al. (2007) have recently presented the first systematic study of highly ionized gas associated with DLA systems at $z_{\rm abs} = 2.1 - 3.1$. They have found 35 UVES/VLT spectra with data covering O VI and other high ions at a SNR > 10. They con-

firm, based on their photoionization models with `Cloudy`, that no single-phase solution is possible, i.e., that the hot gas in DLA systems contains two phases: a photoionized phase (with typically $\sim 10^4$ K) seen in Si IV, C IV, and O VI, and a collisionally ionized phase (with typically $\sim 10^5 - 10^7$ K) seen in O VI and N V. In Fig. 8.9 Fox et al. (2007) have compared their photoionization model calculations (black line) with measurements in DLA systems (red dots), regions in the Galactic halo (yellow dot), and high-velocity clouds (HVC; blue dot).

When we compare their results with the values derived in this study (Fig. 8.9; green square), we find that the gas in complex D is close to the collisional ionization equilibrium with $T \approx 10^{5.32}$ K. Hence, the velocity component we see at $-42\,\mathrm{km\,s^{-1}}$, i.e., complex D, is a true intermediary component between complex B ($+16\,\mathrm{km\,s^{-1}}$) and complex C ($-145\,\mathrm{km\,s^{-1}}$). We know further that the gas in complex D is collisionally ionized and consequently dense and hot ($T \approx 10^{5.32}$ K is well within the range of $10^5 - 10^7$ K). Recalling the different overall metallicities of complex B ($^7/_{20}$ solar) and complex C ($^1/_{20}$ solar) we feel confident to state that complex D is a region where two different (proto) galaxies, i.e., complex B and complex C, are about to merge, creating a zone of hot, ionized gas as the two gaseous environments are ramming into each other.

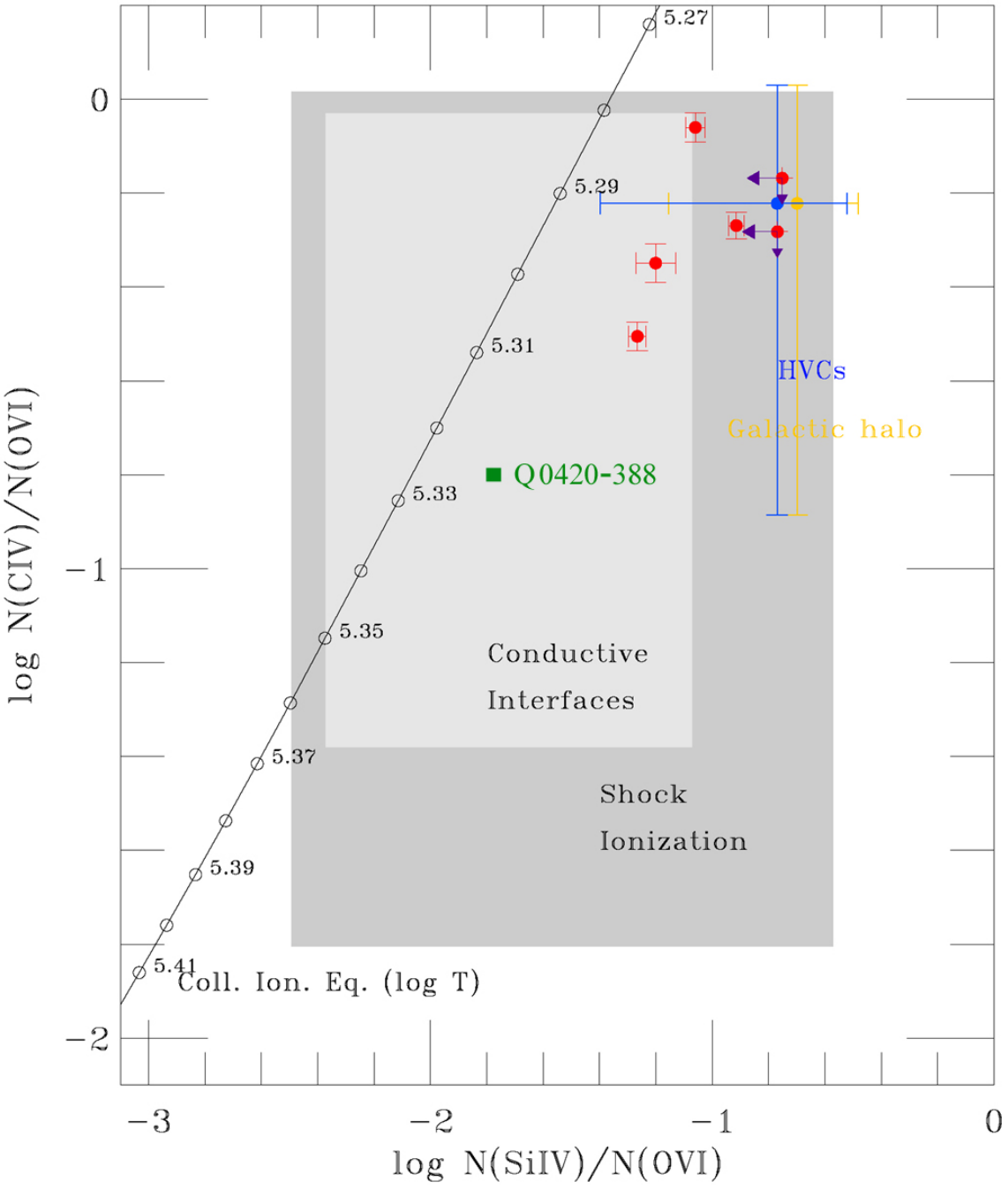

Figure 8.9.: log-log plot of $N(\mathrm{Si\,IV})/N(\mathrm{O\,VI})$ versus $N(\mathrm{C\,IV})/N(\mathrm{O\,VI})$. Shown are photoionization model calculations (black line) and DLA systems (red dots) from the study of Fox et al. (2007), predictions from various collisional ionization models (gray shaded regions; open cirles), the average value in the Galactic halo (yellow dot), and the average value from HVCs (blue dot) from Fox et al. (2005). The values derived in this study (green square) agree well with a collisional ionization equilibrium at $T \approx 10^{5.32}\,K$ but also with shock ionization. Reproduction with kind permission from A. J. Fox.

9. The Line of Sight toward 004345.8−294733: Unveiling the Nature of Dark Clumps

9.1. Introduction

The inspiration to this project was not a scientific meeting or an interesting publication but, as odd as it may sound, a simple cup of coffee with colleagues from the same institute working on weak gravitational lensing. These people look at very large fields and deduce from statistical image deformations the position and mass of the deflecting object that causes this lensing effect. From time to time they happen to find a clear lensing signal, caused by a substantial mass concentration on the order of a galaxy group (i.e., $\sim 10^{13}\,M_{\odot}$), but without any luminous counterpart at the deflector's position. Consistency checks with deeper observations and in other wavelength regimes have shown none or only insignificant mass accumulations (within a statistical random mass distribution). Hence the striking contradiction. None or by far not enough luminous matter or hot gas is detected in order to explain the observed lensing effect, where, on the other hand, theory and model calculations show that it is impossible that objects on the order of galaxy clusters have no star formation activities, i.e., remain dark. The term *dark clump* is commonly used to refer to these kind of objects.

Table 9.1.: Size and baryonic mass of galaxies and galaxy clusters

	galaxy	galaxy cluster
size [Mpc]	~ 0.025	~ 2
baryonic mass $[M_{\odot}]$	$\sim 10^{11}$	$\sim 10^{13}$
dark matter $[M_{\odot}]$	$\sim 10^{12}$	$\sim 10^{14}$

Whether dark clumps are real or just statistical flukes in the lensing signal can be tested via quasar absorption line spectroscopy. Already relatively small

amounts of gaseous matter that should reside in such an enormous gravitational potential well can be seen in absorption of a background source. It is a very fortunate coincidence that one out of 63 dark clump candidates lies in the projected vicinity of a sufficiently bright background quasar, 004345.8−294733, and that no interfering objects are present in the periphery of the line of sight. This enables us to search for gaseous matter related to the dark clump in the direction of this QSO.

The quasar 004345.8−294733

The existence of dark clumps is controversial and highly debated. We therefore proposed to spectroscopically verify the reality of a non-luminous mass concentration ($\sim 2 \times 10^{14} M_{\odot}$) at $0.1 \lesssim z \lesssim 0.3$ as detected by weak gravitational lensing observation. Dark clumps might, in fact, not be real (statistical fluke), but the striking possibility that spectroscopic analyses could lead to reliable constraints on the existence of such objects, and the increasing evidences of the existence of dark galaxies from H I-surveys (Minchin et al. 2005), outweigh such concerns. Our target is the quasar 004345.8−294733 ($V = 19\overset{\mathrm{m}}{.}57, z = 1.675$), $3'9''$ off the dark clump candidate SSMC−007 (see also Fig. 9.4), with the objective (1) to confirm/infirm the existence of SSMC−007, and (2) if real, to study important absorption lines such as Mg I and Mg II, Ca II, Mn II, and Fe II.

For Period 77 (P77: April 1, 2006 - September 30, 2006) the ESO Observing Programmes Committee (OPC) panel granted a total time of 12 h to the programme 077.B-0758(A) – "Unveiling the nature of dark clumps via QSO absorption line spectroscopy" (PI / CoIs: Erni / Richter / Schneider / Erben / Schirmer / Bergeron / Ledoux).[1]

[1] OPC comment for the programme: *There was some disagreement within the panel regarding whether the approach proposed by the applicants is the best way to conduct the main test that they propose (detecting/non-detecting the "dark cloud"). Also, the proposal was found slim in explaining the statistical significance of the lensing detection, and of the probability of detecting something in the redshift bin of interest due to a random distribution of absorbers. Nonetheless, the proposal was generally well received, and the panel agreed on the importance of this project. The consensus was that this was an investment with probably no return, but worth trying as the return would be large if the dark cloud was really confirmed/identified. The proposal was thus ranked relatively high. However, its implementation will depend on scheduling constraints.*

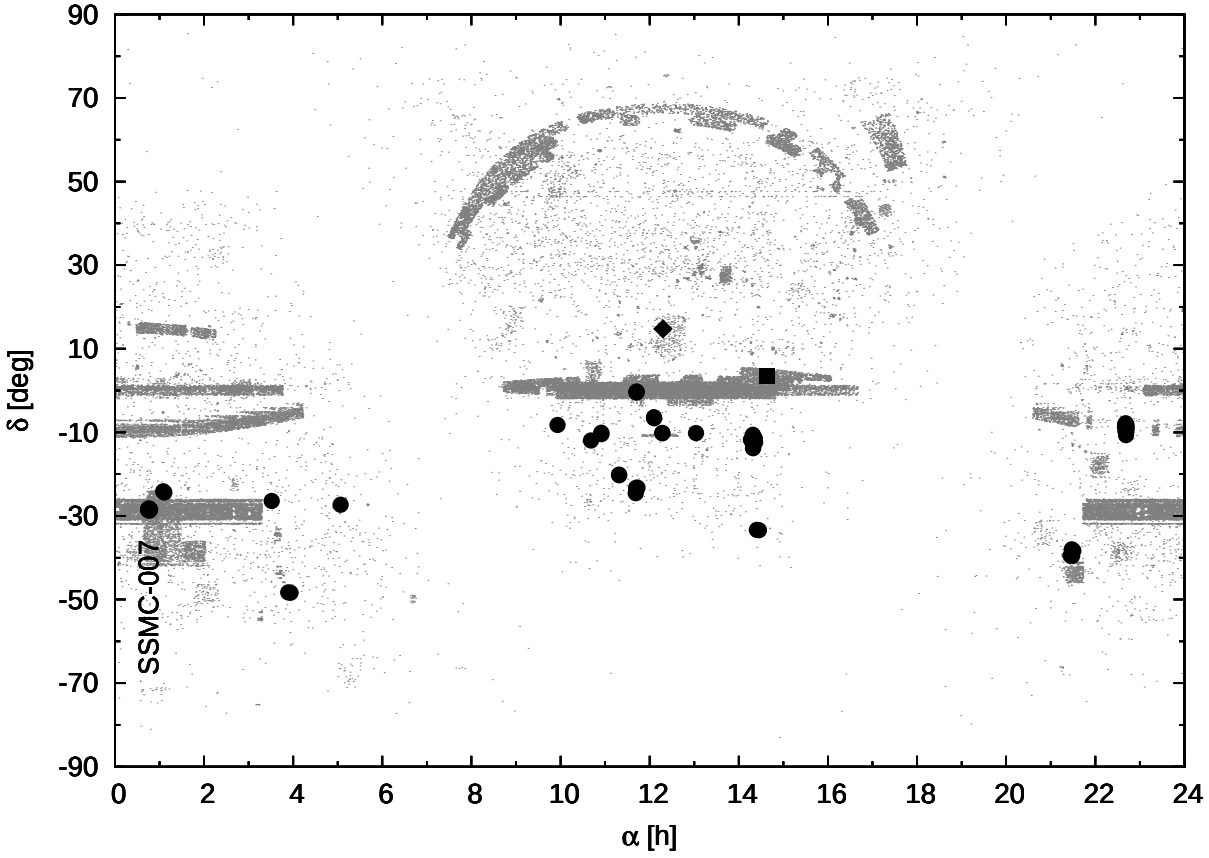

Figure 9.1.: Plot of the over 60 000 known quasars from large surveys and 63 dark clump candidates in equatorial coordinates: QSOs (dots), the dark clump candidates SSMC−007 (filled circles), VIRGO HI21 (diamond), and the dark clump candidate near Abell 1942 (square) analyzed by von der Linden et al. (2006).

9.2. Scientific Rationale

Galaxy formation in the framework of collisionless cold dark matter (CDM) cosmology is the currently most favored model but yet still not satisfactorily understood. If weakly interacting massive particles (WIMPs) account for most of the matter in the Universe, the first structures to collapse might have been of galaxy size, or smaller. Galaxies themselves then would be built from these smaller fragments through merging. At present, each should have a massive dark matter (DM) halo made largely of WIMPs. Galaxies form early and then fall together to form groups, clusters and larger structures (bottom-up picture). Observations support this theory: we see more irregular, small galaxies at higher redshifts, and galaxies at lower redshifts show evidence from recent mergers. For decades, computer simulations have consistently predicted far more small

galaxies than have been observed. Milky Way (MW)-type galaxies should contain about 500 sub-halos with masses $M \gtrsim 10^8 M_\odot$ (Moore et al. 1999; Klypin et al. 1999; Governato et al. 2004) within 500 kpc. However, only 13 dwarfs have been found within a distance of 500 kpc around the MW, where the observed dwarfs may only sample a sub-set of the actually present CDM substructures (Stoehr et al. 2002; Hayashi et al. 2003; Bullock et al. 2000; Susa & Umemura 2004; Kravtsov et al. 2004).

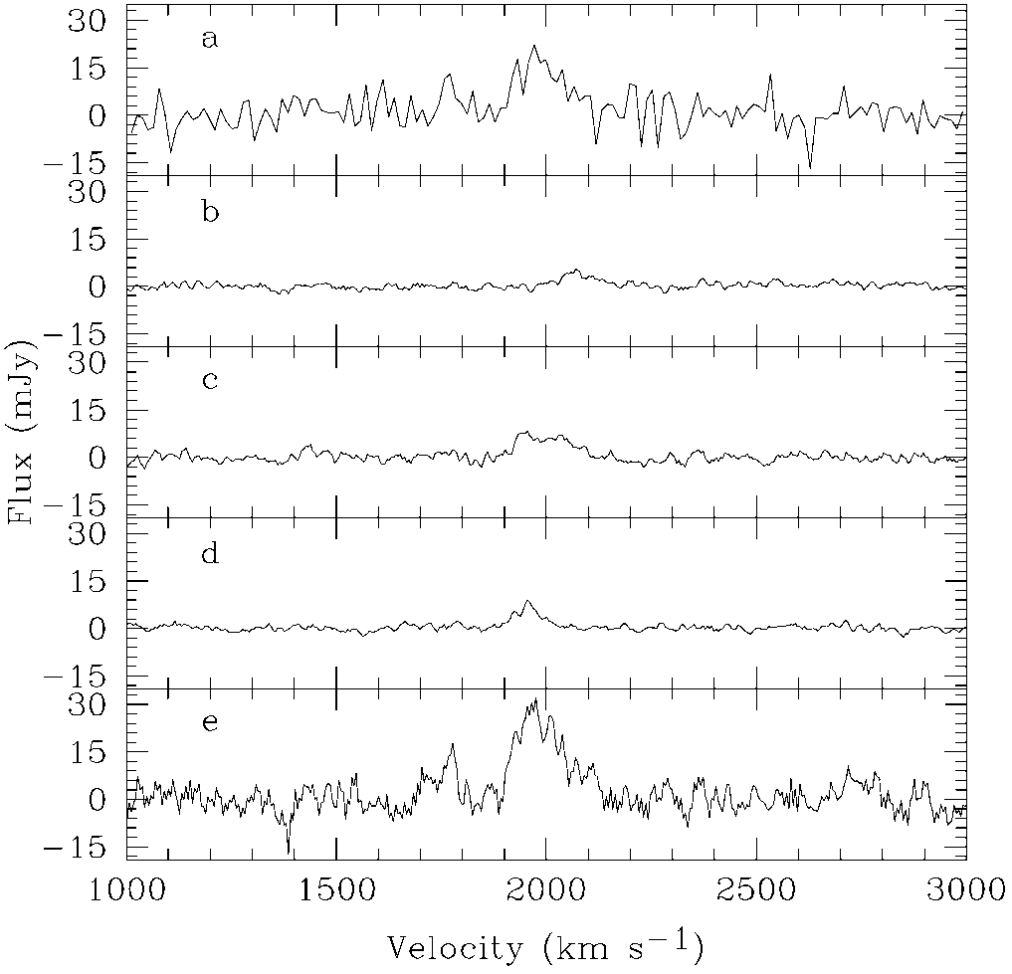

Figure 9.2.: The H I spectrum of VIRGOHI21 plotted in velocity space, with (a) the discovery spectrum from Jodrell Bank, (b) to (d) the Arecibo follow-up spectra, and (e) the sum of all Arecibo spectra. The peak at $\sim 1750\,\mathrm{km\,s^{-1}}$ in spectrum (e) can be clearly associated with a small nearby galaxy (Minchin et al. 2005).

A possible explanation would be the existence of *dark galaxies*, i.e., dark matter halos with no luminous matter content (e.g., Jimenez et al. 1997; Verde

et al. 2002). In the past, 21 cm surveys often claimed to have found dark galaxies (e.g., HIPASS survey, Barnes et al. 2001) but when using powerful optical telescopes, they all turned out to be false detections, except for one: the dark galaxy candidate VIRGOHI21 (Minchin et al. 2005), found by the multibeam system of the Lovell telescope at Jodrell Bank Observatory (Davies et al. 2004), reobserved by the Arecibo telescope (Davies et al. 2004), the VLA (Minchin et al. 2005), and optically examined by the 2.5 m Isaac Newton Telescope (INT) on La Palma (Minchin et al. 2005). ALFALFA (Arecibo Legacy Fast ALFA Survey), a new 21 cm search, has already turned up some potential new dark galaxy candidates and is expected to find many more in the coming years of its projected duration.

In contrast to H I surveys, gravitational weak lensing provides a unique possibility of identifying matter concentrations, regardless of its luminous, gaseous or exotic nature, its virial state or stellar populations, and is insensitive to effects such as dust depletion or photoionization which could alter the results significantly. Supported by the apparently robust detection of a first dark galaxy, one can imagine larger structures in the same context, i.e., dark matter halos of the *size of galaxy clusters*, with no luminous content. The first dark clump candidate was presented by Erben et al. (2000), identified by its significant weak lensing signal without a corresponding galaxy overdensity or X-ray emission. Other dark clump candidates have been reported and investigated by Umetsu & Futamase (2000); Miralles et al. (2002); Dahle et al. (2003); Erben et al. (2003); von der Linden et al. (2006). In the systematic 20 $\deg^2$ weak lensing survey for clusters, conducted with the Wide Field Imager (WFI) at the ESO/MPG−2.2 m telescope and one of the first of its kind, about 60 more dark clump candidates were detected in addition to a series of *bright clumps*, i.e., mass concentrations with optical counterparts.

Objective – The main objective is to test a new and novel idea to investigate and analyze dark clump candidates via high-resolution quasar absorption line (QAL) spectroscopy. QAL spectroscopy allows, similar to gravitational lensing, to study dark clump candidates without relying on light emission (but gas absorption) of these objects in any part of the electromagnetic spectrum. Moreover, QAL spectroscopy is an excellent independent and reliable method to cross-check the concept of non-luminous DM halos. We believe this to be the most appropriate and promising approach for the quest of revealing the nature of those mysterious, massive (cluster-size) and non-luminous matter accumulations. The existence of a dark-clump-like object would call for a critical re-evaluation of our current understanding of structure formation in the Universe.

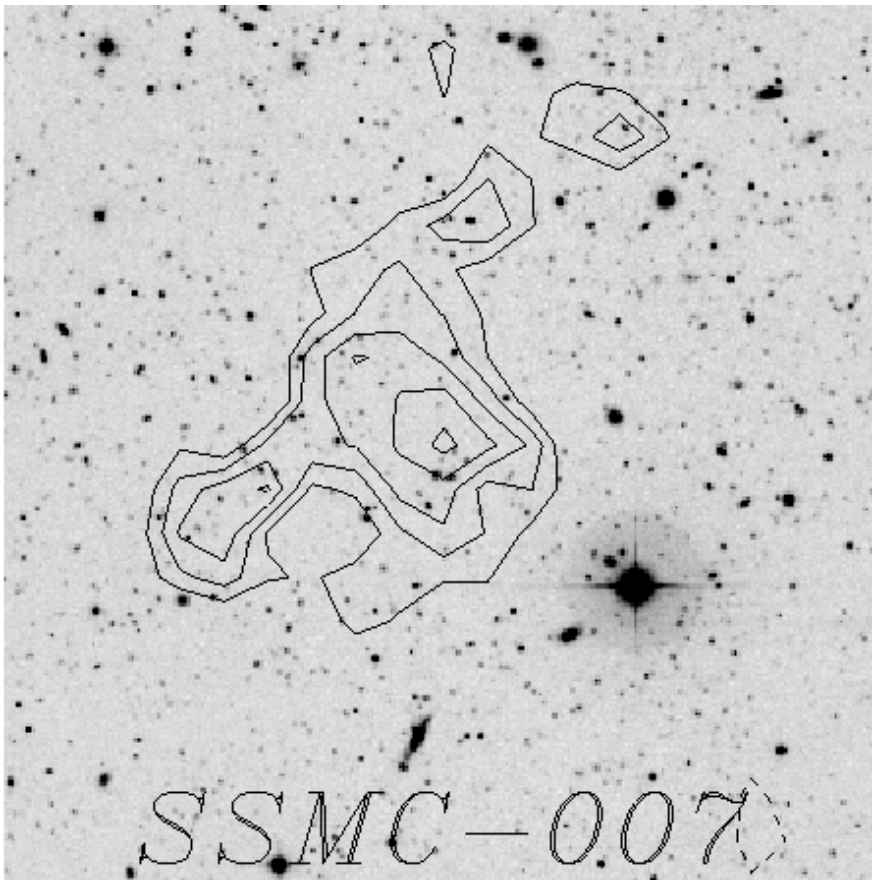

Figure 9.3.: Shear-detection of the dark clump candidate SSMC−007. The contours delineate the detected tangential shear in the image. The contour lines start with a value of 2σ and increase in steps of 0.5σ. The peak significance is 4.2σ. The field shown is $5' \times 5'$ wide (WFI survey at the ESO/MPG−2.2 m telescope). The position of the background quasar 004345.8−294733 is shown in Fig. 9.4.

The controversy – A cluster-sized halo, very poor or devoid of luminous matter, would require a mechanism to drive the gas out of all the smaller halos from which it assembled or from the massive halo itself. Both cases are highly unlikely and there is no well-motivated physical process to explain either scenario. If the gaseous content was still present, one would expect the H atoms to cool, form molecules, clump together and, under the influence of gravity, start to form stars. Thus, preventing star formation would call for a mechanism which hampers the cooling process, yet no such mechanism is currently known.

Dark clumps: Just an illusion? – The noise in weak lensing analyses, due to intrinsic ellipticities of galaxies, can have a profound effect: intrinsic ellipticities may mimic tangential alignment, thereby causing false peaks, boosting or lowering the significance of lensing signals (e.g., Hamana et al. 2003). Another

explanation for the alleged dark clump detections might be some coincidental alignment of a filamentary structure along the line of sight, mocking an important mass concentration only.

The dark galaxy VIRGOHI21 – Using the Arecibo H I flux, Minchin et al. (2005) calculate for VIRGOHI21 a neutral hydrogen mass of $(2 \pm 1) \times 10^8 M_\odot$ but when analyzing the rotation curve, the total neutral hydrogen mass amounts to an order of $10^{11} M_\odot$. Using the Tully-Fisher relation, Minchin et al. estimate VIRGOHI21 to be 12 mag or brighter. However, deep CCD imaging has failed to turn up a counterpart down to a surface brightness level of $27.5\,B$ mag arcsec^{-2}. Is VIRGOHI21 a dark matter halo that contains no stars but only gas?

The Mg II $\lambda\lambda$2796, 2803 *doublet lines in SSMC−007* – In the past, a lot of effort was invested in the quest of finding and understanding metal absorbing systems at low redshift. Mg II absorption systems have been well studied, and their incidence at redshifts $0.1 \leq z \leq 2.2$ as a function of the Mg II rest equivalent width, $W_0^{\lambda 2796}$, is well known. The lensing signal of SSMC−007 is tracing a mass on the order of a galaxy cluster. We therefore may expect a distinct N(H I) excess, which is indirectly detectable through the Mg II $\lambda\lambda$2796, 2803 and Fe II λ 2600 lines (Rao & Turnshek 2000).

9.3. Observation and Data Handling

We proposed to observe the quasar 004345.8−294733 ($V = 19\overset{\text{m}}{.}57$, $z = 1.675$, and $0^{\text{h}}.46^{\text{m}}.12^{\text{s}}.26$ $-29°31'10.7''$) with VLT/UVES at high resolution ($R \sim 42\,500$) in order to verify the possible existence of the dark clump candidate SSMC−007 at $0^{\text{h}}.45^{\text{m}}.58^{\text{s}}$ $-29°30'41''$, and at an estimated redshift range of $z = 0.1 - 0.3$. The latter is estimated from the sample of bright clumps we obtained in our lensing survey. Smaller redshifts can be ruled out by the weak-lensing method itself, and higher redshifts due to the limiting depth of the WFI survey.

63 dark clump candidates have been compared with a database of over 60 000 quasars (see Fig. 9.1), including those of the latest data release from the Sloan Digital Sky Survey (SDSS). The best choice[2] out of this sample is the dark clump candidate SSMC−007 because (1) the weak lensing analyses show a big and robust shear signal above the 4σ-detection limit, (2) the closest back-

[2]There are few other background quasars close by to other dark clump candidates. However, the dark clump candidate SSMC−007 and the quasar 004345.8−294733 is by far the most promising combination for the reasons mentioned hereafter.

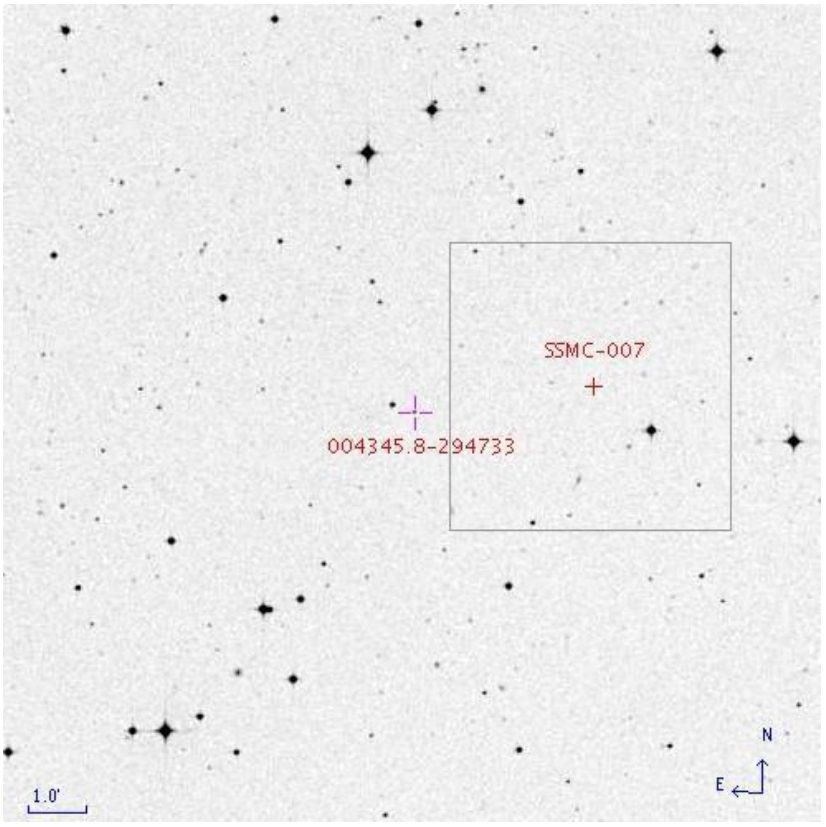

Figure 9.4.: The background quasar 004345.8−294733 ($V = 19\overset{\mathrm{m}}{.}57$, $z = 1.675$) lies $3'9''$ off the center of the dark clump candidate SSMC−007 ($0^{\mathrm{h}}.45^{\mathrm{m}}.58^{\mathrm{s}}$ $-29°\,30'\,41''$), where the square represents the zoom-in shown in Fig. 9.3 (SERC-J DSS1 scan).

ground quasar, 004345.8−294733, lies only $3'9''$ off the estimated center ($3'9''$ correspond to 0.34 Mpc at $z = 0.1$, and 0.84 Mpc at $z = 0.3$, respectively, assuming $H_0 = 71$, $\Omega_M = 0.27$ and $\Omega_\Lambda = 0.73$) and is sufficiently bright to obtain a high SNR spectrum with a $8-10$ m class telescope, (3) the background quasar is at a redshift of only $z_{QSO} = 1.675$, that will prevent the important Mg II $\lambda\lambda$2796, 2803 doublet lines from being blended by intervening hydrogen, (4) no galaxy concentration or other anomalies can be seen in its vicinity, (5) the ROSAT PSPC All-Sky Survey does not detect highly ionized or hot gas, (6) the only galaxy cluster in its proximity (at a distance of $1'47''$) lies at a redshift of $z = 1.10$ and is therefore clearly not responsible for the lensing-signal, and (7) the ESO Imaging Survey (EIS) detected three quasar candidates at distances of $44''$ ($V = 20\overset{\mathrm{m}}{.}15$), $2'18''$ ($V = 20\overset{\mathrm{m}}{.}33$), and $2'31''$ ($V = 20\overset{\mathrm{m}}{.}35$), respectively, which might be highly interesting for further observation in the case of a positive detection (the typical QSO density ($b_J < 20.85$) is ~ 35 QSOs per deg^2, i.e., in average, one would expect the next QSO to be at an average mean distance

of $\sim 5'43''$).

Although the nature of dark clumps is not known, we can expect, by analogy with bright clumps from the same survey, that they lie in a similar distance-range (i.e., $0.1 \lesssim z \lesssim 0.3$) with similar masses. Deriving the expected mass directly from the shear signal leads, in agreement with bright clumps, to $(2 \pm 1) \times 10^{14} M_{\odot}$ for an assumed redshift of the dark clump of $z = 0.2$. In the case of a cluster-mass object and when assuming an isothermal spherical model, we estimate for SSMC−007 a total hydrogen surface/column density of $\sim 10^{-4}\,\mathrm{g\,cm^{-2}}$ and $\sim 5 \times 10^{20}\ \mathrm{cm^{-2}}$ at the projected quasar location. We expect to (1) verify the existence or give detection constraints of a dark-clump-like object and to learn more about (2) its possible substructure, (3) metal abundances, and (4) velocity distribution.

With a $5\,\sigma$ detection and a SNR of 10, we are able to detect Mg II absorption lines having equivalent widths $W_0^{\lambda 2796} \geq 60\,\mathrm{m\AA}$ in the restframe (and $W_0^{\lambda 2796} \geq 70\,\mathrm{m\AA}$ observed), corresponding to a column density of $N(\mathrm{Mg\,II}) \geq 10^{12}\,\mathrm{cm^{-2}}$. The most prominent absorption lines we expect to detect in neutral gas are Mg I and Mg II, Ca II, Mn II, and Fe II, respectively, where the Mg II $\lambda\lambda 2796, 2803$ doublet lines are of greatest interest to the questions we ask. Mg II is a singly ionized species that traces H I commonly associated with galaxy environments, and, as an α-element, it traces the earliest stages of stellar evolution (i.e., SNe II) but is not significantly produced in secondary or later stages. Extensive studies on low and intermediate redshifts of Mg II absorbers have been carried out in the past with great success (e.g., Churchill & Vogt 2001; Churchill et al. 2003). Observations of Mg II in the local Universe (Churchill et al. 1999) imply that the number of random field Mg II systems per unit redshift is $\mathrm{d}N/\mathrm{d}z(\mathrm{Mg\,II}) \approx 0.5$ at $z = 0.2$ and for a column density limit of $\sim 10^{12}\,\mathrm{cm^{-2}}$. This means, in the case of our dark clump sight line with $\Delta z = 0.2$, that the chance to detected random-field Mg II absorbing system is only 10 percent. Therefore, any Mg II absorption at $z = 0.2$ in our data will be associated with a 90 percent chance to the dark clump.

9.3.1. Telescope and Time Justification

For the analysis we require a high-resolution spectrum because Mg II absorbing systems typically contain a subcomponent structure, having a characteristic strength of $W_r(2796) \simeq 0.1\,\mathrm{\AA}$ (Petitjean & Bergeron 1990). This calls for a $8-10\,\mathrm{m}$ class telescope, making the VLT/UVES the first choice for this kind of observation.

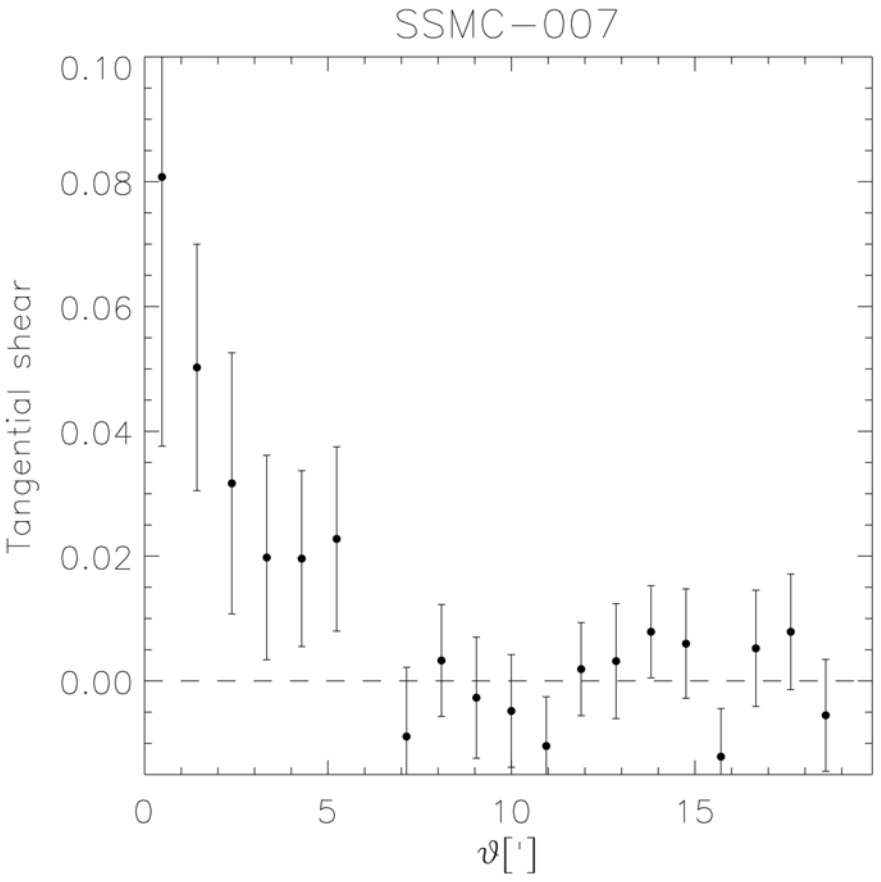

Figure 9.5.: This plot shows the azimuthally averaged strength of the tangential shear as a function of distance from the centre (the position of highest significance) for the dark clump candidate SSMC−007. Note that all data points are independent and that the signal can be traced out to a distance of $\sim 5'$ (WFI / M. Schirmer).

The Mg II $\lambda\lambda$2796, 2803 doublet lines are the main target of our analyses. They are easy to identify as we do not have any interference with Ly α forest lines. We aim at detecting Mg II absorbing systems with rest-frame equivalent widths larger than 0.1 Å and therefore require a high-resolution spectrum of $R \sim 42\,500$ ($\sim 7\,\mathrm{km\,s^{-1}}$ on the velocity scale). At the given redshift range and the resolution requirements, we adopted a setting of Dic#1 346 (blue arm) CD1 binning 2×2, and Dic#1 564 (red arm) CD3 binning 2×2, which covers the spectral range of $\sim 3050 - 3880$ Å, and $\sim 4640 - 6640$ Å, respectively. For achieving a spectral resolution of $\sim 42\,500$, a $1''$-slit was used. The bluest setting, centered at 3460 Å and starting at ~ 3050 Å, is very close to the atmospheric cutoff. This setting allows us to obtain the Mg II doublet lines in the lower spectral band, i.e., the lower redshift range, too. For 11 hours integration

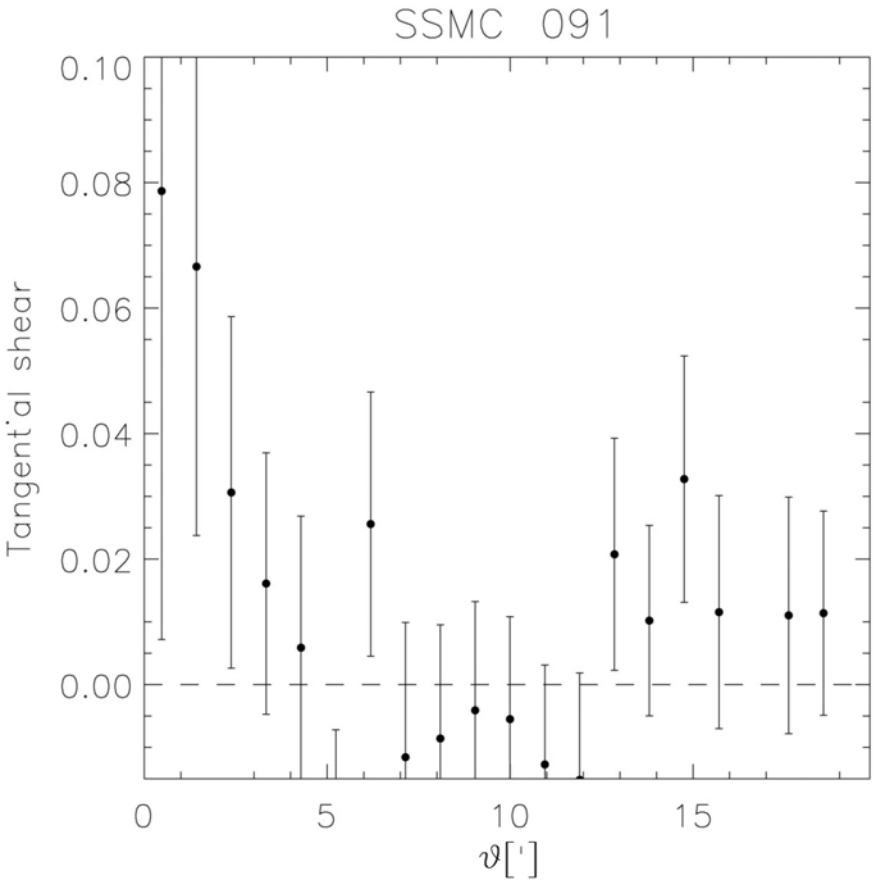

Figure 9.6.: This plot shows the azimuthally averaged strength of the tangential shear as a function of distance from SSMC-091, a cluster-mass mass detection with an optical counterpart (*bright clump*). Comparing also with other lensing-signals with optical counter parts, we find that the tangential shear signal seen in SSMC−007 is not unusual but typical if compared to bright clumps (WFI / M. Schirmer).

time on the quasar 004345.8−294733 ($V = 19\overset{\text{m}}{.}57$), the ESO/UVES Exposure Time Calculator (ETC) gives SNR ~ 6.2 for the Mg II $\lambda\lambda$2796, 2803 range at $z = 0.2$. A later pixel binning will boost the SNR above a value of 10. Taking into account one hour overhead we had asked for 12 hours observing time.

9.3.2. Waiver Request and Conducted Observations

Because of the relatively faint target it is most helpful to have longer exposure times in order to circumvent difficulties in extracting low signals from the blue camera. We therefore requested a phase 2 waiver in order to be able to exceed the execution time limit of 1 h. We asked for 5576s exposure time for each of

the seven OBs, leading to a total exposure time of 10 h 50 min 32 s and a total execution time of 11 h 59 min 57 s (p2pp version 2.10). Our waiver request was granted and all seven OBs were observed – using the telescope settings described above – between July 31 and September 23, 2006.

9.3.3. Data Handling

The raw data were reduced using the UVES pipeline implemented in the ESO-MIDAS software package. The pipeline reduction includes flat-fielding, bias- and sky-subtraction and a relative wavelength calibration. The individual spectra then have been coadded and corrected to air wavelengths. The SNR per resolution element in the spectrum ranges from 15 at 3360 Å to a maximum of 27 around 5100 Å. The spectrum was analyzed using the FITLYMAN program (Fontana & Ballester 1995) implemented in the ESO-MIDAS software package. The routine uses a χ^2-minimization algorithm for multi-component Voigt-profile fitting. Simultaneous line fitting of the high-resolution spectrum allows us to determine the column density, N, and the Doppler parameter, b.

9.4. Absorption Line Detections

The putative absorption system is predicted by the weak lensing analysis to be in the redshift range of $z = 0.1 - 0.3$, while the spectrum obtained with UVES covers the wavelength ranges from $3050 - 3870$ Å, $4625 - 5595$ Å, and $5680 - 6650$ Å. The transition lines of our main interest are, of course, the Mg II $\lambda\lambda$2796, 2803 doublet lines, but we have also looked for other (double) transition lines with strong oscillator strengths that fall into the corresponding range of our spectrum. These are: Mg I $\lambda\lambda$2026, 2852, Mg II $\lambda\lambda$2796, 2803, S II λ2515, Ca II $\lambda\lambda$3934, 3969, Fe I $\lambda\lambda$2166, 2463, 2484, 2501, 2523, 2719, 3021, 3720, Fe II $\lambda\lambda$2344, 2374, 2382, 2586, Zn I λ2139, Zn II $\lambda\lambda$2026, 2062, 2139, and Cr II $\lambda\lambda$2056, 2062, 2066. We find several absorption features with typical equivalent widths of $W \sim 0.5$ Å: nine such absorptions are below the quasar's H I Ly α emission (at 3251.9 Å), nine in the range of $4625 - 5595$ Å, and only one in the range of $5680 - 6650$ Å.

9.5. Expected Results and Discussion

The redshift of a possible baryonic mass concentration, e.g., a gas cloud, is not known but can only be restricted by the predictions from the weak lensing measurements ($z = 0.1 - 0.3$). Hence, we have to search for two or more transition lines of the same species in order to detect a potential alignment in a velocity plot of a given restframe. We have varied the latter from $z = 0.1$ to $z = 0.3$ (and even up to $z = 0.5$) but could not confirm any positive agreement. Fig. 9.8 shows a representative part of the spectrum, more precisely, it is the region where Mg II absorption would take place if any magnesium in this phase along the LOS would be present at a redshift of $z_{\rm abs} = 0.2$. What we would expect to observe, however, is shown in Fig. 9.7. Consequently, we have to conclude that we cannot confirm the presence of a significant (baryonic) mass concentration as this is predicted by the weak lensing signal. For the case of Mg II, any gas cloud that gives rise to a column density of $\log N(\mathrm{Mg\,II}) \geq 12$ would have been detected in our analysis.[3]

Possible Scenarios

Pure DM halo – One possible explanation for the non-detection of any of the species we have been searching for could be that the dark clump candidate SSMC−007 contains only very little (no) baryonic matter, i.e., that the detected lensing signal is due to a (pure) DM halo. Why such a DM halo should form without any baryonic matter content or what kind of stripping mechanism could separate the baryonic matter from the DM is not known. The concept of DM – together with the concept of dark energy – is not only strongly suggested by numerical models but is also widely accepted in the scientific community. However, the reader should keep in mind that the nature of DM still remains unknown and that DM has never been directly observed down to the present day. Further, note that in the past the concept of DM has been fundamentally questioned by several authors (see, e.g., Milgrom 1983; Desai et al. 2004; Dodelson & Liguori 2006).

False lensing signal – Could it be that we are chasing an object that is not there at all? This possibility, as uncomfortable it might be, has to be considered as well. It is possible that the lensing signal does arise from a tangential chance

[3] The detection significance is similar for the other species mentioned in Section 9.4, i.e., we could have confirmed a positive detection in the case of two or more transition lines of the same element, X, with column densities of $\log N(X) \geq 12$.

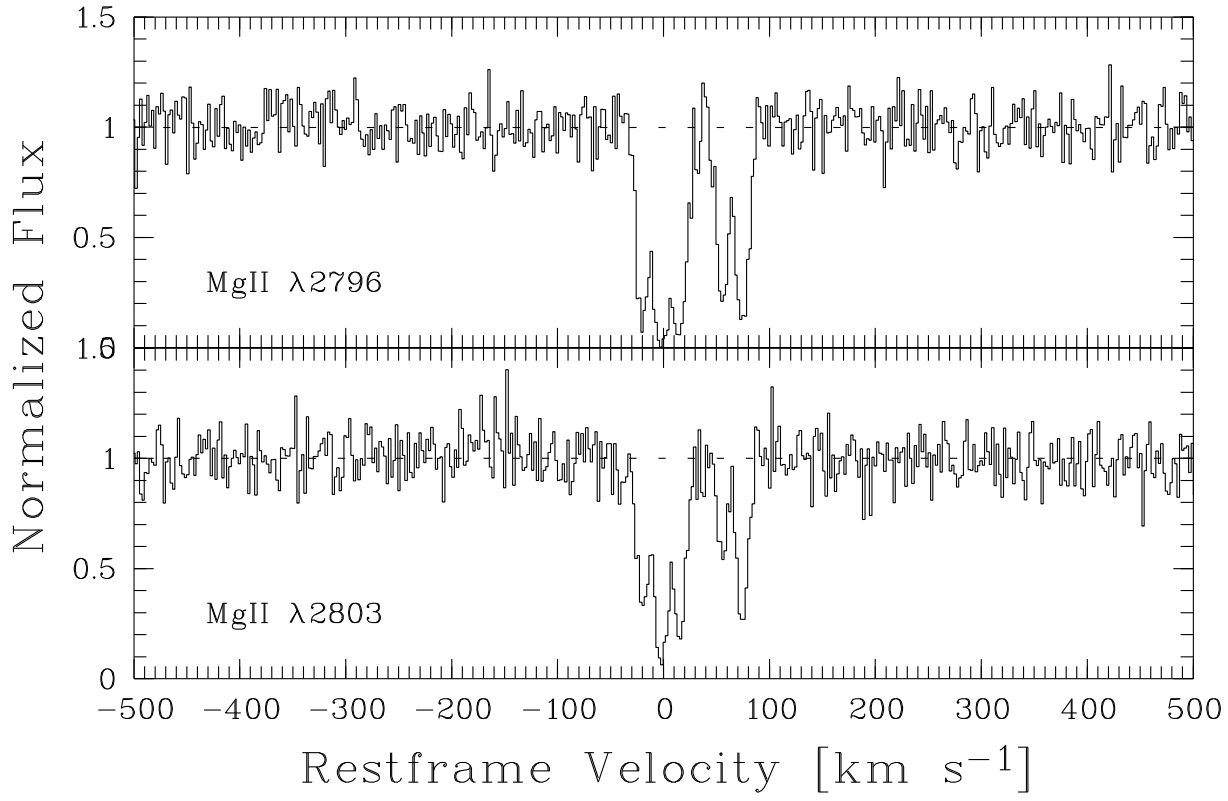

Figure 9.7.: A typical absorption feature that we would expect to find. For illustration, we have chosen $z_{\rm abs} = 0.2$ and, in analogy with the Mg II absorption detection in the sub-DLA system toward the quasar HE 0001−2340 (Richter et al. 2005), column densities varying from $\log N({\rm Mg\,II}) = 12.4$ to 13.5 and a velocity dispersion of about 100 km s^{-1}. Additionally, the (synthetic) spectrum was blurred with a poissonian noise that results in a final SNR of 10.

alignment of the measured background galaxies, hence, that the lensing signal is not real in the sense that it does not arise because of a significant mass concentration. The occurrence of such statistical flukes is, indeed, common in large fields. However, the dark clump candidate in this study was chosen (among other favorable criteria) because of its robust lensing signal and because of the relatively narrow field within which it was detected. Therefore, a false lensing signal cannot be excluded, though it seems unlikely.

Fully ionized gas – The potential well of such a dark clump is enormous and infalling gas will inevitably be heated by collisional ionization. Fully ionized gas can no longer be detected in absorption and could explain why we were unsuccessful in finding any absorption lines in the here presented case. However, without any ongoing star formation and, hence, without any energy input

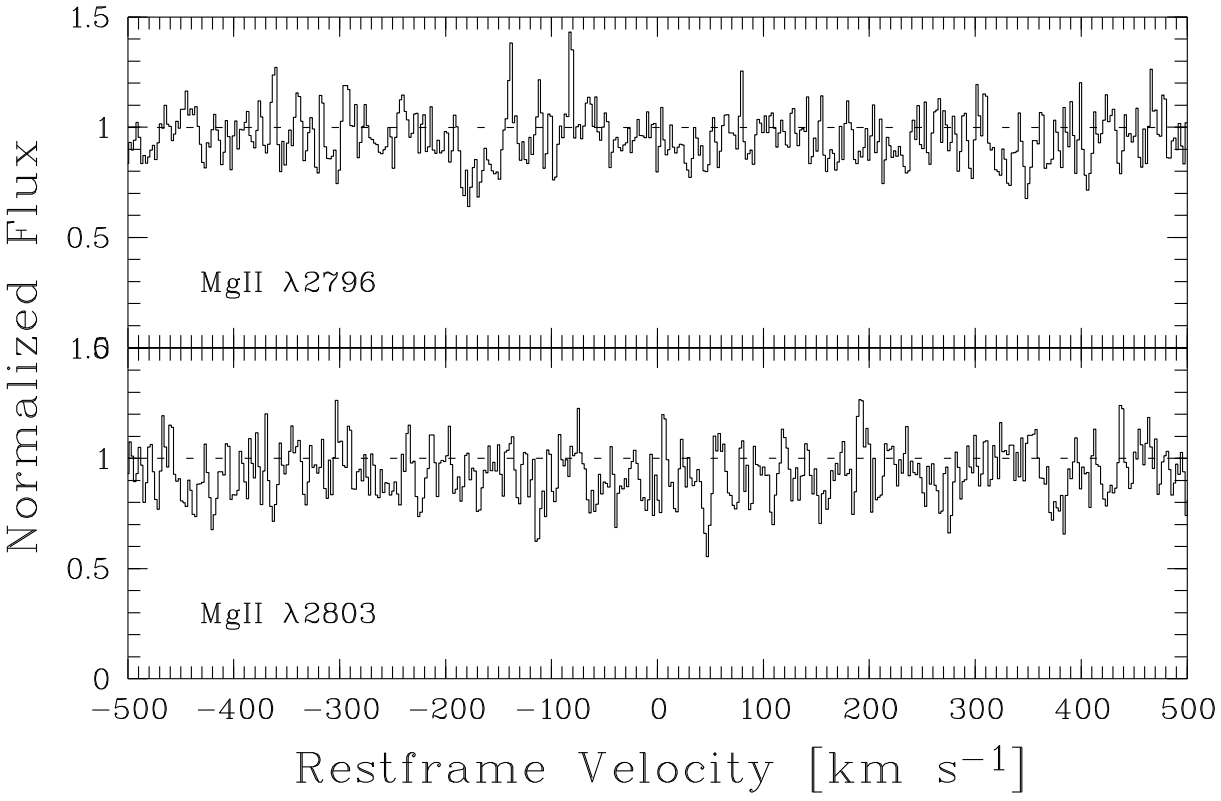

Figure 9.8.: Representative part of the observed spectrum. For illustration, the wavelength was chosen such that any Mg II absorptions features at $z_{\rm abs} = 0.2$ and with $\log N({\rm Mg\,II}) > 12$ would be easily observable (LOS toward the quasar 004345.8−294733).

that could maintain the gas fully ionized, it is not clear what kind of mechanism could prevent the gas from cooling. Further, hot and fully ionized gas would be detected in X-ray observations (what is not the case) for SSMC−007. These are two strong arguments that speak against the possibility that the detected lensing signal could be caused by fully ionized gas.

Unusual matter distribution – The background quasar 04345.8−294733 with an impact parameter (offset) of $3'9''$ lies (in projection) only 0.34 Mpc ($z = 0.1$) to 0.84 Mpc ($z = 0.3$) away from the mass center that is predicted by the weak lensing analysis. The predicted mass is on the order of a galaxy cluster and, hence, there is a realistic chance that the LOS toward 04345.8−294733 passes through a galaxy or the outskirts of a galaxy of this cluster. Even if this should not be the case, we would expect the intracluster medium[4] (ICM) to

[4] with typical temperatures of $\sim 10^7 - 10^8$ K and typical densities of $\sim 10^{-27}$ g cm^{-3}

give rise to column densities large enough to be detected by our observation. Assuming that there actually is such a mass concentration as predicted by the lensing analysis, the non-detection in our study could possibly be explained by an unusual matter distribution that differs from typical galaxy clusters or "bright clumps". However, there is no evidence from numerical model calculations or from observation that the mass distribution in galaxy clusters could possibly be altered in such a radical manner.

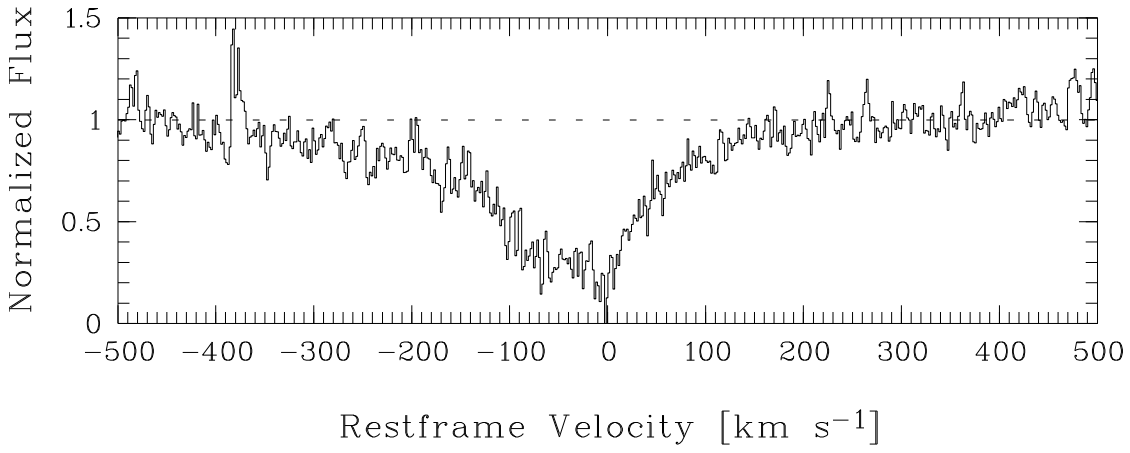

Figure 9.9.: Unknown broad absorption feature observed at 5900.9 Å (LOS toward the quasar 004345.8−294733).

Finally, we want to mention that the absorption feature seen at 5900.9 Å is with an equivalent width of $W > 2.5$ Å by far the broadest and most prominent absorption feature we detect (see Fig. 9.9) – even when compared with the absorptions seen below the 3251.9 Å, i.e., in a range where H I Ly α absorption could take place. Even though this absorption feature shows possible damping wings, we can obviously exclude that this absorption is caused by hydrogen. An extended search with a redshift range of $z = 0.1 - 0.5$ and all possible transition lines that fall into this range in regard was, unfortunately, also without success. The possibility that we observe an effect that is intrinsic to the quasar or due to the instrument itself, cannot be excluded but is unlikely. Hence, the question about the nature of this absorption feature, and if it could possibly explain the gravitational distortion detected by weak lensing, has to remain unanswered at this point.

10. The Line of Sight toward PKS1448−232: Temperature and Ionization of the IGM at $z \sim 2$

10.1. Introduction

This chapter addresses, like Chapter 6, 8, and Chapter 9, one observational project and describes it in detail. In this case it is the ESO project 077.A-0646(A) – "Temperature and Ionization of the IGM at $z \sim 2$" (PI / CoI: Erni / Richter). Despite the A-priority assigned by the ESO Observing Programmes Committee (OPC) panel to this project, unfortunately, only 6 to 12 observation blocks (OBs) in total were observed in service mode during Period 77 (P77: April 1, 2006 - September 30, 2006). There is justified hope that this observation will be completed during the succeeding periods, though not in time that the data could be analyzed and included in this thesis. Below I will give a summary of the driving idea behind this project as well as some technical details. A preliminary analysis of some portion of these incomplete data is presented at the end.

10.2. The driving Idea behind this Project

As seen to a large extent in the ESO public Large Program (LP) titled "The Cosmic Evolution of the Intergalactic Medium"[1], many O VI and C IV absorbing

[1]The LP (Program ID 116.A-0106A) consists of around 40 nights allocated for the observation of about twenty quasars at high signal-to-noise (SNR ~ 50) and high resolution ($R \sim 40\,000$). These observations are done with UVES at the VLT/Kuyen telescope. This large UVES survey aims at (1) characterizing the transition in the evolution of the IMG as traced by the Ly α forest, (2) investigating the clustering of low column density structures and metal-enriched regions as a function of z and $N(\mathrm{H})$, (3) estimating the IGM metal-enrichment and its evolution in time and constraining the enrichment process, (4) determining the intensity and shape of

systems apparently consist of a wealth of intrinsically narrow sub-components with Doppler parameters less than $\sim 7\,\mathrm{km\,s^{-1}}$. Even with the excellent "standard" resolution of UVES of $R \sim 40\,000$, these sub-components cannot be resolved and hence appear to consist of larger and fewer components than it is the case in reality. However, a UVES spectrum at very high resolution ($R \sim 75\,000$) would allow us to resolve the intrinsic structure in O VI and C IV absorbing systems and thereby to deduce crucial parameters in order to unveil the ionization mechanism of the IGM at redshifts of $z \sim 2$. We therefore proposed to observe the QSO PKS 1448−232 ($z_{\mathrm{em}} = 2.208, V = 16.9$), already observed within the frame of the LP, but this time with the UVES maximum resolution.

For Period 77 the ESO OPC panel granted a total time of 13 h to the programme 077.A-0646(A) – "Temperature and Ionization of the IGM at $z \sim 2$" (PI / CoI: Erni / Richter).[2]

10.3. Scientific Rationale

Physical conditions and state of the IGM at $z \sim 2$

The ionization state of the IGM is the key to understand the nature, distribution, and evolution of the gaseous intergalactic matter at low to intermediate redshifts ($z \sim 2-4$). Numerical model calculations of hierarchical structure formation of the Universe (Cen & Ostriker 1999a; Davé et al. 2001) imply that in this redshift range a large fraction of baryons resides in the IGM in the form of hot and ionized gas. This gas can be traced by the absorption of O VI and C IV where the absorption lines fall for $z \sim 2$ into the optical part of the spectrum. For this reason ground based spectrographs on a $8-10\,\mathrm{m}$ class telescope, like UVES at VLT Kuyen, are the best choice for this investigation. The physical conditions (like the temperature and ionization) of the IGM are expected to show strong evolutionary effects from high to low redshifts. Absorption line studies with FUSE and STIS in the low-redshift regime at $z < 1.5$ (see e.g., Tripp et al.

the UV ionizing background flux, (5) determining the occurrence, ionization level, and cosmological evolution of the O VI phase, and (6) reconstructing the thermal history of the IGM from $z \sim 2-5$.

[2]OPC comment for the programme: *This is a very good project with the goal to constrain the physical state of O VI absorbing gas at $z = 2$, and discriminate between photoionization and shocks. The proposal convincingly argues why high resolution is needed to resolve the velocity width and potential blends in O VI systems. One concern is that the observations are very challenging, near the atmospheric cutoff, and would be considerably easier to perform at only slightly higher redshift, a point which could have been addressed. The proposal was very well ranked (in the top quartile) and was fully recommended.*

2000; Richter et al. 2004) imply the existence of a warm-hot IGM (WHIGM) phase with a temperature of $T \approx 10^5 - 10^7$ K. These UV measurements are limited in resolution and cannot rule out photoionization, but they are consistent with the concept of a collisionally ionized gas phase. Yet the situation for redshifts of $z \sim 2$ and above remains uncertain (Carswell et al. 2002; Simcoe et al. 2002) and is what we intend to study here. Theoretical model calculations (Theuns et al. 2002) show that galactic winds are probably the major cause for collisionally ionized gas at higher redshifts. Identifying and separating this gas phase from the photoionized gas phase is important and a crucial factor in constraining feedback processes in the IGM. This constrictions are important because feedback processes in the IGM play a key role in galaxy formation theories. Possibly, the more tenuous regions at higher redshift are photoionized by a hard UV background radiation, while collisional ionization dominates the regions with higher column densities. Clearly, spectra with high resolution and high SNR are required to investigate the complicate ionization conditions at $z \sim 2$ via O VI and C IV absorption. O VI / C IV column density ratios serve as powerful spectral diagnostics to investigate the ionization conditions in the hot IGM. The line width, characterized by the Doppler parameter, yields important information on the temperature of the gas. According to (4.6), the Doppler parameter is, for the case of pure thermal broadening, accurately approximated by $b_{\rm th} = 0.129\sqrt{T/A}\,[{\rm km\,s^{-1}}]$, with A the atomic weight. In the case of oxygen ($A = 16$) and photoionized gas ($T \approx 2 \times 10^4$ K) it is $b_{\rm th} \approx 4.5\,{\rm km\,s^{-1}}$. Hence, we need high resolution date in order the measured narrow line widths that will yield stringent upper limits for the temperature and will allow us to identify photoionized gas with $T \sim 10^4$ K.

Previous observations suggesting the existence of narrow O VI absorbers

The data from the ESO LP "The Cosmic Evolution of the Intergalactic Medium" suggest that there are many narrow O VI absorbers (with $b \leq 10\,{\rm km\,s^{-1}}$) present yet not resolved. O VI absorption lines that narrow are associated with photoionized gas with temperatures below $\sim 10^5$ K, i.e., temperatures at which collisional ionization from O V to O VI cannot take place. Recent UVES measurements of O VI and C IV absorbers at $z \sim 2$ have shown that many of these systems exhibit significant small-scale structures. Fig. 10.1 illustrates the b-value distribution of O VI absorbers toward the quasar Q 0329−385, based on intermediate-resolution data from the ESO LP (Bergeron et al. 2002). The b-value cut-off at around $6\,{\rm km\,s^{-1}}$ is due to the limited spectral resolution. Even

though the UVES "standard" resolution of $R \sim 40\,000$ is sufficient for most studies, it does, however, not suffice to resolve smaller velocity structure at scales (≤ 6 km s^{-1}). It is crucial to entirely decompose the overall O VI absorption structure and to derive accurate O VI/C IV column density ratios without systematic errors from unresolved velocity components.

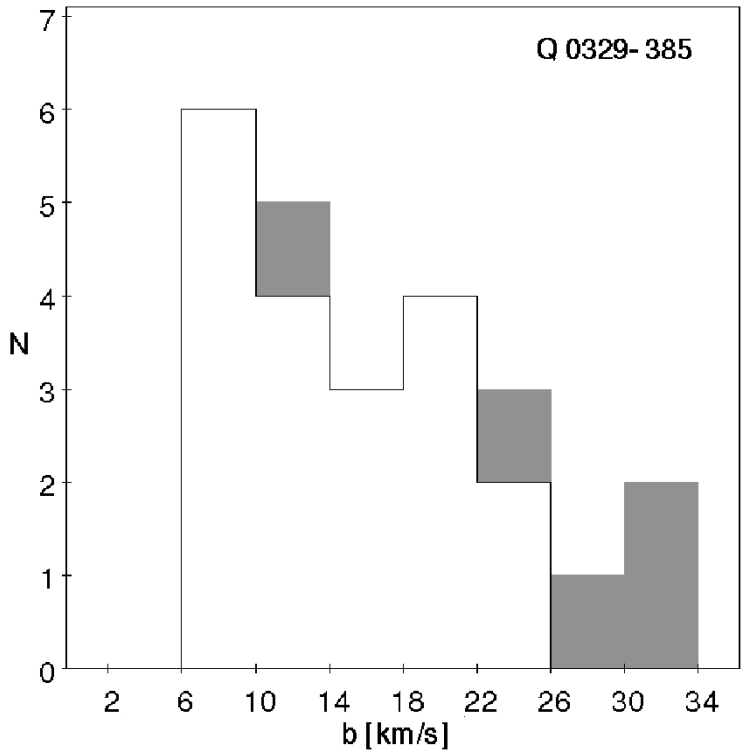

Figure 10.1.: Number distribution of O VI b-values in IGM absorption line systems along one line of sight from the Large Programme (Q 0329-385; Bergeron et al. 2002). The number distribution rises toward lower b-values with a cut-off at ~ 6 km s^{-1}, which indicates the point at which further possible sub-components with lower b-values cannot be resolved.

While the UVES Large Programme is designed to study the IGM at $z = 1.5 - 5$ along a large number of sight lines at "standard" resolution ($R \sim 40\,000$) in order to improve the statistics on intervening absorption line systems, we suggested to re-observe one of the object from the ESO Large Programme, the quasar PKS 1448−232, at very high resolution ($R \sim 75\,000$) in order to (1) improve our knowledge of the narrow absorption components in this spectrum, (2) to understand their implications for interpreting and understanding spectra at lower spectral resolution, and (3) to improve on our understanding of the ionization state of the IGM at $z \sim 2$.

10.4. Immediate Objective

The quasar PKS 1448−232 at high resolution

In our ESO programme 077.A-0646(A) we proposed to observe the quasar PKS 1448−232 ($z = 2.208, V = 16.9$) with UVES on VLT/Kuyen at very high resolution ($R = \lambda/\Delta\lambda \sim 75\,000$, corresponding to a velocity resolution of $\sim 4\,\mathrm{km\,s^{-1}}$ at 4000 Å) in order to study at high precision the (1) O VI / C IV column density ratios, (2) the *b*-value distribution, and (3) the velocity structure of the O VI and C IV absorption features in several intervening IGM absorbers along this line of sight with high precision. We have chosen the line of sight toward PKS 1448−232 because it contains a variety of particularly interesting O VI and C IV systems with pronounced small-scale velocity structure. These will be the highest resolution observations of a QSO taken so far, superceeding previous observations of Q 1422+231 with KECK (Rauch et al. 1999). The data will demonstrate impressively the powerful capabilities of the UVES instrument. Spectroscopic data with high resolution and with a high SNR for background objects with $V \approx 17$ require observations with a $8-10\,\mathrm{m}$ class telescope, as demonstrated by the UVES Science Verification and previous results obtained with the KECK telescope. UVES on VLT/Kuyen is the only instrument that allows us to study the important redshift range between $z \sim 1.5-2.5$ at the requested resolution.

O VI substructure

In Fig. 2 we show an example for such a particularly interesting O VI system toward the quasar PKS 1448−232, located at $z = 2.166$. Clearly, this systems exhibits significant velocity substructure. The current UVES data (~ 7 km s^{-1} resolution) imply the presence of at least 8 individual velocity components. Probably, there are many more velocity components present that are very narrow and thus yet unresolved. As long as these sub-components remain unresolved, any profile fitting to this system will lead to erroneous results with respect to *b*-values and column densities. To obtain realistic values for this complex O VI system, higher-resolution data for O VI is required. This observation can be regarded as a test case for our studies on the temperature evolution of the IGM with data from the ESO LP.

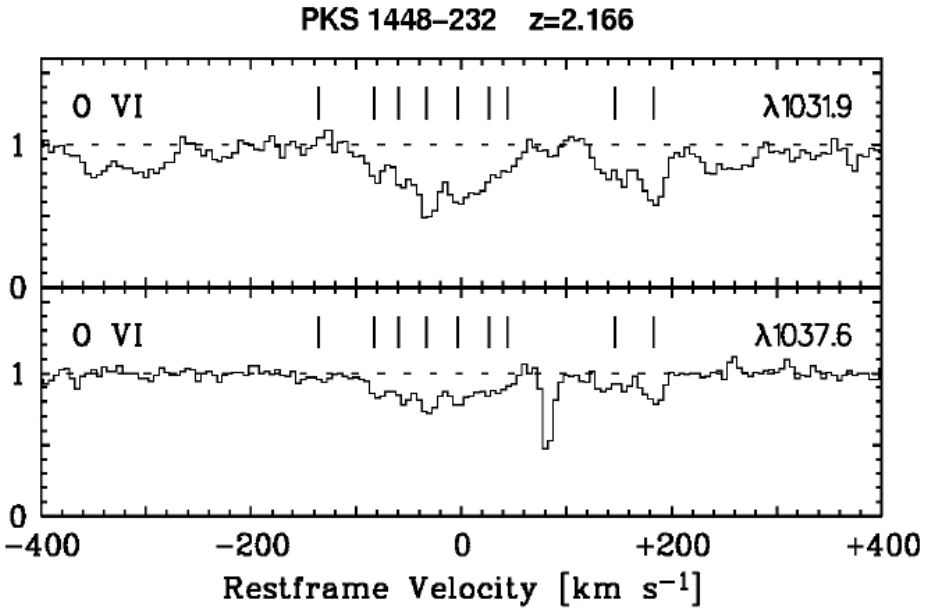

Figure 10.2.: Example for a complex O VI system at $z = 2.166$ toward the quasar PKS 1448−232 from data of the Large Programme. $7 - 8$ individual O VI absorption components are visible (as indicated by the tic marks). More velocity sub-components most likely are present, but they cannot be resolved in these ESO/LP intermediate-resolution data.

C IV substructure

Besides O VI we are also interested in the small-scale structure of the C IV absorption. In fact, with the new observations of PKS 1448−232 we will gain resolution particularly for the C IV part of the spectrum, from which we can conclude on those O VI absorbers that follow the distribution of C IV. This aspect is important for two reasons: (1) to learn more about the incidence of O VI absorbers related to photoionized gas, and (2) to investigate the possible influence of a sub-component structure on the interpretation of *b*-values of highly ionized ions. The latter point is particularly important for other UVES sightlines for which high resolution data will not be available. Unresolved substructure will probably bias the number distribution for *b* toward the higher end, since at lower resolution several narrow lines with low *b*-values may give the appearance of one single component with a high *b*-value.

Possible shift in the absorption centroids of O VI and C IV

The third important aspect of our high-resolution observation, next to the substructure components of O VI and C IV lines, is that we can obtain information on the ionization mechanisms by looking for possible velocity differences of O VI and C IV by measuring the mean absorption centroids over all components. If photoionization is dominant for some of these systems, absorption by O VI and C IV may actually occur in physically distinct regions that could possibly be separated in velocity space by a few $\mathrm{km\,s^{-1}}$ only. With the high-resolution data for PKS 1448−232 we will have the opportunity to search for such possible offsets.

10.5. Strategy

We aim at a high SNR at the highest resolution (over the C IV range) compatible with the brightness of the background quasar PKS 1448−232. With a slit of 0.5 arcsec we can achieve very high resolution on the order of $R \sim 75\,000$. With such an excellent resolution we can resolve C IV lines even for thermal broadening at temperatures as low as $T = 10^4$ K (see above). We will make use of a UVES standard setting, using the dichroic beam-splitter DIC#1 and CD3 R564, 0.5″-slit, 1×1 binned for the red arm, and DC1 B346, 0.8″-slit, 2×2 binned for the blue arm. Note that the choice in the blue arm is a compromise between higher resolution (the slit is narrower than the standard observations we have used up to now) and a decent SNR. For one hour integration time on PKS 1448−232 ($m_\mathrm{V} = 16.^\mathrm{m}9$) the ETC V 3.0.6 gives SNR ~ 15 over the C IV wavelength range. Therefore, in 11 h we should achieve a SNR $\sim$ 50 . Taking into account two hours overhead we request 13 h observing time.

10.6. Continuation of the Project

Unfortunately, ESO scheduled our programme 077.A−0646(A) by mistake in B-priority although the ESO OPC panel ranked it in A-priority. Consequently, only 6 of 13 OBs in total were observed during P77. With only 6 OBs it is not possible to fully exploit the data and to achieve our scientific goal. Therefore, I have asked for 7 additional hours on UVES/VLT for P79 (April 1, 2007 - September 30, 2007) in order to complete the data set (Proposal ID 079.A-

0303). Our proposal was accepted by the ESO OPC panel, ranked in A-priority, and obtained the highest ranking in its category.[3]

10.7. Analysis of the hitherto existing Data

Although the SNR in the current data is not as good as it would be with 13 OBs in total, we have preliminarily analyzed the spectrum. We find that the data from our high resolution (HR) proposal, to some extent, already unveil a somewhat more complex structure than what is found in the LP data. In particular, we have analyzed the C IV $\lambda\lambda$1548, 1550 and the O VI $\lambda\lambda$1031, 1037 transition lines for an ionized absorption line system at $z_{\rm abs} = 2.11$. In the regions of the C IV $\lambda\lambda$1548, 1550 and the O VI $\lambda\lambda$1031, 1037 transition lines we measure for the HR (LP) data a SNR per resolution element of 24 (193) and 2 (33), respectively, and a SNR per pixel element of 18 (101) and 1 (19), respectively. The C IV and O VI absorption features at about -25 to $+10\,{\rm km\,s^{-1}}$

Table 10.1.: Outcome of a simultaneous fit with four (three) components for the HR (LP) spectrum in a velocity restframe at $z_{\rm abs} = 2.11$. We find a very good agreement between the two different data sets. Apparently, the incomplete HR data hold information with at least the same quality as the LP data, although the SNR of the previous is distinctively lower. The asterisks denote forced fitting parameters. In the case of the two smaller absorption lines of the HR data, we had to restrict the Doppler parameter to $b \geq 2.5$. Otherwise, the `FITLYMAN` output yields unrealistically small b values (possibly due to the low SNR).

LP line centers $[{\rm km\,s^{-1}}]$	-23	-13	$+11$	
$\log N$(C IV)	12.91	12.82	12.21	
b $[{\rm km\,s^{-1}}]$	9.7	3.3	3.3	
$\log N$(O VI)	13.74	14.20	13.56	
b $[{\rm km\,s^{-1}}]$	13.8	11.7	6.2	
HR line centers $[{\rm km\,s^{-1}}]$	-22	-18	$+2$	$+10$
$\log N$(C IV)	12.94	12.79	12.19	11.98
b $[{\rm km\,s^{-1}}]$	9.7	3.3	3.2	2.5*
$\log N$(O VI)	13.74	14.16	13.07	13.80
b $[{\rm km\,s^{-1}}]$	13.8	7.5	2.5*	11.2

[3] OPC comment for the programme: *A very good and clear proposal that was already started in a previous cycle. The panel expects that these observations will help in tackling the long-standing issue of the very narrow fine structure in* O VI *and* C IV *absorbers.*

(relative to a velocity restframe at $z_{\rm abs} = 2.11$) in the LP data can accurately be fitted simultaneously with a 3-component fit. For the line centers FITLYMAN yields -23, -13, and $+11\,{\rm km\,s^{-1}}$, respectively (see Fig. 10.3). In the case of the HR data we find that a 4-component fit is more adequate. FITLYMAN yields line centers with -22, -18, $+2$, and $+10\,{\rm km\,s^{-1}}$, respectively (see Fig. 10.4). The corresponding column densities and Doppler parameters are summarized in Table 10.1. When we compare the outcome of the fit from the HR data with the outcome from the fit of the LP data we note that fits of the two dominant and redmost components are in very good agreement (within 0.03 dex). This is, however, not the case when the smaller component from the LP data is compared with the two smaller components from the HR data. We note that the column densities derived from the LP data are larger by 0.19 dex in the case of C IV, and larger by 0.49 dex in the case of O VI. However, this discrepancy should not be overemphasized because it is most likely due to a marginally different continuum placement (due to the lower SNR ratio), for which the higher column densities are, of course, less sensitive.

Given the low *b*-values in Table 10.1 the question might arise how this can be possible. The motivation for this proposal was to obtain a high-resolution spectrum ($R \sim 75\,000$) that allows us to identify components in the absorption system's substructure with widths below $\sim 7\,{\rm km\,s^{-1}}$. Why the need for a spectrum with $R \sim 75\,000$ if, apparently, a spectrum with $R \sim 45\,000$ can do the job? As the reader may have guessed, this is not the case. The *b*-value indicated by FITLYMAN includes always the resolution limit (e.g., $7\,{\rm km\,s^{-1}}$) if the total *b*-value (a convolution of the resolution width and the *b*-value derived from the fit) is above the resolution limit. However, if the *b*-value that is derived from the fit drops below the resolution limit, then the FITLYMAN program will yield the *b*-value derived from the fit only and will omit to include the width of the resolution limit. Hence, in the latter case, no information can be drawn from the *b*-values.

Although the scientific goal of our proposal cannot be achieved with this (incomplete) data set, we clearly show here that a full data set, i.e., a QAL spectrum with a resolution of $R \sim 75\,000$ and high SNR, holds an enormous potential and will yield interesting findings about narrow substructure features that could not be resolved by previous observations (with typically $R \sim 45\,000$). Hence, we expect new and insightful findings about the temperature and ionization of the IGM at $z \approx 2$.

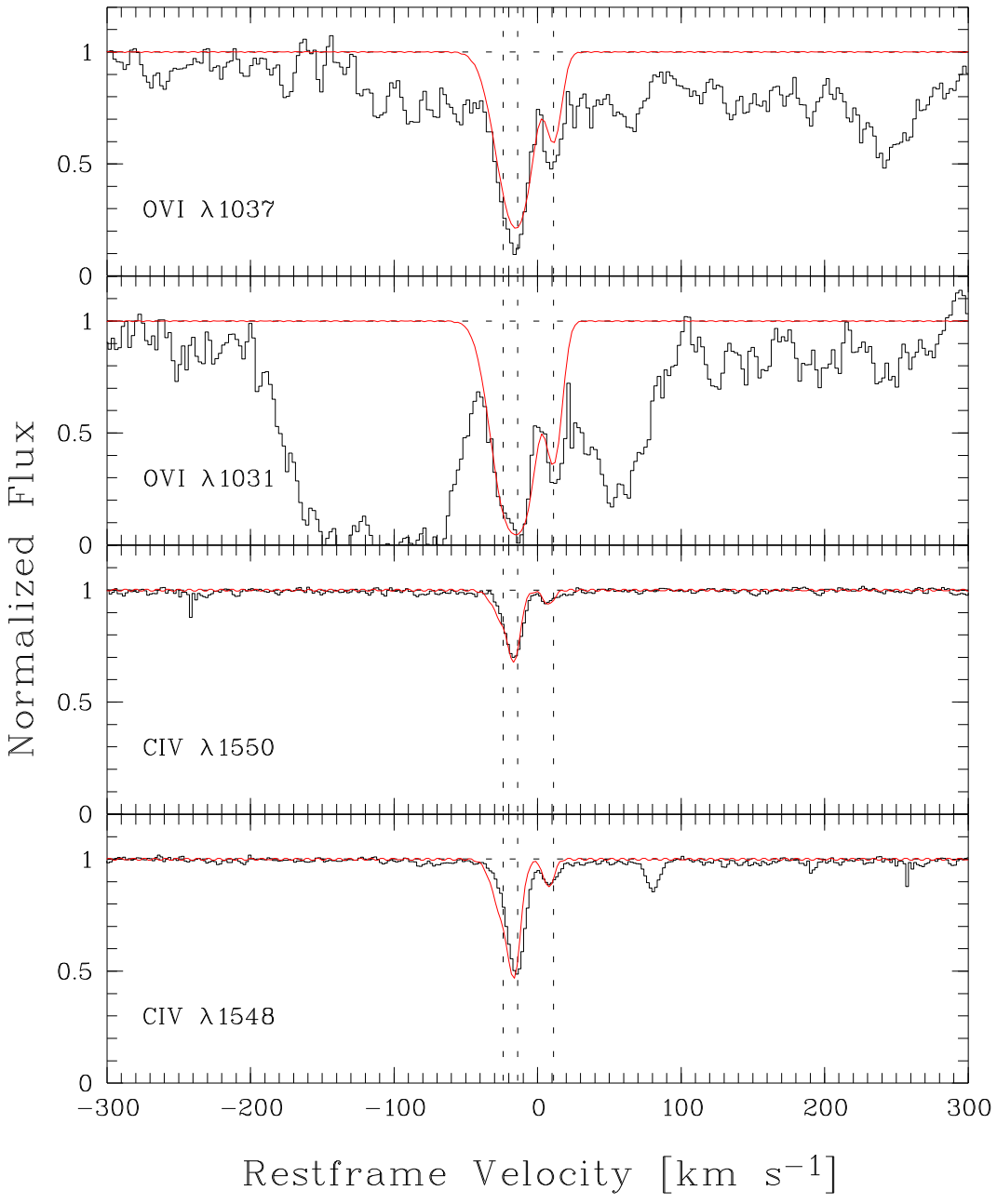

Figure 10.3.: C IV and O VI absorption feature at about -25 to $+10\,\mathrm{km\,s^{-1}}$ as seen in the absorption line system at $z_{\mathrm{abs}} = 2.11$ toward the quasar PKS 1448−232. We note that the LP data can accurately be fitted with a simultaneous 3-component fit. The velocity restframe was chosen to be at $z_{\mathrm{abs}} = 2.11$ (LP data, LOS toward PKS 1448−232).

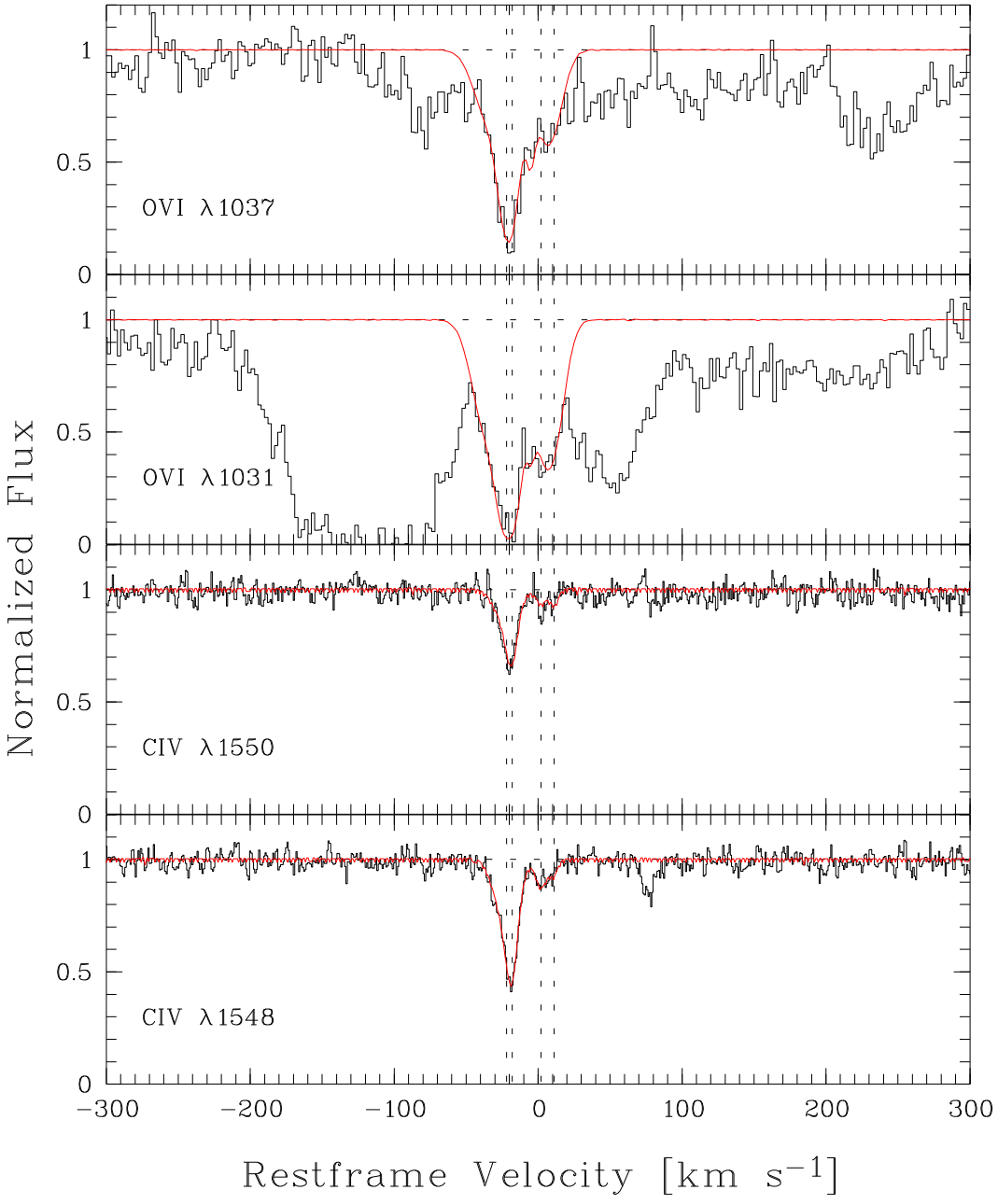

Figure 10.4.: C IV and O VI absorption feature at about -25 to $+10\,\mathrm{km\,s^{-1}}$ as seen in the absorption line system at $z_{\mathrm{abs}} = 2.11$ toward the quasar PKS 1448−232. We note that the HR data can accurately be fitted with a simultaneous 4-component fit. The velocity restframe was chosen to be at $z_{\mathrm{abs}} = 2.11$ (HR data, LOS toward PKS 1448−232.

A. Collisional Ionization and the Saha Equation

The number of collisional ionizations per unit volume and time is given by

$$R_{\mathrm{u}\to\infty} = n_e n_{\mathrm{i}}^{\mathrm{u}} \alpha_{\mathrm{u}\to\infty}, \tag{A.1}$$

with $\alpha_{\mathrm{u}\to\infty}$ the collision-ionization coefficient, n_e the electron volume density, and $n_{\mathrm{i}}^{\mathrm{u}}$ the atomic volume density with i the ionization level and u the excitation state. In the case of hydrogen and hydrogen-like atoms, (A.1) can be approximated (see Seaton 1960) as

$$\alpha_{\mathrm{u}\to\infty} \approx 7.8\times10^{-11}\sqrt{T}\mathfrak{n}^3 \exp\left(-\frac{E_{\mathrm{ion},\mathfrak{n}}}{k_{\mathrm{B}}T}\right), \tag{A.2}$$

with $\mathfrak{n}$ the principal quantum number of the corresponding energy level $E_{\mathrm{ion},\mathfrak{n}}$.

When assuming local thermodynamical equilibrium (LTE), the ionization of the gas is described by the *Saha equation* [1] and we can write

$$\frac{n_{2,\forall}\, n_e}{n_{1,\forall}} = \frac{\gamma_1(T)}{\gamma_2(T)}\left(\frac{4\pi m_e k_{\mathrm{B}}T}{h^2}\right)^{2/3} \exp\left(-\frac{E_{\mathrm{ion}}}{k_{\mathrm{B}}T}\right), \tag{A.3}$$

where, by definition,

$$\gamma(T) \doteq \sum_{\mathrm{i}=1}^{\infty} g_{\mathrm{i}} \exp\left(\frac{-E_{1\mathrm{i}}}{k_{\mathrm{B}}T}\right). \tag{A.4}$$

[1] The Saha equation describes the degree of ionization in LTE as a function of the temperature, density, and ionization energies of the atoms, i.e., $\frac{n_{2,1}n_e}{n_{1,1}} = \frac{g_{2,1}}{g_{1,1}}\left(\frac{4\pi m_e k_{\mathrm{B}}T}{h^2}\right)^{2/3}\exp\left(-\frac{E_{\mathrm{ion}}}{k_{\mathrm{B}}T}\right)$.

B. Equivalent Width

Using (4.8) and (4.1), (4.23) can be written as

$$
\begin{aligned}
W_\lambda &= \int_{\lambda_1}^{\lambda_2} 1 - \exp\left(- \int_{\mathrm{a}}^{\mathrm{b}} \frac{\pi e^2}{m_\mathrm{e} c} n_\mathrm{l} f_\mathrm{lu} \phi(\lambda) \mathrm{d}x \right) \mathrm{d}\lambda \\
&= \int_{\lambda_1}^{\lambda_2} 1 - \exp\left(- \int_{\mathrm{a}}^{\mathrm{b}} \frac{\pi e^2}{m_\mathrm{e} c} n_\mathrm{l} f_\mathrm{lu} \frac{1}{\sqrt{\pi} 2\pi \Delta_\mathrm{t}} H(\alpha, z) \mathrm{d}x \right) \mathrm{d}\lambda,
\end{aligned}
$$

using (4.5) and the fact that $c = \lambda \nu$ will then yield

$$
= \int_{\lambda_1}^{\lambda_2} 1 - \exp\left(- \int_{\mathrm{a}}^{\mathrm{b}} \frac{\pi e^2}{m_\mathrm{e} c} n_\mathrm{l} f_\mathrm{lu} \frac{\lambda_0}{\sqrt{\pi} 2\pi b_\mathrm{th}} H(\alpha, z) \mathrm{d}x \right) \mathrm{d}\lambda. \qquad \text{(B.1)}
$$

C. Solar Abundances

Table C.1.: Ionization potentials and solar abundances as listed in (1) Morton (2003), based on data from Grevesse & Sauval (2002), (2) Allende Prieto et al. (2001), and (3) Asplund et al. (2005).

Element	Symbol	Atomic	Ionization Potentials [eV]			$\log(N(\mathrm{X})/N(\mathrm{H}))_\odot + 12$		
		Number	I	II	II	(1)	(2)	(3)
Hydrogen	H	1	13.59843			12.00		12.00
Deuterium	D	1	13.60213			7.00		
Helium	He	2	24.58739	54.41776		10.99		10.93
Lithium	Li	3	5.39172	75.6400	122.4542	3.31		1.05
Beryllium	Be	4	9.32270	18.21115	153.8954	1.42		1.38
Boron	B	5	8.29802	25.1548	93.9306	2.79		2.70
Carbon	C	6	11.26030	24.3833	47.8878	8.52		8.39
Nitrogen	N	7	14.53413	29.6013	47.4492	7.95		7.78
Oxygen	O	8	13.61805	35.12113	54.9355	8.73	8.69	8.66
Fluorine	F	9	17.42282	34.9708	62.7083	4.48		4.56
Neon	Ne	10	21.56454	40.96296	63.4227	8.06		7.84
Sodium	Na	11	5.13908	47.2864	71.6200	6.32		6.17
Magnesium	Mg	12	7.64623	15.03527	80.1437	7.58		7.53
Aluminum	Al	13	5.98577	18.82855	28.44764	6.49		6.37
Silicon	Si	14	8.15168	16.34584	33.49300	7.56		7.51
Phosphorus	P	15	10.48669	19.76946	30.20263	5.56		5.36
Sulfur	S	16	10.36001	23.33788	34.79	7.20		7.14
Chlorine	Cl	17	12.96763	23.8136	39.61	5.28		5.50
Argon	Ar	18	15.75961	27.62966	40.735	6.40		6.18
Potassium	K	19	4.34066	31.63	45.8060	5.13		5.08
Calcium	Ca	20	6.11316	11.87172	50.9131	6.35		6.31
Scandium	Sc	21	6.56149	12.79977	24.75685	3.10		3.05
Titanium	Ti	22	6.82812	13.576	27.4917	4.94		4.90
Vanadium	V	23	6.74619	14.618	29.311	4.02		4.00
Chromium	Cr	24	6.76651	16.4857	30.959	5.69		5.64
Manganese	Mn	25	7.43402	15.6400	33.668	5.53		5.39
Iron	Fe	26	7.9024	16.188	30.651	7.50		7.45
Cobalt	Co	27	7.88101	17.084	33.50	4.91		4.92
Nickel	Ni	28	7.6398	18.16884	35.187	6.25		6.23
Copper	Cu	29	7.72637	20.29239	36.841	4.29		4.21
Zinc	Zn	30	9.39420	17.9644	39.7233	4.67		4.60
Gallium	Ga	31	5.99930	20.5151	30.726	3.13		2.88

D. Ionization Calculus Chapter 8

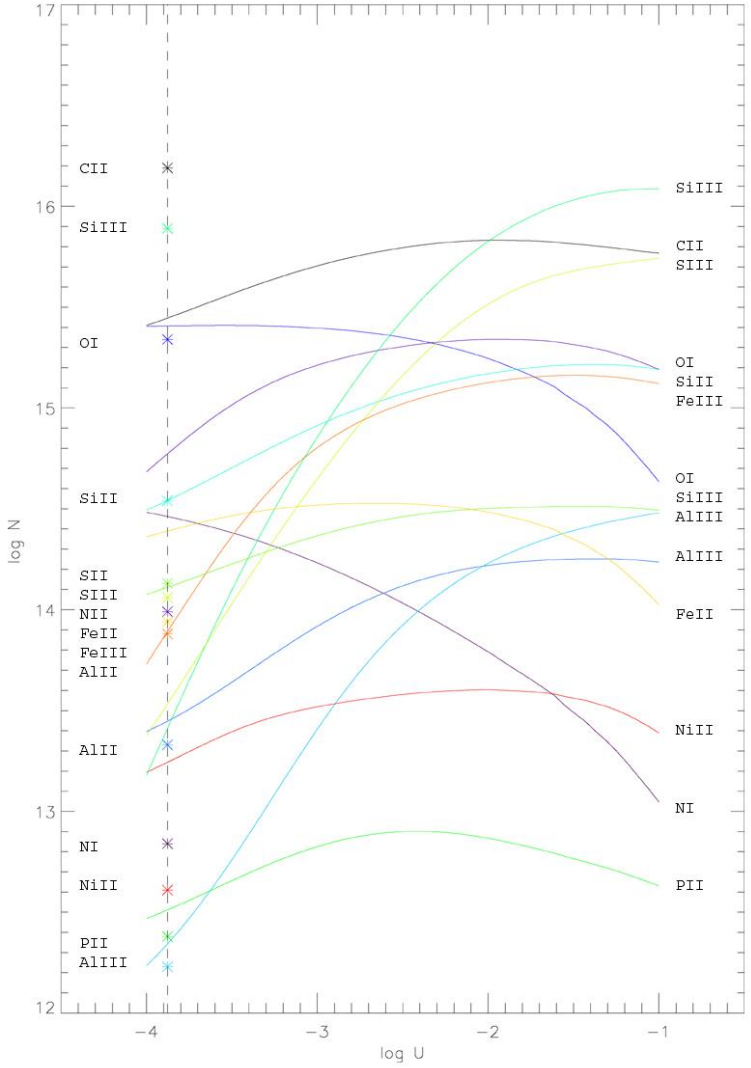

Figure D.1.: `Cloudy` model for the ionization correction of complex B.

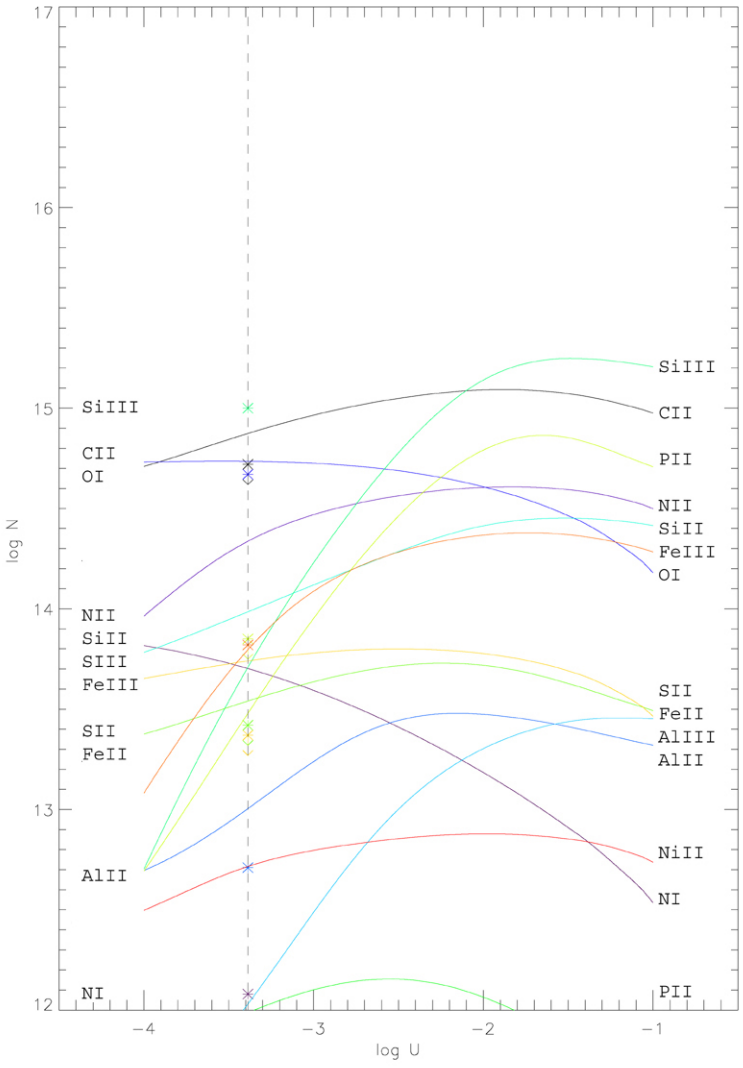

Figure D.2.: `Cloudy` model for the ionization correction of complex C.

E. The FITLYMAN Software Package

With the introduction of echelle spectrographs at 4 m class telescopes in the early 90's it became feasible to observe faint objects (up to 18^{m}) with high resolution ($R = \lambda/\Delta\lambda > 20\,000$). This made it possible to derive independently the column density, N, and the Doppler parameter, b, from line profile fitting – a data reduction method with significant advantage to the classical approaches like the derivation of these values from the COG analysis. Voigt profile fitting by numerical minimization of χ^2 (e.g., Carswell et al. 1991; Giallongo et al. 1993) is also more efficient and more precise than other approaches like (1) the interactive construction of a Voigt profile until a satisfactory solution has been achieved (Mar & Bailey 1995) or (2) the comparison of absorption lines from a photoionization model with the observed spectra (Wampler et al. 1995).

With the FITLYMAN package Fontana & Ballester (1995) have realized a software tool that is properly tailored for all the different needs and special aspects regarding absorption line systems. FITLYMAN is released together with the ESO MIDAS software package and is available in the Lyman context of MIDAS 94SEP and above. For the analyses presented in this work, I have used the MIDAS 03SEPpl1.0 and MIDAS 05SEPpl1.3 releases. The FITLYMAN user interface consist of four menu items (FILE, PARAMETERS, OPERATIONS, and GRAPHICS) which will be discussed in the remaining part of this section. The aim of section is not give a full program description, which does unfortunately not exist, but rather a kind of guideline for the daily use of the FITLYMAN package.

E.0.1. Starting FITLYMAN

FITLYMAN is an interactive command-line interface for the fitting of absorption lines in high resolution spectra and runs in the ESO MIDAS environment. It uses a menu-driven interface to allow the user to specify the lines to be fitted and displays the data on the default graphics window. FITLYMAN performs a global χ-square minimization using the MINUIT package developed at CERN. A complete trace of all the fits performed by FITLYMAN is stored in suited tables in

the ESO MIDAS tbl-format, where the parameters are permanently stored in three tables: LYPAR.tbl, LYLIM.tbl , and LYMIN.tlb. In order to start the FITLYMAN program, the following commands in ESO MIDAS have to be executed:

```
Midas 001> SET/CONTEXT lyman
Midas 002> CREATE/GRAPH
Midas 003> FIT/LYMAN spectrum.tbl ?  ?  ?  Y
```

The first line enables the lyman context in MIDAS and makes the following new commands available:

BATCH/LYMAN	Procedure for non-interactive fitting of a list of lines.
COMPUTE/LYMAN	Computes a synthetic spectrum (normalized at unit flux) from a list of absorption lines.
CONVERT/LYMAN	Converts a spectrum in image format into the FIT/LYMAN table format.
CURSOR/LYMAN	Reads the cursor from the plot of a spectrum made with PLOT/LYMAN.
INIT/LYMAN	Initializes the Lyman package. Creates or updates LYPAR, LYMIN.tbl, and LYLIM.tbl.
FIT/DIRECT	Performs a single fit of absorption lines without any interaction with the user.
FIT/LYMAN	An interactive program for the fitting of absorption lines in high resolution spectra.
PLOT/LYMAN	Plots a spectrum table on a multiple window in the FIT/LYMAN fashion.
PLOT/REDSHIFT	Plots a spectrum table on a multiple window in the FIT/LYMAN fashion.

The focus of this section will be on the FIT/LYMAN command. After the lyman context is enabled the CREATE/GRAPH command in the second line creates a graphics window (using XWindow), necessary for the graphical output. Finally, the third line launches the program itself, where the full syntax is

```
FIT/LYMAN spec [outtab] [log] [session] [graph(Y/N)].
```

More details about the different commands can also be found in the ESO MIDAS help section.

When FITLYMAN is started it automatically loads the data from the previous session (unless the session parameter was specified). The user interface consists of four main menu items:

```
FILE              PARAMETERS      OPERATIONS        GRAPHICS

sa(V)e session    (N)ew           (S)TANDARD MINIM. define (W)indow
(R)ecover session (I)terate       edit (P)aram      plot (B)ackwards
se(T)up           load from lo(G) edit (L)imits     plot (F)orward
(E)ND                             edit (M)inuit     (C)ursor
                                  (D)irect minimize
```

E.0.2. The FILE Menu Item

The FILE menu item manages the storage of different sessions (but does not save any fitting results) and allows the user to modify the setup options for the tables and parameters used, the minimization parameters, as well as the graphic output.

sa(V)e session – Saves all the settings of the current session (including program settings and the current parameter table) to a tbl-file. The spectrum of the resulting fit is *not* saved but can be easily reproduced once the session is reloaded. Note that the program does not warn the user if a session file with the same name already exists but overwrites it without prompting.

(R)ecover session – Recovers any session which has been saved with the sa(V)e session command.

se(T)up – The table names and options for the in- and output (output table, log name, graphic output, and turbulence parameter) can be defined with the (P)rogram set-up option. The (D)ata set-up option allows the user to restrict fitting parameter ranges such as the wavelength, the column density, and the non-turbulent and the turbulent *b*-parameter. Further, the iterations steps for the wavelength (0.0050), the column density (0.0100), and the non-turbulent (0.0100) and the turbulent (0.0100) Doppler parameter can be modified (default values in brackets). Finally, the colors, heights, labels, residuals, variance, reference lines, tick marks, and other parameters for the graphical output can be set in the (G)raphic set-up menu. The user should note that, in general, the FITLYMAN program only accepts changes or settings when an option is com-

pleted by the (E)nd command. No changes or options will be saved when the user quits the previous menu item using the (Q)uit command.

(E)ND – Terminates the program and returns back to MIDAS without prompting.

E.0.3. The PARAMETERS Menu Item

(N)ew – The current parameter table can be viewed and edited by the edit (P)aram command. The command (N)ew resets the current parameter table, by default, to an empty table.

(I)terate – Shows the current line configuration (that can be viewed or edited by the (S)TANDARD MINIM. command) and the current parameter table.

load from lo(G) – Reloads fitting results that were saved after the fitting procedure was accomplished. The fitting results are identified with ID numbers and are stored in a file with the extension "FIT" to the spectrum name, e.g., spectrumFIT.tbl. The corresponding parameter table and the line configuration are automatically loaded together with the fitting results.

E.0.4. The OPERATIONS Menu Item

(S)TANDARD MINIM. – This is the menu item in which the user specifies the current line configuration. This includes the number of absorbing components (Number of groups of lines), the number and identifier of the different absorption lines (Number of lines and Element name), the line grouping (S = single, M = multiple), some estimated values for the line center, column density, and *b*-parameter, and the wavelength intervals. The transition lines have to be from the same element and must have identical ionization levels, i.e., a common column density and *b*-parameter. Species from different elements and different ionization levels can be fitted using the edit (P)aram menu item.

edit (P)aram – Allows the user to edit the current parameter table and therefore to simultaneously fit a combination of absorption lines from different elements and with different ionization levels, i.e., absorption lines with different values for *b* and *N*. Only individual values can be edited or added via a rather user-unfriendly line-command syntax. A practical method that is more efficient and strongly improves the usability is given in E.0.7. Typing exit or quit returns back to the main menu with or without, respectively, saving the modification.

edit (L)imits – The wavelength intervals in which the absorptions take place are either specified at the end of the (S)TANDARD MINIM. command or directly by the edit (L)imits menu item.

edit (M)inuit – The numerical minimization is performed using the MINUIT software package developed at CERN. Numerous fitting options are available, where the most frequently used fit options are the (S)tandard procedure (MINIMIZE+HESSIAN ERRORS) and the (C)urrent instruction set commands.

(D)irect minimize – Executes the minimization procedure using the current parameter settings.

E.0.5. The GRAPHICS Menu Item

define (W)indow – Allows the user to define specific and multiple sections of the spectrum in the graphics window, either in wavelength or velocity space.

plot (B)ackwards – Displaces the selected section of spectrum down by 80 % of the selection width.

plot (F)orward – Displaces the selected section of spectrum up by 80 % of the selection width.

(C)ursor – Right click provides the flux and position in wavelength in units of Å (in wavelength space), or the flux and relative position to the velocity restframe in units of $\mathrm{km\,s^{-1}}$ (in velocity space) of the actual cursor position. Left click quits this function.

E.0.6. Modus Operandi

Modus operandi for a set of absorption lines of the same element and the same ionization level:

- define (W)indow
- (S)TANDARD MINIM.: The number of components, the number of absorption lines, their identifier and other information have to be entered (use M=multiple). The fit options are (S)tandard procedure (MINIMIZE+HESSIAN ERRORS) in case no fitting restrictions are required, or

(C)urrent instruction set if the previously defined fitting restriction (see edit (M)inuit command) shall be used.

- If necessary, the fitting parameters can be forced using the commands edit (M)inuit→(I)nput commands →(F)ix command. Eventually, the fitting procedure can be directly initiated by using the commands (M)inimize →(E)nd→(D)irect minimize.

Modus operandi for a set of absorption lines of different elements and/or with different ionization levels:

- define (W)indow
- edit (P)aram
- edit (L)imits
- (D)irect minimize
- If necessary, fitting parameters can be forced to their initial values, analog to the first case above.

E.0.7. Parameter Table and Output

When the user requires to simultaneously fit absorption lines of different element and / or with different ionization levels, it is no longer possible to make use of the (S)TANDARD MINIM. menu item but one has to directly edit or create the parameter table using the edit (P)aram command. However, editing the parameter table is a very unpleasant and time consuming affair because of its user-unfriendly command-line interface. A more efficient way consists in establishing a text file (which can be easily modified with any text editor program) with all the necessary commands. Instead of entering manually line by line, all required commands compiled in one single file can very simply be copied into the FITLYMAN command line interface. The text editor nedit is most appropriate for this purpose as the carriage return command is simply entered with <Ctrl><Alt><M>. This makes the compilation of the individual commands not only very compact but allows a better overview and handling too. This way FITLYMAN can be fed with hundreds of commands by simply pasting the previously prepared commands from a text editor into the FITLYMAN command line

interface. Note that the number of parameters is limited by the number of absorption lines (`Number of lines`) times the number of components (`Number of groups of lines`) which cannot exceed a value of 100. As an example I show below the parameter table for the low-ionization species for the case of the DLA system toward the Quasar Q0913+072 (see also Chapter 6).

```
 # Element        lambda          column den.      b             bT

 1 CII_1036       3749.78 [   1]  13.540 [ 2.F]    0.00 [19.F]    5.30 [20.F]
 2 CII_1334      (4828.72)[ 1.z] (13.540)[ 2.F] (  0.00)[19.F] (  5.30)[20.F]
 3 NI_1199       (4340.32)[ 1.z]  13.000 [   3] (  0.00)[19.F] (  5.30)[20.F]
 4 OI_1039       (3760.24)[ 1.z]  14.120 [ 4.F] (  0.00)[19.F] (  5.30)[20.F]
 5 OI_1302       (4711.63)[ 1.z] (14.120)[ 4.F] (  0.00)[19.F] (  5.30)[20.F]
 6 MgII_2803     (*******)[ 1.z]  13.000 [   6] (  0.00)[19.F] (  5.30)[20.F]
 7 AlII_1670     (6045.41)[ 1.z]  13.000 [   7] (  0.00)[19.F] (  5.30)[20.F]
 8 SiII_1193     (4317.67)[ 1.z]  12.890 [ 8.F] (  0.00)[19.F] (  5.30)[20.F]
 9 SiII_1260     (4560.57)[ 1.z] (12.890)[ 8.F] (  0.00)[19.F] (  5.30)[20.F]
10 SiII_1304     (4719.59)[ 1.z] (12.890)[ 8.F] (  0.00)[19.F] (  5.30)[20.F]
11 SiII_1526     (5524.08)[ 1.z] (12.890)[ 8.F] (  0.00)[19.F] (  5.30)[20.F]
12 FeII_1096     (3968.83)[ 1.z]  12.580 [ 9.F] (  0.00)[19.F] (  5.30)[20.F]
13 FeII_2344     (8482.04)[ 1.z] (12.580)[ 9.F] (  0.00)[19.F] (  5.30)[20.F]
14 FeII_2600     (9408.17)[ 1.z] (12.580)[ 9.F] (  0.00)[19.F] (  5.30)[20.F]
15 FeIII_1122    (4061.61)[ 1.z]  13.000 [  10] (  0.00)[19.F] (  5.30)[20.F]
16 CII_1036       3749.78 [   5]  13.890 [11.F] (  0.00)[19.F]    4.70 [21.F]
17 CII_1334      (4828.72)[ 5.z] (13.890)[11.F] (  0.00)[19.F] (  4.70)[21.F]
18 NI_1199       (4340.32)[ 5.z]  13.000 [  12] (  0.00)[19.F] (  4.70)[21.F]
19 OI_1039       (3760.24)[ 5.z]  14.390 [13.F] (  0.00)[19.F] (  4.70)[21.F]
20 OI_1302       (4711.63)[ 5.z] (14.390)[13.F] (  0.00)[19.F] (  4.70)[21.F]
21 MgII_2803     (*******)[ 5.z]  13.000 [  14] (  0.00)[19.F] (  4.70)[21.F]
22 AlII_1670     (6045.41)[ 5.z]  13.000 [  15] (  0.00)[19.F] (  4.70)[21.F]
23 SiII_1193     (4317.67)[ 5.z]  13.170 [16.F] (  0.00)[19.F] (  4.70)[21.F]
24 SiII_1260     (4560.57)[ 5.z] (13.170)[16.F] (  0.00)[19.F] (  4.70)[21.F]
25 SiII_1304     (4719.59)[ 5.z] (13.170)[16.F] (  0.00)[19.F] (  4.70)[21.F]
26 SiII_1526     (5524.08)[ 5.z] (13.170)[16.F] (  0.00)[19.F] (  4.70)[21.F]
27 FeII_1096     (3968.83)[ 5.z]  12.930 [17.F] (  0.00)[19.F] (  4.70)[21.F]
28 FeII_2344     (8482.04)[ 5.z] (12.930)[17.F] (  0.00)[19.F] (  4.70)[21.F]
29 FeII_2600     (9408.17)[ 5.z] (12.930)[17.F] (  0.00)[19.F] (  4.70)[21.F]
30 FeIII_1122    (4061.61)[ 5.z]  13.000 [  18] (  0.00)[19.F] (  4.70)[21.F]
```

The parameter for b (`19.F`) was forced to zero, because in the case of the DLA system toward the quasar Q0913+072, it is $b_{\rm th}^2 \ll b_{\rm turb}^2$. Further, the parameter `1`, the center of the C II λ 1036 line, was forced using the menu option `edit (M)inuit` → `(I)nput commands` → `(F)ix`. The outcome is shown below:

```
  LamCen  +/-  N     +/-   b   +/-  bT  +/-

3749.78 0.00  13.54 0.00  0.0 0.0  5.3 0.0  CII_1036
4828.72 0.00  13.54 0.00  0.0 0.0  5.3 0.0  CII_1334
```

```
 4340.32 0.00  12.13 0.11  0.0 0.0  5.3 0.0  NI_1199
 3760.24 0.00  14.12 0.00  0.0 0.0  5.3 0.0  OI_1039
 4711.63 0.00  14.12 0.00  0.0 0.0  5.3 0.0  OI_1302
10143.99 0.00  12.68 0.07  0.0 0.0  5.3 0.0  MgII_2803
 6045.41 0.00  11.38 0.04  0.0 0.0  5.3 0.0  AlII_1670
 4317.67 0.00  12.89 0.00  0.0 0.0  5.3 0.0  SiII_1193
 4560.57 0.00  12.89 0.00  0.0 0.0  5.3 0.0  SiII_1260
 4719.59 0.00  12.89 0.00  0.0 0.0  5.3 0.0  SiII_1304
 5524.08 0.00  12.89 0.00  0.0 0.0  5.3 0.0  SiII_1526
 3968.83 0.00  12.58 0.00  0.0 0.0  5.3 0.0  FeII_1096
 8482.04 0.00  12.58 0.00  0.0 0.0  5.3 0.0  FeII_2344
 9408.17 0.00  12.58 0.00  0.0 0.0  5.3 0.0  FeII_2600
 4061.61 0.00  12.87 0.05  0.0 0.0  5.3 0.0  FeIII_1122
 3749.94 0.00  13.89 0.00  0.0 0.0  4.7 0.0  CII_1036
 4828.92 0.00  13.89 0.00  0.0 0.0  4.7 0.0  CII_1334
 4340.50 0.00  12.39 0.07  0.0 0.0  4.7 0.0  NI_1199
 3760.39 0.00  14.39 0.00  0.0 0.0  4.7 0.0  OI_1039
 4711.83 0.00  14.39 0.00  0.0 0.0  4.7 0.0  OI_1302
10144.41 0.00  13.38 0.13  0.0 0.0  4.7 0.0  MgII_2803
 6045.66 0.00  11.66 0.02  0.0 0.0  4.7 0.0  AlII_1670
 4317.85 0.00  13.17 0.00  0.0 0.0  4.7 0.0  SiII_1193
 4560.76 0.00  13.17 0.00  0.0 0.0  4.7 0.0  SiII_1260
 4719.79 0.00  13.17 0.00  0.0 0.0  4.7 0.0  SiII_1304
 5524.31 0.00  13.17 0.00  0.0 0.0  4.7 0.0  SiII_1526
 3969.00 0.00  12.93 0.00  0.0 0.0  4.7 0.0  FeII_1096
 8482.39 0.00  12.93 0.00  0.0 0.0  4.7 0.0  FeII_2344
 9408.57 0.00  12.93 0.00  0.0 0.0  4.7 0.0  FeII_2600
 4061.77 0.00  13.14 0.03  0.0 0.0  4.7 0.0  FeIII_1122
```

After the output of the fitting results the user is asked by `FITLYMAN` if the results shall be saved. When prompting `Y`, then the "synthetic spectrum", i.e., the minimized absorption line profile, will be saved to `spectrumFIT.tbl`, where `spectrum.tbl` is the input file.

E.0.8. Continuum Normalization

A spectrum can be normalized in many different ways. Although there exists a large variety of different algorithms, practice has shown that the human eye is still more efficient and especially more reliable for the normalization of stellar spectra or spectra from QAL systems[1] than any existing program. I have found the `Spectralyzor` software package (Marggraf 2004) especially useful in order to normalize spectra from QAL systems. Any spectrum in text-format can be loaded (`File`→`Spectrum`→`Load Spectrum`) and normalized by simply clicking onto the spectrum. The normalized spectrum then can be exported

[1] An exception is, of course, the case when one does not focus on one main absorbing system at a given redshift but rather on the numerous Ly α absorbing systems in the whole spectrum.

(File→Spectrum→Save normalized) in text-format. In order to convert the txt-file into a tbl-file, the following command have to be executed within the MIDAS environment:

```
Midas 001> CREATE/TABLE q0913norm 4 195808 q0913norm.txt formatnorm.fmt
Midas 002> COMPUTE/TABLE q0913norm :FWHM =:WAVE/45000
Midas 003> COMPUTE/TABLE q0913norm :STDEV =0.01
```

More detailed information about the individual commands can be found in the MIDAS help section, simply by typing, e.g., Midas 001> HELP CREATE/TABLE.

E.0.9. Hints for the Daily Use and Bug Report

Abnormal program termination during fitting process

FITLYMAN sometimes abnormally quits a fitting process with the error message:

```
(ERR) Problems in executing
/usr/astro/midas03SEP/03SEP/contrib/exec/fitlyman.exe
Child killed by signal 6
```

A new start of FITLYMAN is no longer possible until the files LY*.tbl and fd*.* are deleted. The settings will be lost (unless the session was previously saved) and FITLYMAN restarts with default settings.

Fitting boundaries not taken into account

An other common but not documented problem is when the se(T)up option is used. If, for example, the very helpful sub-menu (D)ata set-up is used in order to constrain fitting limits, one has to note that the changes are not automatically taken into account for the next fitting process unless all entries under (S)TANDARD MINIM. are re-entered or confirmed.

Graphics display in velocity space

The option (V)elocity space causes, on some installations, an abnormal program termination. The reason for this is not known but apparently depends on the installation of the FITLYMAN software package or the computer's configuration.

Problems with the Conversion into the `tbl` format

When a `tbl`-file is created from an other table, it can happen that the fitting lines in `FITLYMAN` are not smooth but appear rather in jagged shape, especially on the outer sides of the absorption lines. However, this problem can be easily fixed when copying the corresponding wavelength values for a previous `tbl` file, e.g.,

```
Midas 004> copy/tt q0913 :wave q0913norm :wave
```

F. Lookback Time

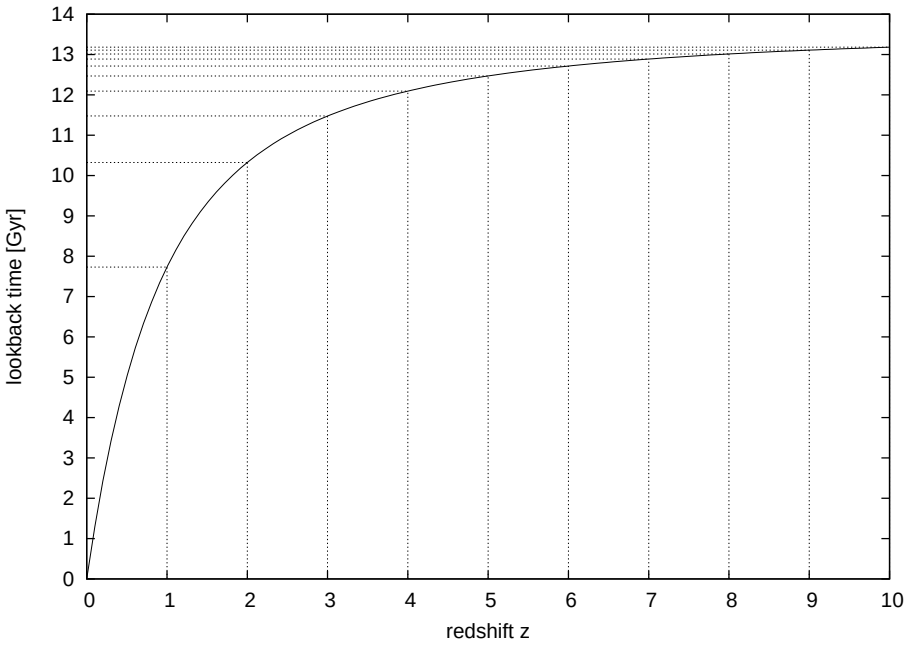

Figure F.1.: Lookback time in Gyr versus redshift, using $H_0 = 71\,\mathrm{km\,s^{-1}}$, $\Omega_\mathrm{m} = 0.27$, and $\Omega_\mathrm{tot} = 1$.

z	lookback time
0.1	1.286
0.2	2.408
0.5	5.019
1	7.731
2	10.324
3	11.476
4	12.094
5	12.469
6	12.715
7	12.888
8	13.014
9	13.109
10	13.183
15	13.391
20	13.483
1000	13.665
∞	13.665

lookback time	z
1	0.08
2	0.16
3	0.26
4	0.37
5	0.50
6	0.65
7	0.84
8	1.07
9	1.36
10	1.81
11	2.50
12	3.81
13	7.88
13.665	∞

G. Common Acronyms & Abbreviations

AAT	Anglo-Australian Telescope
ALFALFA	Arecibo Legacy Fast ALFA (Arecibo L-band Feed Array) Survey
AGB	Asymptotic Giant Branch (shell He burning)
AGN	Active Galactic Nucleus
AIFA	Argelander-Institut für Astronomie, Bonn, Germany
ALMA	Atacama Large Millimeter Array
AOD	Apparent Optical Depth
APEX	Atacama Pathfinder EXperiment
BB	Big Bang
BBN	Big Band Nucleosynthesis
SBBN	Standard Big Band Nucleosynthesis
BH	Black Hole
CCDF	Column Density Distribution Function
CDM	Cold Dark Matter
CELT	California Extremely Large Telescope (30 m)
CERN	Centre Européen pour la Recherche Nucleaire
CES	Coudé Echelle Spectrometer (ESO 3.6 m)
CFHT	Canada-France-Hawaii Telescope (20 m)
CIE	Collisional Ionization Equilibrium
CM	Color Magnitude (Diagram)
CM	Cold Medium (dust)
CMB	Cosmic Microwave Background
COG	Curve of Growth
CoI	Co-Investigator
COS	Cosmic Origins Spectrograph
CRIRES	High-Resolution IR Echelle Spectrometer (VLT/UT1)
CTIO	Cerro Tololo Inter-American Observatory

DEX	Decimal Exponent
DLA	Damped Ly α (system)
DM	Dark Matter
EAS	European Space Agency
ETC	Exposure Time Calculator
EIS	ESO Imaging Survey
ELT	Extremely Large Telescope
EMMI	ESO Multi-Mode Instrument (NTT)
EMP	(also EMS or XMP) Extremely Metal-Poor (Star): $[\mathrm{Fe/H}] < -3.0$
EMS	see EMP
EoR	Epoch of Reionization
ESA	European Space Agency
ESI	Echelle Spectrograph and Imager (Keck)
ESO	European Southern Observatory
ETC	Exposure Time Calculator
EURO50	European 50 m Telescope
EW	Equivalent Width
E-ELT	European Extremely Large Telescope (ESO)
FEROS	Fiber-fed Extended Range Optical Spectrograph (MPG/ESO 2.2 m)
FLAMES	Fiber Large Array Multi Element Spectrograph (VLT/UT2)
FMF	First Mass Function (i.e., the IMF of the first stars)
FORS1	Visual and near UV FOcal Reducer and low dispersion Spectrograph (VLT/UT2)
FORS2	Visual and near UV FOcal Reducer and low dispersion Spectrograph (VLT/UT1)
FUSE	Far Ultraviolet Spectroscopic Explorer (launched June 24, 1999)
GALEX	Galaxy Evolution Explorer (launched April 28, 2003)
GC	Globular Cluster
GIRAFFE	Medium-high resolution ($R = 7500 - 30\,000$) spectrograph for the entire visual range, fed by FLAMES
GMT	Giant Magellan Telescope (with the resolving power of a 24.5 m primary mirror)
GP	Gunn-Peterson
GPE	Gunn-Peterson Effect
GRB	Gamma-Ray Burst
GSMT	Giant Segmented Mirror Telescope (30 m)
HARPS	High Accuracy Radial velocity Planet Searcher (ESO 3.6 m)

HB	Horizontal Branch (core He burning)
HIPASS	H I Parkes All-Sky Survey (installed at the 64 m Parkes Telescope, Australia)
HIRES	High Resolution Echelle Spectrometer (Keck Telescope on Mauna Kea, Hawaii, USA)
HN	Hypernova (pl.: HNe – Hypernovae)
HM	Hot Medium (dust)
HMP	Hyper Metal-Poor (Star): $[\mathrm{Fe/H}] < -5.0$
HR	High Resolution
HRD	Hertzsprung-Russel Diagram
HST	Hubble Space Telescope
HVC	High-Velocity Cloud
IAU	International Astronomical Union
ICF	Ionization Correction Factor
ICM	Intra-Cluster Medium
IGM	Inter-Galactic Medium
IMF	Initial Mass Function
IMPRS	International Max-Planck Research School
INT	Isaac Newton Telescope
IP	Ionization Potential
IR	Infrared
ISAAC	Infrared Spectrometer And Array Camera (VLT/UT1)
ISM	Interstellar Medium
JELT	Japanese ELT Telescope (30 m)
JWST	James-Webb Space Telescope
KECK	Two 10 m telescopes (*Keck I* and *Keck II*) on Mauna Kea, Hawaii, named after William Myron Keck (1880-1964)
LAT	Large Atacama Telescope (25 m infrared telescope)
LBG	Lyman Break Galaxy
LLS	Lyman Limit System
LMC	Large Magellanic Cloud
LOS	Line of Sight
LP	Large Programme
LSS	Large Scale Structures
LTE	Local Thermodynamic Equilibrium
Ly α	Lyman alpha
MACHO	MAssive Compact Halo Object
ML	Mass Luminosity

MMP	Mega Metal-Poor (Star): $[\mathrm{Fe/H}] < -6.0$
MP	Metal-Poor (Star): $[\mathrm{Fe/H}] < -1.0$
MPG	Max-Planck-Gesellschaft
MS	Main Sequence (core H burning)
MW	Milkyway
NASA	National Aeronautics and Space Administration
NIR	Near Infra-Red
NS	Neutron Star
NTT	New Technology Telescope, an Alt-Az, 3.58 m Richey-Chrétien telescope which pioneered the use of active optics
OB	Observation Block
OPC	Observing Programmes Committee
OWL	Overwhelmingly Large (Telescope)
PDF	Probability Distribution Function
PN	Planetary Nebula
PI	Project Investigator
PIC	Photoionization Correction
PISN	Pair Instability Supernova – sometimes also referred to as Pair Production Supernova (PPSN or $\mathrm{SN}_{\gamma\gamma}$)
PSPC	Position Sensitive Proportional Counters (aboard ROSAT)
QAL	Quasar Absorption Line (system / spectroscopy)
QSO	Quasi Stellar Radio-Object (or Quasar for short)
REW	Rest-Frame Equivalent Width
RG	Red Giant
RGB	Red Giant Branch (shell H burning)
ROSAT	ROentgen SATellite (launched June 1990, turned off in February 1999)
SBBN	Standard Big Bang Nucleosynthesis
SDSS	Sloan Digital Sky Survey
SED	Spectral Energy Distribution
SERC	Science and Engineering Research Council (UK)
SFR	Star Formation Rate
SGB	Subgiant Branch (transition from core to shell H burning)
SMC	Small Magellanic Cloud
SMR	Super Metal-Rich (Star)
SN	Supernova (pl.: SNe – Supernovae)
SNR	Supernova Remnant
SNR	(also S/N) Signal-To-Noise Ratio

SPH	Smoothed Particle Hydrodynamics
STIS	Space Telescope Imaging Spectrograph (aboard HST)
SWIFT	A multi-wavelength observatory (launched on November 20, 2004) dedicated to the study of GRB science, and that "swiftly" ($\sim 20-75$ s) points itself onto GRB events.
SZE	Sunyaev-Zeldovic Effect
TMT	Thirty Meter Telescope
UMP	Ultra Metal-Poor (Star): $[\mathrm{Fe/H}] < -4.0$
UV	Ultraviolet
UVES	UV-Visual Echelle Spectrograph (VLT/UT2)
V	Visual
VLA	Very Large Array, New Mexico
VLT	Very Large Telescope (ESO), Mount Paranal, Chile
VMBH	Very Massive Black Hole
VMP	Very Metal-Poor (Star): $[\mathrm{Fe/H}] < -2.0$
VMS	Very Massive Stars
WD	White Dwarf
WFC3	Wide Field Camera 3 (aboard HST)
WHIM	Warm Hot Intergalactic Medium
WHIMP	Weakly Interacting Massive Particle
WIFI	Wide Field Imager at the ESO/MPG-2.2 m telescope, La Silla, Chile
WIM	Warm Intercloud Medium
WR	Wolf-Rayet (Star)
XMP	see EMP
ZAMS	Zero Age Main-Sequence
ΛCDM	Lambda Cold Dark Matter

Bibliography

Abazajian, K., Adelman-McCarthy, J., Agüeros, M., et al. 2005, AJ, 129, 1755 39

Abgrall, H., Le Bourlot, J., Pineau des Forêts, G., et al. 1992, A&A, 253, 525 97

Adelberger, K. 2005, IAU Colloquium Proceedings of the International Astronomical Union 199, held March 14-18, 2005, Shanghai, People's Republic of China, edited by Williams, P.R., Shu, C.G., and Menard. B., Cambridge University Press, 341 26

Akerman, C., Carigi, L., Nissen, P., Pettini, M., & Asplund, M. 2004, A&A, 414, 931 82, 84, 120

Allende Prieto, C., Lambert, D., & Asplund, M. 2001, ApJ, 556, 63 81, 89, 142, 144, 181

Aoki, W., Norris, J., Ryan, S., Beers, T., & Ando, H. 2002, PASJ, 54, 933 83

Asplund, M., Grevesse, N., & Sauval, A. 2005, ASP Conference Series, Vol. 336, Proceedings of a symposium held 17-19 June, 2004, Austin, Texas. Eds. Barnes, T.G., and Bash, F.N., 336, 25 89, 181

Baade, W. 1944, ApJ, 100, 137 105

Bahcall, J. & Salpeter, E. 1966, ApJ, 144, 847 37

Bajtlik, S., Duncan, R., & Ostriker, J. 1988, ApJ, 327, 570 21

Ballester, P., Modigliani, A., Boitquin, O., et al. 2000, ESO Messenger, volume = 101, pages = 31 49

Barnes, D., Staveley-Smith, L., & de Blok, W. 2001, MNRAS, 322, 486 153

Becker, R., Fan, X., White, R., et al. 2001, AJ, 122, 2850 34

Beers, T. & Christlieb, N. 2005, ARA&A, 43, 531 82, 106

Bergeron, J., Aracil, B., Petitjean, P., & Pichon, C. 2002, A&A, 396, 11 167, 168

Bergeron, J. & Herbert-Fort, S. 2005, IAU 199 Conference Proceeding 22

Bergeron, J., Petitjean, P., Aracil, B., et al. 2004, The ESO Messenger, 118, 40 126

Blades, J., Turnshek, D., & Norman, C. 1988, Proceedings of the QSO Absorp-

tion Line Meeting, Baltimore, MD, May 19-21, 1987. Cambridge University Press 1988, 28977 14

Bouwens, R. & Illingworth, G. 2006, NewAR, 50, 152 27

Bowen, D., Huchtmeier, W., Brinks, E., Tripp, T., & Jenkins, E. 2001, A&A, 372, 820 25

Bregman, J., Dupke, R., & Miller, E. 2004, ApJ, 614, 31 28

Bromm, V., Kudritzki, R., & Loeb, A. 2001, ApJ, 552, 464 70

Bruenn, S. & Haxton, W. 1991, ApJ, 376, 678 104

Bullock, J., Kravtsov, A., & Weinberg, D. 2000, ApJ, 539, 517 152

Bunker, A., Stanway, E., Ellis, R., & McMahon, R. 2004, MNRAS, 355, 374 27

Burbidge, E., Lynds, C., & Stockton, A. 1968, ApJ, 152, 1077 37

Burles, S. & Tytler, D. 1998a, ApJ, 499, 699 144

Burles, S. & Tytler, D. 1998b, ApJ, 507, 732 144

Carswell, B., Schaye, J., & Kim, T. 2002, ApJ, 578, 43 167

Carswell, R., Lanzetta, K., Parnell, H., & Webb, J. 1991, ApJ, 371, 36 185

Carswell, R., Webb, J., Baldwin, J., & Atwood, B. 1987, ApJ, 319, 709 16

Carswell, R., Webb, J., Lanzetta, K., et al. 1996, MNRAS, 278, 506 126, 142, 144, 145

Cayrel, R., Depagne, E., Spite, M., et al. 2004, A&A, 416, 1117 109, 113

Cen, R. & Ostriker, J. 1999a, ApJ, 519, 109 166

Cen, R. & Ostriker, J. 1999b, ApJ, 514, 1 28

Centurión, M., Molaro, P., Vladilo, G., et al. 2003, A&A, 403, 55 78, 80, 115

Chernomordik, V. 1988, Soviet Astr., 32, 362 126

Chernomordik, V. 1995, ApJ, 440, 431 126

Chiappini, C. & Matteucci, F. 2000, IAUS, 198, 540 142

Chieffi, A. & Limongi, M. 2002, ApJ, 577, 281 83, 84, 120

Christlieb, N., Bessell, M. S., Beers, T. C., et al. 2002, Nature, 419, 904 70, 106, 113

Churchill, C., Rigby, J., Charlton, J., & Vogt, S. 1999, ApJS, 120, 15 157

Churchill, C. & Vogt, S. 2001, AJ, 122, 679 157

Churchill, C., Vogt, S., & Charlton, J. 2003, AJ, 125, 98 157

Churchill, C. W. 1997, PhD thesis, University of California, Santa Cruz 47

Ciardi, B. & Ferrara, A. 2005, Space Science Reviews, 116, 625 69

Coc, A., Vangioni-Flam, E., Descouvemont, P., Adahchour, A., & Angulo, C. 2004, ApJ, 600, 544 142

Cowan, R. & Dieke, G. 1948, Rev. Mod. Phys. 20, 20, 418 46
Cruddace, R., Paresce, F., Bowyer, S., & Lampton, M. 1974, ApJ, 187, 497 30
Dahle, H., Pedersen, K., Lilje, P., Maddox, S., & Kaiser, N. 2003, ApJ, 591, 662 153
Daigne, F., Olive, K. A., Vangioni-Flam, E., Silk, J., & Audouze, J. 2004, ApJ, 617, 693 88
Danforth, C. & Shull, J. 2005, ApJ, 624, 555 28
Dartois, E. 2005, ASPC, 344, 113 63
Davé, R., Cen, R., Ostriker, J., et al. 2001, ApJ, 552, 473 12, 166
Davé, R., Hernquist, L., Katz, N., & Weinberg, D. 1999, ApJ, 511, 521 28
Davies, J., Minchin, R., & Sabatini, S. 2004, MNRAS, 349, 922 153
Dekker, H., D'Odorico, S., Kaufer, A., Delabre, B., & Kotzlowski, H. 2000, SPIE, 4008, 534 51
Desai, S., Ashie, Y., Fukuda, S., Fukuda, Y., et al. 2004, Physical Review D, 70, 10 161
Dessauges-Zavadsky, M., D'Odorico, S., McMahon, R., et al. 2001, A&A, 370, 426 115
Dessauges-Zavadsky, M., Prochaska, J., & D'Odorico, S. 2002, A&A, 391, 801 115
Dobrzycki, A., Bechtold, J., Scott, J., & Morita, M. 2002, ApJ, 571, 654 19
Dodelson, S. & Liguori, M. 2006, Physical Review Letters, 97, 23 161
D'Odorico, V. & Molaro, P. 2004, A&A, 415, 879 81, 82, 84
Domínguez, I., Höflich, P., Straniero, O., & Wheeler, C. 2000, MmSAI, 71, 449 102
Drake, G. 1996, AIP, Woodbury, NY 45
Ellison, S. & Lopez, S. 2001, A&A, 380, 117 115
Ellison, S. & Lopez, S. 2002, A&A, 392, 489 115
Erben, T., Miralles, J., Clowe, D., et al. 2003, A&A, 410, 45 153
Erben, T., van Waerbeke, L., & Mellier, Y. 2000, A&A, 355, 23 153
Erni, P., Richter, P., Ledoux, C., & Petitjean, P. 2006, A&A, 451, 19 80, 82, 84, 87, 108, 115
Erni, P. & Tammann, G. 2006, astro-ph/0610291 102
Fall, S., Pei, Y., & McMahon, R. 1989, ApJ, 341, 5 63
Fan, X. 1995, PhD thesis, University of California, San Diego 81
Fan, X. 2006, NewAR, 50, 665 38
Fan, X., Carilli, C. L., & Keating, B. 2006, ARA&A, 44, 415 107

Fan, X., Srauss, M., Schneider, D., et al. 2003, AJ, 125, 1649 27, 37, 38
Fang, L., Bi, H., Xiang, S., & Boerner, G. 1993, ApJ, 413, 477 33
Ferguson, H. C. 2000, ASPC, 216, 395 119
Ferland, G., Korista, K., Verner, D., et al. 1998, PASP, 110, 761 62, 82, 141
Ferrara, A. 2007, 36th Saas Fee Advanced Course: *Cosmological Feedbacks from the First Stars* (Berlin: Springer Verlag), in press 92
Field, G. & Steigman, G. 1971, ApJ, 166, 59 81
Fishman, G. & Meegan, C. 1995, ARA&A, 33, 415 105
Fontana, A. & Ballester, P. 1995, ESO The Messenger, 80, 37 72, 126, 160, 185
Fox, A., Petitjean, P., Ledoux, C., & Srianand, R. 2007, A&A, in press 145, 146, 147
Fox, A., Wakker, B., & Savage, B. 2005, ApJ, 630, 332 147
Frebel, A., Aoki, W., & Christlieb, N. 2005, Nature, 434, 871 70, 106, 113
Giallongo, E., Cristiani, S., Fontana, A., & Trevese, D. 1993, ApJ, 416, 137 185
Giavalisco, M., Dickinson, M., Ferguson, H., et al. 2004, ApJ, 600, 103 27
Glass, I. 1980, MNRAS, 192, 37 126
Gould, R. & Salpeter, E. 1963, ApJ, 138, 393 96
Governato, F., Mayer, L., Wadsley, J., et al. 2004, ApJ, 607, 688 152
Greenstein, J. & Schmidt, M. 1967, APJ, 148, 13 37
Grevesse, N. & Anders, E. 1991, in: *Solar Interior and Atmosphere*, University of Arizona Press, 1227 81
Grevesse, N. & Sauval, A. 2002, Adv. Space Res., 30, 3 89, 142, 144, 181
Griem, H. 1974, Pure and Applied Physics, New York: Academic Press 46
Gunn, J. & Peterson, B. 1965, ApJ, 142, 1633 33
Haardt, F. & Madau, P. 1996, ApJ, 461, 20 141
Hachisu, I., Kato, M., & Nomoto, K. 1996, ApJ, 470, 97 102
Haehnelt, M., Steinmetz, M., & Rauch, M. 1998, ApJ, 495, 647 26
Hamana, T., Miyazaki, S., Shimasaku, K., et al. 2003, ApJ, 597, 98 154
Hayashi, E., Navarro, J., Taylor, J., Stadel, J., & Quinn, T. 2003, ApJ, 584, 541 152
Heger, A. & Woosley, S. 2002, ApJ, 567, 532 69, 70
Henry, R., Edmunds, M., & Köppen, J. 2000, ApJ, 541, 660 79
Hoeflich, P. & Khokhlov, A. 1996, ApJ, 457, 500 102
Hoell, J. & Priester, W. 1991, A&A, 251, 23 126
Hollenbach, D. & McKee, C. 1989, ApJ, 342, 306 98

Hook, I. 2005, ed., *The science case for the European Extremely Large Telescope : the next step in mankind's quest for the Universe*, OPTICON and ESO 35

Howell, D., Sullivan, M., Nugent, P., et al. 2006, Nature, 443, 308 102

Hoyle, F. & Fowler, W. 1960, ApJ, 132, 565 102

Hu, E., Kim, T., Cowie, L., Songaila, A., & Rauch, M. 1995, AJ, 110, 1526 17

Hunstead, R., Murdoch, H., Pettini, M., & Blades, J. 1988, ApJ, 329, 527 20

Iben, I. & Tutukov, A. 1984, ApJ Supplement Series, 54, 335 102

Irwin, M. 2006, *Statistics in Astronomy*: statistics in astronomy lecture notes, http://www.ast.cam.ac.uk/˜mike 65

Israelian, G., Shchukina, N., Rebolo, R., et al. 2004, A&A, 419, 1095 83

Izotov, Y. & Thuan, T. 2004, ApJ, 616, 768 78

Jannuzi, B., Bahcall, J., Bergeron, J., et al. 1998, ApJS, 118, 1 22

Jimenez, R., Heavens, A., Hawkins, M., & Padoan, P. 1997, MNRAS, 292, 5 152

Kahre, P. 2006, Seminar on March 20, 2006, at the Indian Institute of Astrophysics, Bangalore, India 64

Kawata, D. 2001, ApJ, 558, 598 84

Keel, W. 2000, http://www.astr.ua.edu/keel/galaxies/ 14

Kirkman, D., Tytler, D., Burles, S., Lubin, D., & O'Meara, J. 2000, ApJ, 529, 655 144

Kitaura, F., Janka, H., & Hillebrandt, W. 2006, A&A, 450, 345 103

Klebesadel, R., Strong, I., & Olson, R. 1973, ApJ, 182, 85 105

Klypin, A., Kravtsov, A., Valenzuela, O., & Prada, F. 1999, ApJ, 522, 82 152

Knuth, E. 1996, *The art of computer programming*, Vol. II: Seminumerical algorithms, Addison Wesley 65

Kobayashi, C., Tsujimoto, T., Nomoto, K., Hachisu, I., & Kato, M. 1998, ApJ, 503, 155 83, 102

Kobayashi, C., Umeda, H., Nomoto, K., Tominaga, N., & Ohkubo, T. 2006, astro-ph/0608688 84, 86, 88, 110, 112, 118, 119

Kobayashi, N., Terada, H., Goto, M., & Tokunaga, A. 2002, ApJ, 569, 676 27

Konjević, N. 1999, Proceedings of the XII National Conference of Yugoslav Astronomers and International Workshop on the Development of Astronomical Databases, Belgrade, 19-21 November, 1999. Eds.: Popović, L.Č and Dačić 46

Kravtsov, A., Gnedin, O., & Klypin, A. 2004, ApJ, 609, 482 152

Kroupa, P., Tout, C., & Gilmore, G. 1993, MNRAS, 262, 545 86
Kulkarni, V. & Fall, S. 2002, ApJ, 580, 732 64
Lanfranchi, G. & Friaça, A. 2003, MNRAS, 343, 481 78, 80
Lanzetta, K., Wolfe, A., & Turnshek, D. 1995, ApJ, 440, 435 71
Larson, R. 2003, ASPC, 287, 65 100
Le Bourlot, J., Pineau des Forêts, G., & Flower, D. 1999, MNRAS, 305, 802 95
Le Brun, V., Bergeron, J., Boisse, P., & Deharveng, J. 1997, A&A, 321, 733 26
Ledoux, C., Petitjean, P., Bergeron, J., Wampler, E., & Srianand, R. 1998, A&A, 337, 51 71, 75
Ledoux, C., Petitjean, P., & Srianand, R. 2003, MNRAS, 346, 209 82, 141
Ledoux, C., Srianand, R., & Petitjean, P. 2002, A&A, 392, 781 115
Lehner, N., Savage, B., Wakker, B., Sembach, K., & Tripp, T. 2006, ApJS, 164, 1 28
Levshakov, S., Agafonova, I., Centurión, M., & Mazets, I. 2002a, A&A, 383, 813 81
Levshakov, S., Agafonova, I., Centurión, M., & Molaro, P. 2003a, A&A, 397, 851 81
Levshakov, S., Agafonova, I., D'Odorico, S., Wolfe, A., & Dessauges-Zavadsky, M. 2003b, ApJ, 582, 596 81
Levshakov, S., Dessauges-Zavadsky, M., D'Odorico, S., & Molaro, P. 2002b, ApJ, 565, 696 115
Limongi, M. & Tornambe, A. 1991, ApJ, 371, 317 102
Lockman, F., Hobbs, L., & Shull, J. 1986, ApJ, 301, 380 25
Loewenstein, M. 2001, ApJ, 557, 573 105
Lopez, S., Reimers, D., D'Odorico, S., & Prochaska, J. 2002, A&A, 385, 778 115
Lopez, S., Reimers, D., Rauch, M., Sargent, W., & Smette, A. 1999, ApJ, 513, 598 115
Lu, L., Sargent, W., Savage, B., et al. 1998, AJ, 115, 162 115
Lu, L., Sargent, W. W., Barlow, T., Churchill, C., & Vogt, S. 1996, ApJS, 107, 475 115
Madau, P., Ferguson, H., Dickinson, M., et al. 1996, MNRAS, 283, 1388 119
Madau, P., Ferrara, A., & Rees, M. 2001, ApJ, 555, 92 26
Malhotra, S. 1997, ApJ, 488, 101 63
Mar, D. & Bailey, G. 1995, PASA, 12, 239 185
Marggraf, O. 2004, PhD thesis, University of Bonn 192

Matteucci, F. & Calura, F. 2005, MNRAS, 360, 447 80
McKee, C. & Ostriker, J. 1977, ApJ, 218, 148 63
McWilliam, A., Preston, G. W., Sneden, C., & Searle, L. 1995, AJ, 109, 2757 82
Milgrom, M. 1983, ApJ, 270, 384 161
Miller, G. & Scalo, J. 1979, ApJS, 41, 513 86
Minchin, R., Davies, J., Disney, M., et al. 2005, ApJ, 622, 21 150, 152, 153, 155
Miralda-Escudé, J., Cen, R., Ostriker, J., & Rauch, M. 1996, ApJ, 471, 582 20
Miralles, J., Erben, T., Hämmerle, H., et al. 2002, A&A, 388, 68 153
Mitchell, A. & Zemanski, M. 1971, Cambridge Univeristy Press 46
Molaro, P., Levshakov, S., D'Odorico, S., Bonifacio, P., & Centurión, M. 2001, ApJ, 549, 90 115
Montier, L. A. & Giard, M. 2004, A&A, 417, 401 94
Moore, B., Ghigna, S., Governato, F., et al. 1999, ApJ, 524, 19 152
Moorwood, A., Cuby, J., Biereichel, P., et al. 1998, ESO Messenger, 94, 7 27
Morton, D. 1991, ApJS, 77, 119 126
Morton, D. 2003, ApJ, 149, 205 75, 89, 141, 142, 144, 181
Nakamura, F. & Umemura, M. 2001, ApJ, 548, 19 70
Nestor, D. 2004, University of Pittsburgh, Publication Number: AAT 3188281. DAI-B 66/08, p. 4272 21
Nissen, P., Asplund, M., Lambert, D., Primas, F., & Smith, V. 2005, ESO Messenger, 122, 32 47
Nomoto, K. 1980, Space Science Reviews, 27, 563 102
Nomoto, K. 1982, ApJ, 253, 798 102
Nomoto, K., Iwamoto, K., & Kishimoto, N. 1997, Science, 276, 1378 102
Nomoto, K. & Sugimoto, D. 1977, Publications of the Astronomical Society of Japan, 29, 765 102
Nomoto, K., Yamaoka, H., Shigeyama, T., Kumagai, S., & Tsujimoto, T. 1994, Proceedings of the 54th École d'été de physique théorique, session LIV, held in Les Houches, Haute-Savoie, France, 31 July - 1 September, 1990. Eds. Bludman, S.A., Mochkovitch, R., and Zinn-Justin, J. Published by Elsevier Science B. V. 1994 102
Noterdaeme, P. 2005, M2R Astrophysique et Milieux Dilués, Grenoble, France 66
Oh, S., Nollett, K., Madau, P., & Wasserburg, G. 2001, ApJ, 562, L1 70

O'Meara, J., Tytler, D., Kirkman, D., et al. 2001, ApJ, 552, 718 142, 144
Omukai, K. 2000, ApJ, 534, 809 97
Omukai, K. & Nishi, R. 1999, ApJ, 518, 640 99
Omukai, K. & Palla, F. 2003, ApJ, 589, 677 69
Omukai, K. & Yoshii, Y. 2003, ApJ, 599, 746 70
Oort, J. 1926, Publications of the Kapteyn Astronomical Laboratory Groningen, 40, 1 105
Osterbrock, D. & Ferland, G. 2006, in *Astrophysics of Gaseous nebulae & Active Galactic Nuclei*, second edition, University Science Press 63
Pei, Y., Fall, S., & Bechtold, J. 1991, ApJ, 378, 6 63
Penton, S. V., Stocke, J. T., & Shull, J. M. 2004, AAS, 204, 7901 19
Péroux, C., Dessauges-Zavadsky, M., Kim, T., D'Odorico, S., & McMahon, R. 2003, MSAIS, 3, 261 22, 23, 71, 125
Péroux, C., Petitjean, P., Aracil, B., & Srianand, R. 2002, NewA, 7, 577 115
Petitjean, P. & Bergeron, J. 1990, A&A, 231, 309 157
Petitjean, P. & Charlot, S. 1997, Proceedings of the 13th IAP Astrophysics Colloquium, 1-5 July, 1997, IAP. Editions Frontieres 1997. 14
Petitjean, P., Srianand, R., & Ledoux, C. 2002, MNRAS, 332, 383 115
Petitjean, P., Webb, J., Rauch, M., Carswell, R., & Lanzetta, K. 1993, MNRAS, 262, 499 17
Pettini, M., Ellison, S., Bergeron, J., & Petitjean, P. 2002, A&A, 391, 21 78, 115
Pettini, M., Ellison, S., Steidel, C., & Bowen, D. 1999, ApJ, 510, 576 115
Pettini, M., Madau, P., Bolte, M., et al. 2003, ApJ, 594, 695 27
Pettini, M., Smith, L., Hunstead, R. W., & King, D. 1994, ApJ, 426, 79 64
Pettini, M., Steidel, C., Adelberger, K., Dickinson, M., & Giavalisco, M. 2000, ApJ, 528, 96 115
Porciani, C. & Madau, P. 2005, ApJ, 625, 43 26
Prochaska, J., Gawiser, E., Wolfe, A., Castro, S., & Djorgovski, S. 2003, ApJ, 959, L9 23, 24, 75
Prochaska, J., Henry, R., O'Meara, J., et al. 2002, PASP, 114, 993 79
Prochaska, J., Weiner, B., Chen, H., & Mulchaey, J. 2006, ApJ, 643, 680 28
Prochaska, J. & Wolfe, A. 1997, ApJ, 487, 73 25
Prochaska, J. & Wolfe, A. 2002, ApJ, 566, 68 115, 118
Prochaska, J., Wolfe, A., Tytler, D., et al. 2001, ApJS, 137, 21 115
Rao, S., Nestor, D., Turnshek, D., et al. 2003, ApJ, 595, 94 26

Rao, S. & Turnshek, D. 2000, ApJS, 130, 1 24, 26, 71, 155
Rauch, M. 1998, ARA&A, 36, 267 14
Rauch, M., Sargent, W., & Barlow, T. 1999, ApJ, 515, 500 169
Richter, P., Fang, T., & Bryan, G. 2006, A&A, 451, 767 31
Richter, P., Ledoux, C., Petitjean, P., & Bergeron, J. 2005, A&A, 440, 819 71, 78, 115, 125, 162
Richter, P., Savage, B., Tripp, T., & Sembach, K. 2004, ApJS, 153, 165 167
Ripamonti, E., Haardt, F., Ferrara, A., & Colpi, M. 2002, MNRAS, 334, 401 99
Ryan-Weber, E., Pettini, M., & Madau, P. 2006, MNRAS, 371, 78 27
Salpeter, E. 1955, ApJ, 121, 161 86
Sargent, W., Boksenberg, A., & Steidel, C. 1988, ApJS, 68, 539 26
Sargent, W., Young, P., Boksenberg, A., & Tytler, D. 1980, ApJS, 42, 41 20
Savage, B., Lehner, N., Wakker, B., Sembach, K., & Tripp, T. 2005, ApJ, 626, 776 28
Savage, B. & Sembach, K. 1991, ApJ, 379, 245 57
Scalo, J. 1986, Fundamentals of Cosmic Physics, 11, 1 86
Scheuer, P. 1965, Nature, 207, 963 33
Schmidt, M. 1963, Nature, 197, 1040 37
Schneider, R. 2006, NewAR, 50, 64 101
Schneider, R., Ferrara, A., Natara, P., & Omukai, K. 2002, ApJ, 571, 30 70, 97
Schultz, D. 2004, *General Physics I: Mechanics Lab Manual*,CWRU Bookstore 67
Seaton, M. 1960, MNRAS, 120, 326 177
Sembach, K., Tripp, T., Savage, B., & Richter, P. 2004, ApJ Supplement Series, 155, 351 28
Simcoe, R., Sargent, W., & Rauch, M. 2002, ApJ, 578, 737 167
Songaila, A. 2001, ApJ, 561, 153 23, 26
Songaila, A. 2005, AJ, 130, 1996 26
Songaila, A. & Cowie, L. 1996, AJ, 112, 335 81
Spergel, D., Bean, R., Dore, O., et al. 2006, astro-ph/0603449 11
Spergel, D., Verde, L., Peiris, H., et al. 2003, ApJS, 148, 175 33
Spite, M., Cayrel, R., Hill, V., et al. 2006, A&A, 455, 291 109, 113, 115
Spite, M., Cayrel, R., Plez, B., et al. 2005, A&A, 430, 655 78, 82, 84, 109
Spitzer, L. J. & Fitzpatrick, E. 1995, ApJ, 445, 196 25
Stocke, J., Penton, S., Danforth, C., et al. 2006, ApJ, 641, 217 28
Stoehr, F., White, S., Tormen, G., & Springel, V. 2002, MNRAS, 335, 84 152

Storrie-Lombardi, L. & Wolfe, A. 2000, ApJ, 543, 552 24, 71
Strolger, L., Riess, A., & Dahlen, T. 2004, ApJ, 613, 200 83, 102
Susa, H. & Umemura, M. 2004, ApJ, 610, 5 152
Theuns, T., Viel, M., & Kay, S. 2002, ApJ, 578, 5 167
Tosi, M. 1996, ASPC, 98, 299 142
Tripp, T., Aracil, B., Bowen, D., & Jenkins, E. 2006, ApJ, 643, 77 28
Tripp, T., Savage, B., & Jenkins, E. 2000, ApJ, 534, 1 28, 166
Tumlinson, J., Shull, J., Rachford, B., et al. 2002, ApJ, 566, 857 66
Tumlinson, J., Venkatesan, A., & Shull, J. 2004, ApJ, 612, 602 85
Tytler, D. 1987, ApJ, 321, 49 16, 17, 20
Tytler, D. & Burles, S. 1997, in *Origin of matter and evolution of galaxies in the universe*, Atami, Japan, 18-20 January 1996. World Scientific 1997, eds. T. Kajino, Y. Yoshii, and S. Kubono, Singapore, 37 144
Tytler, D., Fan, X., & Burles, S. 1996, Nature, 381, 207 144
Ulmer, A. 1996, ApJ, 473, 110 19
Umeda, H. & Nomoto, K. 2001, in: *Birth and Evolution of the Universe*, eds. K. Sato & M. Kawasaki, Universal Academy Press, 257 88
Umeda, H. & Nomoto, K. 2002, ApJ, 565, 385 87, 88, 104, 111, 112
Umetsu, K. & Futamase, T. 2000, ApJ, 539, 5 153
Varshni, Y. P. 1989, 1989Ap&SS, 153, 153 126
Verde, L., Oh, S., & Jimenez, R. 2002, MNRAS, 336, 541 152
Viegas, S. 1995, MNRAS, 276, 268 25, 62
Vladilo, G. 2002, A&A, 391, 407 82, 141
Vladilo, G., Centurión, M., Bonifacio, P., & Howk, J. 2001, ApJ, 557, 1007 25
Voit, G. 2005, Rev. Mod. Phys., 77, 207 28
von der Linden, A., Erben, T., Schneider, P., & Castander, F. J. 2006, A&A, 454, 37 151, 153
Wampler, E., Chugai, N., & Petitjean, P. 1995, ApJ, 443, 586 185
Wegmann, C. 1939, Geologische Rundschau, 30, 389 8
Weinberg, D., Burles, S., Croft, R., et al. 1998, astro-ph/9810142 33, 34
Westphalen, G., Kalberla, P., Hartmann, D., & Burton, W. 1997, Ap&SS, 252, 289 25
Weymann, R., Carswell, R., & Smith, M. 1981, ARA&A, 19, 41 14, 16
Weymann, R., Jannuzi, B., & Lu, L. a. d. 1998, ApJ, 506, 1 22
Wheeler, J., Akiyama, S., & Williams, P. 2005, Ap&SS, 298, 3 104
Wolfe, A., Lanzetta, K., Flotz, C., & Chaffee, F. 1995, ApJ, 454, 698 24, 71

Wolfe, A., Turnshek, D., Smith, H., & Cohen, R. 1986, ApJS, 61, 249 22
Woosley, S. & Weaver, T. 1994, ApJ, 423, 371 102
Woosley, S. E. 1993, ApJ, 405, 273 105
Wright, E. & Kleinmann, D. 1978, Nature, 275, 298 126
York, D., Khare, P., Vanden Berk, D., et al. 2006, MNRAS, 367, 945 39

Publications

Early Nucleosynthesis Studies with Quasar Absorption Line Spectroscopy
Erni, P., 2006, PhD thesis,
http://hss.ulb.uni-bonn.de/diss_online/math_nat_fak/2007

Unveiling the nature of dark clumps via QSO absorption line spectroscopy
Erni, P., Richter, P., Schneider, et al. 2006, A&A, in prep.

Colliding galaxies detected by quasar absorption line spectroscopy
Erni, P., Richter, P., Ledoux, C., Petitjean, P., & Bergeron, J. 2006, A&A, in prep.

Can Λ be determined from nearby Type Ia Supernovae?
Erni, P. & Tammann, G.A. 2006, astro-ph/0610291

The most metal-poor damped Lyman α system at $z < 3$: constraints on early nucleosynthesis
Erni, P., Richter, P., Ledoux, C., & Petitjean, P. 2006, A&A, 451, 19

The damped Lyman Alpha absorber toward Q0913+072
Erni, P., Richter, P. & Ledoux, C.
Proceedings of the conference *Baryons in Dark Matter Halos*, Novigrad, Croatia, 5-9 Oct 2004
Editors: R. Dettmar, U. Klein, P. Salucci. Published by SISSA

Die mysteriöse Dunkle Energie im Universum
Erni, P. 2004, Orion 320, 4

Conferences, Seminars, Talks, and Posters

Early Nucleosynthesis Studies with Quasar Absorption Line Spectroscopy
Argelander-Institut für Astronomie, Univeristy of Bonn, Germany, March 2007 (PhD defense)

Quasar Absorption Line Spectroscopy, the Intergalactic Medium and early Nucleosynthesis
MPIfR Bonn, Germany, July 2006 (IMPRS seminar talk)

The most metal-poor DLA system at $z < 3$: constraints on early Nucleosynthesis
Poster at the conference *The First Stars and Evolution of the Early Universe*, UW/INT Seattle, USA, July 3-7 2006

36th Saas Fee Advanced Course: *First light in the Universe*, Les Diablerets, Switzerland, April 3 - 8 2006

The most metal-poor DLA system at $z < 3$: constraints on early Nucleosynthesis
Poster at the annual meeting of the german *Astronomische Gesellschaft*, Cologne, Germany, September 2005

The most metal-poor DLA system at $z < 3$: constraints on early Nucleosynthesis
Poster at the conference *Open Questions in Cosmology*, Garching, Germany, 22-26 August 2005

Primordial imprints in very metal-deficient DLA systems
RTN Meeting, Seeon, Germany, August 2005 (RTN seminar talk)

Chemical Abundances in Quasar Absorption Line Systems
MPIfR Bonn, Germany, July 2005 (IMPRS seminar talk)

Time Variations of the Fine Structure Constant α
AIFA Bonn, Germany, May 2005 (group seminar talk)

Carbon and Nitrogen Abundances in QSO Absorption Line Systems
Geneva Observatory, Switzerland, January 2005 (invited seminar talk)

Nearby Type Ia Supernovae and their Implication on Cosmology
Universidad de Concepción, Chile, December 2004 (seminar talk)

Chemical Abundances of the DLA system at $z = 2.618$ toward Q0913+072
Poster at the *Second Advanced Chilean School of Astrophysics*, Universidad Católica de Chile,
Santiago de Chile, 6-10 December 2004

Abundances from QSO Absorption Line Systems and very early Nucleosynthesis
MPIfR Bonn, Germany, November 2004 (IMPRS seminar talk)

Chemical Abundances of the DLA system at $z = 2.618$ toward Q0913+072
Poster and Talk at the conference *Baryons in Dark Matter Halos*, Novigrad, Croatia, 5-9 October 2004

Can Λ be determined by nearby Type Ia Supernovae?
IAEF Bonn, Germany, May 2003 (group seminar talk)

Evolution Effects in Type Ia Supernovae
IMPRS Retreat, Braunfels, Germany, May 2005 (group seminar talk)

Nearby Type Ia Supernovae and their cosmological Implications
University of Concepción, Chile, December 2004 (invited seminar talk)

Bestimmung der kosmologischen Konstante mittels SNe Ia
AIP, Potsdam, Germany, November 2003 (invited seminar talk)

Bestimmung der kosmologischen Konstante mittels SNe Ia
GRK Meeting, University of Bochum, Germany, October 2003 (invited seminar talk)

Acknowledgements

I would like to thank Prof. Dr. Peter Schneider and Prof. Dr. Klaas S. de Boer for all their energy, professionalism and knowledge that they have brought to my thesis. Special thanks go to Dr. Philipp Richter for his valued direction and for his continued support for my varied professional and personal endeavors and achievements. I further thank Prof. Dr. Herbert Petry and Prof. Dr. Reinhard Klein for being part of my thesis committee. Next, I would like to thank all my collaborators: Dr. Patrick Petitjean, Dr. Thomas Erben, Dr. Jacqueline Bergeron, Dr. Mischa Schirmer, Alessio Fangano, and especially Dr. Cédric Ledoux for his unerring assistance and expertise. Also, I would like to thank Dr. Chiaki Kobayashi, Prof. Dr. Kenichi Nomoto, Dr. Monique Spite, Prof. Dr. Andrea Ferrara, and Prof. Dr. Richard Ellis for their kind guidance through their field of expertise, for their inspiration and for having provided the necessary data for my research. Many thanks go to Prof. Dr. Frank Bertoldi as a member of my IMPRS thesis committee and to Nadya Ben Bekhti for proofreading. Finally, my sincerest thanks to Dr. Ole Marggraf for his unfailing support and enjoyable personality at all times.